NASA Contractor Report 3642

Aeroelastic Loads Prediction for an Arrow Wing

Task III - Evaluation of the Boeing Three-Dimensional Leading-Edge Vortex Code

Marjorie E. Manro

CONTRACT NAS1-15678
APRIL 1983

NASA

NASA Contractor Report 3642

Aeroelastic Loads Prediction for an Arrow Wing

Task III - Evaluation of the Boeing Three-Dimensional Leading-Edge Vortex Code

Marjorie E. Manro
Boeing Commercial Airplane Company
Seattle, Washington

Prepared for
Langley Research Center
under Contract NAS1-15678

National Aeronautics
and Space Administration

Scientific and Technical
Information Branch

1983

CONTENTS

Page

SUMMARY 1

INTRODUCTION 2

SYMBOLS 4

DATA BASE 6
  Wind Tunnel Models 6
  Wind Tunnel Testing 6
  Data 6

BACKGROUND 8

DESCRIPTION OF THE METHOD 9
  Theoretical Model 9
  Numerical Procedure 10
  Solution Procedure 10
    Quasi-Newton Solution 12
    Least-Squares Solution 13
  Physical Model 13
    Wing Paneling 13
    Vortex Paneling 14
    Wakes 14
  Control Parameters 14
  Convergence Criteria 15

EVALUATION 16
  Full-Span Vortex 17
    Comparison to Previous Evaluation 17
    Streamwise Wing Paneling 18
    Twisted and Cambered-Twisted Wings 18
    Flat Wing With Thickness 19
    Effect of Fuselage 19
  Partial-Span Vortex 20
    Standard Solution 21
    Size of Initial Vortex 22
    Weighting Factor on Twist Function 24
    Effect of Thickness 25

CONCLUSIONS AND RECOMMENDATIONS 27

APPENDIX A. DESCRIPTION OF DATA BASE 29

APPENDIX B. DATA REDUCTION 71

REFERENCES 80

LIST OF TABLES

Page

1. Summary of Subsonic/Transonic Test Conditions by Test and Run Number .. 7
2. Network Types, Uses, and Boundary Conditions 11
3. Summary of Results for Partial-Span Vortex with Two Initial Sizes of Vortex 23
4. Summary of Results for Partial-Span Vortex on Flat Wing with Thickness .. 26
A-1. Wing Half-Thickness Distribution, Percent Chord 30
A-2. Wing Section Camber Definition, Percent Chord 32
A-3. Wing Pressure Orifice Locations, Percent Local Chord 34
A-4. Body Pressure Orifice Locations 41
A-5. Summary of Subsonic/Transonic Test Conditions by Run Number (NASA Contract NAS1-12875) 47
A-6. Summary of Subsonic/Transonic Test Conditions by Run Number (NASA Contract NAS1-14962) 50
A-7. Summary of Supersonic Test Conditions by Run Number. Reynolds Number = 8.65×10^6 (NASA Contract NAS1-14141) 51
B-1. Integration Constants 78

LIST OF FIGURES

Page

A-1. General Arrangement and Characteristics 53
A-2. Spanwise Twist Distribution for the Model Wing 54
A-3. Cambered-Twisted Wing Section Geometry 55
A-4. Fin Geometry, Section at 0.725 Semispan 56
A-5. Pressure Orifice Locations 57
A-6. Control Surface Bracket Details 58
A-7. Boeing Transonic Wind Tunnel 59
A-8. Variation of Reynolds Number and Dynamic Pressure With Mach Number .. 60
A-9. Data Acquisition and Reduction System–Boeing Transonic Wind Tunnel 61
A-10. Schematic of 9- by 7-ft Supersonic Leg of NASA Ames Unitary Wind Tunnel 62
A-11. Data Acquisition and Reduction System–9- by 7-ft Supersonic Leg of NASA Ames Unitary Wind Tunnel 63
A-12. Model in Boeing Transonic Wind Tunnel–Flat Wing; L.E. Deflection, Full Span = 0.0°; T.E. Deflection, Full Span = 0.0° (NASA Contract NAS1-12875) 64
A-13. Model in Boeing Transonic Wind Tunnel–Twisted Wing; T.E. Deflection, Full Span = 0.0°; (NASA Contract NAS1-14962) 65
A-14. Model in Boeing Transonic Wind Tunnel–Cambered-Twisted Wing, Fin Off; T.E. Deflection, Full Span = 0.0°; (NASA Contract NAS1-14962) 66
A-15. Model in Boeing Transonic Wind Tunnel–Cambered-Twisted Wing, Fin On; T.E. Deflection, Full Span = 0.0° (NASA Contract NAS1-14962) 67
A-16. Model Installation in Boeing Transonic Wind Tunnel (NASA Contracts NAS1-12875 and NAS1-14962) 68
A-17. Model in 9- by 7-ft Supersonic Leg of NASA Ames Unitary Wind Tunnel–Flat Wing, Rounded L.E. (NASA Contract NAS1-14141) 69
A-18. Model in 9- by 7-ft Supersonic Leg of NASA Ames Unitary Wind Tunnel–Twisted Wing (NASA Contract NAS1-14141) 69
A-19. Model Installation in 9- by 7-ft Supersonic Leg of NASA Ames Unitary Wind Tunnel (NASA Contract NAS1-14141) 70
B-1. Codes Used to Interpolate and Extrapolate 79
1. General Arrangement and Characteristics 82
2. Spanwise Twist Distribution for the Model Wing 83
3. Cambered-Twisted Wing Section Geometry 83
4. Pressure Orifice Locations 84
5. Flow Model for The Boeing Company Three-Dimensional Leading-Edge Vortex (LEV) Code 85
6. Location of Network Singularity Parameters and Control Points 86
7. Initial Free-Sheet Geometry and Size of Fed Sheet for Various Values of 'a' (ref. 18) 87
8. Previous Evaluation of LEV Computer Code (ref. 4), Flat Wing, Zero Thickness, $M = 0.0$, $\alpha = 16^\circ$ 88
9. Current Evaluation of LEV Computer code, Flat Wing, Zero Thickness, $M = 0.40$, $\alpha = 16^\circ$ 89
10. Geometry of Panel Edges at Constant Body Station, Flat Wing, Zero Thickness, $\Delta a = 0.0$, $M = 0.40$, $\alpha = 16^\circ$, Cycle 6 90
11. Pressure Distributions, Flat Wing, Zero Thickness, $\Delta a = 0.0$, $M = 0.40$, $\alpha = 16^\circ$ 92

LIST OF FIGURES (Continued)

Page

12. Planform View of Streamwise Wing Paneling 101
13. Upper Surface Pressure Distributions, Twisted Wing, Zero Thickness, $\Delta a = 0.0$, $M = 0.40$, $\alpha = 16^0$ 102
14. Panel Geometry, Twisted Wing, Zero Thickness, $\Delta a = 0.0$, $M = 0.40$, $\alpha = 16^0$, Several Cycles 105
15. Upper Surface Pressure Distributions, Cambered-Twisted Wing, Zero Thickness, $\Delta a = 0.0$, $M = 0.40$, $\alpha = 16^0$ 108
16. Panel Geometry, Cambered-Twisted Wing, Zero Thickness, $\Delta a = 0.0$, $M = 0.40$, $\alpha = 16^0$, Several Cycles 111
17. Comparison of Upper Surface Pressure Distributions for Three Wing Shapes, Zero Thickness, $\Delta a = 0.0$, $M = 0.40$, $\alpha = 16^0$ 114
18. Geometry of Panel Edges at Constant Body Stations, Flat Wing, Zero Thickness, Revised Side of Body Definition, Denser Wing Paneling, $\Delta a = 0.6$, $M = 0.40$, $\alpha = 16^0$, Several Cycles 120
19. Pressure Distributions, Flat Wing, Zero Thickness, Revised Side of Body Definition, Denser Wing Paneling, $\Delta a = 0.6$, $M = 0.40$, $\alpha = 16^0$ 122
20. Geometry of Panel Edges at Constant Body Stations, Flat Wing With Thickness, $\Delta a = 0.6$, $M = 0.40$, $\alpha = 16^0$, Several Cycles 131
21. Upper Surface Pressure Distributions, Flat Wing With Thickness, $\Delta a = 0.6$, $M = 0.40$, $\alpha = 16^0$ 134
22. Geomertry of Panel Edges at Constant Body Stations, Flat Wing With Thickness and Fuselage, $M = 0.40$, $\alpha = 16^0$, Several Cycles 139
23. Upper Surface Pressure Distributions, Flat Wing With Thickness and Fuselage, $M = 0.40$, $\alpha = 16^0$ 141
24. Effect of Wing Thickness and Fuselage Representation on Pressure Distributions, Flat Wing, $M = 0.40$, $\alpha = 16^0$ 144
25. Experimental Upper Surface Isobars, Flat and Twisted Wings, $M = 0.40$ 153
26. Experimental Upper Surface Pressure Distributions, Flat Wing, $M = 0.40$ .. 155
27. Upper Surface Pressure Distributions Flat Wing, Zero Thickness, $\Delta a = 0.0$, $M = 0.40$, $\alpha = 6^0$ 161
28. Geometry of Panel Edges at Constant Body Stations, Flat Wing, Zero Thickness, $\Delta a = 0.0$, $M = 0.40$, $\alpha = 6^0$, Cycle 15 164
29. Planform View of Conical Wing Paneling 166
30. Geometry of Panel Edges at Constant Body Stations, Flat Wing, Zero Thickness, Denser Wing Paneling, $\Delta a = 0.6$, $M = 0.40$ $\alpha = 6^0$, Several Cycles 167
31. Upper Surface Pressure Distributions, Flat Wing, Zero Thickness, Denser Wing Paneling, Quasi-Newton Solution, $\Delta a = 0.6$, $M = 0.40$, $\alpha = 6^0$ 169
32. Upper Surface Pressure Distributions, Flat Wing, Zero Thickness, Denser Wing Paneling, Least-Squares Solution, Weight Factor = 1.0, $\Delta a = 0.6$, $M = 0.40$, $\alpha = 6^0$ 172
33. Effect of Solution Method on Upper Surface Pressure Distribution, Flat Wing, Zero Thickness, $\Delta a = 0.6$, $M = 0.40$, $\alpha = 6^0$ 175
34. Geometry of Panel Edges at Constant Body Stations, Effect of Initial Vortex Size and Solution Method on Converged Vortex Shape, Flat Wing, Zero Thickness, $M = 0.40$, $\alpha = 6^0$ 178
35. Comparison of Upper Surface Pressure Distributions for Two Cycles, Flat Wing, Zero Thickness, $\Delta a = 0.0$, $M = 0.40$, $\alpha = 6^0$ 180

LIST OF FIGURES (Concluded)

Page

36. Effect of Initial Vortex Size, Upper Surface Pressure Distributions, Flat Wing, Zero Thickness, Least-Squares Solution, $M = 0.40$, $\alpha = 6^0$ 183
37. Upper Surface Pressure Distributions, Flat Wing, Zero Thickness, Denser Wing Paneling, Least-Squares Solution, Weight Factor = 5.0, $\Delta a = 0.6$, $M = 0.40$, $\alpha = 6^0$ 186
38. Upper Surface Pressure Distributions, Flat Wing, Zero Thickness, Denser Wing Paneling, Least-Squares Solution, Weight Factor = 0.5, $\Delta a = 0.6$, $M = 0.40$, $\alpha = 6^0$ 189
39. Upper Surface Pressure Distributions, Flat Wing, Zero Thickness, Denser Wing Paneling, Least-Squares Solution, Weight Factor = 0.2, $\Delta a = 0.6$, $M = 0.40$, $\alpha = 6^0$ 192
40. Effect of Solution Type and Weight Factor (F) on Twist Function, Rear View of Vortex Geometry, Flat Wing, Zero Thickness, $\Delta a = 0.6$, $M = 0.40$, $\alpha = 6^0$ 195
41. Effect of Weight Factor on Twist Function, Upper Surface Pressure Distributions, Flat Wing, Zero Thickness, Least-Squares Solution, $\Delta a = 0.6$, $M = 0.40$, $\alpha = 6^0$ 196
42. Geometry of Panel Edges at constant Body Stations, Flat Wing With Thickness, $\Delta a = 0.6$, Initial Vortex Rotation Outward, $M = 0.40$, $\alpha = 8^0$, Several Cycles 199
43. Pressure Distributions, Flat Wing With Thickness, $\Delta a = 0.6$, Initial Vortex Rotated Outward, $M = 0.40$, $\alpha = 8^0$ 200

SUMMARY

The accurate prediction of loads on flexible, low aspect-ratio aircraft is critical to the design of reliable and efficient vehicles. The conditions for structural design frequently involve nonlinear aerodynamics.

Under previous NASA contracts (NAS1-12875, NAS1-14141, and NAS1-14962), a large experimental data base for three wing shapes was obtained, and linear theoretical methods were evaluated. The current contract, NAS1-15678, extends the evaluation of state-of-the-art theoretical predictive methods to two separated-flow computer programs and also evaluates a semi-empirical method for incorporating the experimentally measured separated-flow effects into a linear aeroelastic analysis.

The resulting three tasks have been documented separately. This volume describes the evaluation of The Boeing Company's Three-Dimensional Leading-Edge Vortex (LEV) code (Task III). The development and evaluation of a semi-empirical method to predict pressure distributions on a deformed wing by using an experimental data base (Task II) is presented in NASA CR-3641. The evaluation of R. P. White's (RASA Division of Systems Research Laboratories) separated-flow method (Task I) is described in NASA CR-3640.

The Boeing Company's LEV computer code is an improved panel method for three-dimensional inviscid flow over a wing with leading-edge vortex separation. The governing equations are the linear-flow differential equation with nonlinear boundary conditions. The solution is an iterative one in which not only the strength of the vortex, but the position of the free and fed sheets that represent the vortex, are determined.

The current evaluation considered cases at high angle of attack with full-span vortices and cases at moderate angles of attack with partial-span vortices. The effect of paneling options was studied as well as options on the solution procedure. The predicted pressures are quite good and adequately reflect changes in the configuration. It was determined that this method would be useful in an aeroelastic solution. This study has identified several necessary modifications of the code.

INTRODUCTION

Accurate analytical techniques for the prediction of the magnitude and distribution of aeroelastic loads are required in order to achieve an optimum design of the structure of large flexible aircraft. Uncertainties in the characteristics of loads may result in an improper accounting for aeroelastic effects, leading to understrength or overweight designs and unacceptable fatigue life. In addition, the correct prediction of load distribution and the resulting structural deformation are essential to the determination of the aircraft stability and control characteristics, control power requirements, and flutter boundaries. The alternative to using satisfactory analytical techniques is the increased use of expensive, time-consuming wind tunnel testing for each aircraft configuration.

The problem of accurate load prediction becomes particularly acute for aircraft with low aspect-ratio wings where critical design conditions occur in the transonic speed regime. In this region, at typical design angles of attack, the flow is generally nonlinear – mixed flow, embedded shocks, separation, and vortex flow.

A program was started in 1974 to systematically obtain experimental pressure data for an arrow wing throughout the subsonic, transonic, and low supersonic Mach numbers. This program was comprised of three NASA contracts: NAS1-12875, NAS1-14141, and NAS1-14962 (documented in refs. 1 through 12). As the specific objective was to understand the change in load with aeroelastic deformation, three wing shapes were tested – all with the same planform and thickness distribution. The first wing was flat (no camber or twist); the second has a spanwise twist (typical of aeroelastic deformation) but no camber; and, the third has the same twist with camber superimposed.

In addition to the creation of a data base, which is useful for evaluating aeroelastic effects, a second objective was to evaluate state-of-the-art theoretical methods that might be used for this purpose. Primarily these methods were linear, and the evaluations showed that linear theories are adequate at low angles of attack, which are typical of cruise conditions, and are basically capable of predicting loading changes due to smooth changes in wing shape at these low angles. However, at the higher angles of attack typical of structural design conditions, these methods are not useful because the flow is nonlinear due to leading-edge separation of the flow. The limited comparisons that were made with advanced separated-flow methods indicated some hope, even though the aerodynamic panel model available at that time was very crude (only a few panels to represent the camber surface).

The current evaluation of methods for predicting pressure distributions when the flow is separated is divided into three tasks. Two currently available computer codes were evaluated in Tasks I and III, and an approach involving semi-empirical corrections to linear theory was investigated in Task II. The three tasks are essentially independent efforts and are documented separately: Task III, an evaluation of Boeing's Three-Dimensional Leading-Edge Vortex computer code in this document; Task I, an evaluaton of R. P. White's computer code in NASA CR-3640; and Task II, the development and evaluation of a semi-empirical method in NASA CR-3641.

The computer code evaluated in Task III is the Boeing Three-Dimensional Leading-Edge Vortex (LEV) code. The evaluation of this code considered both the accuracy of the predicted pressure distributions and the ease of use of the computer program. Cases studied included a range of typical design conditions: some at high angles of attack with a vortex well established along the entire span; and some at moderate angles of attack with the vortex developed only on the outboard portion of the span. Variations on the input parameters were tried so that an understanding of their effect could be developed, and guidelines for use could be established.

The Boeing Company Three-Dimensional Leading-Edge Vortex code, although generally available, has primarily been used by the Aerodynamics Research Staff of The Boeing Company and personnel at the NASA Langley Research Center. Therefore, a great deal of assistance was obtained from Edward N. Tinoco, Forrester T. Johnson, and David Young of the Aerodynamics Research Staff at The Boeing Company.

SYMBOLS

b	wing span, cm
BL	buttock line, cm; distance outboard from model plane of symmetry
c	section chord length, cm
$\bar{c}$, M.A.C.	mean aerodynamic chord length, cm
C_B	surface bending moment coefficient referenced to y_{ref}; positive wingtip up
C_C	surface chord force coefficient; positive aft
C_c	section chord force coefficient; positive aft
C_M	surface pitching moment coefficient, referenced to 0.25 M.A.C.; positive leading edge up
C_m	section pitching moment coefficient referenced to section leading edge; positive leading edge up
$C_{m.25c}$	section pitching moment coefficient referenced to section 0.25c; positive leading edge up
C_N	surface normal force coefficient; positive up
C_n	section normal force coefficient; positive up
C_p	pressure coefficient $= \dfrac{\text{measured pressure} - \text{reference pressure}}{q}$
D	body diameter, cm
M	Mach number
MS	model station, cm; measured aft along the body centerline from the nose
p_s	static pressure, kN/m^2
p_t	total pressure, kN/m^2
q	dynamic pressure, kN/m^2
S	reference area used for surface coefficients, cm^2
S_h	area of streamwise strip associated with a pressure station, cm^2; used in summation of section force coefficients (app. B)

x, y, z	general coordinates for distances in the longitudinal, lateral, and vertical directions respectively
y_{ref}	distance outboard of model centerline of the bending moment reference point, cm
α	corrected angle of attack, degrees; the angle between the wing-root chord and the relative wind measured in the model plane of symmetry; includes compensation for sting deflection, tunnel-flow angularities, and wall effects; positive nose up with respect to relative wind
α_{sec}	wing twist angle relative to wing reference plane, degrees; positive leading edge up
β	angle of sideslip, degrees; positive nose left with respect to relative wind
β^2	$1.0 - M_\infty^2$
ΔC_p	increment between adjacent lines on isobars
δ	control surface deflection, degrees; positive leading edge down for leading edge (see exception in app. B) and trailing edge down for trailing edge
η	fraction of wing semispan, y/(b/2)
Λ	sweep angle, degrees; measured from a line perpendicular to the model centerline, positive aft
ϕ	perturbation potential

Subscripts:

c	compressibility axis
L.E.	leading-edge control surface
r	wing root
s	referenced to segment of local chord
T.E.	trailing-edge control surface

DATA BASE

The data obtained, both experimental and theoretical, have been presented in several papers (refs. 1 through 3) and are presented in more detail in numerous NASA reports (refs. 4 through 12).

WIND TUNNEL MODELS

The configuration chosen for this study was a thin, low aspect-ratio, highly swept wing mounted below the centerline of a high fineness-ratio body. The general arrangement and characteristics of the model are shown in figure 1. Two complete wings were constructed for contract NAS1-12875, one with no camber or twist, and one with no camber but with a spanwise twist variation. A third wing with camber and twist was constructed for contract NAS1-14962. Deflectable control surfaces were available on all three of these wings.

The three wings, body, and fin used to create this data base are described in detail in appendix A. The wings all have the same planform, thickness distribution, and placement of orifices. The twisted wing and the cambered-twisted wing have the same twist, i.e., the coordinates of the leading edges and trailing edges of the two wings are the same. This twist distribution is shown in figure 2. Sections at the root, midspan, and tip of the cambered-twisted wing (fig. 3) show not only the camber but the position of the sections of the cambered-twisted wing and the twisted wing, relative to the wing reference plane (flat wing). The flat wing had a sharp-leading-edge segment in addition to the rounded-leading-edge segment common to all three wings.

The capability to measure the detailed load distribution on the wing and body of this configuration was provided by distributing 300 pressure orifices on the model. Each wing had 217 pressure orifices equally divided into seven streamwise sections on the left half. Orifices were located on both the top and bottom surfaces at the chordwise locations shown in figure 4. Pressure orifices were located on the body in five streamwise rows of 15 orifices each. An additional eight orifices in the area of the wing-body junction made a total of 83 orifices on the left side of the body.

WIND TUNNEL TESTING

The experimental data used in this study were obtained in the Boeing Transonic Wind Tunnel (BTWT) under NASA contracts NAS1-12875 and NAS1-14962. A description of the tunnel and tests is in appendix A. The current study was limited to the wings with both leading-edge and trailing-edge control surfaces undeflected. Table 1 shows a summary of these data.

DATA

The measured pressures were edited, as necessary, to account for plugged or leaking orifices or missing data points. The pressure coefficients were then integrated, as described in appendix B, to obtain streamwise section coefficients and total surface coefficients. When pressure coefficients were required at points other than where measured, a linear interpolation was used.

Table 1.—Summary of Subsonic/Transonic Test Conditions by Test and Run Number

Contract	Test number	Mach number							Data document
		0.40	0.70	0.85	0.95	1.00	1.05	1.10	
Flat wing, rounded leading edge									
NAS1-12875	BTWT 1415	269	263	267	266	268	264	262	NASA CR-132727
Flat wing, sharp leading edge									
NAS1-12875	BTWT 1415	368	366	372	374	373	367	365	NASA CR-132727
Twisted wing, rounded leading edge									
NAS1-12875 NAS1-14962	BTWT 1415 BTWT 1627	450 15	445 14	449 13	447 12	448 11	446 10	444 –	NASA CR-132727 NASA CR-165701
Cambered-twisted wing, rounded leading edge (fin off)									
NAS1-14962	BTWT 1627	43	41	40	39	38	37	–	NASA CR-165701

BACKGROUND

The Three-Dimensional Leading-Edge Vortex (LEV) computer code has been developed by The Boeing Company for NASA Langley under contracts NAS1-12185, NAS1-13833, NAS1-15169, and NAS1-15275 (refs. 13 and 14 show the current status). At the NASA Langley Research Center this method is referred to as the Free Vortex Sheet (FVS) Theory. Although it was developed as a parallel effort, this method can be viewed as an extension for separated flow of the linearized compressible-flow program PAN AIR (ref. 15). PAN AIR is a higher-order panel method, which was evaluated in NASA contract NAS1-14962.

The forces, moments, and detailed surface pressures on thin wings of arbitrary planform are predicted in the LEV method. The wing geometry is arbitrary in the sense that leading and trailing edges may be swept as well as curved or kinked, provided that a single leading-edge vortex describes the flow, and that the origin of the vortex can be specified. The method does not represent the secondary vortices that often form under the primary leading-edge vortex.

Comparisons of the predictions of this method with experimental data were made under contract NAS1-12875 when the computer program was in a very early stage of development. The predictions were very promising especially in light of the crude paneling available. At that time, the code was for incompressible flow only.

The versatility of the code has been increased greatly; added capabilities include the representation of wing thickness, camber, and twist as well as a fuselage. In addition, the effects of compressibility and many improvements on the numerics have been added.

DESCRIPTION OF THE METHOD

The governing equations for the Boeing Three-Dimensional Leading-Edge Vortex (LEV) computer code are the linear-flow differential equation with nonlinear boundary conditions. These boundary conditions require that the flow be parallel to the wing surface and that the free vortex sheet, springing from the leading and trailing edges (see fig. 5), be aligned with the local flow and support no pressure jump. The Kutta condition is imposed and satisfied along all wing edges. The configuration is represented by quadrilateral panels on all surfaces, with quadratically-varying doublet singularities distributed on the panels. The vortex core is modeled as a simple line vortex that receives vorticity from the free sheet through a connecting kinematic sheet. The set of nonlinear equations is solved by an iterative procedure, starting with an assumed initial geometry of the vortex sheet.

The following is a brief description of the method; details may be obtained from references 13 and 14.

THEORETICAL MODEL

The flow model used in the Leading-Edge Vortex (LEV) computer program is illustrated in figure 5. Flow about a highly swept wing at angle of attack separates at the leading edge and forms a spiral vortex. Studies (refs. 16 and 17) of the principal vorex indicate that its shape and strength are relatively independent of Reynolds number. This apparent lack of viscosity dependence suggests that the flow may be regarded as potential, with the free shear layer represented either as a vortex sheet or, equivalently, a doublet distribution supporting a discontinuity in tangential velocity. The problem is governed by the linear subsonic flow differential equation with nonlinear boundary conditions.

The essential elements of the present flow model are the configuration surfaces (wing, body, etc.), the trailing sheet (wake), the sheet emerging from the wing leading edge and tip (free sheet), and the rolled-up core or spiral region (fed sheet) fed by the free vortex sheet emerging from the wing leading edge and tip. The fed sheet is an extension of the free sheet and feeds vorticity to the vortex core (modeled as a simple line vortex). The following nonlinear boundary conditions are imposed on the elements:

- The configuration surface must be impermeable.
- The free sheet and wake cannot support a pressure difference and must be impermeable as well.
- The total force induced on the fed sheet and core by the rest of the configuration must be parallel to the core.
- Kutta conditions are imposed along the appropriate leading, side, and trailing edges of the wing in the presence of free sheets emanating from these edges.

The configuration impermeability condition, the pressure jump condition on the free sheet, and the Kutta edge conditions determine the solution of singularity strengths. The free sheet impermeability condition and the fed sheet zero force condition determine the position of the free and fed sheets.

The Prandtl-Glauert equation is assumed to govern the perturbation velocity potential ϕ in the flow field about the configuration.

In subsonic flow, the Goethert rule is used to account for compressibility by transforming the problem into the equivalent incompressible problem for solution.

NUMERICAL PROCEDURE

This problem can be represented by the proper distribution of logically independent networks of panels, i.e., each network contributes as many equations as it does unknowns to the boundary value problem. As described in references 13 and 14, hyperboloidal (hyperbolic-paraboloid) panels are used to ensure surface continuity. A continuous quadratic doublet distribution is used on the midplane to represent wing, wake, free sheet, and fed sheet networks. If desired, a linear surface source distribution can be used to represent the body and wing thickness. Figure 6 and table 2 show the available network types. The main features of the computational scheme are:

- Geometry input for a network consists of an array of corner point coordinates. These corner points are fitted exactly by hyperbolic-paraboloid patches (hyperboloidal panels). These exact fits ensure surface continuity.
- An analysis-type network is employed on the wing (geometry of the wing is specified), and a design-type network of doublets simulates the free sheet (unknown free sheet geometry, zero pressure jump specified).
- Discrete values of singularity strength are assigned to certain standard points on each network (see fig. 6). A local distribution of surface singularity strength is obtained by fitting a linear source or a quadratic doublet form to those discrete values in an immediate neighborhood by the method of least squares. In order to ensure continuity of doublet strength between panels and networks, nine degrees of freedom splines are used to describe the quadratic panel distributions.
- Certain standard points on each network are assigned as control points where boundary conditions are specified (see fig. 6). These points include panel center points, as well as edge abutment downwash points in the case of doublet networks. The latter serve to impose standard aerodynamic edge conditions automatically (e.g., the Kutta condition, by enforcing zero potential jump at thin edges and continuity of doublet strength or surface vorticity across abutting networks) in order to produce logical independence for each network.
- The number of boundary conditions on each network coincides with the number of assigned surface singularity parameters. The induced potential and velocity integrals of the influence coefficient equations are all evaluated in closed form, although standard far-field expansions are employed when the control point is sufficiently distant from the influencing panel.

SOLUTION PROCEDURE

The boundary value problem of wings with leading-edge vortex separation is nonlinear due to the fact that the shape of the free vortex sheet, as well as its strength, are unknown. Since the problem is nonlinear, an iterative procedure must be used for solution. An initial assumption must be made for the position of the free and fed sheets.

Table 2.—Network Types, Uses, and Boundary Conditions

Network type		Use	Boundary conditions
NT = 1	Source/Analysis	Exterior surface of thick wings Exterior surface of bodies	Impermeable
NT = 2	Doublet/Analysis	Camber surface of wing	Kutta condition imposed on appropriate leading, side, and trailing edges.
NT = 4	Doublet/Design #1	Free sheet	$\Delta C_p = 0$ (second order formula) Stream surface
NT = 6	Doublet/Design #2	Near wake (behind wing)	$\Delta C_p = 0$ (second order formula)
NT = 8	Doublet/Analysis Wake #1	Simple wake Carry-over lifting system	$\Delta C_p = 0$ (linearized formula) Singularity strength constant along columns
NT = 10	Constant Doublet/Wake #4	Wake behind fed sheet Wake behind carry-over lifting system	Singularity strength constant throughout, therefore, carries no shed vorticity
NT = 14	Doublet/Design Wake #2	Fed sheet	Total force induced on fed sheet and core by the rest of the configuration is parallel to core
NT = 16	Doublet/Analysis Wake #3	Wake behind free sheet	$\Delta C_p = 0$ (linearized formula) Singularity strength constant along columns

Usually the results from Smith's conical flow method are used, but the user can also input his own geometry. During the iterative solution, the position and size of the free and fed sheet are updated until all the boundary conditions are satisfied. Two solution procedures are available in the LEV code, a quasi-Newton scheme and a least-squares method.

QUASI-NEWTON SOLUTION

The standard procedure uses a quasi-Newton scheme for the iterative solution of the flow problem. The equivalent incompressible boundary conditions are derived from the compressible formulation by applying the Goethert rule. The equations are divided into two groups. The first group includes the impermeable boundary condition of the wing and body, zero pressure jump across the free sheet and wake, and the Kutta condition. The second group represents the stream surface boundary condition of the free sheet and the global boundary condition of zero net forces acting on the fed sheet and the line vortex.

Starting with the assumed initial geometry, the initial singularity strength parameters are obtained by using the first group of equations. The linear form of the pressure equation is used for the zero pressure jump boundary condition.

To obtain a solution, two phases of iterative procedure are performed alternately. The first phase, which is called subiteration, uses the first group of equations and produces convergence to the nonlinear ΔC_p equation (second order) associated with the pressure jump boundary condition on the free sheet. The spatial location of the free sheet is not updated and the aerodynamic influence coefficients remain the same throughout the iteration. The Jacobian matrix consists of only the small perturbation of the functions in the first set of equations due to the singularity strength parameters.

These functions denote the error residual in the satisfaction of the boundary conditions at intermediate steps in the iteration cycle. The step size scaling parameter is a positive number less than 1.0, and is chosen small enough (by the code) to ensure a decrease in the functions. Newton's method with controlled step size is used and convergence is usually achieved in 2 or 3 iterations.

The second phase uses the second group of equations, which ensure the stream surface boundary condition of the free sheet and the global boundary condition of zero net forces acting on the fed sheet and the line vortex. In general, the assumed initial geometry of the free and fed sheets is not correct, and a full iteration procedure will begin in which this geometry is updated. This requires the recalculation of those aerodynamic influence coefficients affected by the perturbation of the geometry of the free and fed sheets.

Small perturbations of the two groups of equations from the initial starting solution result in a set of linear equations governing the perturbation variables (geometry and singularity strength).

As before, the functions are known and denote the error residual in satisfaction of the boundary conditions at intermediate cycles. These equations are solved iteratively by a quasi-Newton method with controlled step size. The calculation of a complete Jacobian, which includes the effect of the perturbation of geometry, is quite expensive. A new Jacobian is computed after every three iterations in the iterative process. Five to six iterations are generally sufficient to obtain convergence.

LEAST-SQUARES SOLUTION

An alternate iteration procedure, the least-squares method, is also available if the quasi-Newton scheme fails to converge. In these cases, local flow anomalies on the free sheet may cause instabilities that destroy convergence everywhere in the solution. These instabilities cause excessive panel twist, which propagates throughout the free sheet.

One of the simplest methods of damping this instability, whenever it arises, is to limit excessive panel twist. This leads to an additional equation that all free sheet panels be untwisted (flat). When combined with the previous groups of equations, an overdetermined system of equations for the singularity parameters and the geometric degrees of freedom are created.

The system is solved in a least-squares sense after there is a suitable normalization to account for dimensional differences as well as desired weighting. The equation governing panel twist is not weighted heavily, since a free sheet made up entirely of flat panels may not, in general, be a good approximation to a stream surface. The instabilities produced by a local flow anomaly are severe enough that a very small penalty on panel twist forces relaxation of the boundary condition causing the local anomaly.

The procedure for solving the overdetermined equation set is iterative as before. The equation for panel twist is introduced in the second phase. When using the least-squares method, a new Jacobian is computed after every two iterations.

PHYSICAL MODEL

The physical model must represent the actual configuration geometry, as well as the additional networks required to define the vortex and ensure satisfaction of the necessary boundary conditions.

The primary rule of all modeling is that abutting doublet networks must abut along complete edges with the corner points coinciding. This rule places some restrictions on the modeling, e.g., a thin wing, which could be one network for a full-span vortex, must be at least two networks for a partial-span vortex. In addition, there are rules for proper orientation of networks, both as independent entities and relative to each other.

WING PANELING

There are two general styles of paneling available for the wing proper: conical and streamwise. With conical paneling, the primary panel edges radiate from the apex and bend as necessary to accommodate the planform. The other panel edges are usually at constant body stations. With streamwise paneling, the primary panel edges are parallel to the centerline of the vehicle. The other edges are arbitrary, but typically coincide with hinge lines or perhaps are at constant-percent chord.

In the initial development of this code, conical paneling was used exclusively. Because of the position of a fully developed vortex on a wing, conical paneling has the advantage of generally providing denser wing paneling under the free and fed sheets that represent the vortex.

Pressure orifices on wind tunnel models are most often arranged in streamwise cuts; therefore, there is a distinct advantage to using streamwise paneling when planning to compare the theoretical results to experimental data.

Both of these paneling arrangements were tried in this study. The arrangements of panels and networks are shown with the results of the evaluations.

VORTEX PANELING

The leading-edge vortex is represented by the combination of a free sheet and a fed sheet (terminating in a line vortex). The geometry describing an initial position is required. This geometry can be generated within the code based on the conical solution of Smith (ref. 18), in which case the size and position of the free and fed sheets are dependent on the parameter 'a' that is calculated using the angle of attack and the leading-edge sweep (fig. 7). The vortex may be moved closer to, or farther from the wing by incrementing this calculated value of 'a' by adding the parameter 'Δa' and/or by rotating the vortex about the attachment point (rotation was added during this study). In general, convergence is faster if the initial vortex is too large rather than too small. In addition to these options, the geometry of the vortex networks may be specified directly by the user although the method just described is generally satisfactory.

WAKES

Wake networks are included to ensure satisfaction of the boundary conditions. Several types of wake networks are available. The locations of singularity parameters and control points and the boundary conditions compatible with the networks to which they are attached are specified. A special type of wake network, which uses the second order formula for the zero pressure jump boundary condition, was added to be used behind the wing to enforce the Kutta condition on the wing trailing edge. Additional insight into the benefits of the special wake behind the wing are discussed in reference 19.

CONTROL PARAMETERS

The Mach number, angle of attack, and angle of sideslip must be specified for each case. In addition, the solution method (quasi-Newton or least-squares) must be selected. After a data check, the usual procedure is to specify the number of iterations in an execution, look at the results at that point, and if necessary, restart for an additional finite number of iterations.

The choice of panel distribution and arrangement on the wing and the initial position of the vortex also influence the solution.

The function used in the least-squares solution for limiting the amount of panel twist (actually for keeping all free sheet panels individually flat) allows the sheet itself to acquire quite a lot of twist, as the orientation of panels relative to each other is not controlled. The capability to vary the weight given to the twist function was added to the code for evaluation. A factor of 0.0 on the twist function in the least-squares solution should yield, in effect, the same results as the quasi-Newton solution.

CONVERGENCE CRITERIA

The LEV method is iterative as explained above. For any such method, it is necessary to know when to stop – either because an adequate solution has been achieved, or because the solution has ceased to change. Currently, the user specifies the maximum number of iterations, examines various parameters available in the printout, and restarts the solution if desired. In addition, there are some combinations of values for these parameters that cause the program to stop short of the requested number of iterations.

The parameter most frequently examined is the total residual, which is the sum of the squares of all the differences from the specified boundary conditions. These differences are also displayed individually. The current disadvantage encountered with the use of the total residual is that the more singularities used in the solution, the larger the total residual becomes, even though the individual differences are of the same magnitude. Therefore, the generally accepted magnitude (e.g., 0.001) for an adequately small residual is, in fact, problem-size dependent. Luckring, Schoonover, and Frink of NASA Langley have an excellent discussion of the residuals in reference 19.

The second parameter frequently used to determine convergence is the fraction of Newton step. The taking of a full Newton step indicates a well-formulated problem. When the solution advances to the point where a full Newton step is taken, particularly for at least two consecutive iterations, convergence is indicated. Unfortunately, the program compares the total residual from one iteration to that of the immediately preceding one and if it is larger, by even 10^{-9}, the fraction of Newton step is halved or, if a full Newton step had been used in the previous iteration, the solution stops. If the step size is reduced four times, a new Jacobian is formed.

For the current study, these two parameters – the total residual and the fraction of Newton step – were generally used as convergence criteria. In addition, Forrester T. Johnson was frequently called upon to examine the solutions.

EVALUATION

The LEV computer program is a rather complex code, which provides many options on paneling of the geometry along with options on the solution method. The initial planning for the evaluation of the LEV code for possible use in an aeroelastic solution suggested the necessity of examining solutions for the following:

- Full-span vortex
- Partial-span vortex
- Conical wing paneling
- Streamwise wing paneling
- Flat wing
- Twisted wing
- Cambered-twisted wing
- Thick wing
- Model including fuselage representation

All of these various solutions were not attempted simultaneously, nor were they done in a completely sequential order. Therefore, the results of one frequently affected the way others were handled. Some of the additional parameters that were examined are:

- Density of the wing paneling
- Variation of the initial vortex size
- Influence of the weighting factor on the twist function for the vortex sheet in the least-squares solution

The two solution types - quasi-Newton and least-squares - were used but rarely both for one condition. The quasi-Newton solution is also referred to as iteration.

The groups of solutions for the full-span vortex and for the partial-span vortex are the major divisions in the following discussion. The experimental data used for comparisons were obtained by linear interpolation of the measured data. The majority of the conditions do not include a fuselage representation. Rather than extending the wing into this area, a slice was removed and the wing halves were slid together with a resulting reduction of total span. For consistency in the presentations, the locations of the data have been adjusted to fit the entire model semispan.

FULL-SPAN VORTEX

COMPARISON TO PREVIOUS EVALUATION

The first case considered was one previously compared under NASA contract NAS1-12875 (see ref. 4). This case was the flat wing at a Mach number of 0.40 and an angle of attack of 16 degrees.

At the time of the initial comparison, the computer program was rather restricted in its capabilities, particularly for configuration modeling. Some planform restrictions existed and the wing thickness, camber, and twist could not be represented. The simplified paneling scheme shown in figure 8(a) was the best available representation of this configuration. Note that the streamwise tip is not modeled. A total of 98 panels were used: 30 panels to describe the wing; 54 panels to describe the rolled up vortex; and 14 panels to describe the wake. At that time, the code was restricted to incompressible flow as well as these modeling restrictions.

The comparison of the calculations to experimental data is shown in figure 8(b). Because of the sparsity of wing panels in the LEV solution compared to the number of pressure orifices on the wind tunnel model, the LEV results are indicated by symbols while the experimental data (interpolated to the same stations as the theoretical results) are designated by a solid line. The results of the linear theory FLEXSTAB are indicated by a dashed line.

The comparison between the experimental and the LEV data is surprisingly good for those stations ahead of the apex of the wing trailing edge, particularly considering the absence of the body in the theoretical model and the sparsity of the paneling definition. Except at the two sections behind the trailing-edge apex, the approximate location and magnitude of the peak in the lifting pressure distribution are quite well predicted. Considering the stage of development of the computer program, the results were very promising, and the observed problems could well have been caused by the crude modeling.

In the current study, the same type of geometry representation was used - zero thickness wing with conical paneling and no fuselage - although the number of panels on the wing was increased to 121 from the 30 used in the previous comparison. A total of 229 panels were used: 121 panels to describe the wing; 88 panels to describe the rolled-up vortex; eight panels to describe the design wake; and 12 panels to describe the trailing wake. The trailing wake extends over 84 m behind the wing, but only the portion closest to the wing is shown in figure 9(a). Comparison of the predicted to the experimental data are shown in figure 9(b) with the more conventional use of symbols for experimental data and a solid line for the predictions of the LEV code. The predictions using the denser paneling arrangement are better, as expected, although the effect of the secondary vortex at the tip is still not predicted. For this full-span vortex case, the quasi-Newton solution converged well (residual $= 0.5 \times 10^{-8}$) in six full iterations.

The presentations in figures 8 and 9 are isometric. Whereas a good general impression is obtained from isometric drawings, two-dimensional cuts frequently give more insight into the details. Therefore, drawings at constant body stations are shown in figure 10 for the current converged solution with the panel edges marked. The pressure distributions at constant body stations (approximately midway between the geometry stations of fig. 10) are shown in figure 11. The model used for this LEV solution is a zero-thickness flat wing. In figure 11, the predictons are compared to the experimental data obtained for both the rounded- and sharp-leading-edge wings. The three parts of the figure show comparisons of the upper surface pressure distributions, the lower surface pressure distributions, and the net (or lifting) pressure distributions.

For this positive angle of attack, the effect of the vortex is seen on the upper surface. The spanwise location of the primary vortex is very nearly the same for both sets of experimental data and is well predicted by the theory, even though the theory tends to overpredict the pressure level. At the second section, the prediction is an extremely good match of the pressure data for the sharp-leading-edge wing. Farther aft, the LEV computer program overpredicts the pressure peak but matches the rounded-leading-edge wing data better, as the pressures are higher on the rounded-leading-edge wing than on the sharp-leading-edge wing. The plot routine used for these presentations cannot show a peak or valley between data points; therefore, in all the figures, there are some flat spots, which do not represent the best fairing of the data.

Figure 11(b) shows the comparison of pressure distributions on the lower surface. The LEV predictions are generally slightly more positive than the experimental data. The net or lifting pressure distributions are shown in figure 11(c), where the resulting relationship of the LEV predictions to the experimental data are essentially the same as described for the upper surface distributions.

STREAMWISE WING PANELING

The second general option for wing geometry is streamwise paneling. As experimental data are almost always obtained in streamwise sections, the ability to predict pressures at streamwise sections would enhance the comparisons. This wing paneling, as tried in the current study, is shown in figure 12. After five full iterations, using the least-squares method (the quasi-Newton method would not converge), the residual was much larger than it was for the case using conical paneling; in addition, the cost was already considerably higher. Use of this paneling was discontinued; although in retrospect, inadequate denseness of the wing panels may have been the problem.

TWISTED AND CAMBERED-TWISTED WINGS

Cases for the twisted wing and the cambered-twisted wing were executed to evaluate the ability to predict pressures on a deformed shape. These cases used the same conical paneling used in this study for the flat wing (fig. 9) with only the vertical location of panel corner points changed. These pressure predictions for the twisted wing are compared to experimental data in figure 13. Only the upper surface distributions are shown. The placement of the vortex is predicted somewhat inboard of the actual location, and the pressure level is also slightly overpredicted. The initial vortex geometry at constant body stations and that at two, four, and six cycles are shown in figure 14(a). There is very little change in the shape and location of the free and fed sheets except at the wing tip where the change tends to remove the kink introduced at the junction of the wing leading and side edges (fig. 13(b)).

For the cambered-twisted wing, the comparison of predicted pressure distributions to the experimental data is shown in figure 15. The predicted peak pressures, except near the apex, are generally lower and therefore closer to the measured data. The peak is still predicted somewhat inboard of the actual locations. The geometry is shown in figure 16; the changes from cycle to cycle are similar to those for the twisted wing. A comparison of data for all three wing shapes at the same Mach number and angle of attack is shown separately for the experiment and LEV predictions in figure 17. The incremental change in pressure due to wing shape is very well predicted, although the location of the peak pressure in the theoretical predictions is somewhat too far inboard for both the twisted wing and the cambered-twisted wing.

FLAT WING WITH THICKNESS

In all the comparisons shown so far, the pressures near the wing apex, as predicted by the computer code, are considerably higher than the experimental data. It seemed reasonable that omitting the thickness of the wing and the fuselage might account for this. For the previous cases, the slice removed for the fuselage was the one associated with the maximum body radius, 4.374 cm (1.722 in.). When preparing to add the fuselage to the model, it became obvious that as the wing is attached below the centerline of the body, the removed slice was too large. The intersection of the wing midplane and the body surface is 3.035 cm (1.195 in.) from the centerline and was used to define the slice for the subsequent full-span vortex cases. The flat wing without thickness was redone as a base point. The paneling was adjusted longitudinally for the changes in break points, and the density of the panels near the leading edge was increased (because of a paneling change for the partial-span vortex cases). The initial vortex was also made larger than the program default size in an attempt to speed the convergence, since reference 14 states that it is generally easier for the vortex to contract. The initial geometry, compared to that at several subsequent cycles, is shown in figure 18. After several cycles, the free sheet became kinked at the trailing edge of the wing tip. The pressure comparisons are shown in figure 19. In general, the predicted pressure distribution is the same as that on the first flat wing case (fig. 11), except at the tip where neither upper nor lower pressure distributions are well predicted. In the experimental data, the vortex is not evident at section 2, which with the repaneling has moved slightly forward. There is a reversal of pressure at one station, which is probably caused by the doublet strength being matched only at control points.

With this base established, the source networks necessary to represent the wing thickness were added to the zero-thickness wing model for the flat wing. The initial geometry, as well as that for several intermediate cycles, is shown in figure 20. After cycle six, the free and fed sheets no longer change position. The comparison of pressures predicted by the LEV code to experimental data is shown in figure 21(a). The comparison shown is for six cycles of the LEV code; examination of the pressures as a function of cycle shows that the pressures did not change significantly after this cycle (fig. 21(b)). The basic difference in this distribution is that with the thickness added, the pressure peaks have actually become larger near the apex – not smaller as anticipated. Figure 20(b) shows an enlargement of the geometry of sections near the apex. The assumption that the vortex originates at the midchord point at the leading edge is not necessarily correct, particularly for sections close to the wing apex where the section is quite blunt. The lack of improvement in the predicted pressure distributions might also have been influenced by the change in solution type from quasi-Newton to least-squares.

EFFECT OF FUSELAGE

To evaluate the effect of the fuselage, the necessary networks were added to the model of the thick wing. The final position of the free and fed sheet networks, as obtained from the converged solution for the thick wing without fuselage, was used for the starting position in this solution. The geometry is shown in figure 22; the final vortex has slightly increased in size over the initial position. The results for this case are shown in figure 23 and are very much the same as for the thick wing without fuselage, except that with the fuselage included the peak pressure at the apex is somewhat lower.

These three solutions are combined in figure 24 to highlight the changes due to wing thickness and the fuselage. The experimental data are included for comparison. As stated before, the pressures near the apex that were predicted with modeling for wing thickness included, are higher than the pressures for the zero thickness wing; the pressures for all three solutions are higher than the experimental data. The presence of the fuselage lowers the peak a trifle, but the pressures when the wing is represented as having zero thickness, come closest to matching the experimental data. The effect of the thickness representation is seen at all stations; it basically increases the peak pressure, although the location and extent of the vortex are the same for all three solutions, and the pressures away from the vortex peak do not change. On the lower surface of the wings with thickness, the predicted pressures are slightly less positive, and as a consequence match the experimental data better. As would be expected, the effect of the fuselage representation is less noticeable at locations farther from the centerline.

The modeling of the wing thickness and the fuselage required the addition of networks and singularities beyond the capability of the standard computer code. The code was modified to allow this. As the number of networks and singularities increase, the cost of a solution also increases - both in terms of computer storage required and execution time. As a result of this series of comparisons, it seems unprofitable to include either the fuselage or the wing thickness in the model.

PARTIAL-SPAN VORTEX

On a wing with thickness, the vortex starts to form at the wing tip at moderate angles of attack and moves inboard as the angle of attack increases. Figure 25 shows isobars* of the experimental upper surface pressures for both the flat and twisted wings of the data base used in this study. The vortex is first observed on the tip of the flat wing at 4^0 angle of attack, and it then progresses inboard as the angle of attack increases. On the twisted wing, which has a washout of about 4.5^0 at the tip, the vortex first appears at about 8^0 as would be expected. By 16^0 angle of attack, the difference between the flow patterns on the two wings is very small.

During the design process, solutions are also needed for design conditions at moderate angles of attack. The second general line of investigation, therefore, was to evaluate the LEV code with a partial-span vortex. The vortex exists only where the free and fed sheet networks are defined. For this evaluation the apex of these networks was placed at mid-semispan ($\eta = 0.5$), and an appropriate angle of attack was selected using Kulfan's method (see NASA CR-3641, report for Task II of this contract). In Kulfan's method, a vortex exists on a rounded-leading-edge wing in that area where the theoretical leading-edge suction force is greater than the parabolic nose drag.

---

*The ΔC_p noted on each of the isobars refers to the increment in pressure level between adjacent isobar lines. These ΔC_p increments are automatically selected within the plot program based on maximum and minimum pressure levels. These increments should be carefully noted when comparing the plots for several angles of attack, since they may vary.

Calculations were made at Mach 0.40 for the flat wing with the angle of attack initially chosen as 6°. Plots (fig. 26) of the experimental data, made only after most of this study was concluded, clearly show that for the rounded-leading-edge flat wing, an angle of attack of 6° is not high enough for vortex flow to be established over the entire outboard half of the semispan. Note that for an angle of attack of 6°, the data for the sharp-leading-edge flat wing definitely shows vortex flow at the third section from the apex, but the data for the rounded-leading-edge flat wing does not show this phenomenon until the eighth section (outboard 30 percent). Part (b) of this figure shows data for an angle of attack of 8°. The vortex has moved inboard, but it is not well developed for the rounded-leading-edge wing until section seven (outboard 40 percent).

The theoretical formulation of this method assumes that the vortex has a clean origin at a precise point. Observation of the experimental data indicates that the origin of the vortex is actually weak and diffuse. In order to improve the results, changes were tried in wing paneling and initial vortex size, and variations were made of the weighting factor on the twist function in the least-squares solution. The configuration used was the zero-thickness flat wing without the fuselage and, as previously mentioned, at Mach 0.40 and an angle of attack of 6°.

Both the conical and streamwise paneling were initially tried. The first full iteration cycle did not converge after 10 subiteration cycles with the streamwise paneling scheme (fig. 12), even though the least-squares solution was specified. This paneling scheme was then abandoned; although, as mentioned for the full-span vortex case, perhaps adding more panels would have helped.

STANDARD SOLUTION

Using the quasi-Newton solution scheme, the case with conical paneling (11 by 11 on the wing) did execute; but after six iterations, the residual was still large (2.18) with only a small decrease in the residual per iteration. Changing to the least-squares solution method caused more rapid convergence although an acceptably small residual (0.07 after 15 cycles) was not achieved. These results, using the least-squares method, compared to the experimental data for the flat wing (both the rounded- and the sharp-leading edges) are shown in figure 27. The first four wing sections are in a network without a vortex network attached and exhibit the typical large leading-edge pressure peak associated with thin wings having attached flow. The fifth section also has a large leading-edge pressure, but none of the phenomena usually associated with a leading-edge vortex.

An examination of this paneling at constant body stations (fig. 28) indicated that there were not enough (only two to four) wing panels under the vortex for a good solution. The wing paneling was, therefore, made denser in the spanwise direction (14 instead of 11) with all of the additional panels placed near the leading edge. These two paneling arrangements are shown in figure 29. It also appeared that the vortex, as predicted directly by the Smith method, was too close to the wing. Therefore, the assumed initial size of the free and fed sheets was made larger as discussed earlier (using a value of 0.60 for 'Δa'). The initial geometry, as well as the final geometry, are shown in figure 30. This case converged very well using the quasi-Newton scheme with the results shown in figure 31 (residual = 0.7×10^{-7} at 12 cycles). The additional panels under the vortex help; the vortex in the theoretical solution now starts at section five as modeled. This spanwise location of the vortex origin still does not match either of the sets of experimental data. To determine if a further improvement was possible, this modeling was also executed using the least-squares solution with the standard weighting factor (1.0) on the twist function. This solution converged somewhat more rapidly considering both of the convergence criteria. Although the residual was higher (0.02 (excluding the twist residual) at six iterations), a fraction of Newton step of 1.0 was used for the last three full iterations. Comparisons to experimental data are shown in figure 32. Figure 33 shows the comparison of results for the two solution types. The spanwise location of the vortex for the two solutions is about the same with only minor differences in the maximum pressure.

SIZE OF INITIAL VORTEX

At that point, the separate effects of increasing the density of the panels and of starting the solution with the vortex farther from the wing were not clear. Therefore, using the least-squares solution, a case was executed with denser wing paneling but with the vortex position as originally used, i.e., the program default size. Figure 34(a) shows the starting geometry of the free and fed sheets for the two initial sizes, as well as the position of these sheets when convergence was assumed. The free and fed sheets, which were initially default-sized, are farther from the wing at convergence. The vortex segments have become longer, and the vortex has apparently rotated outward as well. This final position is still closer to the wing than the final position of the vortex that was started farther from the wing. The initially larger vortex is somewhat closer to the wing, primarily through rotation, except for the section through the trailing edge of the tip ($x/L = 0.851$) where the vortex has merely shrunk a little. For the two solution types, a direct comparison of the position of the vortex at assumed convergence is shown in figure 34(b); the starting position of the vortex in both cases was established using 'Δa' = 0.60.

The summary of values for the parameters used to evaluate convergence is shown in table 3 for both of the least-squares cases. The case started with a vortex known to be too large maintained a fraction of Newton step of 1.0 for three cycles, and the residual was no longer changing very rapidly. Hence, the results obtained at cycle six were accepted as being the best possible. The other case still had a relatively large residual at six cycles and had just reached a fraction of Newton step of 1.0, so the solution was restarted. Due to an operations error, the print of this execution was not available. Some of the results of the iterations were saved on a file; but as the history of the fraction of Newton step was not part of the available data, the solution was restarted yet again. In retrospect, reviewing the data shown in table 3 would indicate that the third execution was not necessary. Reviewing plots of pressures at each location as a function of cycle, show that at some of the locations the pressures are changing noticeably with each iteration, even after cycle 10. Figure 35 shows the distributions at 10 cycles and at 15 cycles. The values at specific locations change; but as the peak is very abrupt, the resulting lift at a given section does not change significantly nor does the actual location of the peak pressure. As cycle 10 probably would have been the final solution available if the print had not been lost, it is the solution compared in figure 36 to the converged solution with the larger starting vortex. In this case, the starting vortex position has definitely affected the results. The final pressures for the case with the vortex started close to the wing, show a higher pressure peak, which is located farther outboard on the wing than for the case with the vortex started farther from the wing. The peak pressures for both solutions are farther outboard and greater than those in the experimental data for the sharp-leading-edge flat wing also shown in figure 36.

Table 3.—Summary of Results for Partial-Span Vortex with Two Initial Sizes of Vortex

Flat wing, zero thickness
M = 0.40, $\alpha = 6^\circ$
Least-squares solution
Weight factor = 1.0

	$\Delta a = 0.6$			$\Delta a = 0.0$		
Iteration cycle	Residual		Fraction of Newton step	Residual		Fraction of Newton step
	Total	On boundary conditions only		Total	On boundary conditions only	
0	.9271	.9271	—	8.2466	8.2465	—
1	.4505	.4476	.3013	6.8502	6.8499	.0828
2	.1459	.1359	.4433	5.4885	5.4878	.0949
3	.0565	.0343	.7163	3.1688	3.1669	.2472
4	.0497	.0213	1.0	1.5037	1.4998	.3497
5	.0492	.0210	1.0	.3733	.3637	.5305
6	.0490	.0204	1.0	.0743	.0562	1.0
*7				.0743	.0562	—
8				.0669	?	?
9				.0514	?	?
10				.0449	.0267	?
*11				.0449	.0267	—
12				.0447	.0271	1.0
13				.0445	.0269	1.0
14				.0443	.0268	1.0
15				.0442	.0268	1.0

*Solution restarted

? = Values not available, see text

WEIGHTING FACTOR ON TWIST FUNCTION

The difference between the two solution types – quasi-Newton and least-squares – is the inclusion of the twist function in the least-squares method. Using a weighting factor of 0.0 on the twist function in the least-squares solution is equivalent to using the quasi-Newton method. Additional cases were executed to determine the effect of different weights on the twist function. With all other input to the starting solution remaining the same, weighting factors of 5.00 and 0.50 were used in addition to the original factor of 1.00. The results are shown in figures 37 and 38 for weighting factors of 5.00 and 0.50, respectively.

In figure 37, using the larger factor of 5.00 on the twist function, the predicted vortex initially stays close to the leading edge and matches the position but not the value of the peak pressure of the experimental data for the rounded-leading-edge flat wing at sections eight and nine. The vortex then moves farther inboard than shown in the experimental data for the rounded-leading-edge wing.

Examination of the data from the solution using a factor on the twist function of 0.50, shows that the vortex moves inboard quite rapidly from its apex at section five and matches very well the experimental pressure distributions for the sharp-leading-edge wing at the last three sections. It should be noted that the vortex is clearly evident in the experimental data for the sharp-leading-edge wing at section four. To determine whether an even smaller factor would improve the solution, this case was restarted using a factor of 0.20 on the twist function. This resulted in only a small increase in the peak values of the pressures at some of the aft sections; it did not improve the match with experimental data (fig. 39). The solution might have been improved if it had been started with a factor of 0.20 rather than starting with a converged solution. This, however, was not tried.

A rear view of all the geometry for the wing and vortex modeling illustrates quite well the effect of the terms used to limit panel twist. The initial geometry used for several solutions is shown on the left in figure 40. On the right in this same figure, the geometry at the end of six full iteration cycles is shown for a solution using the quasi-Newton scheme and for three solutions using the least-squares method with various factors (0.5, 1.0, 5.0) on the weighting function. Comparison of the parts of this figure shows clearly that the twist factor may keep individual panels flat but does not keep the vortex sheet untwisted.

Figure 41 shows a comparison of the pressure data resulting from solutions for which all input was constant except the weighting factors on the twist function. The solution with the smallest factor (0.50) on the twist function is identified by the solid line in figure 41. The solution with the largest factor (5.00) on the twist function is identified by the dashed line, and the solution with the standard factor (1.00) by the dotted line. As this was a solution for the flat wing without thickness, it would seem better to try matching data for the sharp-leading-edge wing rather than for the rounded-leading-edge wing; therefore, only the experimental data for the sharp-leading-edge wing is shown. As the factor gets smaller, the peak pressure moves inboard and is smaller. The smallest of these twist functions produces the best match of the experimental data; it actually appears to be a better match than the solution using the quasi-Newton method, which has no factor on twist (fig. 31).

EFFECT OF THICKNESS

The same wing paneling was used to evaluate the effect of wing thickness on the partial-span vortex case that was used on the flat wing with thickness for the full-span vortex case. Note that the slice removed to represent the body is smaller than that of the previous partial-span vortex cases. The apex of the free and fed sheets representing the vortex is again at the mid-semispan point. As the rounded-leading-edge wing geometry was to be used, the angle of attack was increased to 8° so that the start of the vortex in the experimental data would be farther inboard and forward than in the previous cases. The vortex size was increased using the same value of 'Δa' as before, which would have made the vortex slightly larger anyway because of the higher angle of attack. The initial attempt to execute this solution failed to converge in subiteration. The cause of this failure to converge was diagnosed as a probable intersection of the vortex sheet and the wing thickness representation between sections five and six. To avoid a completely manual repaneling of the vortex sheet, an option was added to the code to allow rotation of the vortex. With the paneling modified to rotate the forward vortex network out 13.5° and the aft votex network out 10° the program did execute. This initial geometry and that at six and 12 cycles are shown in figure 42. It appears from this figure that if the aft network had been rotated more, the convergence would have been more rapid. The least-squares method was used with a weighting factor of 0.50 on the twist function through cycle six and then with a factor of 0.20.

Comparison of the predicted pressure distributions to the experimental data for the rounded-leading-edge flat wing is shown in figure 43. The prediction at the first four sections, which have attached flow, are very good; adding the wing thickness definitely improved the results. Unfortunately, in the experimental data, the vortex is still not clearly defined inboard of 60 percent semispan (section seven).

The peak pressures in the experimental data have moved inboard with the higher angle of attack, and the peak pressures in the theoretical predictions are closer to the leading edge. The latter is presumably an effect of thickness and/or of the rotation of the vortex networks. The spanwise position of the peak pressure is now a much better match for this rounded-leading-edge flat wing data, but the value of this pressure, as predicted, is too high; and the peak extends over much less of the span than in the experimental data. The values of the residual and fraction of Newton step are shown in table 4 as a function of cycle. Even though the residual, excluding the twist function, has fallen to a relatively low value, the fraction of Newton step has never been 1.0. As the cost was already more than three times that of a typical case without thickness, the solution was not continued. Examination of the pressures as a function of cycle shows that many were still changing; in fact, there was some tendency for the peak pressures to be increasing. The total normal force coefficient was becoming larger on each iteration and by cycle six was already larger than that obtained by integrating the experimental pressures.

The addition of the thickness representation to the partial-span vortex case only improved the solution in the region of attached flow on the inboard portion of the wing.

Table 4.–Summary of Results for Partial-Span Vortex on Flat Wing With Thickness

$M = 0.40, \alpha = 8^\circ$
Least-squares solution

Iteration cycle	Weight on twist function	Residual		Fraction of Newton step
		Total	On boundary conditions only	
0	0.50	2.5587	2.5585	–
1	0.50	1.7880	1.7871	.1725
2	0.50	1.2181	1.2157	.2065
3	0.50	.6088	.6037	.2351
*4	0.50	.6088	.6037	–
5	0.50	.2544	.2451	.3538
6	0.50	.1194	.1042	.6047
*7	0.20	.1066	.1042	–
8	0.20	.0429	.0396	.4113
9	0.20	0241	.0198	.6568
*10	0.20	.0241	.0198	–
11	0.20	.0121	.0083	.5512
12	0.20	.0111	.0074	.4350

*Solution restarted

CONCLUSIONS AND RECOMMENDATIONS

This evaluation of the Boeing Company's Three-Dimensional Leading-Edge Vortex (LEV) computer code shows a large improvement in capability over a previous evaluation of the code using this same experimental model (NAS1-12875, ref. 4). In the time between these two evaluations, the modeling capability, as well as the mathematical procedures, have been improved. Although many of the currently available options have been tried, there are still many combinations that should be evaluated.

The current study included the use of both conical and streamwise paneling of the wing. The solutions using streamwise paneling did not converge satisfactorily, although it is likely that a denser arrangement of panels should have been tried. For the conical paneling, the solution was improved when the number of panels under the vortex was increased. Options used in modeling the vortex sheet included increasing the size of the sheet and, when thickness was added to the wing representation, rotating the vortex away from the wing. The solutions are apparently better, but definitely different, when the initial vortex is farther from the wing and must contract rather than expand to a final position.

During this study, the two solution methods were used but rarely both on one case. The quasi-Newton method is preferred because there are exactly as many equations as unknowns. The other method, least-squares, adds some equations to keep the vortex panels flat and is, therefore, overdetermined. The quasi-Newton method worked very well for the cases with a full-span vortex and zero wing thickness. When wing thickness and the fuselage representation were added, the least-squares solution was used, as it is generally recommended for difficult cases. The predicted pressures were not better than those for the zero thickness representation, but this lack of improvment might have been due to changing the solution method used.

For the partial-span vortex cases, the least-squares solution appears to work better than the quasi-Newton solution, especially when only a small weight or penalty is used on the terms designed to keep the panels of the free and fed sheets flat. It is not clear why this solution is better; the smaller this weighting function, the closer the least-squares solution should have been to the quasi-Newton solution.

As a result of this study, some modifications to the LEV code are recommended. The calculation of the total residual should be modified so that the magnitude is not dependent on the number of singularities in the solution. While being totaled, these residuals should be scaled by the ratio of the panel area to the total area. Also, for the least-squares solution, the twist function should be applied so as to minimize the change in position between panels in the free and fed sheets, rather than keeping individual panels flat.

As shown, the predicted pressures are quite good and adequately reflect changes in configuration. The full effect of reasonable variations on the parameters studied have not been fully explored at this time; but based on those completed, it is recommended that more work be done. The use of this method as the aerodynamics module in an aeroelastic analysis, would appear to be a viable plan.

Boeing Commercial Airplane Company
P. O. Box 3707
Seattle, Washington 98124
May 1982

APPENDIX A

DESCRIPTION OF DATA BASE

WIND TUNNEL MODELS

The configuration chosen for this study was a thin, low aspect-ratio, highly swept wing mounted below the centerline of a high fineness-ratio body. The general arrangement and characteristics of the model are shown in figure A-1. Two complete wings were constructed for contract NAS1-12875, one with no camber or twist and one with no camber but with a spanwise twist variation. A third wing with camber and twist was constructed for contract NAS1-14962. Deflectable control surfaces were available on all three of these wings.

FLAT WING

The mean surface of the flat wing is the wing reference plane. The nondimensional wing thickness distributions (shown in table A-1) deviate slightly from a constant for all streamwise sections to satisfy a manufacturing requirement for a finite thickness of 0.0254 cm (0.01 in.) at the trailing edge. The wing was designed with a full-span, 25-percent chord, trailing-edge control surface. Sets of fixed angle brackets allowed streamwise deflections of $\pm 4.1^{\circ}$, $\pm 8.3^{\circ}$, $\pm 17.7^{\circ}$, and $\pm 30.2^{\circ}$, as well as 0.0°. A removable full-span leading-edge control surface (15 percent of streamwise chord) could be placed in an undeflected position and also drooped 5.1° and 12.8° with fixed angle brackets. Both the leading- and trailing-edge control surfaces extended from the side of the body (0.087 b/2) to the wingtip and were split near midspan (0.570 b/2). The inboard and outboard portions of the control surfaces were able to be deflected separately and were rotated about points in the wing reference plane. An additional leading-edge control surface for this wing was constructed with a sharp (20° included angle) leading edge to examine the effects of leading-edge shape. The surface ordinates and slopes of this leading-edge segment were continuous with those of the flat wing at the leading-edge hingeline (table A-1). The sharp leading edge was smoothly faired from 0.180 b/2 into the fixed portion of the rounded leading edge at 0.090 b/2.

TWISTED WING

The mean surface of the twisted wing was generated by rotating the streamwise section chord lines about the 75-percent local chord points (trailing-edge control surface hingeline). The spanwise variation of twist is shown in figure A-2. The hingeline was straight and located in the wing reference plane at its inboard end (0.087 b/2) and 2.261 cm (0.890 in.) above the wing reference plane at the wingtip. The airfoil thickness distribution (table A-1) and the trailing-edge control surface location and available deflections were identical to those of the flat wing.

CAMBERED-TWISTED WING

The mean surface of the cambered-twisted wing was generated by superimposing a camber on the twisted-wing definition but keeping the coordinates of the leading edge and trailing edge of the cambered-twisted wing the same as those of the twisted wing.

Table A-1.—Wing Half-Thickness Distribution, Percent Chord

x/c, percent chord	0 b/2	0.09 b/2	0.20 b/2	0.35 b/2	0.50 b/2	0.65 b/2	0.80 b/2	0.93 b/2	1.00 b/2
Flat wing with rounded leading edge, twisted wing, and cambered-twisted wing									
.0000	.0000	.0000	.0000	.0000	.0000	.0000	.0000	.0000	.0000
.1250	.3359	.3359	.3359	.3359	.3360	.3360	.3360	.3362	.3364
.2500	.4506	.4506	.4506	.4506	.4507	.4507	.4508	.4509	.4512
.5000	.6064	.6064	.6064	.6064	.6065	.6065	.6066	.6068	.6072
.7500	.7247	.7247	.7247	.7248	.7248	.7249	.7250	.7253	.7258
1.0000	.8182	.8182	.8182	.8183	.8183	.8184	.8185	.8188	.8194
1.5000	.9520	.9520	.9520	.9521	.9522	.9523	.9525	.9530	.9538
2.5000	1.1191	1.1191	1.1192	1.1192	1.1194	1.1195	1.1199	1.1206	1.1219
5.0000	1.3448	1.3448	1.3449	1.3450	1.3453	1.3456	1.3462	1.3475	1.3497
8.5000	1.4809	1.4809	1.4811	1.4813	1.4816	1.4822	1.4832	1.4855	1.4892
10.0000	1.5195	1.5196	1.5197	1.5200	1.5204	1.5210	1.5222	1.5250	1.5293
12.5000	1.5444	1.5445	1.5447	1.5450	1.5456	1.5463	1.5479	1.5514	1.5568
15.0000	1.5630	1.5631	1.5634	1.5638	1.5644	1.5654	1.5673	1.5715	1.5781
17.5000	1.5720	1.5722	1.5724	1.5729	1.5737	1.5748	1.5770	1.5821	1.5898
20.0000	1.5813	1.5815	1.5818	1.5823	1.5832	1.5845	1.5871	1.5929	1.6018
30.0000	1.6214	1.6217	1.6222	1.6230	1.6242	1.6262	1.6301	1.6389	1.6522
40.0000	1.6398	1.6402	1.6408	1.6419	1.6435	1.6462	1.6514	1.6630	1.6807
45.0000	1.6282	1.6286	1.6293	1.6305	1.6324	1.6354	1.6413	1.6544	1.6742
50.0000	1.5901	1.5906	1.5914	1.5927	1.5948	1.5981	1.6046	1.6192	1.6412
60.0000	1.4344	1.4350	1.4359	1.4375	1.4400	1.4440	1.4518	1.4692	1.4956
65.0000	1.3121	1.3127	1.3137	1.3155	1.3181	1.3225	1.3310	1.3498	1.3784
70.0000	1.1627	1.1634	1.1644	1.1663	1.1692	1.1739	1.1831	1.2034	1.2341
72.5000	1.0792	1.0799	1.0810	1.0830	1.0860	1.0908	1.1003	1.1213	1.1532
75.0000	.9921	.9928	.9940	.9960	.9991	1.0041	1.0139	1.0357	1.0686
77.5000	.9006	.9013	.9025	.9046	.9078	.9129	.9231	.9456	.9796
80.0000	.8069	.8077	.8089	.8111	.8143	.8197	.8302	.8534	.8885
85.0000	.6132	.6140	.6153	.6176	.6211	.6268	.6379	.6626	.6999
90.0000	.4156	.4165	.4178	.4203	.4240	.4300	.4418	.4679	.5074
95.0000	.2153	.2162	.2177	.2202	.2241	.2305	.2430	.2706	.3122
100.0000	.0113	.0123	.0138	.0165	.0206	.0273	.0405	.0695	.1134
Sharp leading edge									
.0000	.0000	.0000	.0000	.0000	.0000	.0000	.0000	.0000	.0000
.1250	.3359	.3359	.0293	.0307	.0329	.0364	.0433	.0585	.0815
.2500	.4506	.4506	.0557	.0580	.0614	.0670	.0781	.1024	.1392
.5000	.6064	.6064	.0998	.1021	.1055	.1111	.1222	.1465	.1833
.7500	.7247	.7247	.1439	.1462	.1496	.1552	.1663	.1906	.2274
1.0000	.8182	.8182	.1880	.1903	.1937	.1993	.2103	.2347	.2715
1.5000	.9520	.9520	.2761	.2784	.2818	.2875	.2985	.3229	.3596
2.5000	1.1191	1.1191	.4524	.4547	.4581	.4638	.4748	.4992	.5359
5.0000	1.3448	1.3448	.8933	.8956	.8990	.9046	.9156	.9400	.9768
8.5000	1.4809	1.4809	1.3413	1.3429	1.3453	1.3493	1.3570	1.3741	1.4001
10.0000	1.5195	1.5196	1.4547	1.4559	1.4578	1.4609	1.4669	1.4803	1.5007
12.5000	1.5444	1.5445	1.5203	1.5210	1.5221	1.5238	1.5272	1.5347	1.5461
15.0000	1.5630	1.5631	1.5634	1.5638	1.5644	1.5654	1.5673	1.5715	1.5781

The camber is defined analytically in two parts: a typical cruise airfoil (basic) camber; and, an estimate of the aeroelastic deformation at a moderate positive angle of attack. The aeroelastic deformation was based on calculations – using a typical configuration – of deformation under load. This definition was modified slightly to provide zero camber at the model centerline so this wing would fit on the existing model body. This was achieved by using a factor k (fig. A-3) on the basic camber term, which provides a transition from no camber at the model centerline to the definition camber at 0.25 b/2. The defined wing is smoother than indicated in this figure as section geometry was directly calculated at only those sections marked in figure A-3. The full equation for the camber is:

$$\frac{z}{c} = \left(\frac{z}{c}\right)_{\text{Basic}} + \left(\frac{z}{c}\right)_{\text{Aero}}$$

$$\left(\frac{z}{c}\right)_{\text{Basic}} = k \left(\frac{4.0}{3.0}\right) \left(0.078 + \frac{\alpha \sec}{57.3}\right) \left(\frac{x}{c}\right) \left(\frac{x}{c} - 1.0\right) \left(\frac{x}{c} - 0.75 - \frac{1.0}{4.0} \left(\frac{2y}{b}\right)\right)$$

$$k = \left(\frac{2y}{b}\right) \left(1.0 + 12.0 \left(\frac{2y}{b}\right)\right) \qquad \text{for } \left(\frac{2y}{b}\right) \leq 0.25$$

$$k = 1.0 \qquad \text{for } \left(\frac{2y}{b}\right) \geq 0.25$$

$$\left(\frac{z}{c}\right)_{\text{Aero}} = -\frac{57.3}{3.0} \left(\frac{9.0}{4.0}\right) \left(\frac{2y}{b}\right) \left(1.0 - 0.75 \left(\frac{2y}{b}\right)^2\right) \left(\sec\left(\frac{3.0}{57.3}\right) - \sec\left(\frac{(3.0)\left|1.0 - 2.0\left(\frac{x}{c}\right)\right|}{57.3}\right)\right)$$

The resulting nondimensional camber is shown in table A-2. The camber at the tip is approximately a 6° arc of a circle with the leading and trailing edges up. Sections at the root, midspan, and tip (fig. A-3) show not only the camber but the position of the sections of the cambered-twisted wing and the twisted wing relative to the wing reference plane (flat wing). The airfoil thickness distribution (table A-1) and the trailing-edge control surface location and available deflections were identical to those of the flat wing.

BODY

The body was circular in cross section and had a straight centerline. The body geometry is shown in figure A-1. The sting was an integral part of the model body.

RELATIVE WING AND BODY LOCATION

The wing reference plane was located 3.149 cm (1.240 in.) below and parallel to the body centerline (zero incidence). The apex (extension of the wing leading edge to the centerline) of the wing was located 33.496 cm (13.187 in.) aft of the model nose.

Table A-2.—Wing Section Camber Definition, Percent Chord

x/c, percent chord	0 b/2	0.09 b/2	0.20 b/2	0.35 b/2	0.50 b/2	0.65 b/2	0.80 b/2	0.93 b/2	1.00 b/2
.0000	.0000	.0000	.0000	.0000	.0000	.0000	.0000	.0000	.0000
.1250	–.0005	–.0014	.0015	.0000	–.0048	–.0076	–.0064	–.0042	–.0200
.2500	–.0005	–.0023	.0024	–.0017	–.0120	–.0177	–.0159	–.0118	–.0256
.5000	–.0005	–.0038	.0033	–.0067	–.0277	–.0394	–.0367	–.0297	–.0403
.7500	–.0005	–.0054	.0043	–.0115	–.0433	–.0608	–.0573	–.0473	–.0547
1.0000	–.0005	–.0071	.0054	–.0164	–.0591	–.0823	–.0780	–.0651	–.0695
1.5000	–.0005	–.0107	.0072	–.0263	–.0897	–.1240	–.1184	–.1003	–.0993
2.5000	–.0005	–.0174	.0080	–.0474	–.1480	–.2025	–.1946	–.1673	–.1567
5.0000	–.0005	–.0332	.0027	–.1035	–.2870	–.3878	–.3740	–.3233	–.2888
8.5000	–.0004	–.0577	–.0117	–.1876	–.4826	–.6449	–.6200	–.5312	–.4581
10.0000	–.0004	–.0695	–.0201	–.2257	–.5677	–.7552	–.7249	–.6184	–.5275
12.5000	–.0004	–.0910	–.0378	–.2922	–.7102	–.9377	–.8979	–.7613	–.6407
15.0000	–.0004	–.1139	–.0607	–.3624	–.8510	–1.1147	–1.0654	–.8991	–.7497
17.5000	–.0004	–.1375	–.0892	–.4359	–.9869	–1.2823	–1.2239	–1.0296	–.8530
20.0000	–.0004	–.1613	–.1229	–.5115	–1.1162	–1.4385	–1.3716	–1.1511	–.9493
30.0000	–.0004	–.2542	–.2941	–.8168	–1.5559	–1.9432	–1.8468	–1.5368	–1.2525
40.0000	–.0003	–.3359	–.4894	–1.0939	–1.8638	–2.2613	–2.1419	–1.7666	–1.4261
45.0000	–.0003	–.3695	–.5830	–1.2098	–1.9658	–2.3531	–2.2248	–1.8263	–1.4670
50.0000	–.0003	–.3968	–.6677	–1.3048	–2.0313	–2.4002	–2.2652	–1.8504	–1.4791
60.0000	–.0002	–.4273	–.7928	–1.4143	–2.0430	–2.3551	–2.2147	–1.7922	–1.4189
65.0000	–.0002	–.4275	–.8242	–1.4182	–1.9819	–2.2577	–2.1195	–1.7074	–1.3456
70.0000	–.0002	–.4154	–.8280	–1.3806	–1.8708	–2.1068	–1.9746	–1.5836	–1.2424
72.5000	–.0001	–.4041	–.8179	–1.3444	–1.7955	–2.0108	–1.8831	–1.5068	–1.1796
75.0000	–.0001	–.3892	–.7990	–1.2959	–1.7067	–1.9008	–1.7787	–1.4201	–1.1093
77.5000	–.0001	–.3704	–.7707	–1.2344	–1.6039	–1.7768	–1.6613	–1.3235	–1.0315
80.0000	–0001	–.3476	–.7324	–1.1593	–1.4870	–1.6386	–1.5308	–1.2169	–.9464
85.0000	–.0001	–.2893	–.6236	–.9864	–1.2095	–1.3190	–1.2304	–.9737	–.7541
90.0000	–.0001	–.2127	–.4683	–.7126	–.8714	–.9409	–.8762	–.6903	–.5324
95.0000	–.0000	–.1166	–.2622	–.3928	–.4697	–.5021	–.4668	–.3661	–.2811
100.0000	.0000	.0000	.0000	.0000	.0000	.0000	.0000	.0000	.0000

WING FIN

The wing fin is a 3-percent biconvex airfoil placed streamwise and perpendicular to the wing reference plane on the upper surface of the cambered-twisted wing at 0.725 semispan. The dimensions of the fin and its relationship to the wing are shown in figure A-4. To obtain configurations with the outboard trailing-edge control surface deflected, the fin is extended down to touch the top of the control surface. (See fig. A-4.)

PRESSURE ORIFICE LOCATIONS

All pressure orifices were located on the left side of the model and distributed as shown in figure A-5 and tables A-3 and A-4. The flat wing with rounded leading edge, the twisted wing, and the cambered-twisted wing each had 214 orifices distributed in streamwise pressure stations of 31 (or 30) orifices at each of seven spanwise locations. One of these orifices was located at the leading edge; the remainder were distributed so that upper- and lower-surface orifices were located at the same chordwise locations. The orifice locations on the sharp leading edge were identical except for the omission of the leading-edge orifice at each spanwise station. The 83 orifices on the body were located at 15 stations along the length of the model. At each station, orifices were located at angles of 0°, 45°, 90°, 135°, and 180° measured from the top of the body. In the area of the wing-body intersection, the orifices that are nominally identified as being at 135° and 180° were located on the wing lower surface at the same lateral location as the orifices at 45° and 0°, respectively. Eight additional orifices were placed on the body, close to the juncture of the body with the wing upper surface.

DESIGN AND CONSTRUCTION

The objectives of this study dictated that the contours and physical characteristics of the flat wing, the twisted wing, and the cambered-twisted wing be as nearly identical as possible. The model was constructed of steel to minimize aeroelastic deflections and to provide strength for testing to a Mach number of 3.0. The aft body was flared approximately 4° from 194.310 cm (76.500 in.) aft of the nose to provide the required safety factor on predicted loads (fig. A-1). The model size was selected as the best compromise between minimizing potential tunnel blockage and providing adequate room to install orifices in the model.

A computerized lofting program was used to provide the wing definition. This definition was then used to machine the model components using numerically controlled machines. The tolerance on the contour was +0.1524, −0.0 mm (+0.006, −0.0 in.). The leading- and trailing-edge control surfaces were cut from the wings after they had been machined to final contour. A cut along the 15-percent chord line of the twisted wing removed enough material to simulate the elastic characteristics of the flat wing (fig. A-6). As a result of the previous tests it was determined that it was not necessary to remove this material on the cambered-twisted wing as the wings were very rigid. Fixed angle brackets (arranged as shown in fig. A-6) were used to obtain the required control surface deflections with all pivot points located midway between the upper and lower surfaces at the hingelines. The brackets were also machined on numerically controlled machines. The same sets of trailing-edge brackets were used on all three wings, and the same sets of leading-edge brackets were used for both the rounded and sharp leading edges.

Table A-3.—Wing Pressure Orifice Locations, Percent Local Chord

(a) Section at $0.09\frac{b}{2}$, chord = 102.89 cm

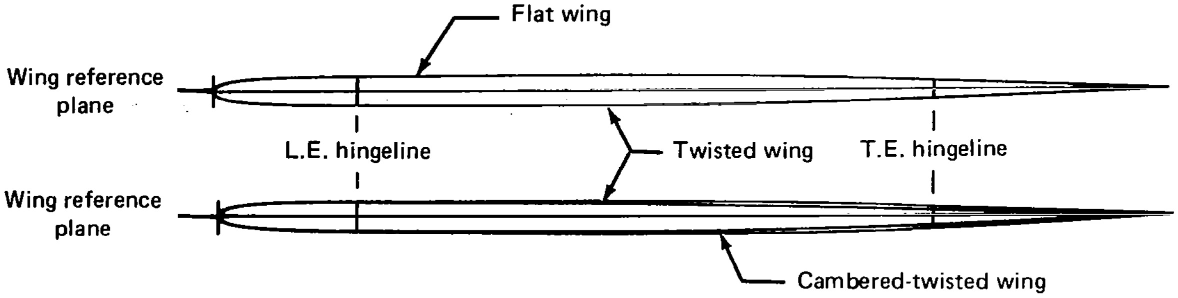

Nominal	Flat wing, $\alpha_{sec} = 0.0°$				Twisted wing, $\alpha_{sec} = -0.01°$		Cambered-twisted wing, $\alpha_{sec} = -0.01°$	
	Rounded leading edge		Sharp leading edge		Rounded leading edge		Rounded leading edge	
	Upper surface	Lower surface	Upper surface	Lower surface	Upper surface	Lower surface	Upper surface	Lower surface
0.00	0.00		–	–	0.00		0.00	
2.50	2.45	2.59	2.61	2.54	2.26	2.26	2.58	2.51
5.00	4.95	5.07	5.06	5.03	4.76	4.76	5.10	5.04
8.50	8.45	8.53	8.59	8.58	8.40	8.26	8.64	8.56
11.30	–	–	–	11.31	–	–	–	–
12.25	–	–	–	–	12.23	12.27	–	–
12.50	12.45	12.55	12.58	–	–	–	12.63	12.54
17.50	17.49	17.62			17.59	17.66	17.64	17.55
20.00	19.94	20.08			20.03	20.03	20.14	20.00
30.00	29.92	30.09			29.98	29.89	30.14	30.00
45.00	45.00	45.07			44.96	44.89	45.12	45.03
60.00	59.98	60.08			60.01	59.97	60.11	60.00
70.00	70.03	70.13			70.05	69.95	70.09	70.04
72.50	72.55	72.60			72.58	72.51	72.62	72.54
77.50	77.53	77.62			77.56	77.51	77.63	77.52
85.00	85.11	85.14			85.03	85.00	85.12	85.04
90.00	90.10	90.10			90.04	89.98	90.12	90.00
95.00	95.09	95.05			94.96	94.98	95.10	95.03

Table A-3.—(Continued)

(b) Section at $0.20\frac{b}{2}$, chord = 91.80 cm

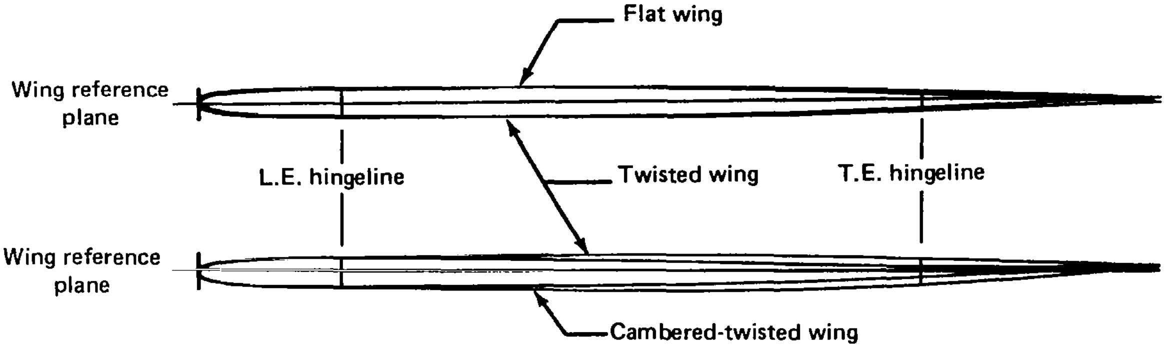

	Flat wing, α_{sec} = 0.0°				Twisted wing, α_{sec} = –0.47°		Cambered-twisted wing, α_{sec} = –0.47°	
	Rounded leading edge		Sharp leading edge		Rounded leading edge		Rounded leading edge	
Nominal	Upper surface	Lower surface	Upper surface	Lower surface	Upper surface	Lower surface	Upper surface	Lower surface
0.00	0.00		–	–	0.00		0.00	
2.50	2.59	2.69	2.62	2.65	2.52	2.42	2.63	2.59
5.00	5.05	5.00	5.14	5.14	5.00	4.93	5.09	5.05
8.50	8.54	8.59	8.67	8.62	8.52	8.40	8.61	8.64
11.40	–	–	–	11.37	–	–	–	–
12.50	12.54	12.49	12.63	–	12.53	12.42	12.51	12.62
17.50	17.63	17.61			17.65	17.52	17.59	17.63
20.00	20.08	20.07			20.00	19.90	19.95	20.05
30.00	30.04	30.09			30.02	29.89	30.05	29.97
45.00	45.08	45.09			45.03	44.92	45.04	45.01
60.00	60.02	60.13			60.03	59.91	60.02	60.06
70.00	70.11	70.13			70.06	69.96	70.03	70.01
72.50	72.63	72.61			72.55	72.50	72.59	72.67
77.50	77.59	77.65			77.59	77.52	77.53	77.57
85.00	85.07	85.13			85.02	85.00	85.09	85.10
90.00	90.14	90.11			90.07	89.97	90.04	89.98
95.00	95.14	95.10			95.05	95.08	95.06	94.98

Table A-3.—(Continued)

(c) Section at $0.35\frac{b}{2}$, chord = 76.69 cm

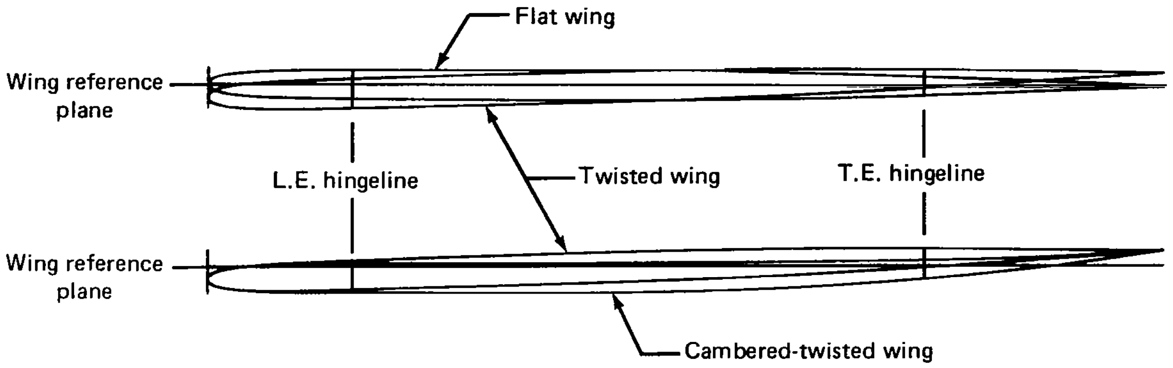

Nominal	Flat wing, α_{sec} = 0.0°				Twisted wing, α_{sec} = −1.70°		Cambered-twisted wing, α_{sec} = −1.70°	
	Rounded leading edge		Sharp leading edge		Rounded leading edge		Rounded leading edge	
	Upper surface	Lower surface	Upper surface	Lower surface	Upper surface	Lower surface	Upper surface	Lower surface
0.00	0.00		–	–	0.00		0.00	
2.50	2.45	2.59	2.59	2.58	2.39	2.33	2.76	2.60
5.00	4.93	5.07	5.11	5.04	5.12	4.78	5.05	5.10
8.50	8.60	8.54	8.65	8.63	8.49	8.32	8.68	8.70
10.50	–	–	–	10.46	–	–	–	–
11.00	–	11.03	–	–	–	–	–	–
12.50	12.37	–	12.57	–	12.50	12.33	12.59	12.68
17.50	17.64	17.63			17.54	17.53	17.64	17.62
20.00	20.00	20.09			19.94	19.84	20.03	20.07
30.00	30.01	30.10			29.88	29.87	30.00	29.93
45.00	44.99	45.09			44.96	44.79	45.00	45.13
60.00	60.03	60.08			59.97	59.89	60.00	60.10
70.00	70.07	70.08			70.03	69.90	70.04	70.03
72.50	72.55	72.58			72.56	72.44	72.61	72.52
77.50	77.60	77.61			77.54	77.51	77.50	77.60
85.00	85.11	85.14			85.08	84.96	85.09	84.93
90.00	90.06	90.09			89.89	89.89	89.98	90.04
95.00	95.07	95.09			94.95	94.86	94.98	95.10

Table A-3.–(Continued)

(d) Section at 0.50 $\frac{b}{2}$, chord = 61.57 cm

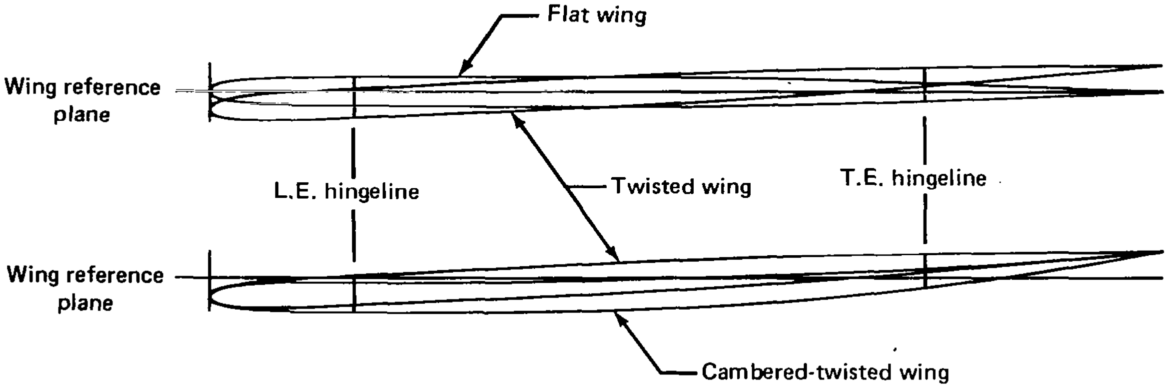

Nominal	Flat wing, α_{sec} = 0.0°				Twisted wing, α_{sec} = –2.85°		Cambered-twisted wing, α_{sec} = –2.85°	
	Rounded leading edge		Sharp leading edge		Rounded leading edge		Rounded leading edge	
	Upper surface	Lower surface	Upper surface	Lower surface	Upper surface	Lower surface	Upper surface	Lower surface
0.00	0.00		–	–	0.00		0.00	
2.50	2.47	2.53	2.69	2.60	2.44	2.38	2.78	2.62
5.00	4.99	4.95	5.13	5.06	4.92	4.80	5.13	5.15
8.50	8.48	8.38	8.66	8.61	8.46	8.38	8.64	8.56
10.10	–	–	–	10.14	–	–	–	–
11.10	–	11.08	–	–	–	–	–	–
12.50	12.39	–	12.61	–	12.50	12.31	12.71	12.55
17.50	17.64	17.52			17.54	17.24	17.71	17.44
20.00	19.98	19.97			19.92	19.83	20.15	19.89
30.00	30.07	30.06			29.91	29.85	30.04	29.72
45.00	44.98	45.06			45.00	44.85	44.95	44.97
60.00	59.97	60.00			59.95	59.92	59.96	59.94
70.00	70.07	70.10			70.03	69.88	69.93	69.86
72.50	72.65	72.61			72.56	72.44	72.53	72.34
77.50	77.66	77.65			77.61	77.43	77.58	77.43
85.00	85.19	85.18			84.85	84.90	84.96	84.92
90.00	90.22	90.12			89.93	89.93	89.94	89.91
95.00	95.05	94.94			94.88	94.93	94.98	94.88

Table A-3.—(Continued)

(e) Section at 0.65$\frac{b}{2}$, chord = 46.46 cm

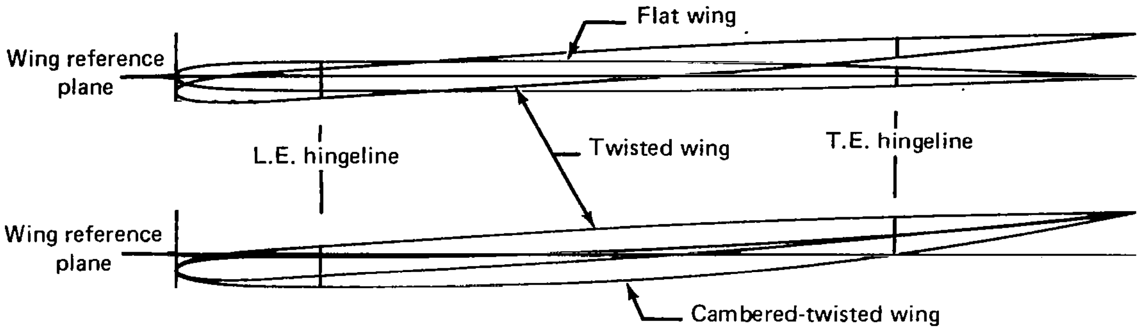

Nominal	Flat wing, α_{sec} = 0.0°				Twisted wing, α_{sec} = –3.59°		Cambered-twisted wing, α_{sec} = –3.59°	
	Rounded leading edge		Sharp leading edge		Rounded leading edge		Rounded leading edge	
	Upper surface	Lower surface	Upper surface	Lower surface	Upper surface	Lower surface	Upper surface	Lower surface
0.00	0.00		–	–	0.00		0.00	
2.50	2.56	2.66	2.49	2.38	2.18	2.49	2.76	2.79
5.00	5.06	5.12	4.94	4.95	4.76	5.01	5.35	5.40
8.50	8.55	8.55	8.46	8.40	8.32	8.45	8.85	8.74
12.20	–	–	12.12	–	12.21	–	–	–
12.60	12.57	–	–	–	–	–	12.71	12.77
17.50	17.60	17.65			17.24	17.44	17.74	17.58
20.00	20.17	20.11			19.70	19.88	20.19	19.96
30.00	30.05	30.11			30.26	29.73	30.13	29.85
45.00	45.16	45.23			44.75	44.89	45.03	44.75
60.00	60.13	60.13			59.81	59.87	60.02	59.99
70.00	69.89	70.12			69.92	69.90	70.09	69.88
72.50	72.59	72.69			72.38	72.49	72.83	72.15
77.50	77.74	77.76			77.22	77.49	77.56	77.43
85.00	85.25	85.32			84.79	84.93	84.93	84.76
90.00	90.22	90.21			89.70	89.92	89.95	89.98
95.00	95.13	95.27			95.12	94.86	94.97	94.98

Table A-3.—(Continued)

(f) Section at $0.80\frac{b}{2}$, chord = 31.35 cm

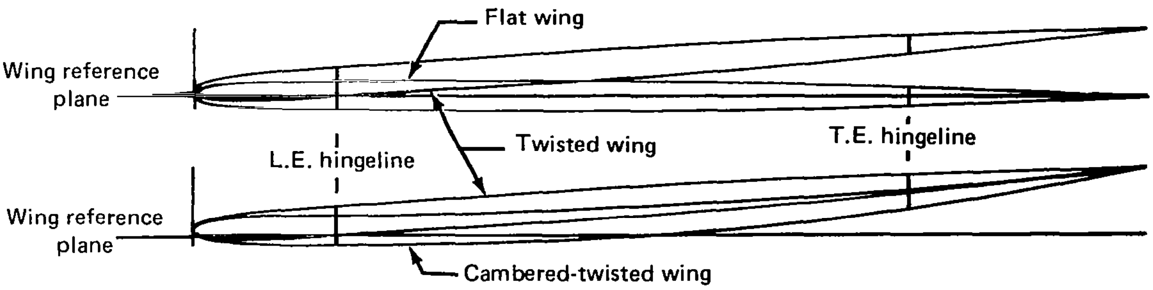

Nominal	Flat wing, α_{sec} = 0.0°				Twisted wing, α_{sec} = −3.84°		Cambered-twisted wing, α_{sec} = −3.84°	
	Rounded leading edge		Sharp leading edge		Rounded leading edge		Rounded leading edge	
	Upper surface	Lower surface	Upper surface	Lower surface	Upper surface	Lower surface	Upper surface	Lower surface
0.00	0.00		–	–	0.00		0.00	
2.50	2.55	2.47	2.50	2.46	2.33	2.43	2.76	2.62
5.00	5.01	5.02	5.01	4.93	4.86	4.74	5.27	5.21
8.50	8.55	8.59	8.58	8.41	8.32	–	8.78	8.54
12.50	12.50	–	12.58	–	12.47	12.43	12.69	12.58
17.50	17.53	17.57			17.36	17.47	17.83	17.34
20.00	20.16	20.13			19.79	19.82	20.11	19.79
30.00	30.00	30.11			29.83	29.83	30.15	29.48
45.00	44.91	45.15			44.81	44.91	44.81	44.75
60.00	59.94	60.10			59.80	59.92	59.84	59.79
70.00	70.06	70.11			69.89	69.87	69.77	69.94
72.50	72.61	72.60			72.22	72.39	72.50	72.33
77.50	77.73	77.72			77.29	77.41	77.22	77.40
85.00	85.25	85.18			84.80	84.95	84.92	84.92
90.00	90.20	90.34			90.62	90.03	90.19	90.09
95.00	95.41	95.49			95.71	95.00	95.05	94.94

Table A-3.—(Concluded)

(g) Section at $0.93\frac{b}{2}$, chord = 18.25 cm

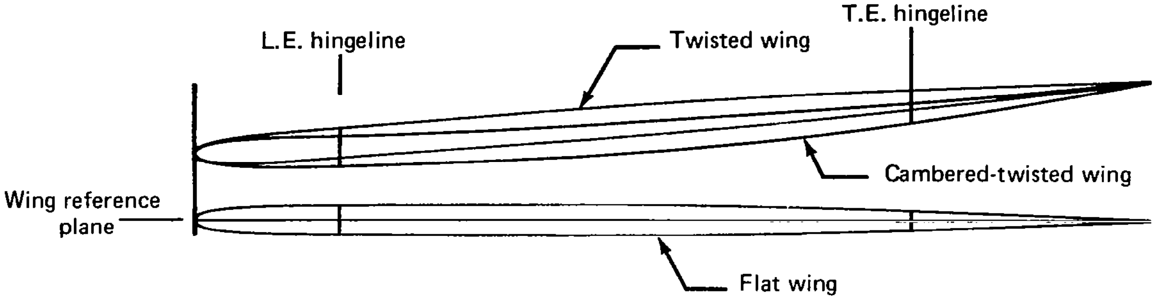

Nomina	Flat wing, α_{sec} = 0.0°				Twisted wing, α_{sec} = –4.14°		Cambered-twisted wing, α_{sec} = –4.14°	
	Rounded leading edge		Sharp leading edge		Rounded leading edge		Rounded leading edge	
	Upper surface	Lower surface	Upper surface	Lower surface	Upper surface	Lower surface	Upper surface	Lower surface
0.00	0.00		–	–	0.00		0.00	
2.51	1.70	1.81	2.12	1.86	1.74	2.59	2.77	2.26
5.00	4.38	4.68	4.72	4.52	4.41	4.65	5.11	4.79
8.50	7.89	8.24	8.21	8.06	7.92	8.23	8.64	8.13
11.59	–	–	–	–	11.59	–	–	–
12.25	12.33	–	12.19	–	–	–	12.64	12.16
17.50	17.36	16.60			16.60	17.49	18.03	16.83
20.00	19.78	19.81			19.58	19.96	19.94	19.44
30.00	29.67	29.00			29.17	29.62	30.22	28.66
45.00	44.70	44.80			44.12	44.44	44.33	44.77
60.00	59.68	59.47			59.18	59.71	59.47	59.38
70.00	69.69	70.33			68.99	69.31	69.10	70.07
72.50	72.15	71.89			71.59	72.01	71.78	72.74
77.50	77.38	77.31			76.80	77.12	76.49	77.36
85.00	84.62	84.90			84.54	84.82	84.93	85.29
90.00	89.51	89.81			89.21	89.74	90.72	90.35
95.00	94.46	94.68			94.41	94.56	95.26	94.87

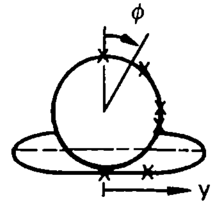

Table A-4.—Body Pressure Orifice Locations

Nominal locations	x/L, percent body length														
	4.5	7.5	11.0	14.5	21.8	25.0	33.0	39.0	50.0	55.0	60.0	64.0	70.0	75.5	80.0
$\phi = 0.0°$	0.0	0.0	0.0	0.0	0.0	0.0	0.0	0.0	0.0*	0.0*	0.0*	0.0	0.0	0.0	0.0
$\phi = 45.0°$	44.3	44.3	44.5	44.7	44.4	44.8	45.0	44.8	45.0	44.8	44.8	45.0	44.8	45.0	44.8
$\phi = 90.0°$	90.0	89.9	90.5	90.3	90.4	89.9	90.1	90.2	90.2	90.0	89.9	89.9	89.8	90.1	89.8
$\phi \approx 110.0°$	———	———	———	———	110.2	110.0	110.1	110.1	110.2	116.8	119.9	124.2	———	———	———
Body, $\phi = 135.0°$	136.1	135.3	135.0	135.2									134.6	134.5	134.8
Flat wing, y = 3.094 cm					3.025	3.028	3.028	3.056	3.071	3.056	3.043	3.045			
Twisted wing, y = 3.094 cm					3.132	3.106	3.048	3.048	3.005	2.926	3.094	3.094			
Cambered-twisted wing, y = 3.094 cm					3.040	3.056	3.075	3.072	3.079	3.067	3.084	3.069			
Body, $\phi = 180.0°$	180.0	180.0	180.0	180.0						180.0*	180.0*	180.0	180.0	180.0	180.0
Flat wing, y = 0.0 cm					–.018	–.030	–.064	.081	–.048						
Twisted wing, y = 0.0 cm					.020	–.008	–.041	–.043	–.056						
Cambered-twisted wing, y = 0.0 cm					–.046	–.060	–.027	.002	–.032						

*For the first 149 runs of the first test in the BTWT, pressure readings at these orifices did not always stabilize.

Pressure tubing used in this model was 1.016 mm (0.040 in.) o.d. Monel with a 0.1524 mm (0.006 in.) wall thickness. The major channels for wing pressure tubing were machined into the surface. The detailed grooves required to route tubing from the orifices to these channels were cut by hand. The pressure orifices were installed normal to and flush with the local surface. After installation of the pressure tubing, the grooves were filled with solder and brought back to contour by hand-filing to match templates prepared by numerically controlled machining.

Quick disconnects were used at the wing-body junction to reduce the time required for installing a different wing. Unfortunately, by the time the cambered-twisted wing was installed in the test section, one quick-disconnect block had become worn out due to the two previous tests and model checkout. The connection did not seal properly and measurements at a series of orifices (x/c from 0.125 through 0.600) on the lower surface at 0.80 b/2 were not sufficiently accurate to be used. Data values to be used in the integration were obtained by linear spanwise interpolation between adjacent sections.

The tubing for body pressure orifices was run through the hollow center of the model body rather than running it in grooves in the outside contour. Tubing from all the orifices was routed through the hollow body to the scanivalves located in the body nose. Wiring from the scanivalves was routed through the body to the sting.

The nose portion of the body was removable to provide access to the fifteen 24-position scanivalves. Figure A-1 shows the aft body location of the strain gages that were used to measure normal force and pitching moment.

PRESSURE INSTRUMENTATION

The model was instrumented with fifteen 24-position scanivalves. Each scanivalve contained a 103.42-kN/m^2 (15-psi) differential Statham, variable resistance, unbonded strain gage transducer. These transducers are calibrated against a high accuracy standard and, if placed in a temperature-controlled environment, will read within an accuracy of 0.1 percent of full scale. The transducers were located inside the model and subjected to large temperature excursions. During testing in the Boeing Transonic Wind Tunnel (BTWT), temperatures recorded at the scanivalves indicated that the accuracy of the readout was 0.75 percent of full-scale capability based on the calibration data. For tests in the 9- by 7-ft supersonic leg of the NASA Ames Unitary Wind Tunnel, the accuracy of pressure measurements was better than ±0.3 percent, based on the maximum temperature measured in the test section.

During the first test in the BTWT (NAS1-12875), two problems were encountered. For the first 149 runs, the data filter for one of the scanivalves was inadvertently set at too low of a cutoff frequency. This caused a lag that affected five body pressure measurements, which produced a maximum error of approximately 0.684 kN/m^2 (0.1 psi) at an angle of attack of 16° and $M = 0.95$. Table A-4 identifies the specific data affected. During the first half (approximately) of the test, the scanivalve that recorded lower surface pressures between the hingelines for the sections at $2y/b = 0.09$, 0.20, 0.35, and 0.50 was intermittent at an angle of attack of 16°. This problem was eventually traced to an electrical problem in the strut. Rather than sacrifice all of these data, the incorrect measurements were replaced by extrapolating the data from angles of attack of 12° and 14°.

In the second test in the BTWT (NAS1-14962), damage to one of the quick disconnects for the wing caused the loss of measurements at a series of orifices (x/c from 0.125 through 0.600) on the lower surface at 0.80 b/2. Replacement values were obtained by a linear-spanwise interpolation between the adjacent sections.

WIND TUNNEL FACILITIES AND CAPABILITIES

The majority of testing (NASA contracts NAS1-12875 and NAS1-14962) of this model was conducted in the Boeing Transonic Wind Tunnel (BTWT). There was also limited testing (NASA contract NAS1-14141) of the flat and twisted wings in the 9- by 7-ft supersonic leg of the NASA Ames Unitary Wind Tunnel. These two facilities are described in some detail.

BOEING TRANSONIC WIND TUNNEL (BTWT)

The BTWT is a continuous-flow, closed-circuit, single-return facility with an operating range of Mach number from 0.0 to nearly 1.1. The test section is 2.438 by 3.658 by 4.420 m (8 by 12 by 14.5 ft) with 11.0 percent of the wall area in slots.

The tunnel layout is shown in figure A-7. The tunnel stagnation pressure is atmospheric with a total temperature range of 300 K to 356 K (540^0 to 640^0 R). The variation with Mach number of Reynolds number based on the mean aerodynamic chord (M.A.C.) of this model is shown in figure A-8., which also shows the variation of dynamic pressure with Mach number. The 26 856-kW (36 000-hp) wound-rotor induction motor in tandem with a 13 428-kW (18 000-hp) synchronous motor provides the power to drive a 7.315-m (24-ft) diameter fan up to a maximum speed of 470 rpm. The fan is made up of a 5.486-m (18-ft) diameter hub with 72 fixed-pitch fiberglass blades 0.914 m (36 in.) long in two stages and directs circuit air through two stages of 67 hollow steel stators.

Data System

The BTWT data system provides the capabilities of real-time test data acquisition, feedback control computation, and display. The data system consists of an Astrodata acquisition subsystem and a computing subsystem that uses a Xerox data system (XDS 9300) digital computer. The Astrodata system acquires signals from the sensors, conditions them, and passes them directly to the computer. Test data (averaged from as many as 256 samples per test point) are recorded on a rapid-access data drum. As final computations are performed, selected on-line displays are provided on analog X-Y plotters and teletypewriters. Real-time computations and displays are performed every 200 milliseconds for control and test monitoring functions. Any test data may be retrieved from rapid-access drum storage and displayed on an oscilloscope. On-line programs also provide for the preparation of magnetic tapes for plotting or interfacing with off-line programs. Figure A-9 is a schematic of the data acquisition and reduction system.

Mach Number

Mach number in the BTWT is referenced to the horizontal and lateral center of the test section at tunnel station 1000, which was the pitch point of this model (40-percent M.A.C.).

The pressures used in determining the Mach number, p_s, and p_t are measured through permanently positioned sensors. Static pressure p_s is measured by a 103.42-kN/m^2 (15-psi) absolute transducer. A 103.42-kN/m^2 (15-psi) differential transducer is used to obtain total pressure by measuring (p_t-p_s). These transducers are temperature compensated in addition to being in a ±1.11° C (±2° F) environment. Transducer performance is checked periodically, and both the static and differential transducers have shown a maximum deviation of ±0.02 percent of full scale.

The static pressure tap is located out of the test section above the ceiling in the pressure cap plenum. A correction is made to adjust this static pressure reading to the measured test-section-centerline static pressure determined during calibrations at station 1000. The tunnel total pressure is obtained from a total pressure probe mounted near the tunnel ceiling in the bellmouth throat (fig. A-7).

Signals from the pressure sensors are fed to the XDS 9300 computer. The XDS system computes and updates the Mach display five times per second. Accounting for the entire system, calculated Mach number is accurate within ±0.002. Data are recorded only when the tunnel is within a preselected Mach tolerance. For this test, a tolerance of ±0.003 was used.

Dynamic Pressure

The dynamic pressure q is computed from the Mach number and the corrected static pressure. The estimated tolerance on dynamic pressure is ±95.8 N/m^2 (±2.0 psf).

Angle of Attack

The angle of attack of the reference point (0.25 M.A.C. for this model) for a sting-mounted model is a combination of the input angle measured at the base of the sting and several incremental corrections. The input angle of attack is determined by an encoder mounted in the strut. This angle is accurate within ±0.02°. This angle is then modified by the effects of sting deflection, up-flow, and wall corrections.

Sting deflections due to load were determined during the calibrations of the strain gages, which are mounted on the integral sting body of the model. These deflections are known within ±0.02°. The corrections for sting deflection are based on the normal force and pitching moment loads obtained during wind-on data acquisition. The sting deflection was taken into account when setting test angles of attack, to minimize the variation in final angle of attack for the various model configurations. The strain gages attached to the sting body of this model have an estimated accuracy of ±5 percent of full-scale reading. This means that the sting deflections based on maximum model loads were known within ±0.11°.

During run 55 of the second test in the BTWT, the wiring for the pitching moment gage broke, affecting both the normal force and pitching moment measurements and, therefore, the calculation of sting deflection under load. For the remainder of that test, the model angle was set using the angle of attack as determined by the encoder for the most similar previously run configuration. After the test, the normal force and pitching moment obtained by integrating the pressure data were used to correct the final angle of attack. To verify this procedure, a comparison of these two methods was made using data obtained prior to run 55; the results matched within ±0.01°.

Up-flow corrections were made based on data obtained from upright and inverted runs on a calibration model of similar span. These corrections were less than 0.2°. It is generally accepted that the up-flow values are known within ±0.05°.

A correction to model angle was made for the effect of lift interference for 11-percent slotted walls. The lift interference is a function of the ratio of model-to-test section size, test section shape, C_N, and wall geometry. For $C_N = 1.0$, this correction is on the order of $-0.48°$. Due to the limited amount of experimental substantiation, the wall correction could be in error by ±20 percent.

NASA AMES UNITARY WIND TUNNEL, 9- BY 7-FT SUPERSONIC LEG

The 9- by 7-ft supersonic leg of the NASA Ames Unitary Wind Tunnel is a continuous-flow, closed-return, variable-density facility with an operating range of Mach number from 1.54 to 2.50. (A schematic is shown in fig. A-10.) The tunnel is equipped with an asymmetrical sliding-block nozzle and a flexible upper plate; variation of the test section Mach number is achieved by translating, in the streamwise direction, the fixed-contour block that forms the floor of the nozzle. For this test, the Reynolds number was selected as 8.65 by 10^6 based on the mean aerodynamic chord ($\bar{c}$) of this model. The test section is 2.74 by 2.13 by 5.49 m (9 by 7 by 18 ft).

The tunnel air is driven by an 11-stage axial-flow compressor that is powered by four variable-speed, wound-rotor induction motors with a combined output of 134 280 kW (180 000 hp). Four 850 m^3 (30 000 ft^3) spherical storage tanks provide dry air for tunnel pressurization. The temperature is controlled by aftercooling.

Data System

The data acquisition system is comprised of a Beckman 210 analog-digital recorder and a minicomputer. Output from the Beckman 210 is converted to an acceptable format and transmitted by the minicomputer to an IBM 360 computer, which is located in the AMES Research Center central computer facility for the processing and preparation of final data. This flow is illustrated in figure A-11.

Angle of Attack

The angle of attack of the reference point (0.25 M.A.C. for this model) for a sting-mounted model is a combination of the input angle at the base of the sting and an increment due to sting deflection. The input angle of attack at the base of the sting is accurate within 0.02°.

Sting deflections due to load were determined during the calibration of the strain gages mounted on the integral sting body of the model. The corrections for sting deflection are based on the normal force and pitching moment loads obtained during wind-on data acquisition. The sting deflection was taken into account when setting test angles of attack to minimize the variation in final angle of attack for the various model configurations. Only a crude calibration of the normal force and pitching moment gages was obtained since the force and pitching moment measurements were used primarily for calculating sting deflection. Comparison with the integrated pressure results indicates that both force and moment measurements may be about 10 percent low, which could yield a maximum error in final angle of attack of 0.1°.

TESTS AND DATA ACQUISITION

BOEING TRANSONIC WIND TUNNEL (BTWT)

Tests

As previously stated, tests were conducted in the BTWT under two NASA contracts. Table A-5 shows the 54 configurations that were tested under contract NAS1-12875. The 12 configurations tested under contract NAS1-14962 are shown in table A-6. Two of the configurations were included in both tests to ensure that data from the two tests are consistent. Photographs of some of the configurations are shown in figures A-12 through A-15; a diagram of the model installation in the BTWT is shown in figure A-16.

Pressure and total force data were obtained at Mach numbers of 0.40, 0.85, 0.95, and 1.05 for all configurations and at Mach numbers of 0.70, 1.00, and 1.11 for selected configurations. Test angles of attack were from -8^0 to $+16^0$ in 2^0 increments, however, not all angles of attack were included for all configurations and/or Mach numbers. Tables A-5 and A-6 show the run numbers for each Mach number and configuration for which these data were obtained.

During the first test, wingtip deflection pictures were taken for representative configurations at three Mach numbers to evaluate the stiffness of the wing. These were compared to wind-off reference pictures to determine the relative deflection and twist. Configurations included the flat and twisted wings, and trailing-edge control surfaces deflected $+30.2^0$, 0.0^0, and -17.7^0. Whereas the tip did deflect (less than 2 cm), the change in incidence was negligible even at $M = 1.05$; and, due to model flexibility, no corrections to the data were required.

Data Repeatability

Comparisons of data from both tests (NASA CR-165701), show that the data are within the tolerances expected for repeat runs during a single test. Therefore, data from both tests are compared without regard to the test in which the data were obtained.

Data Acquisition and Initial Processing

The pressure data were recorded through the use of fifteen 24-position scanivalves located in the fore body of the model. Pressure transducers in the scanivalves measured the differential pressure between the local surface pressures and tunnel total pressure. Signals from the scanivalves, force and moment data, tunnel parameters, and model attitude angle were recorded on the Astrodata system and reduced using the XDS 9300 computer

NASA AMES UNITARY WIND TUNNEL, 9- BY 7-FT SUPERSONIC LEG

Tests

Table A-7 lists the 13 configurations that were tested. Photographs of two of these are shown in figures A-17 and A-18; a diagram of the model installation in the test section is shown in figure A-19. Pressure and total force data were obtained at Mach numbers of 1.70, 2.10 and 2.50 for all configurations. Table A-7 shows the run numbers for each Mach number and configuration for which these data were obtained. Test angles of attack were from -8^0 to $+14^0$ in 2^0 increments and $+15^0$.

Table A-5.—Summary of Subsonic/Transonic Test Conditions by Run Number (NASA Contract NAS1-12875)

Leading-edge deflection, deg	Mach. no.	Trailing-edge deflection, deg																
		Full span									Outboard (inboard = 0.0)				Inboard (outboard = 0.0)			
		30.2	17.7	8.3	4.1	0.0	−4.1	−8.3	−17.7	−30.2	17.7	8.3	−8.3	−17.7	17.7	8.3	−8.3	−17.7
Flat wing, rounded leading edge, trip strip off																		
Full span=0.0	0.40					10												
	0.70					15												
	0.85					7												
	0.95					16												
	1.05					14												
	1.11					9												
Flat wing, rounded leading edge, trip strip on																		
Full span=0.0	0.40	37	32	46	48	21,269	55	78	66	75	280	275			252	259		
	0.70	34	29	43	50	23,263	57	80	63	72	277	271			248	255		
	0.85	36	31	45	52	25,267	59	82	65, 69	74	279	274			250	258		
	0.95	35	30	44	51	24,266	58	81	64, 68	73	278	273			249	257		
	1.00					268												
	1.05	33	28	42	49	22,264	56	79	62	71	276	272			247	256		
	1.11			40	47	20,262	54	77				270				254		
Inboard =0.0 Outboard=5.1	0.40					223					215	209	196	202	246	241	235	229
	0.70					218					211	205	192	198	243	237	231	228
	0.85					221					214	208	195	201	245	240	233	227
	0.95					220					213	207	194	200	244	239	232	226
	1.05					219					212	206	193	199	242	238	230	224
	1.11					217					210	204	191	197		236		

Table A-5.—(Continued)

Leading-edge deflection, deg	Mach no.	Trailing-edge deflection, deg																
		Full span									Outboard (inboard = 0.0)				Inboard (outboard = 0.0)			
		30.2	17.7	8.3	4.1	0.0	−4.1	−8.3	−17.7	−30.2	17.7	8.3	−8.3	−17.7	17.7	8.3	−8.3	−17.7
Flat wing, rounded leading edge, trip strip on																		
Inboard = 5.1 Outboard = 0.0	0.40					319					286	313			329	324		
	0.70					315					283	311			326	321		
	0.85					318					285	312			328	323		
	0.95					317					284	310			327	322		
	1.05					316					282	308			325	320		
	1.11					314												
Full span = 5.1	0.40		177	149	138	183		189	132									
	0.70		173	145	140	179		185	134									
	0.85		175	148	142	182		188	136									
	0.95		174	147	141	181		187	135									
	1.05		172	146	139	180		186	133									
	1.11			144	137	178		184	131									
Full span = 12.8	0.40		118	115	109	98		85	126									
	0.70		121	112	105	100		87	128									
	0.85		123	114	108	102		89	130									
	0.95		122	113	107	101		88	129									
	1.05		120	111	106	99		86	127									
	1.11		116		104	97		84	124									

Table A-5.—(Concluded)

Leading-edge deflection, deg	Mach no.	Trailing-edge deflection, deg																
		Full span									Outboard (inboard = 0.0)				Inboard (outboard = 0.0)			
		30.2	17.7	8.3	4.1	0.0	−4.1	−8.3	−17.7	−30.2	17.7	8.3	−8.3	−17.7	17.7	8.3	−8.3	−17.7
Flat wing, sharp leading edge, trip strip on																		
Full span = 0.0	0.40					368												
	0.70					366												
	0.85					372												
	0.95					374												
	1.00					373												
	1.05					367												
	1.11					365												
Flat wing, twisted trailing edge, rounded leading edge, trip strip on																		
Full span = 0.0	0.40		352	347	342	337		358	363									
	0.70		349	344	339	333		354	360									
	0.85		351	346	341	336		356	362									
	0.95		350	345	340	335		357	361									
	1.05		348	343	338	334		353	359									
	1.11					332												
Twisted wing, rounded leading edge, trip strip on																		
Full span = 0.0	0.40	427	422	416	411	450		435	442									
	0.70	424	419	413	408	445		432	439									
	0.85	426	421	415	410	449		434	441									
	0.95	425	420	414	409	447		433	440									
	1.00					448												
	1.05	423	418	412	407	446		431	438									
	1.10					444												

Table A-6.—Summary of Subsonic/Transonic Test Conditions by Run Number (NASA Contract NAS1-14962)

Mach number	Trailing-edge deflection, degrees			
	Full span		Outboard (inbd=0.0)	Inboard (outbd=0.0)
	0.0	8.3	8.3	8.3
Twisted wing				
0.40	15	25	30	20
0.70	14	24	29	19
0.85	13	23	28	18
0.95	12	22	27	17
1.00	11			
1.05	10	21	26	16
Cambered-twisted wing, fin off				
0.40	43	65	80	57
0.70	41			
0.85	40	62	78	59
0.95	39	64	79	58
1.00	38			
1.05	37	61	77	55
Cambered-twisted wing, fin on				
0.40	49	70	75	54
0.70	45			
0.85	48	68	73	52
0.95	47	69	74	53
1.00	46			
1.05	44	67	72	51

Table A-7.—Summary of Supersonic Test Conditions by Run Number. Reynolds Number = 8.65×10^6 (NASA Contract NAS1-14141)

Leading-edge deflection, deg	Mach no.	Trailing-edge deflection, deg							
		Full span				Outboard (inboard = 0.0)		Inboard (outboard = 0.0)	
		8.3	4.1	0.0	−4.1	8.3	4.1	8.3	4.1
Flat wing, rounded L.E.									
Full span = 0.0	1.543			19					
	1.70	26	37	20	44	23	40	30	34
	2.10	27	38	21	45	24	41	31	35
	2.50	28	39	22	46	25	42	32	36
Full span = 5.1	1.70			16					
	2.10			17					
	2.50			18					
Flat wing, sharp L.E.									
Full span = 0.0	1.70			51					
	2.10			52					
	2.50			53					
Full span = 5.1	1.70			48					
	2.10			49					
	2.50			50					
Twisted wing, rounded L.E.									
Full span = 0.0	1.60			1					
	1.70	11		3					
	1.90			4, 6					
	2.10	12		9					
	2.50	13		10					

Data Acquisition and Initial Processing

The pressure data were recorded through the use of fifteen 24-position scanivalves located in the fore body of the model. Pressure transducers in the scanivalves measured the differential pressure between the local surface pressures and a known reference pressure. Signals from the scanivalves, force and moment data, tunnel parameters, and model attitude angle were recorded on the Beckman 210 analog-digital recorder and reduced by the Ames staff.

TRIP STRIP

A trip strip of no. 60 carborundum grit was used throughout the tests with the exception of one series. On the body, the trip strip was 0.32 cm (0.125 in.) wide and placed 2.54 cm (1 in.) from the nose. On the wing, it was 0.32 cm (0.125 in.) wide from the side of body to the midspan control surface break (0.57 b/2), and tapered to 0.16 cm (0.0625 in.) wide at the wingtip. On the upper surface of the wing, the trip strip was placed at 15-percent chord; and, on the lower surface, it was placed just aft of the location of the leading-edge control surface brackets on the flat wing (see fig. A-6). Density of the grit was 4 to 5 grains per quarter-inch (6 to 8 grains per cm) of trip strip length.

FINAL DATA

Final data (pressure coefficients, tunnel parameters, and model attitude) were merged on magnetic tapes with appropriate configuration and test point identification for integration and plotting of these data.

A detailed description of the data editing and integration procedure are included in appendix B.

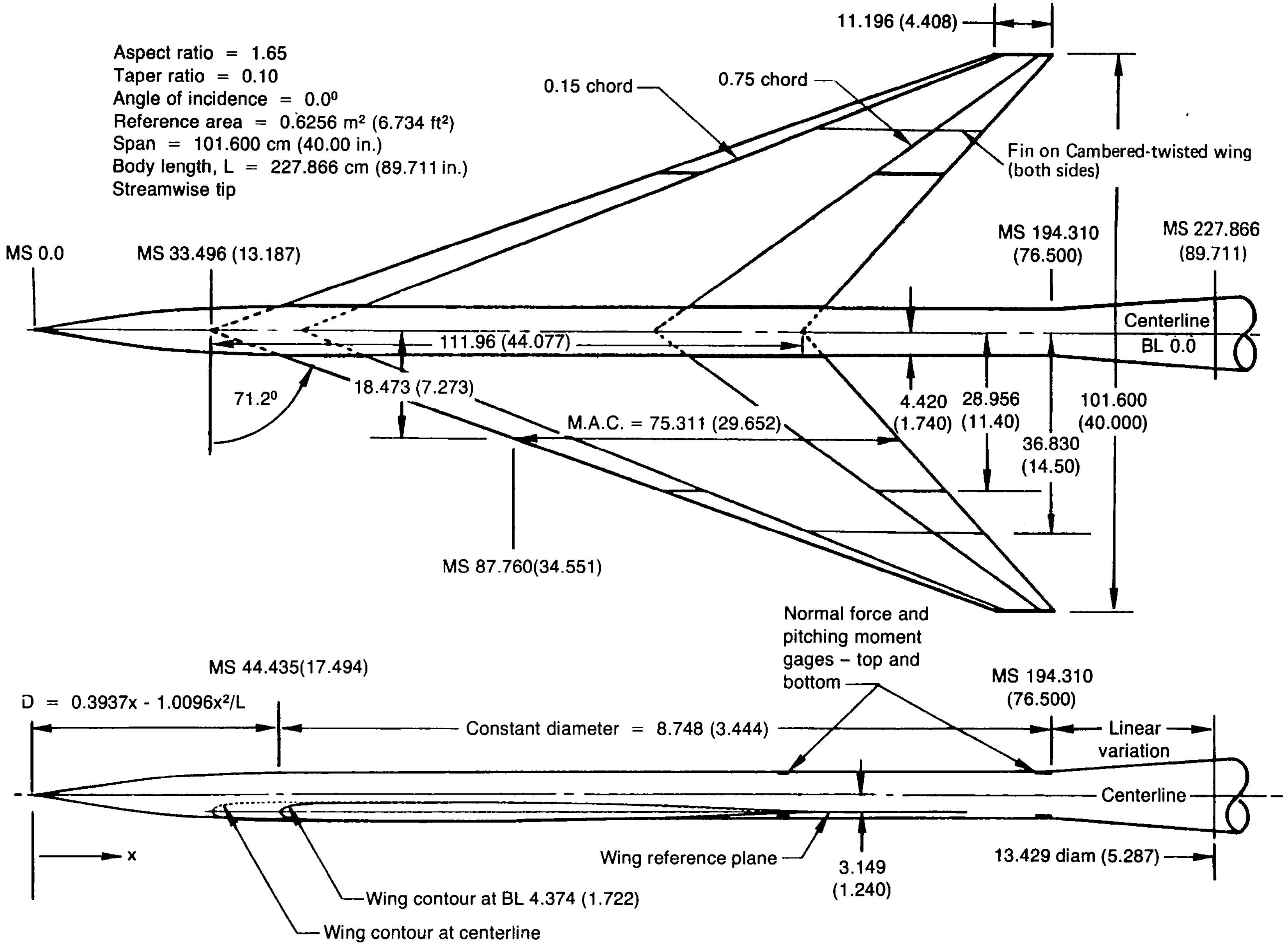

All dimensions in centimeters (inches)

Figure A-1.—General Arrangement and Characteristics

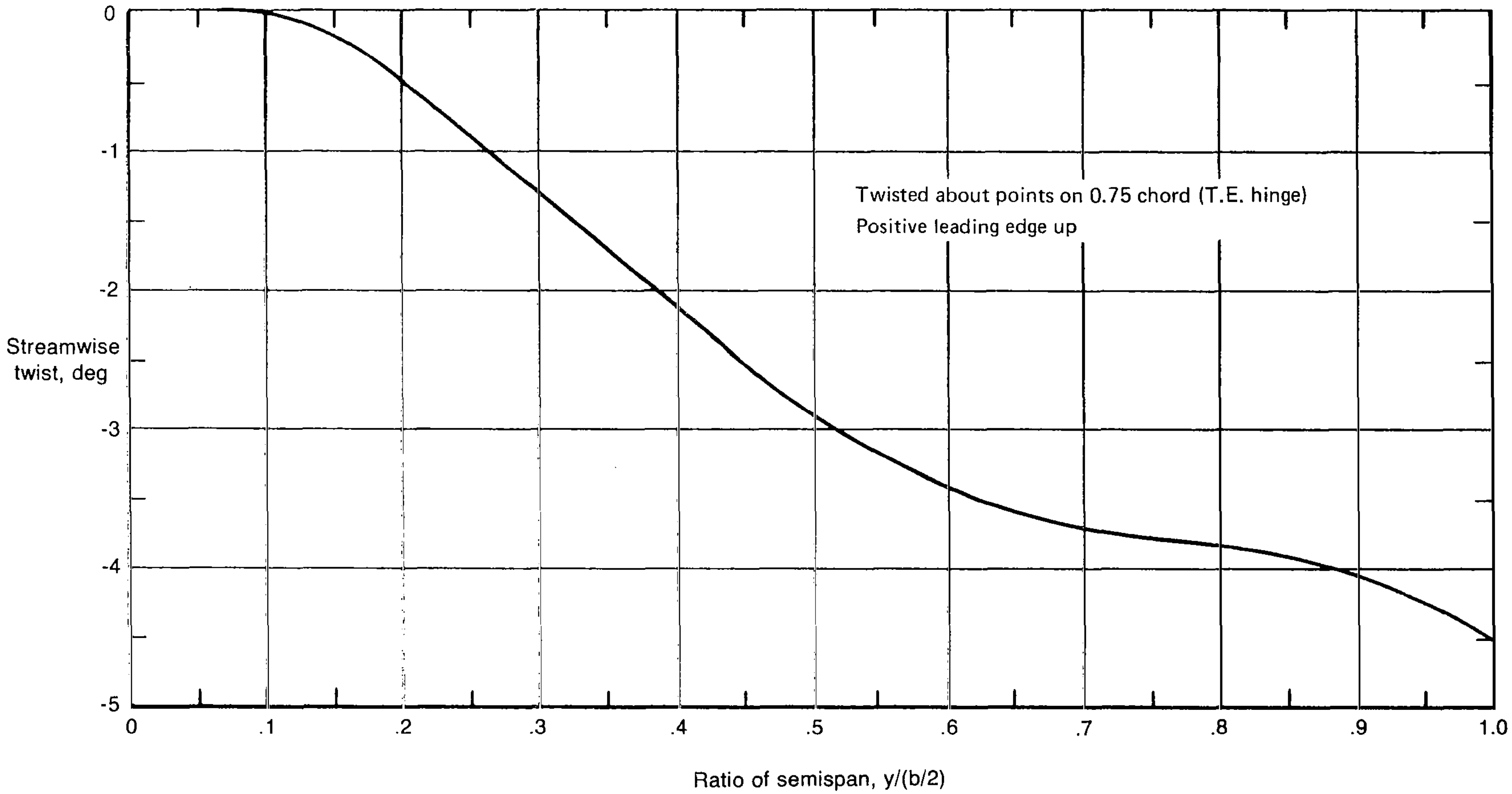

Figure A-2.—Spanwise Twist Distribution for the Model Wing

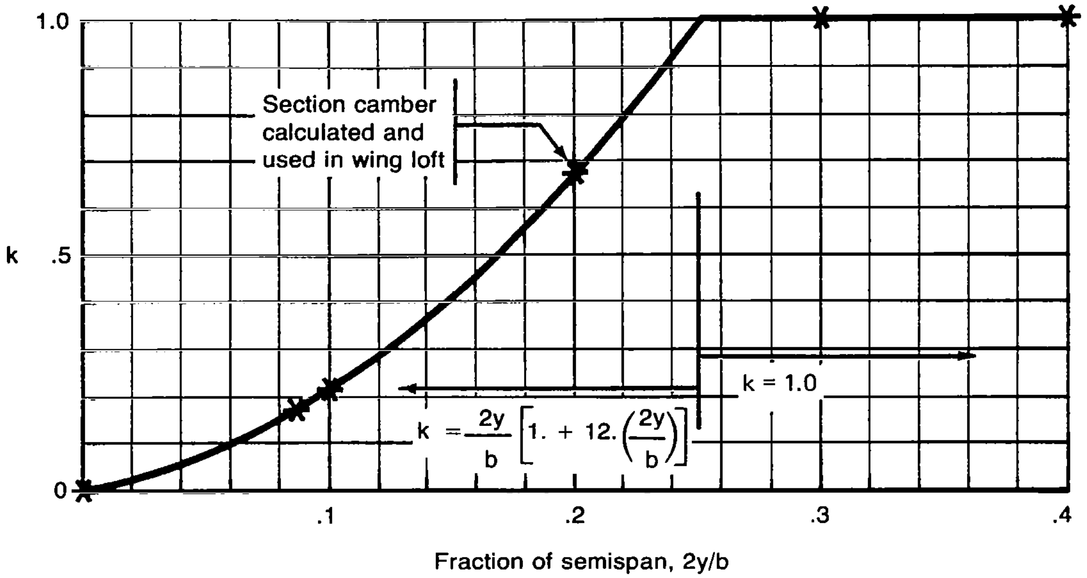

(a) Definition of k, Factor on Basic Camber

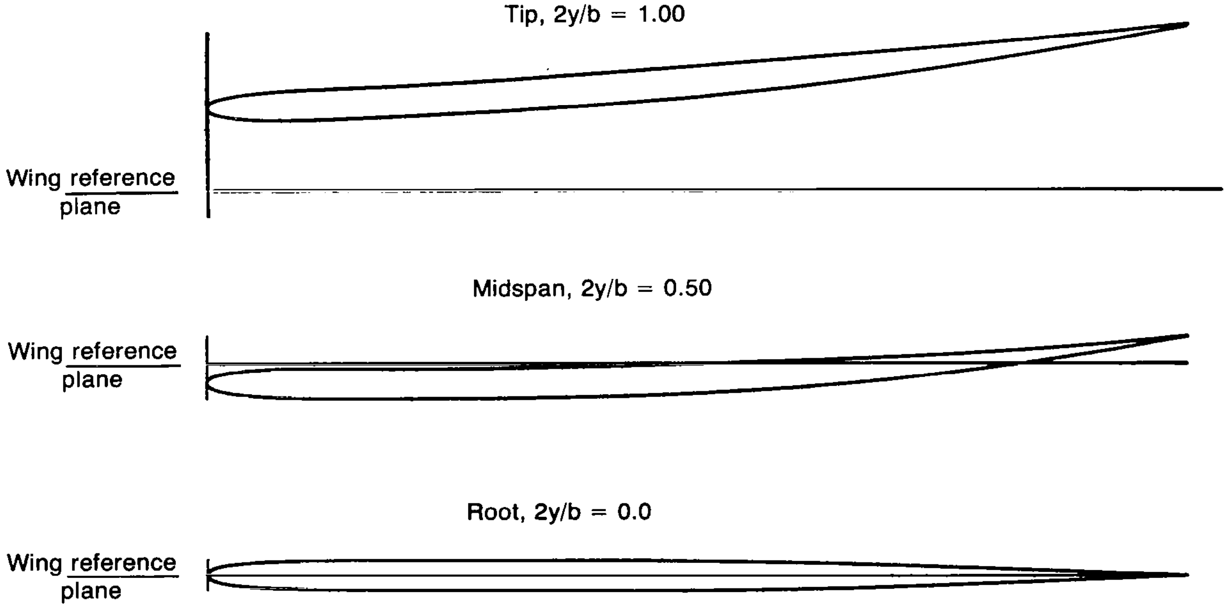

(b) Typical Sections

Figure A-3.—Cambered-Twisted Wing Section Geometry

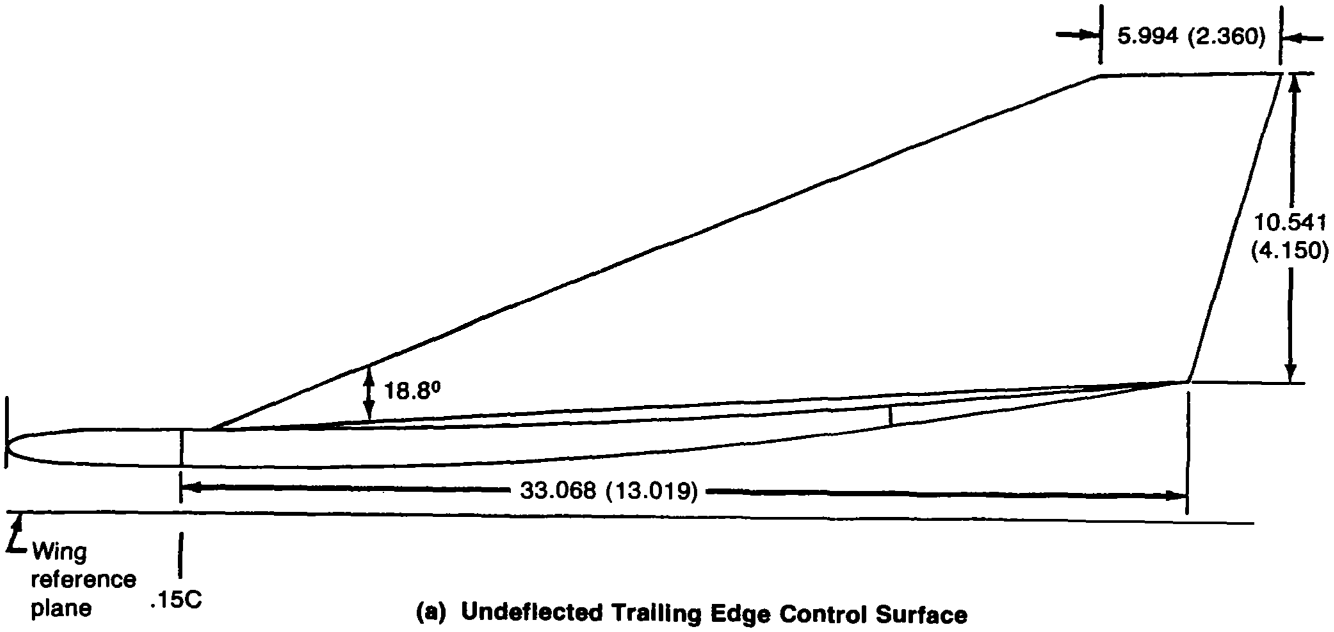

(a) Undeflected Trailing Edge Control Surface

All dimensions in centimeters (inches)

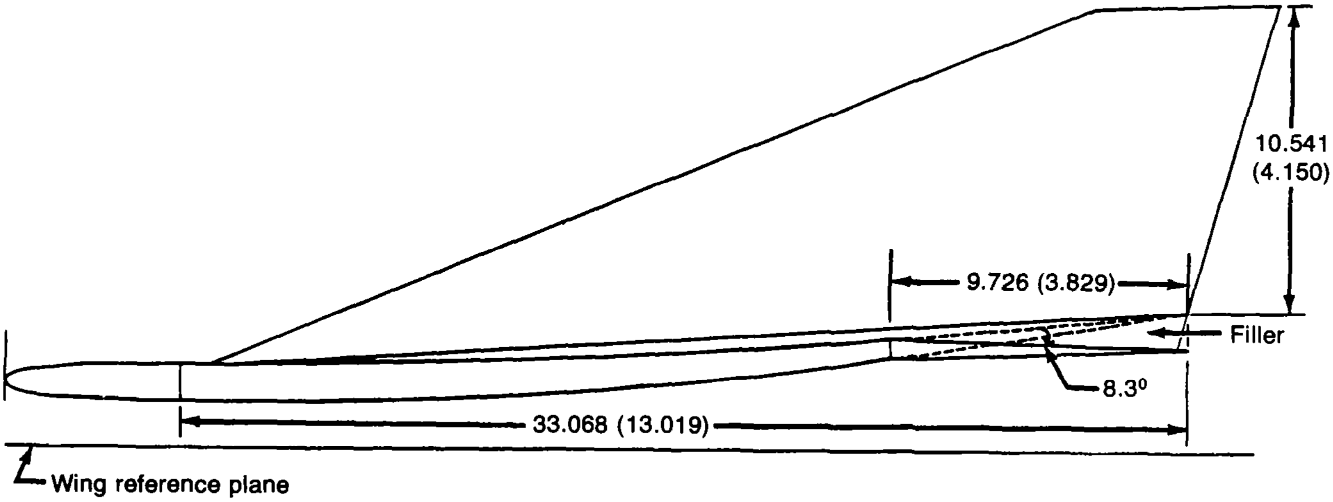

(b) Trailing Edge Control Surface Deflected 8.3°

Figure A-4.—Fin Geometry, Section at 0.725 Semispan

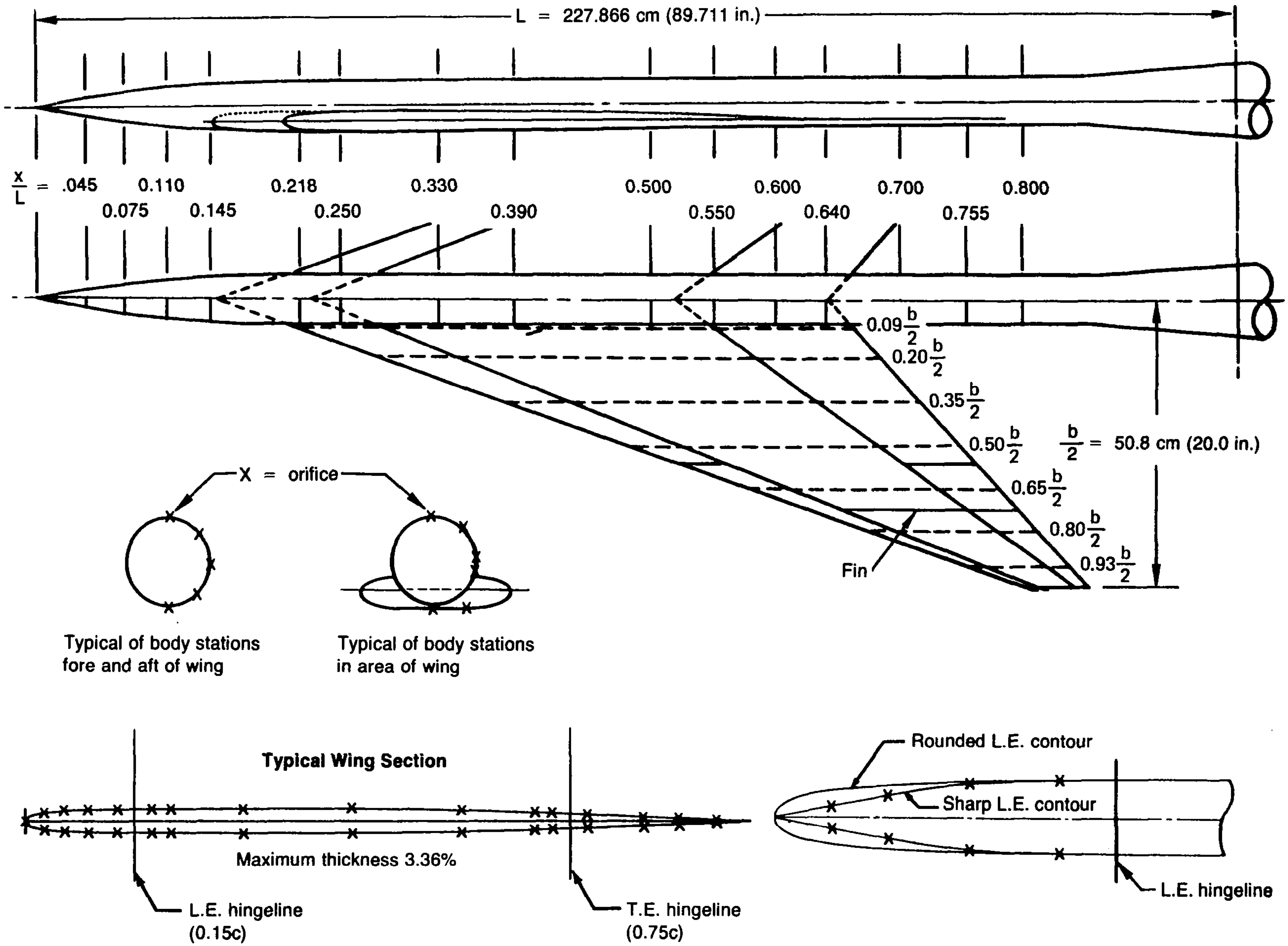

Figure A-5.-Pressure Orifice Locations

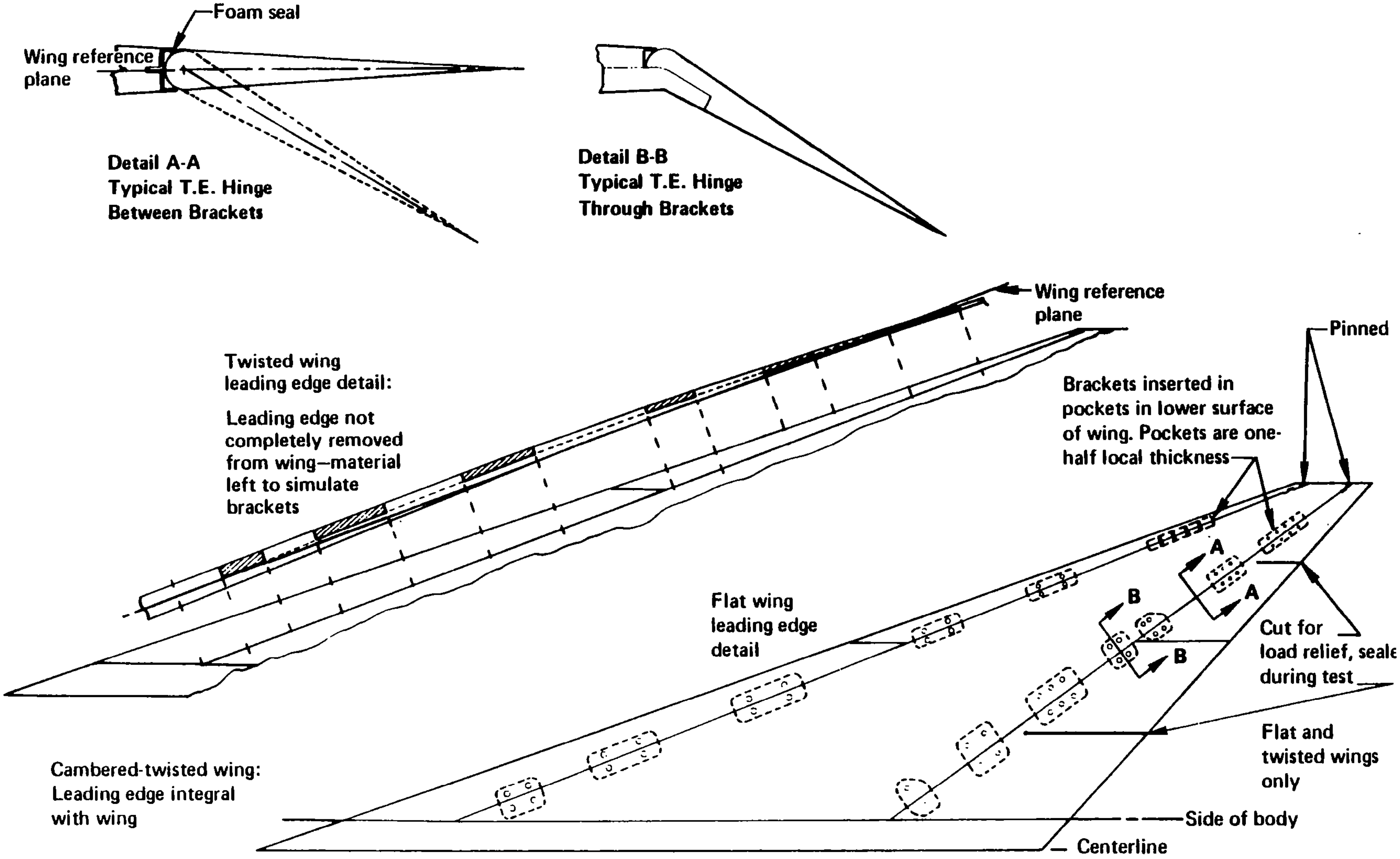

Figure A-6.—Control Surface Bracket Details

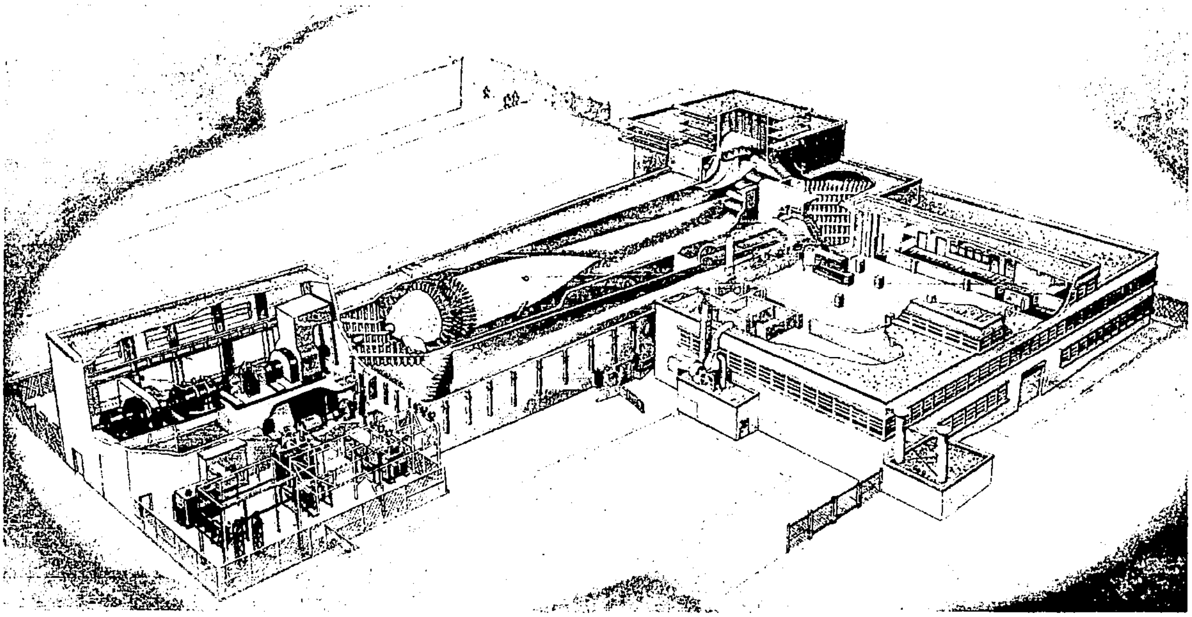

(a) Schematic

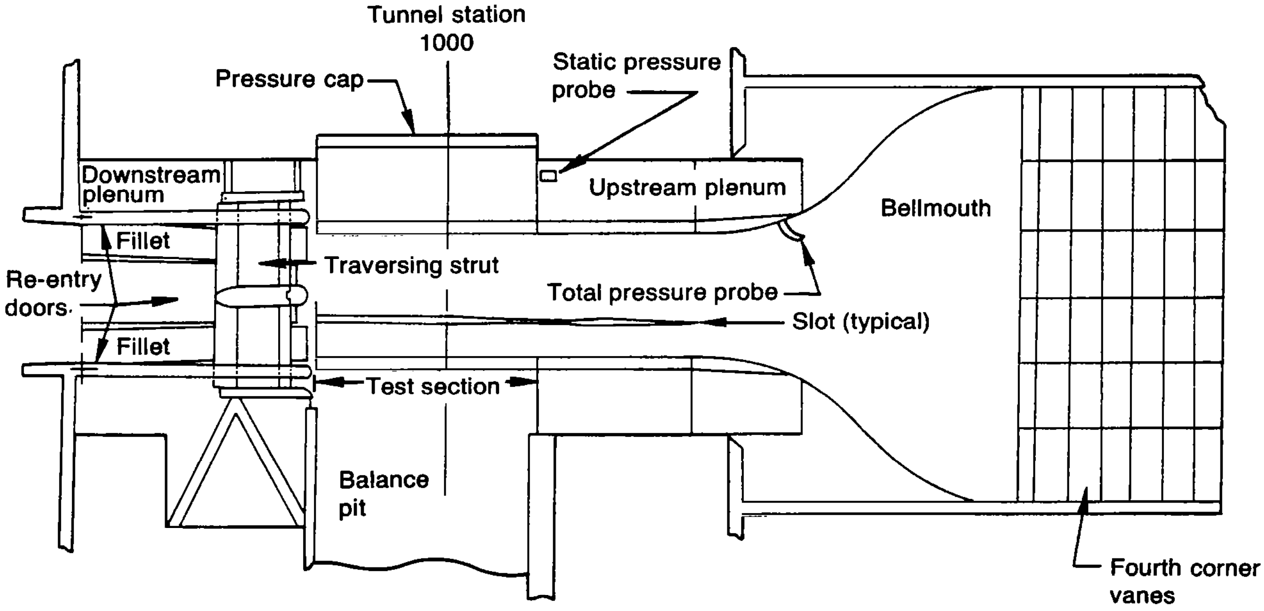

(b) Test Section

Figure A-7.—Boeing Transonic Wind Tunnel

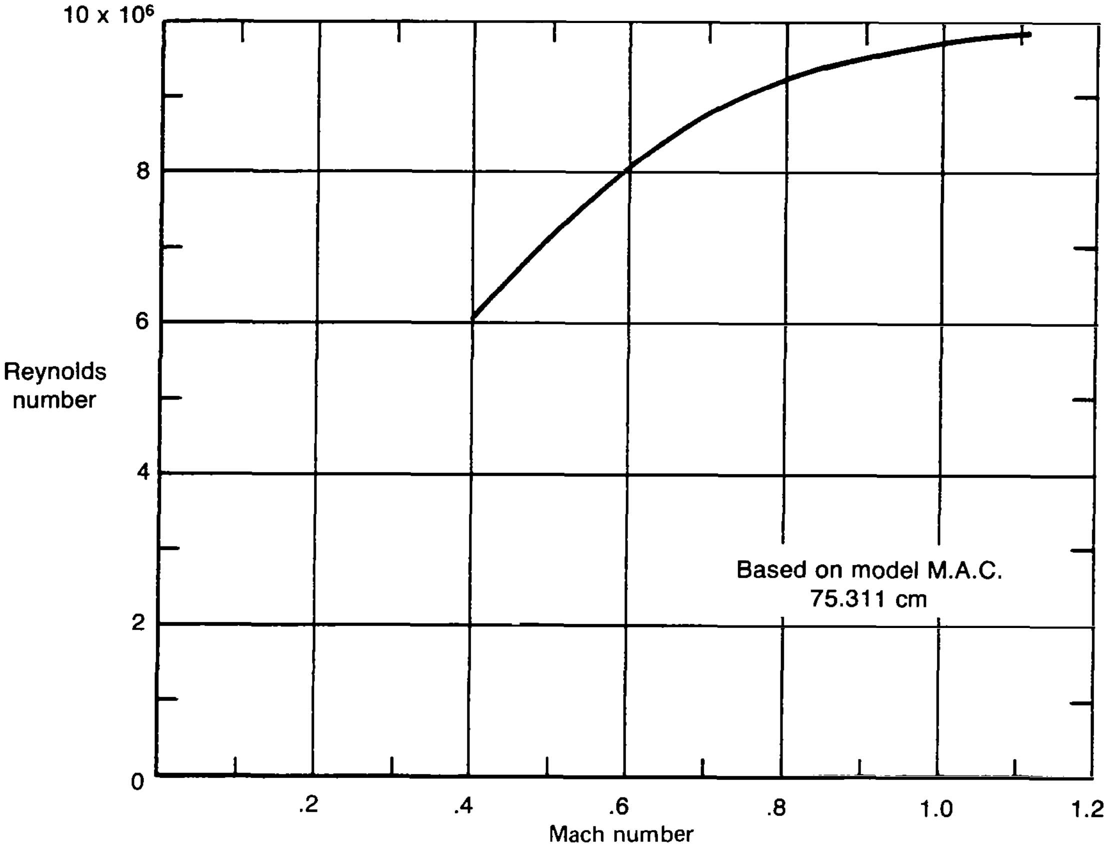

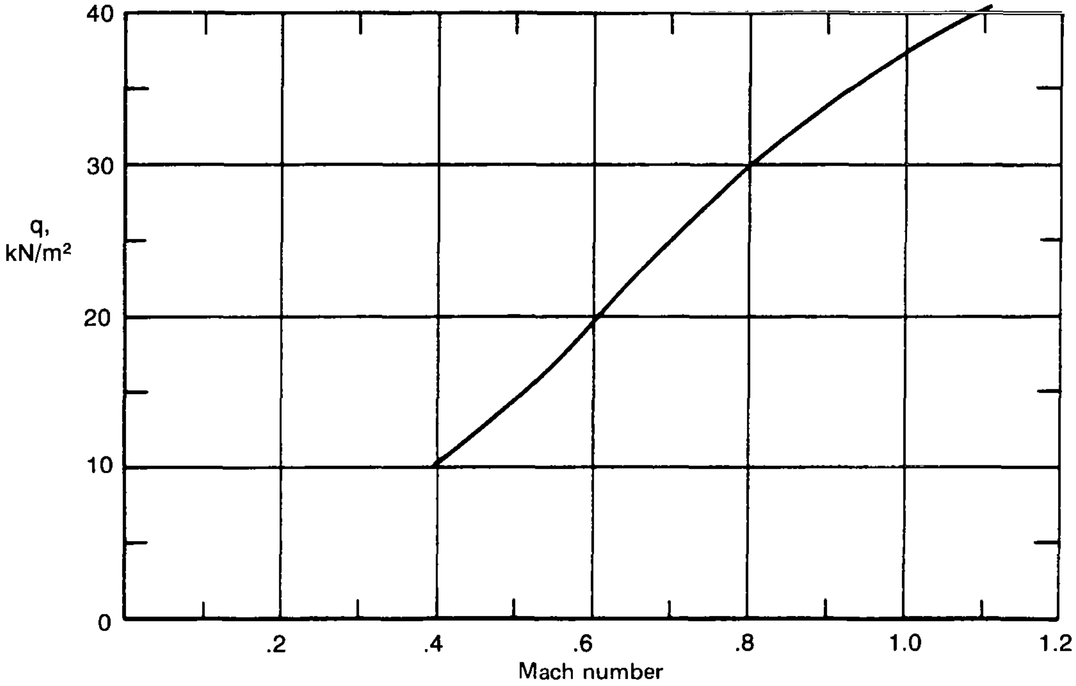

Figure A-8.—Variation of Reynolds Number and Dynamic Pressure With Mach Number

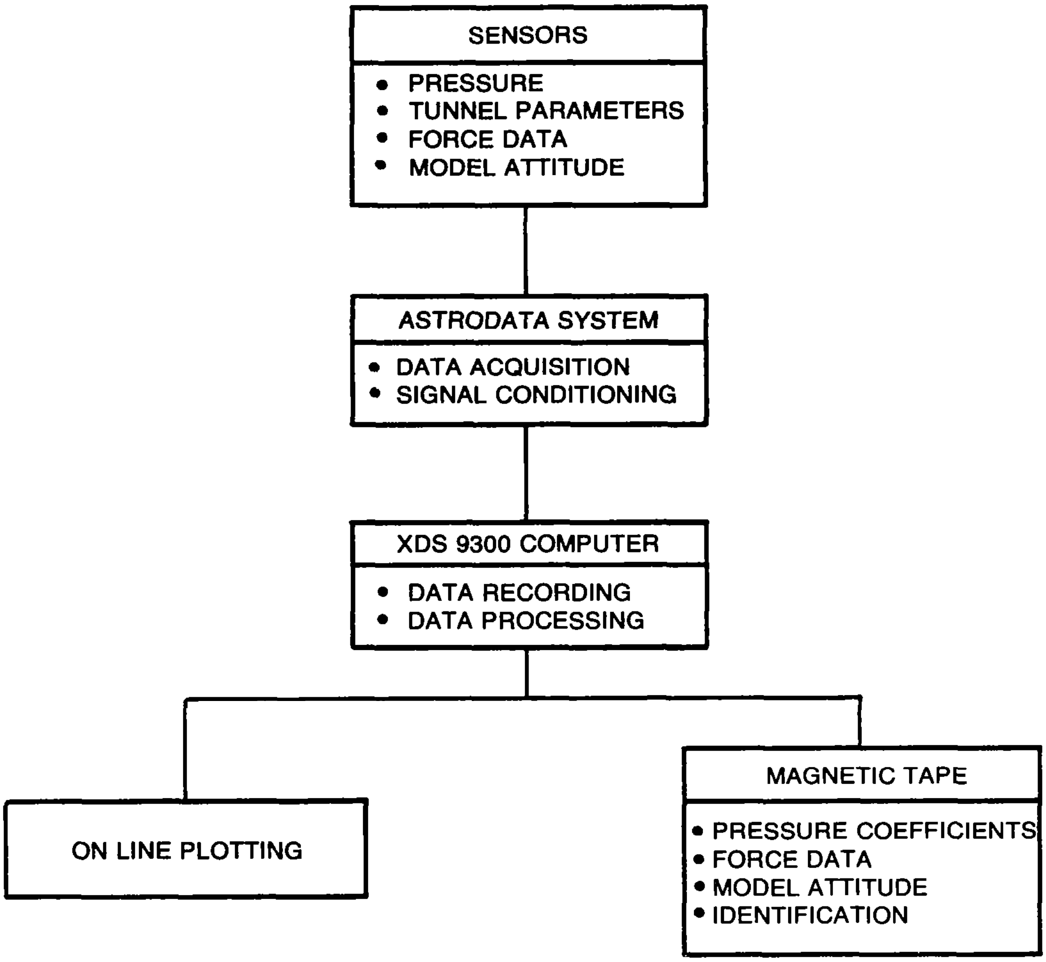

Figure A-9.—Data Acquisition and Reduction System—Boeing Transonic Wind Tunnel

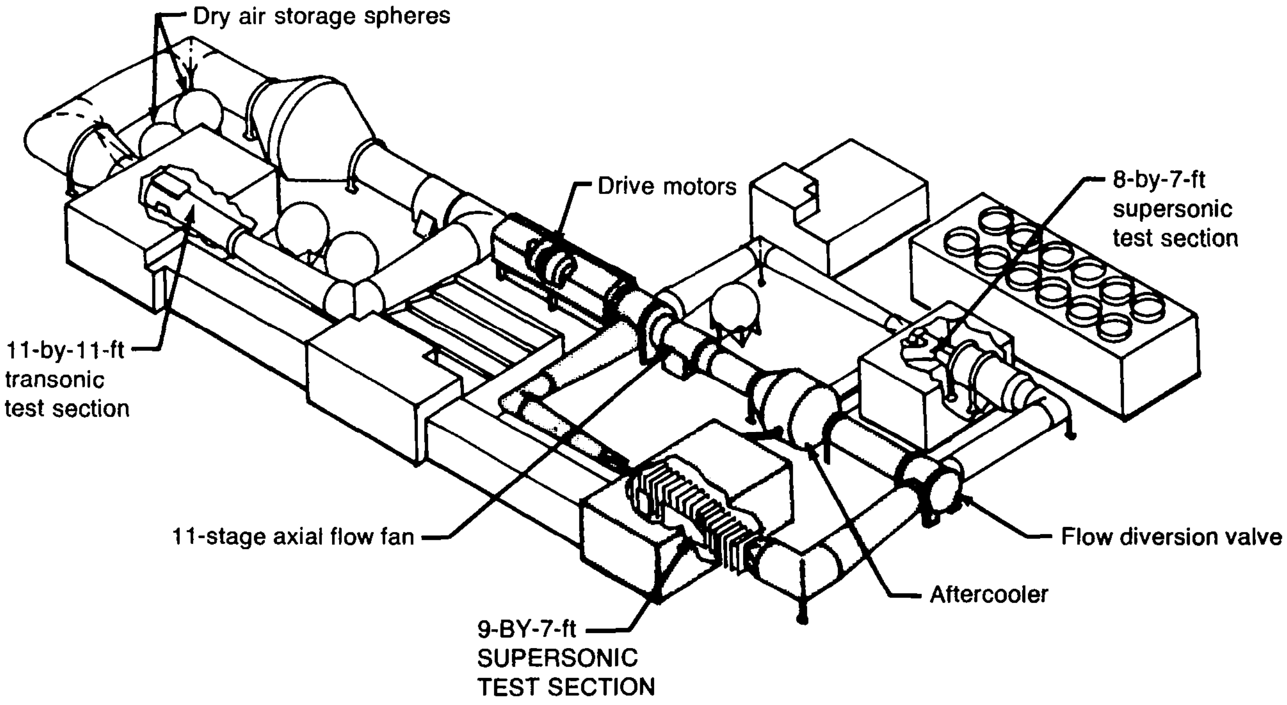

Figure A-10.—Schematic of 9- by 7-ft Supersonic Leg of NASA Ames Unitary Wind Tunnel

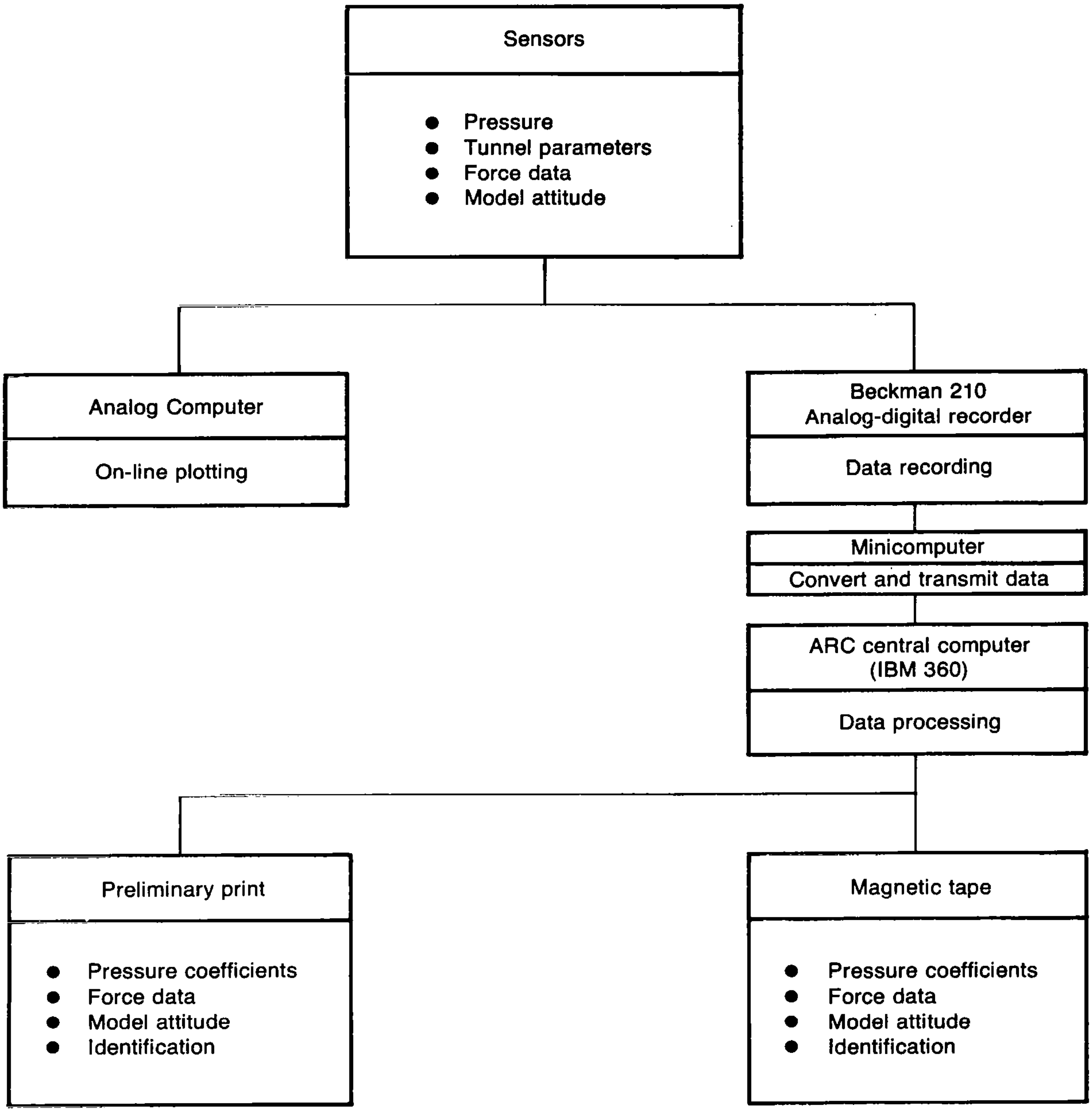

Figure A-11.—Data Acquisition and Reduction System—9- by 7-ft Supersonic Leg of NASA Ames Unitary Wind Tunnel

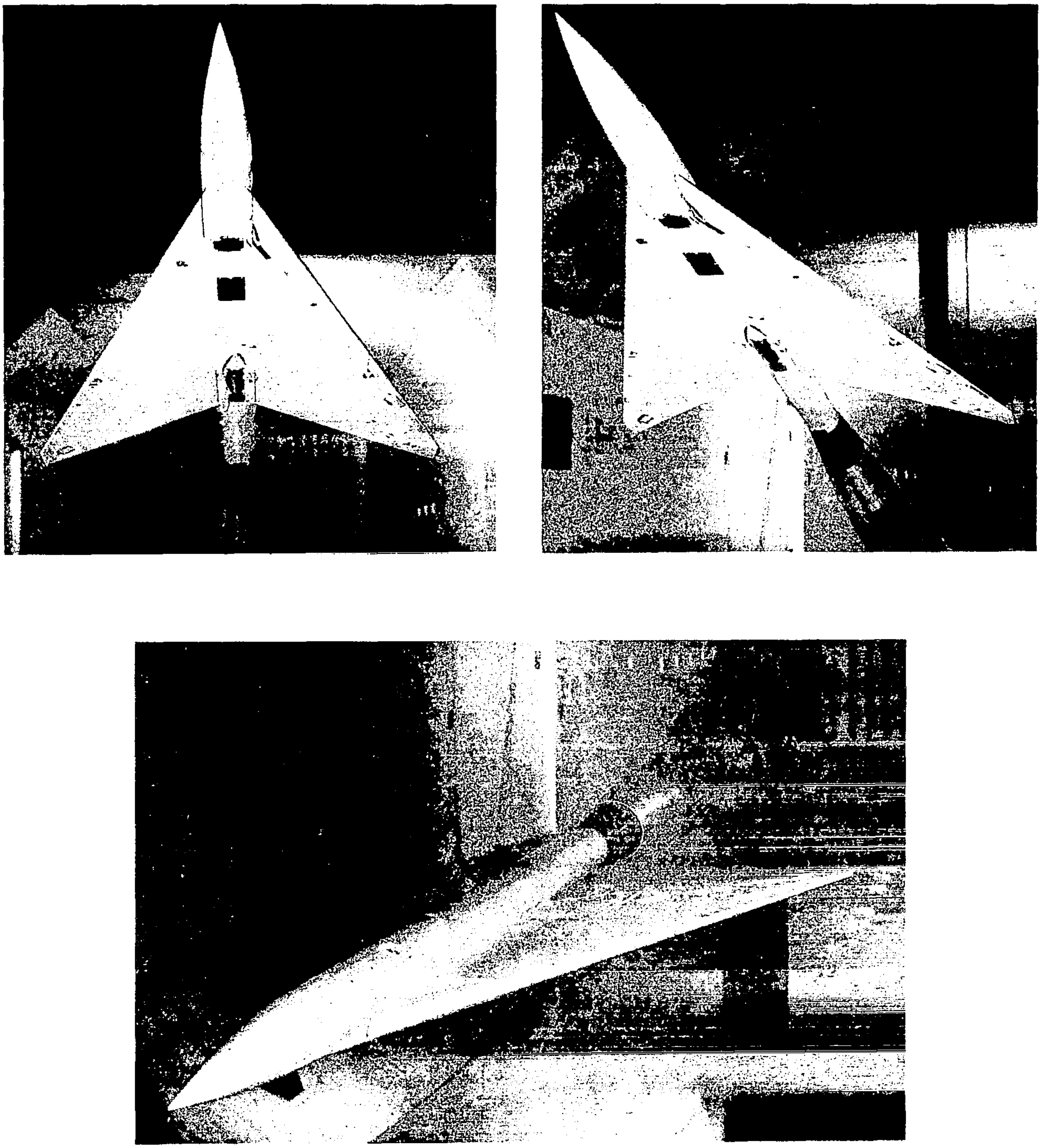

Figure A-12.—Model in Boeing Transonic Wind Tunnel—Flat Wing; L.E. Deflection, Full Span = 0.0°; T.E. Deflection, Full Span = 0.0° (NASA Contract NAS1-12875)

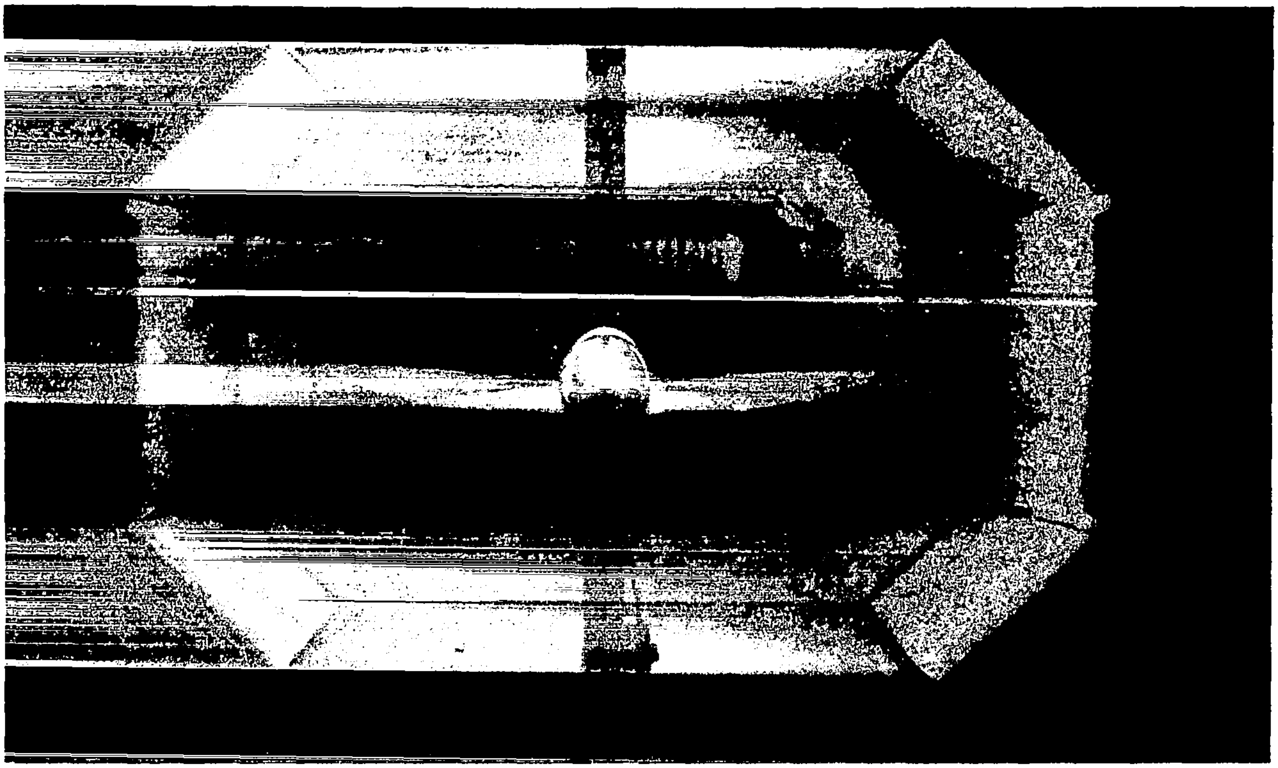

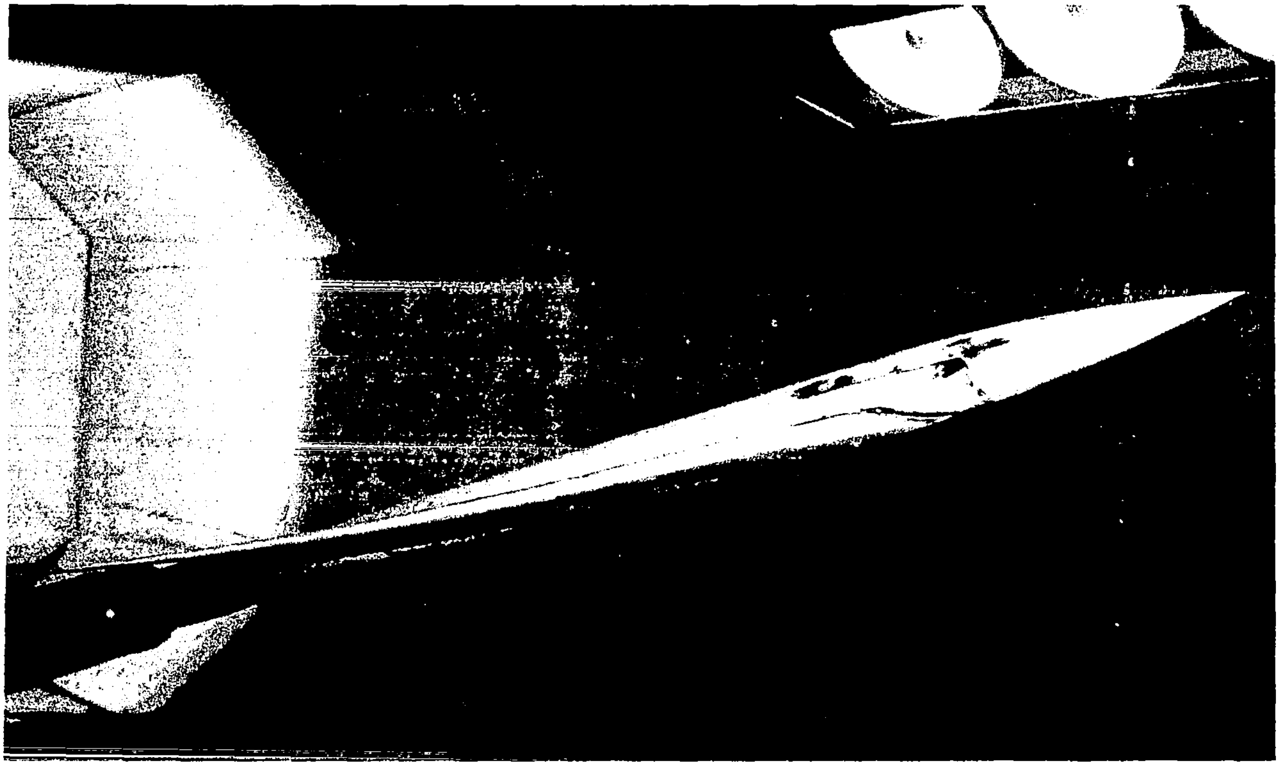

Figure A-13.—Model in Boeing Transonic Wind Tunnel—Twisted Wing; T.E. Deflection, Full Span = 0.0°; (NASA Contract NAS1-14962)

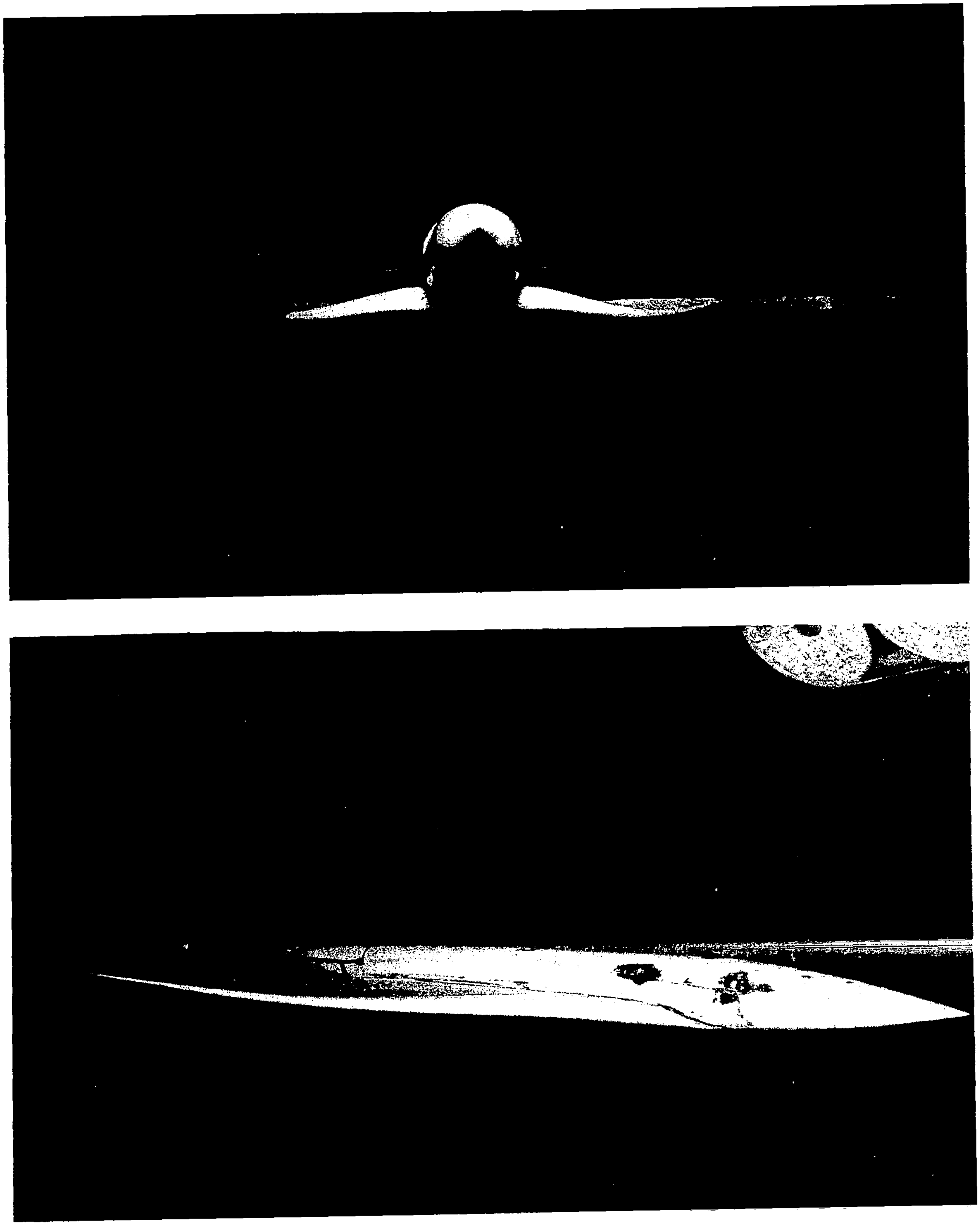

Figure A-14.—Model in Boeing Transonic Wind Tunnel—Cambered-Twisted Wing, Fin Off; T.E. Deflection, Full Span = 0.0°; (NASA Contract NAS1-14962)

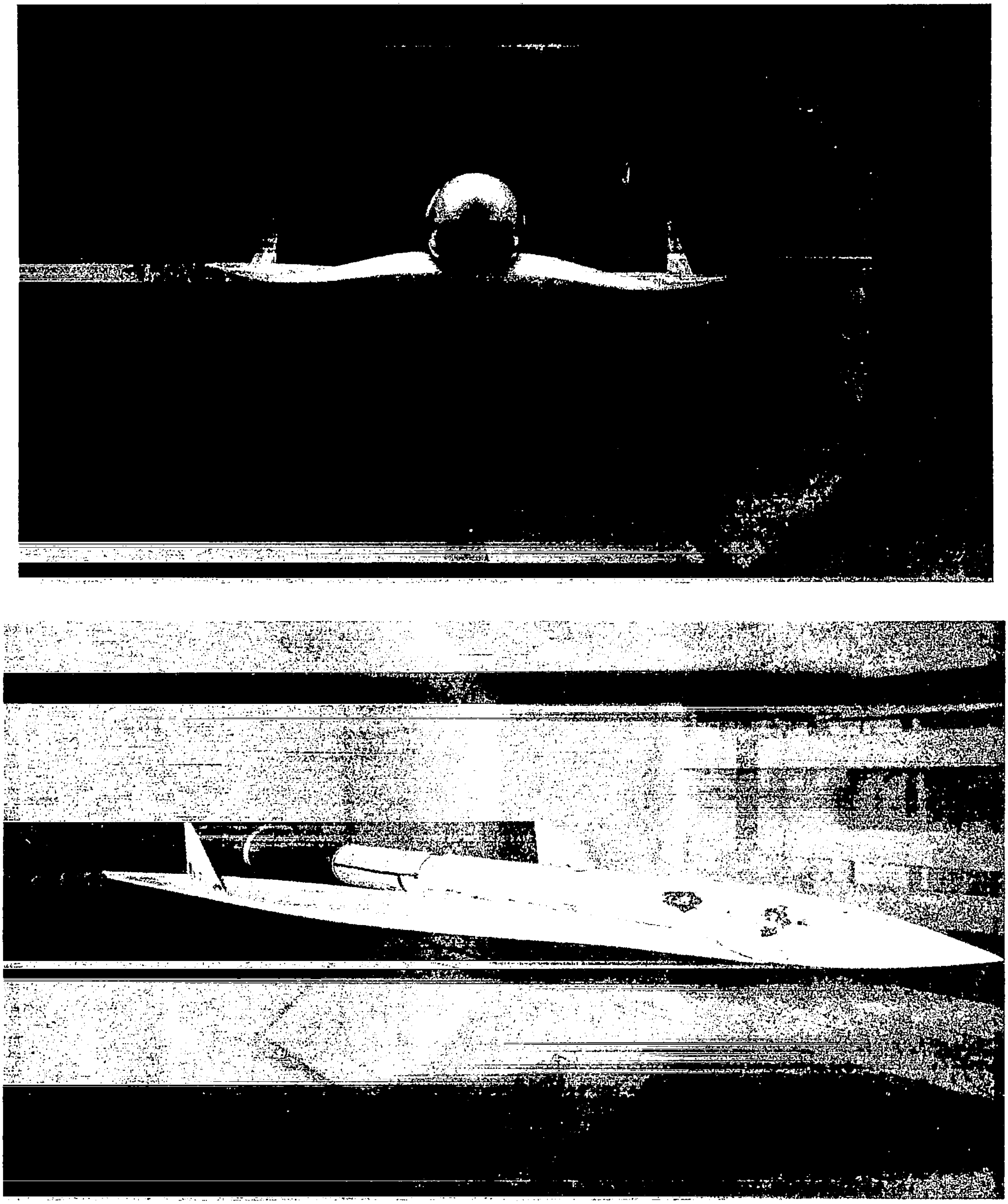

Figure A-15.—Model in Boeing Transonic Wind Tunnel—Cambered-Twisted Wing, Fin On; T.E. Deflection, Full Span = 0.0° (NASA Contract NAS1-14962)

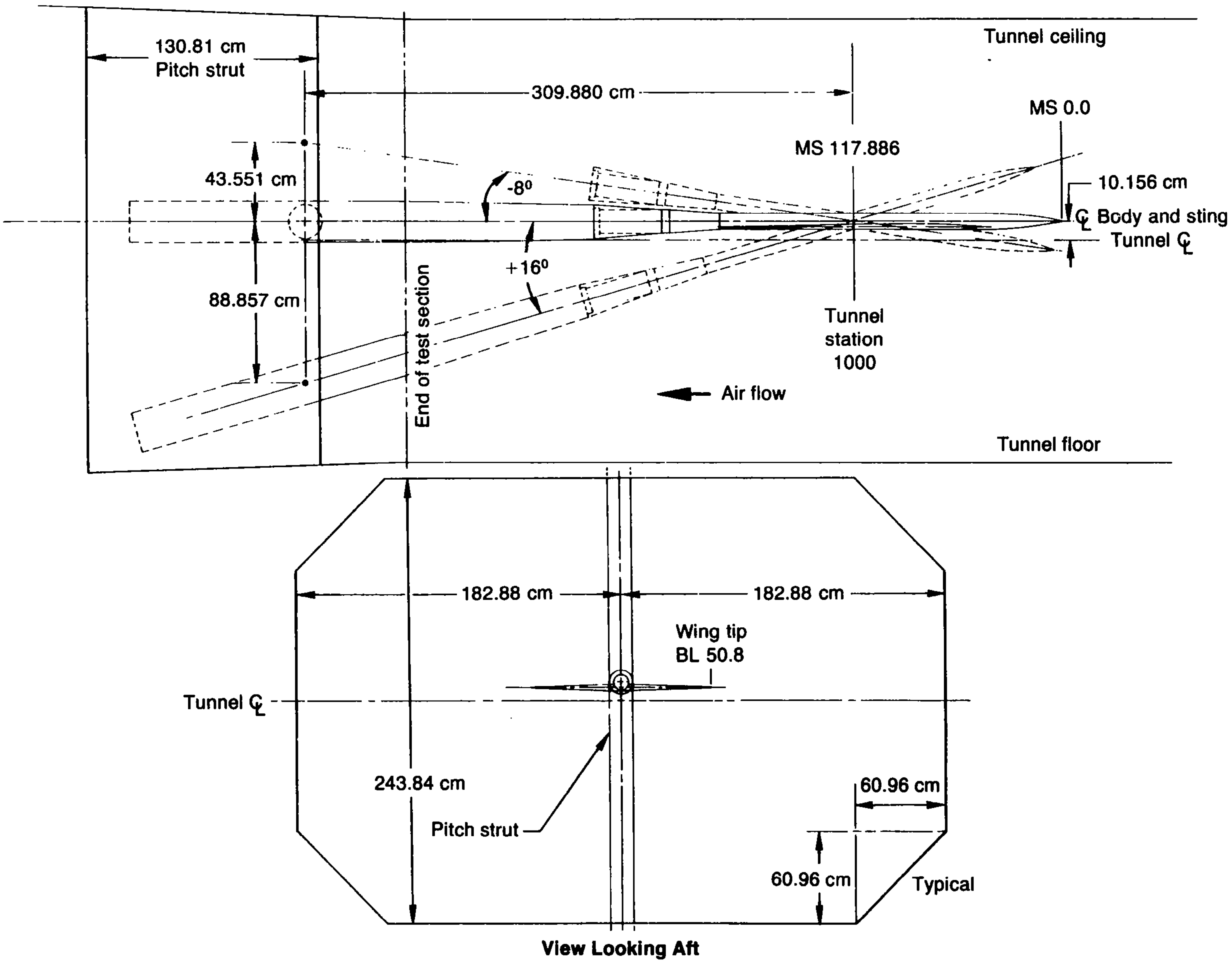

Figure A-16.—Model Installation in Boeing Transonic Wind Tunnel (NASA Contracts NAS1-12875 and NAS1-14962)

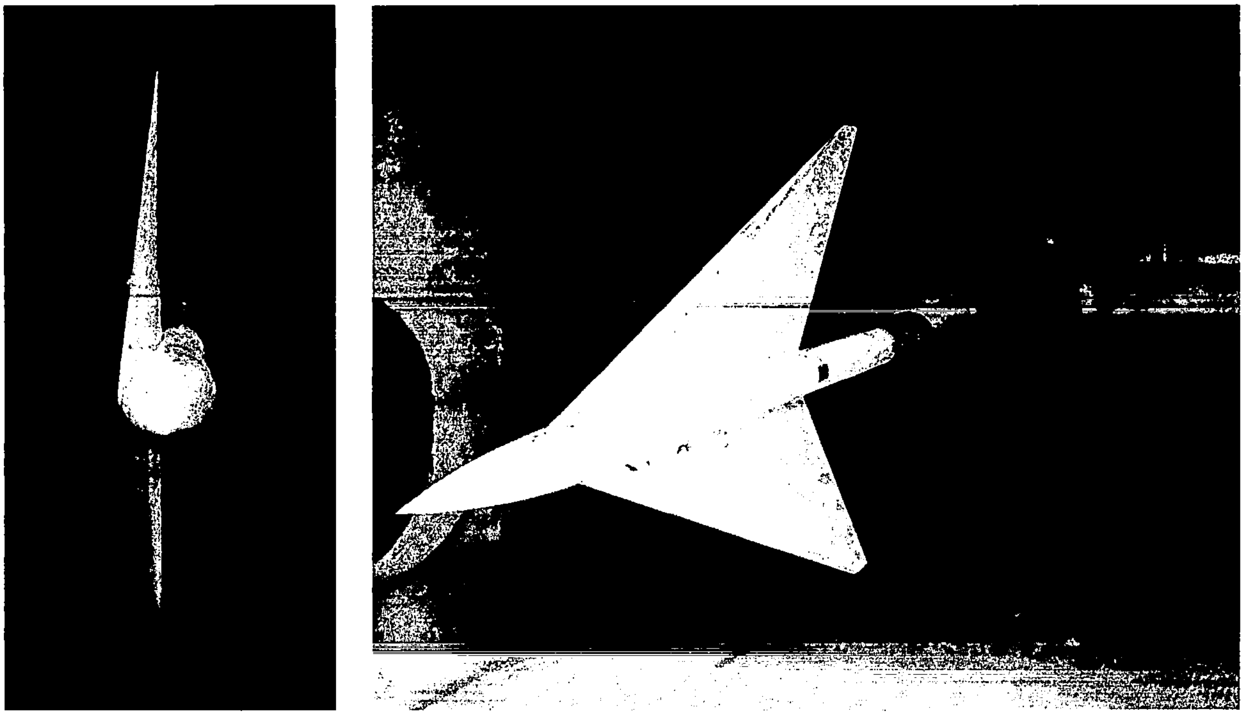

Figure A-17.—Model in 9- by 7-ft Supersonic Leg of NASA Ames Unitary Wind Tunnel—Flat Wing, Rounded L.E. (NASA Contract NAS1-14141)

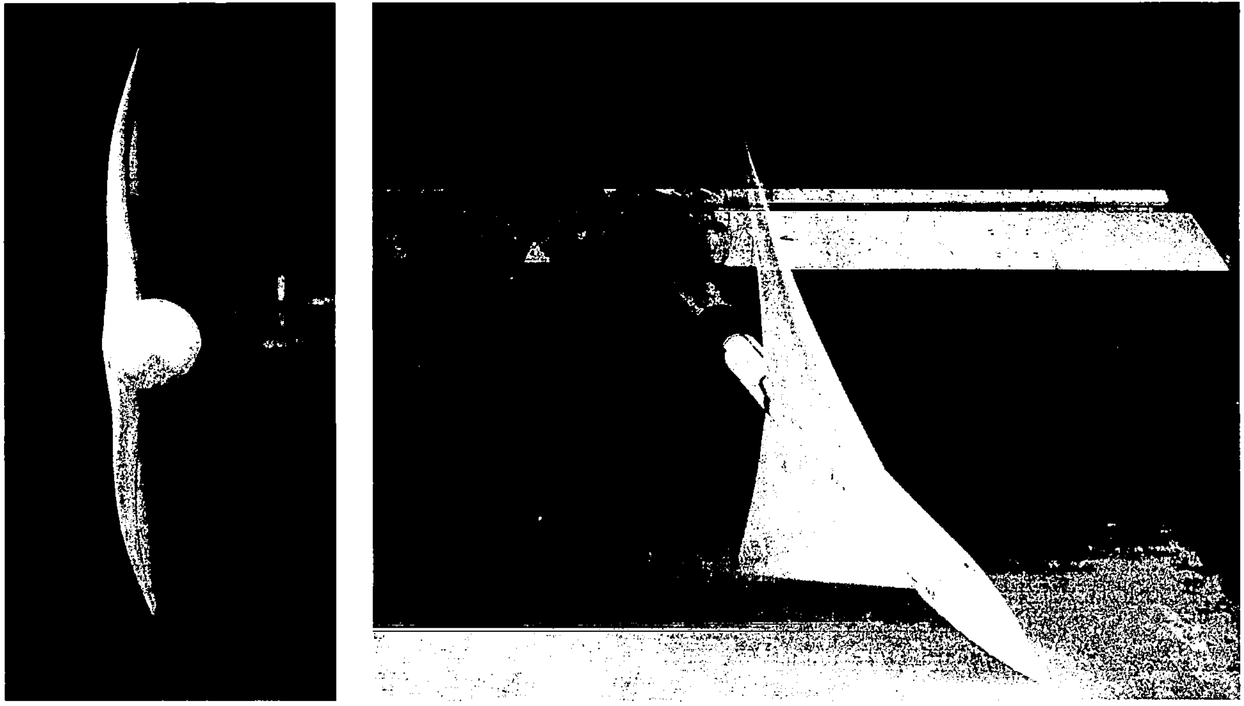

Figure A-18.—Model in 9- by 7-ft Supersonic Leg of NASA Ames Unitary Wind Tunnel—Twisted Wing (NASA Contract NAS1-14141)

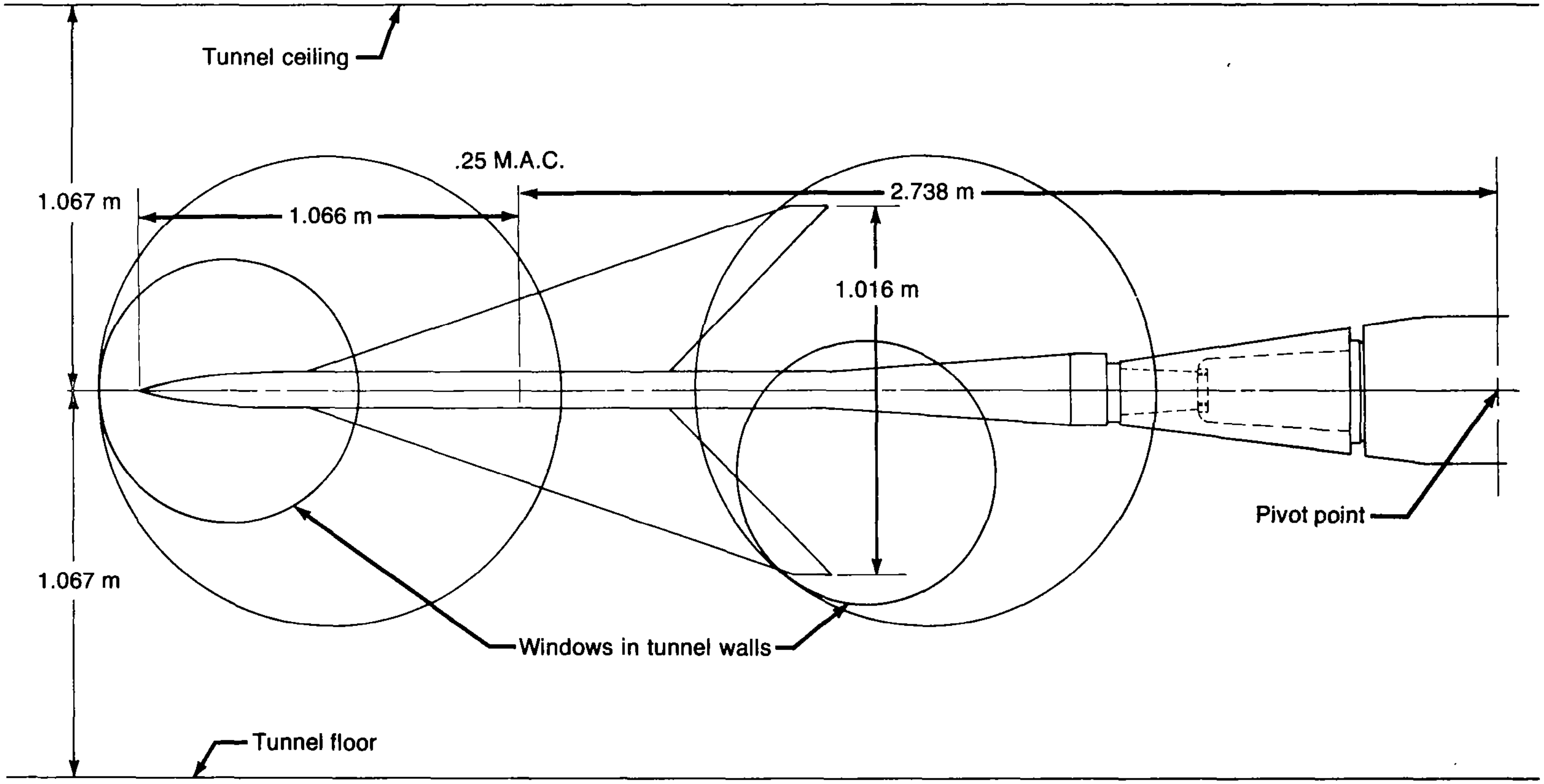

Figure A-19.—Model Installation in 9- by 7-ft Supersonic Leg of NASA Ames Unitary Wind Tunnel (NASA Contract NAS1-14141)

APPENDIX B

DATA REDUCTION

DATA EDITING

There were some cases encountered with these data where the methods of data editing available within the integration programs were not adequate. Because the plotting program assumes that the geometry is the same for all configurations, and the chordwise location of orifices on the various model parts was not absolutely identical, points were added as required. Therefore, some interpolations or extrapolations using selected orifices were done before the integration program was used. The row of orifices on the body at the wing-body intersection was extended in front of the wing and aft of the wing by interpolating between the orifices located at 90° and 135°.

Some specific problems with the data acquisition systems required the replacement of some data for parts of tests. These are identified in appendix A.

Several methods were introduced into the integration program to replace or add data points to account for:

- Plugged or leaking orifices, or bad data points
- Extrapolating the data to leading and trailing edges
- Hingeline discontinuities in the pressure data

These procedures were selected by code for each point. The codes are described in the following list and are illustrated in figure B-1. An additional use of these codes is to ensure that only measured pressure data ($CODE_i = 0$) are identified with symbols on the plots. The subscript i identifies the position of the point from the leading edge of the upper or lower surface of the section.

IF $CODE_i$ = 0, use pressure as entered on tape (measured pressure)

= 20, use as entered on tape (previously replaced value)

= 1, interpolate from adjacent points

= 2, extrapolate from two preceding points

= 3, extrapolate from two following points

= 4, set equal to preceding point

= 5, set equal to following point

= 6, interpolate using points (i-2) and (i+1)

= 7, interpolate using points (i-1) and (i+2)

IF $CODE_i$ = negative of above, evaluate as above but average with corresponding point on opposite surface; used for leading and trailing edges of section only

Editing of the pressure data is done in the following order:

1. Each section is done separately.
2. Each surface (upper or lower) per section is done in the following sequence:
   a. Starting at leading edge, points with codes of 1, 2, and 4.
   b. Starting at trailing edge, points with codes of 3, 5, 6, and 7.
3. Leading- and trailing-edge points with negative codes are evaluated. Both upper and lower surface codes need not be negative and need not be the same negative code.

CALCULATION OF NET PRESSURE COEFFICIENTS

The net lift distribution on the section is calculated by:

$$C_{p,net} = C_{p,lower} - C_{p,upper} \tag{B-1}$$

INTEGRATION OF PRESSURE DATA

To account for the effects on integrated coefficients of the deflected control surfaces, each streamwise section (of which there are NSECT) is divided into segments (of which there are NSEG). These segments are the leading-edge control surface, wing box, and trailing-edge control surface. The upper and lower surfaces of each are integrated separately over the number of points available ((number of orifices + 2) = NP1), and are based on the segment chord length c. Sign conventions are shown in the following sketch. The equations, which use a rectangular integration process, follow.

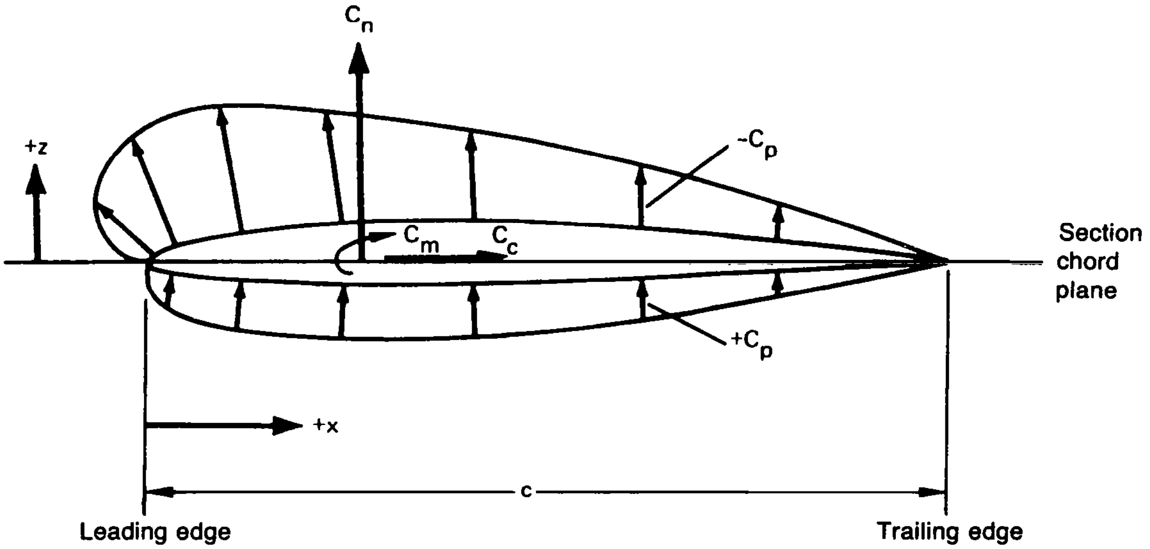

SEGMENT COEFFICIENTS

Integration of the pressures for each segment per surface per section is the first step.

- **Normal force coefficient $C_{n,s}$**

$$C_{n,s} = 0.5 \sum_{i=2}^{NP1} \left[(C_p)_i + (C_p)_{i-1} \right] \left[\left(\frac{x}{c}\right)_i - \left(\frac{x}{c}\right)_{i-1} \right] \qquad \text{(B-2)}$$

$$C_{n,s,net} = C_{n,s,lower} - C_{n,s,upper} \qquad \text{(B-3)}$$

- **Chord force coefficient $C_{c,s}$**

$$C_{c,s} = 0.5 \sum_{i=2}^{NP1} \left[(C_p)_i + (C_p)_{i-1} \right] \left[\left(\frac{z}{c}\right)_i - \left(\frac{z}{c}\right)_{i-1} \right] \qquad \text{(B-4)}$$

$$C_{c,s,net} = C_{c,s,upper} - C_{c,s,lower} \qquad \text{(B-5)}$$

- **Pitching moment coefficient about segment leading edge $C_{m,s}$**

$$C_{m,s} = 0.5 \sum_{i=2}^{NP1} \left[(C_p)_i + (C_p)_{i-1} \right] \left[\frac{x}{c}_{i-1} + \frac{\left(\frac{x}{c}\right)_i - \left(\frac{x}{c}\right)_{i-1}}{2.0} \right] \left[\left(\frac{x}{c}\right)_i - \left(\frac{x}{c}\right)_{i-1} \right]$$

$$= 0.25 \sum_{i=2}^{NP1} \left[(C_p)_i + (C_p)_{i-1} \right] \left[\left(\frac{x}{c}\right)_i^2 - \left(\frac{x}{c}\right)_{i-1}^2 \right] \qquad \text{(B-6)}$$

$$C_{m,s,net} = C_{m,s,upper} - C_{m,s,lower} \qquad \text{(B-7)}$$

- **Pitching moment coefficient about 0.25 c of segment $C_{m.25c,s}$**

$$C_{m.25c,s} = C_{m,s,} + 0.25\, C_{n,s} \qquad \text{(B-8)}$$

SECTION COEFFICIENTS

Total section coefficients are obtained by summing the segment coefficients, taking into account both the segment deflections as defined in the following sketch and the segment chord lengths. These coefficients are based on the section chord length c.

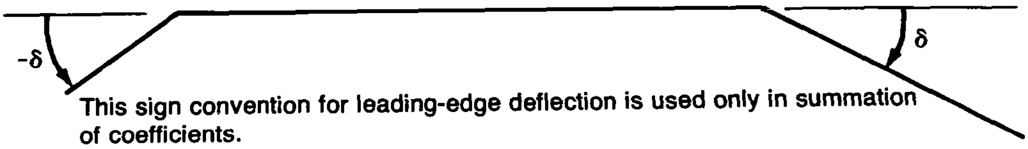

This sign convention for leading-edge deflection is used only in summation of coefficients.

- Normal force coefficient C_n

$$C_n = \sum_{j=1}^{NSEG} \left(C_{n,s}\right)_j \left(\frac{c_s}{c}\right)_j \cos\delta_j - \sum_{j=1}^{NSEG} \left(C_{c,s}\right)_j \left(\frac{c_s}{c}\right)_j \sin\delta_j \qquad \text{(B-9)}$$

- Pitching moment coefficient about section leading edge C_m

$$C_m = \sum_{j=1}^{NSEG} \left(C_{m,s}\right)_j \left(\frac{c_s}{c}\right)_j^2 + \left[\left(C_{n,s}\right)_1 \left(1.0 - \cos\delta_1\right) + \left(C_{c,s}\right)_1 \sin\delta_1\right] \left(\frac{c_s}{c}\right)_1^2$$

$$- \sum_{j=2}^{NSEG} \left[\left(C_{n,s}\right)_j \cos\delta_j - \left(C_{c,s}\right)_j \sin\delta_j\right] \left(\frac{c_s}{c}\right)_j \left[\frac{x_{L.E.,s} - x_{L.E.}}{c}\right]_j \qquad \text{(B-10)}$$

where

c_s	is segment chord length, cm
c	is section chord length, cm
δ	is deflection of segment relative to section chord plane, leading edge up, degrees
$x_{L.E.,s}$	is leading edge of segment, cm
$x_{L.E.}$	is leading edge of section, cm

- Pitching moment coefficient about 0.25 c of section $C_{m.25c}$

$$C_{m.25c} = C_m + 0.25\, C_n \qquad \text{(B-11)}$$

TOTAL SURFACE COEFFICIENTS

To obtain total surface coefficients, the assumption is made that the section coefficients apply for a finite distance on both sides of each row of orifices. The equations for total surface coefficients are as follows:

- o Normal force coefficient C_N

$$C_N = \frac{1}{S} \sum_{k=1}^{NSECT} \left(C_n\right)_k \left(S_h\right)_k \tag{B-12}$$

- o Bending moment coefficient C_B

$$C_B = \frac{1}{S(b/2)} \sum_{k=1}^{NSECT} \left(C_n\right)_k \left(S_h y\right)_k \tag{B-13}$$

- o Pitching moment coefficient about 0.25 M.A.C. C_M

$$C_M = \frac{1}{S\bar{c}} \sum_{k=1}^{NSECT} \left\{ \left(C_m\right)_k \left(S_h c\right)_k + \left(C_n\right)_k \left(S_h\right)_k \left[x_{ref} - \left(x_{L.E.}\right)_k\right] \right\} \tag{B-14}$$

where

$\bar{c}$	is reference chord for pitching moment, cm
x_{ref}	is reference station for pitching moment, cm (0.25 M.A.C.)
$X_{L.E.}$	is leading edge of section chord, cm
b/2	is reference length for bending moment, cm

DETERMINATION OF GEOMETRIC CONSTANTS REQUIRED FOR INTEGRATION

To obtain total surface coefficients, the assumption is made that the section coefficients apply for a finite distance on both sides of each row of orifices. The input geometry required to calculate the areas, and products of area and length required for the summation of total surface coefficients, is shown in the following sketch.

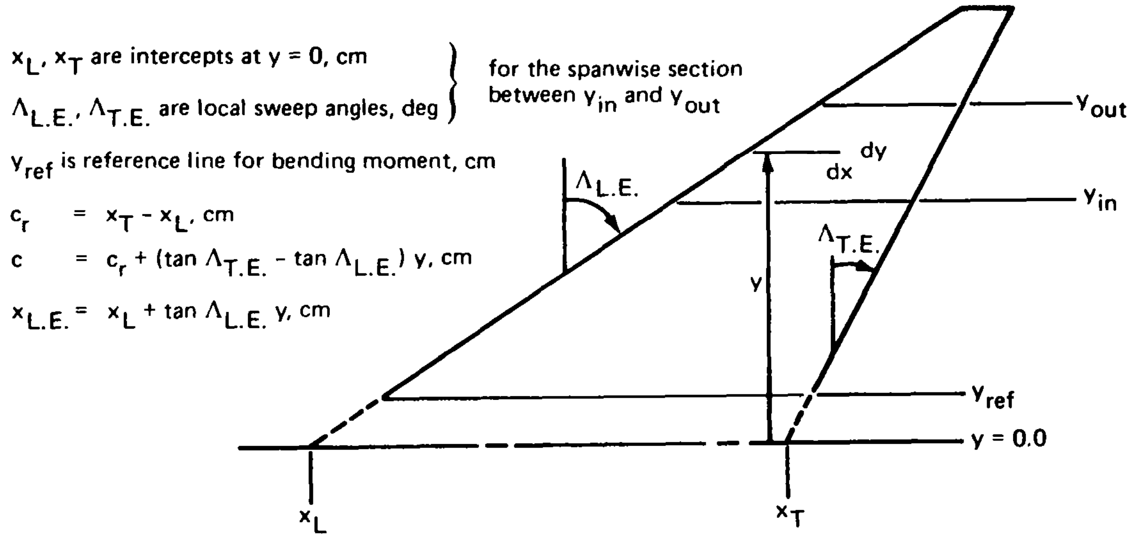

x_L, x_T are intercepts at $y = 0$, cm

$\Lambda_{L.E.}$, $\Lambda_{T.E.}$ are local sweep angles, deg

for the spanwise section between y_{in} and y_{out}

y_{ref} is reference line for bending moment, cm

$c_r = x_T - x_L$, cm

$c = c_r + (\tan \Lambda_{T.E.} - \tan \Lambda_{L.E.})\, y$, cm

$x_{L.E.} = x_L + \tan \Lambda_{L.E.}\, y$, cm

- Section area:

$$S_h = \int_{y_{in}}^{y_{out}} \int_{x_L + \tan \Lambda_{L.E.} y}^{x_T + \tan \Lambda_{T.E.} y} dy\, dx$$

$$= c_r\left(y_{out} - y_{in}\right) + 0.5\left(\tan \Lambda_{T.E.} - \tan \Lambda_{L.E.}\right)\left(y_{out}^2 - y_{in}^2\right) \qquad \text{(B-15)}$$

- Product of section area and mean chord:

$$S_h c = \int_{y_{in}}^{y_{out}} \int_{x_L + \tan \Lambda_{L.E.} y}^{x_T + \tan \Lambda_{T.E.} y} c\, dy\, dx$$

$$= c_r^2\left(y_{out} - y_{in}\right) + c_r\left(\tan \Lambda_{T.E.} - \tan \Lambda_{L.E.}\right)\left(y_{out}^2 - y_{in}^2\right)$$

$$+ \frac{\left(\tan \Lambda_{T.E.} - \tan \Lambda_{L.E.}\right)^2}{3.0}\left(y_{out}^3 - y_{in}^3\right) \qquad \text{(B-16)}$$

- **Product of section area and bending moment arm:**

$$S_h y = \int_{y_{in}}^{y_{out}} \int_{x_L + \tan \Lambda_{L.E.} y}^{x_T + \tan \Lambda_{T.E.} y} \left(y - y_{ref}\right) dy\, dx$$

$$= \frac{c_r - \left(\tan \Lambda_{T.E.} - \tan \Lambda_{L.E.}\right) y_{ref}}{2.0} \left(y_{out}^2 - y_{in}^2\right)$$

$$+ \frac{\tan \Lambda_{T.E.} - \tan \Lambda_{L.E.}}{3.0} \left(y_{out}^3 - y_{in}^3\right) - c_r\, y_{ref} \left(y_{out} - y_{in}\right) \qquad \textbf{(B-17)}$$

- **Product of section area and leading-edge coordinate:**

$$S_h x = \int_{y_{in}}^{y_{out}} \int_{x_L + \tan \Lambda_{L.E.} y}^{x_T + \tan \Lambda_{T.E.} y} x_{L.E.}\, dy\, dx$$

$$= x_L\, c_r \left(y_{out} - y_{in}\right) + \frac{\tan \Lambda_{L.E.}\, c_r + x_L \left(\tan \Lambda_{T.E.} - \tan \Lambda_{L.E.}\right)}{2.0} \left(y_{out}^2 - y_{in}^2\right)$$

$$+ \tan \Lambda_{L.E.} \frac{\left(\tan \Lambda_{T.E.} - \tan \Lambda_{L.E.}\right)}{3.0} \left(y_{out}^3 - y_{in}^3\right) \qquad \textbf{(B-18)}$$

- **Total surface reference area:**

$$S = \sum_{k=1}^{NSECT} \left(S_h\right)_k \qquad \textbf{(B-19)}$$

- **M.A.C. and X coordinate of M.A.C. leading edge:**

$$\bar{c} = \frac{1}{S} \sum_{k=1}^{NSECT} \left(S_h c\right)_k \qquad \textbf{(B-20)}$$

$$x_{L.E.,M.A.C.} = \frac{1}{S} \sum_{k=1}^{NSECT} \left(S_h x\right)_k \qquad \textbf{(B-21)}$$

The required integration constants for the wing and body are shown in table B-1.

Table B-1.—Integration Constants

Reference area = 3128.45 cm²
M.A.C. = 75.311 cm
Half span = 50.80 cm

Pitching moment referenced to 0.25 M.A.C.

Bending moment referenced to $0.086 \frac{b}{2}$ (y_{ref} = 4.374 cm)

L.E. of M.A.C. at B.S. 87.760 cm

Wing

2y/b	$\frac{\Delta y}{(b/2)}$	Area cm²	Area • chord cm³	Area • $(y\text{-}y_{ref})$ cm³
0.09	0.0425	219.69	22 357.	167.
0.20	0.1575	733.51	67 415.	4 206.
0.35	0.1500	580.54	44 374.	7 857.
0.50	0.1400	437.93	27 084.	9 148.
0.65	0.1600	377.64	17 722.	10 729.
0.80	0.1300	210.35	6 794.	7 528.
0.93	0.1400	129.79	2 487.	5 505.

Body

Longitudinal section	Area cm²	Area • L cm³
1	356.61	81 258.
2	504.32	114 916.
3	70.94	16 164.

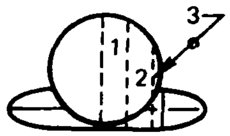

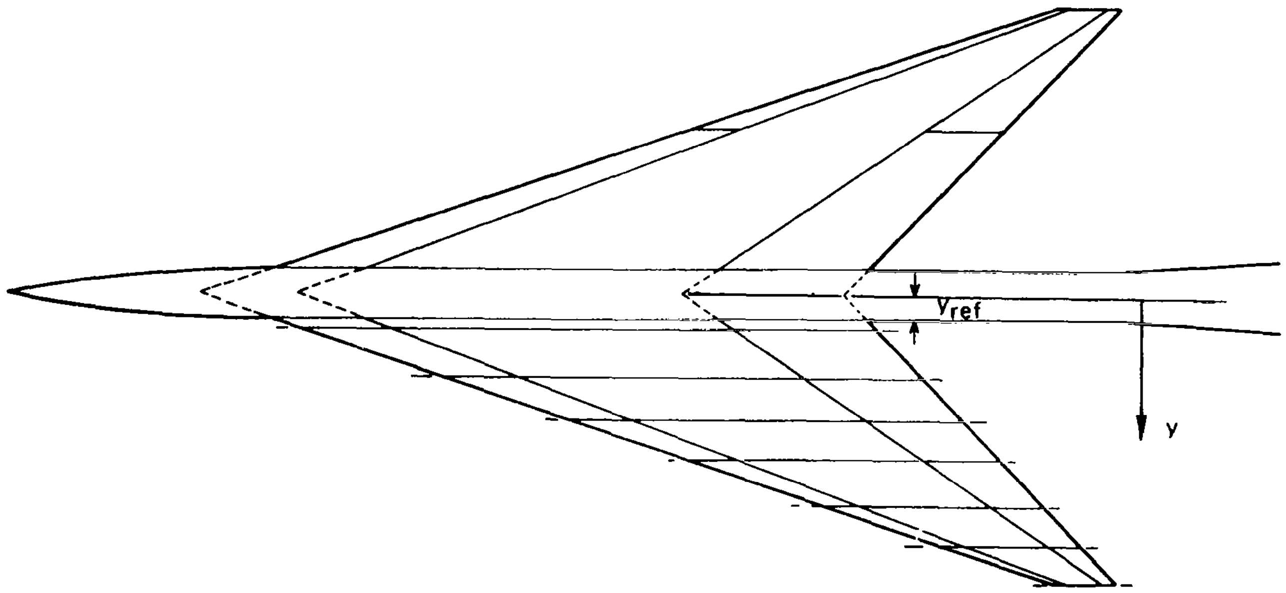

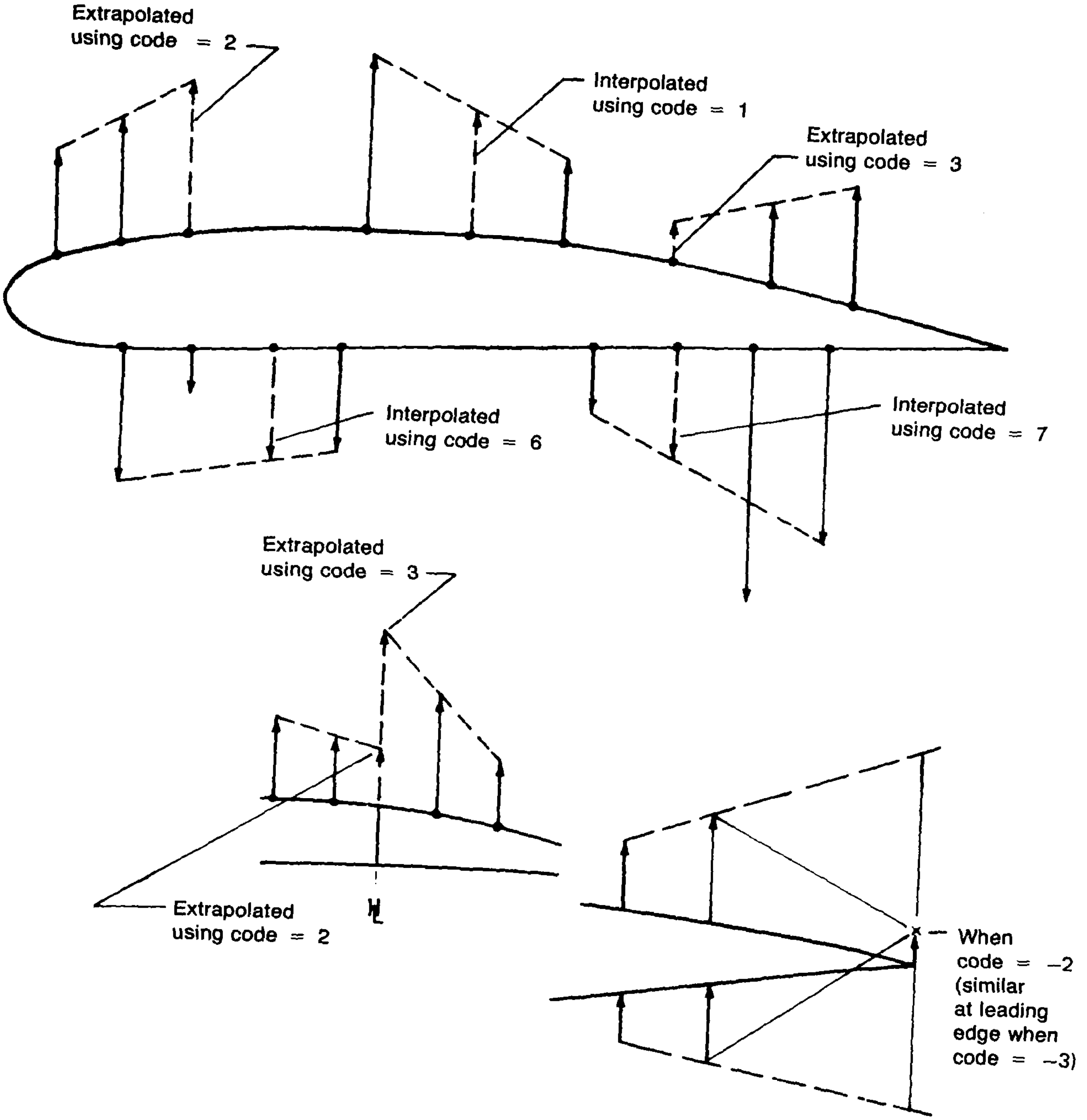

Figure B-1.—Codes Used to Interpolate and Extrapolate

REFERENCES

1. Manro, Marjorie E.; Tinoco, Edward N.; Bobbitt, Percy J.; and Rogers, John T.: Comparisons of Theoretical and Experimental Pressure Distributions on an Arrow-Wing Configuration at Transonic Speeds. Aerodynamic Analyses Requiring Advanced Computers – Part II, NASA SP-347, 1975, pp. 1141-1188.

2. Manro, M. E.; Bobbitt, P. J.; and Rogers, J. T.: Comparisons of Theoretical and Experimental Pressure Distributions on an Arrow-Wing Configuration at Subsonic, Transonic, and Supersonic Speeds. Prediction of Aerodynamic Loading. AGARD CP-204, Feb. 1977, pp. 11-1 – 11-14.

3. Bobbitt, Percy J.; and Manro, Marjorie E.: Theoretical and Experimental Pressure Distributions for a 71.2° Swept Arrow-Wing Configuration at Subsonic, Transonic, and Supersonic Speeds. Proceedings of the SCAR Conference – Part 1, NASA CP-001, 1977, pp. 85-122.

4. Manro, Marjorie E.; Manning, Kenneth J. R.; Hallstaff, Thomas H.; and Rogers, John T.: Transonic Pressure Measurements and Comparison of Theory to Experiment for an Arrow-Wing Configuration – Summary Report. NASA CR-2610, 1976.

5. Manro, Marjorie E.; Manning, Kenneth J. R.; Hallstaff, Thomas H.; and Rogers, John T.: Transonic Pressure Measurements and Comparison of Theory to Experiment for an Arrow-Wing Configuration, Volume I: Experimental Data Report – Base Configuration and Effects of Wing Twist and Leading-Edge Configuration. NASA CR-132727, 1975.

6. Manro, Marjorie E.; Manning, Kenneth J. R.; Hallstaff, Thomas H.; and Rogers, John T.: Transonic Pressure Measurements and Comparison of Theory to Experiment for an Arrow-Wing Configuration, Volume II: Experimental Data Report – Effects of Control Surface Deflection. NASA CR-132728, 1975.

7. Manro, Marjorie E.; Manning, Kenneth J. R.; Hallstaff, Thomas H.; and Rogers, John T.: Transonic Pressure Measurements and Comparison of Theory to Experiment for an Arrow-Wing Configuration, Volume III: Data Report – Comparison of Attached Flow Theories to Experiment. NASA CR-132729, 1975.

8. Manro, M. E.: Supersonic Pressure Measurements and Comparison of Theory to Experiment for an Arrow-Wing Configuration. NASA CR-145046, 1976.

9. Manro, Marjorie E.: Transonic Pressure Measurements and Comparison of Theory to Experiment for Three Arrow-Wing Configurations – Summary Report. NASA CR-3434, 1982.

10. Manro, Marjorie E.: Transonic Pressure Measurements and Comparisons of Theory to Experiment for Three Arrow-Wing Configurations, Volume I: Experimental Data Report – Basic Data and Effect of Wing Shape. NASA CR-165701, 1981.

11. Manro, Marjorie E.: Transonic Pressure Measurements and Comparisons of Theory to Experiment for Three Arrow-Wing Configurations, Volume II: Experimental Data Report - Effect of Trailing-Edge Control Surface Deflection and a Wing Fin. NASA CR-165702, 1981.

12. Manro, Marjorie E.: Transonic Pressure Measurements and Comparisons of Theory to Experiment for Three Arrow-Wing Configurations, Volume III: Data Report - Comparison of Attached-Flow Theories to Experiment. NASA CR-165703, 1981.

13. Johnson, F. T.; Lu, P.; Tinoco, E. N.; and Epton, M. A.: An Improved Panel Method for the Solution of Three-Dimensional Leading-Edge Vortex Flows, Volume I - Theory Document. NASA CR-3278, 1980.

14. Tinoco, E. N.; Lu, P.; and Johnson, F. T.: An Improved Panel Method for the Solution of Three-Dimensional Leading-Edge Vortex Flows, Volume II - User's Guide and Programmer's Document. NASA CR-3279, 1980.

15. Ehlers, F. Edward; Epton, Michael A.; Johnson, Forester T.; Magnus, Alfred E.; and Rubbert, Paul E.: A Higher Order Panel Method for Linearized Supersonic Flow. NASA CR-3062, 1979.

16. Maskell, E. C.: Some Recent Developments in the Study of Edge Vortices. Proceedings of 3rd Congress of Int. Counc. Aero. Sci., 1962. pp. 737-749, Spartan Books, Inc., Washington, 1964.

17. Peckham, D. H.: Low-Speed Wind-Tunnel Tests on a Series of Uncambered Slender Pointed Wings With Sharp Edges. RM 3186, British Aeronautical Research Council, 1961.

18. Smith, J. H. B.: Improved Calculations of Leading-Edge Separation from Slender Delta Wings. RAE Tech. Report 66070, March 1966.

19. Luckring, J. M.; Schoonover, W. E., Jr.; and Frink, N. T.: Recent Advances in Applying Free Vortex Sheet Theory for the Estimation of Vortex Flow Aerodynamics. AIAA Paper No. 82-0095, January 1982.

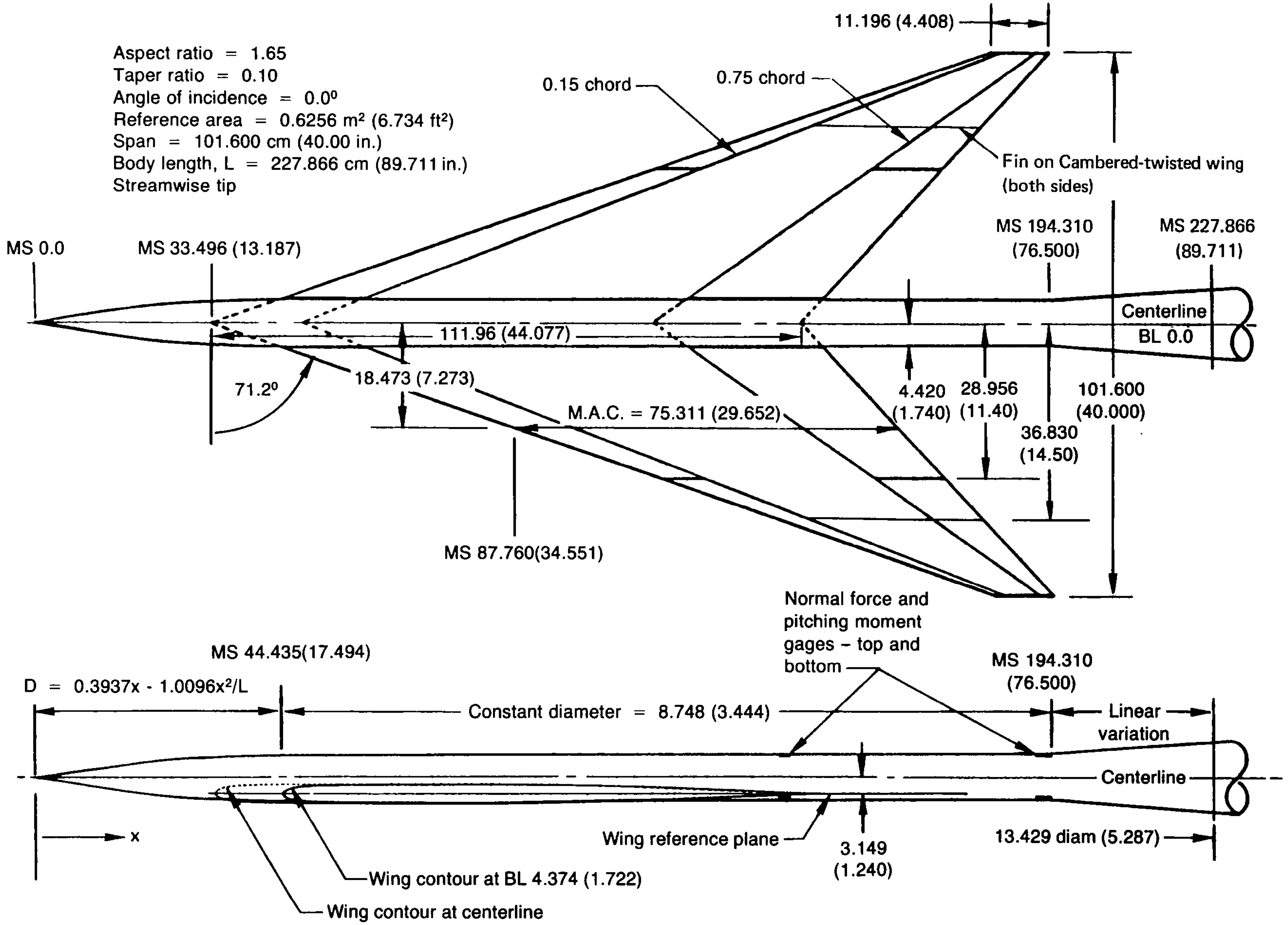

All dimensions in centimeters (inches)

Figure 1.—General Arrangement and Characteristics

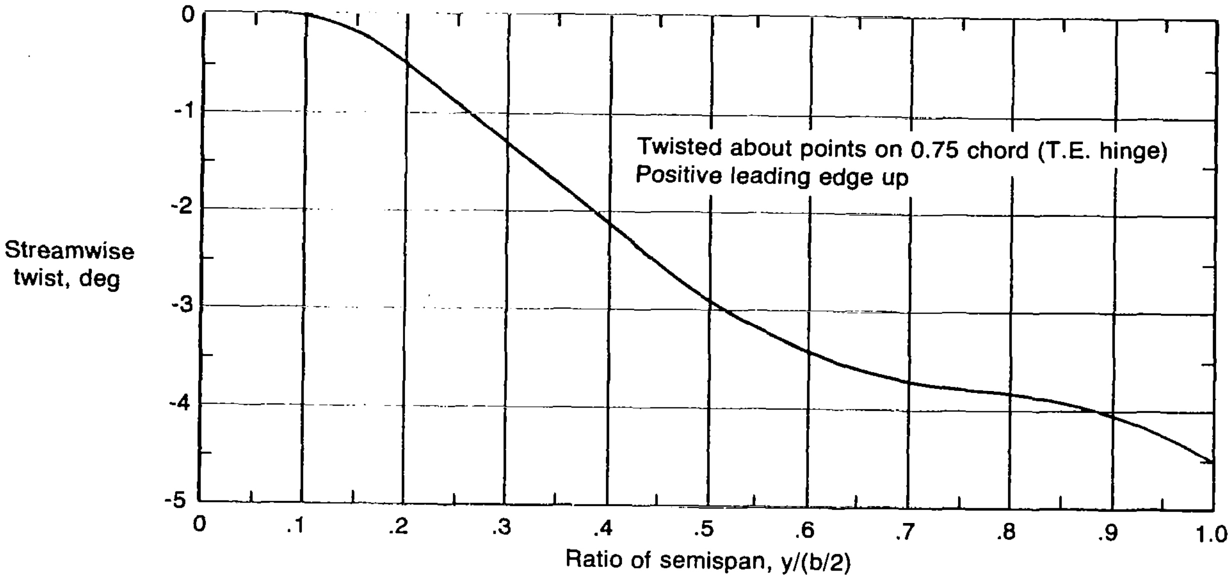

Figure 2.–Spanwise Twist Distribution for the Model Wing

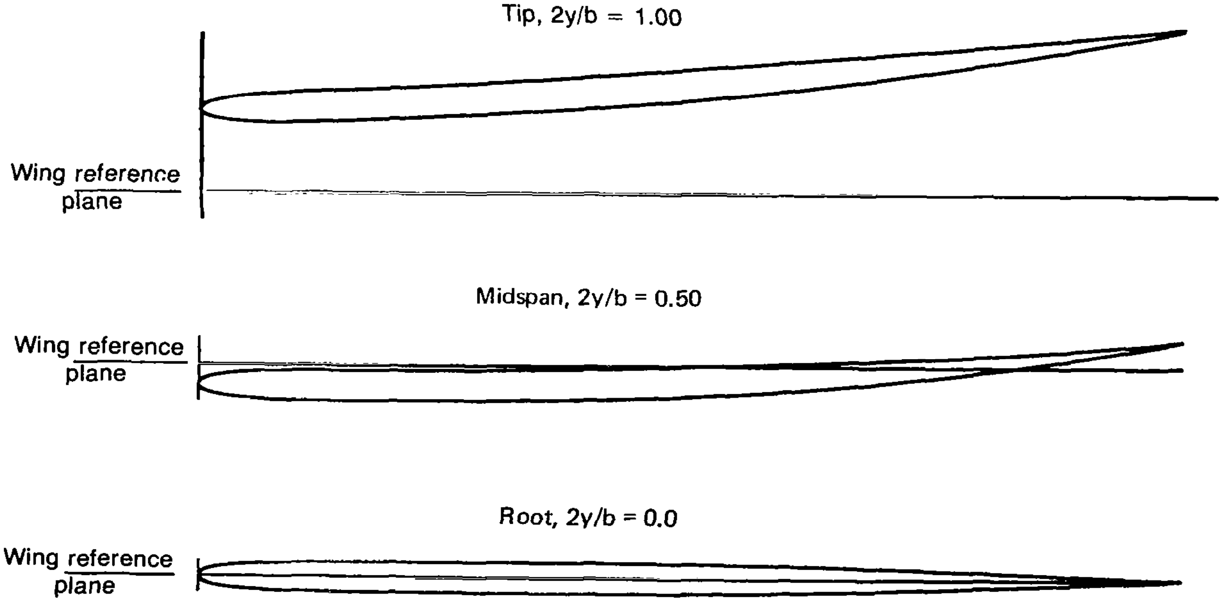

Figure 3.–Cambered-Twisted Wing Section Geometry

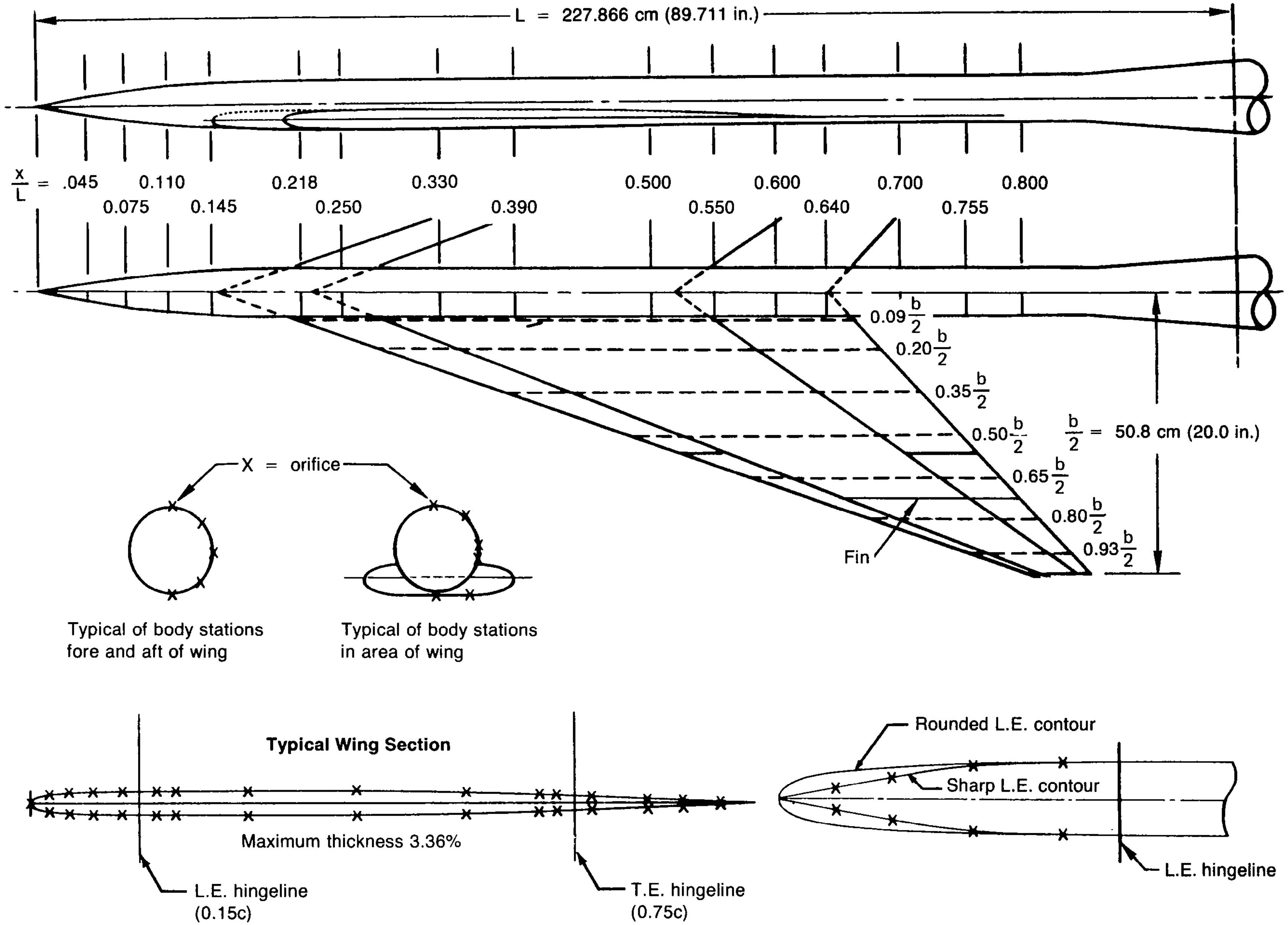

Figure 4.—Pressure Orifice Locations

- Differential equation

  $(1 - M_\infty^2)\,\phi_{xx} + \phi_{yy} + \phi_{zz} = 0$

- Boundary conditions
  - Wing, body:
    impermeable
  - Wake, free sheet:
    impermeable
    zero pressure jump
  - Fed sheet:
    zero total force
  - Kutta condition

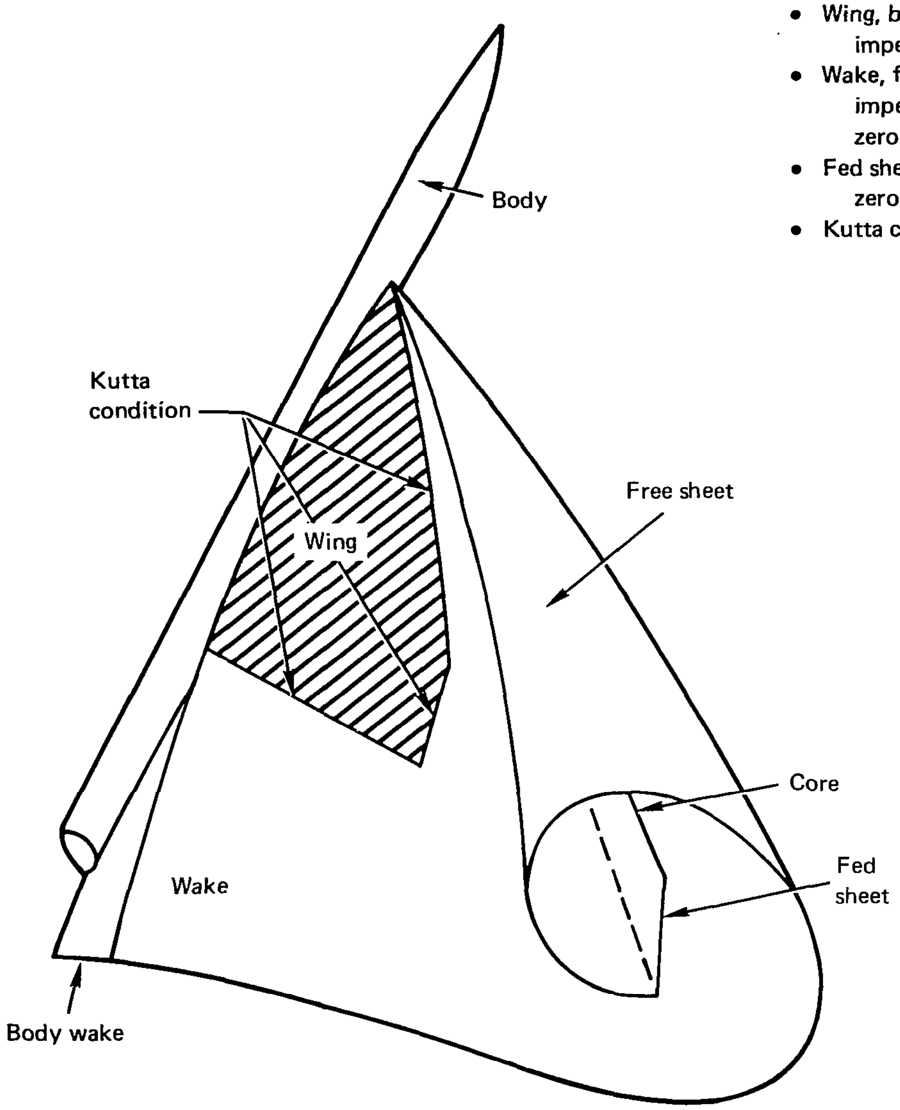

Figure 5.—Flow Model for The Boeing Company Three-Dimensional Leading-Edge Vortex (LEV) Code

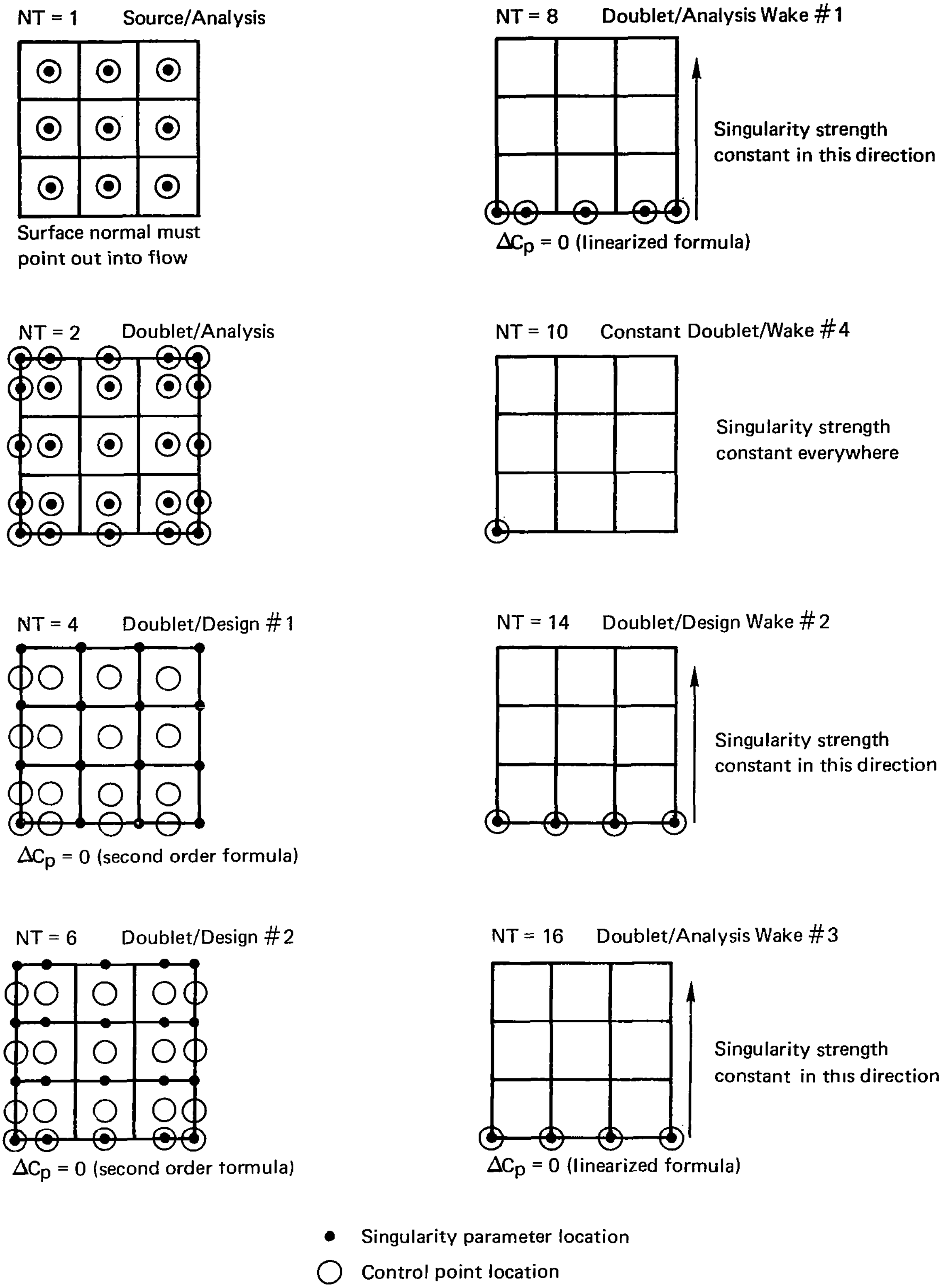

Figure 6.—Location of Network Singularity Parameters and Control Points

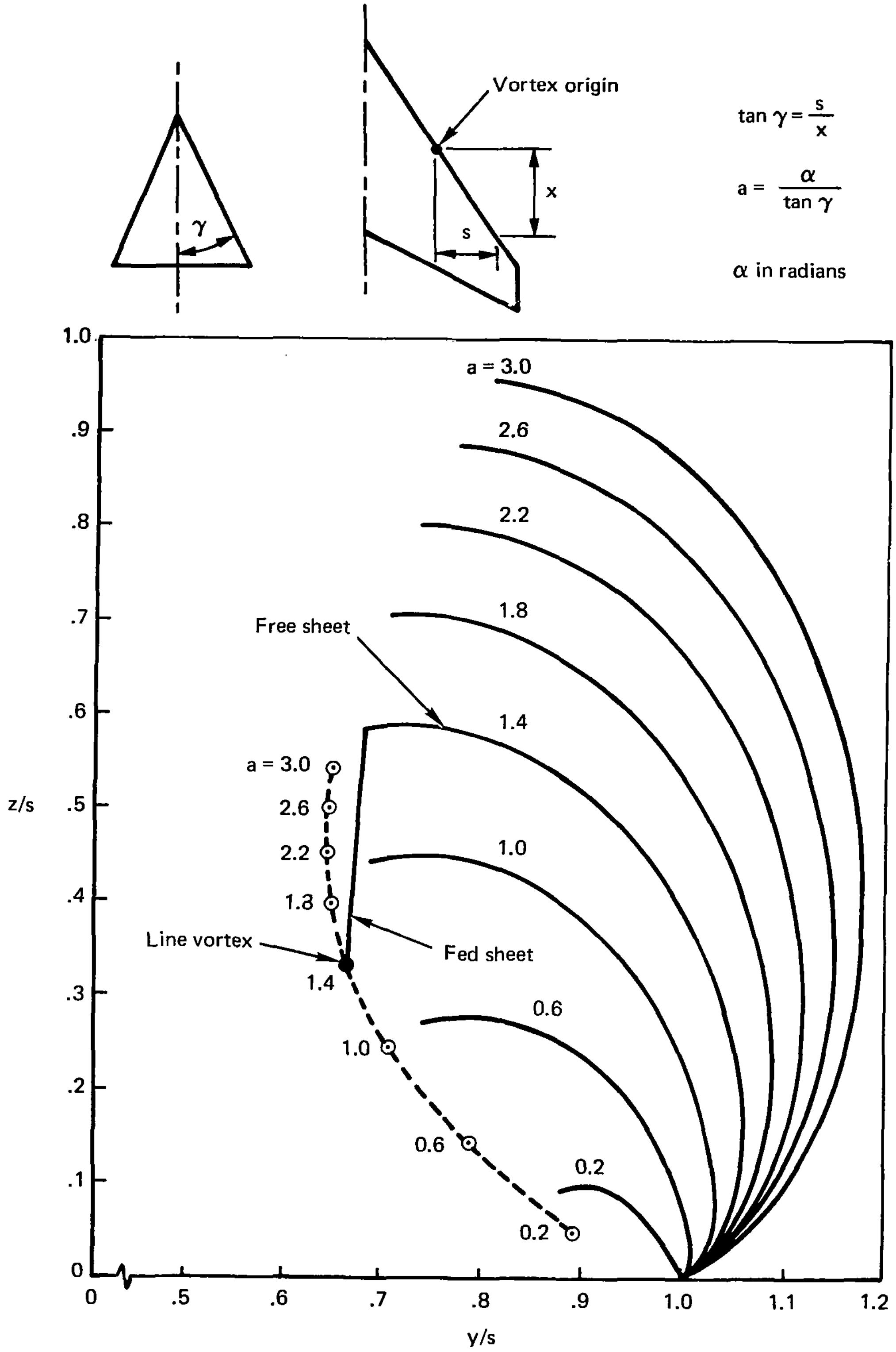

Figure 7.—Initial Free-Sheet Geometry and Size of Fed Sheet for Various Values of 'a' (ref. 18)

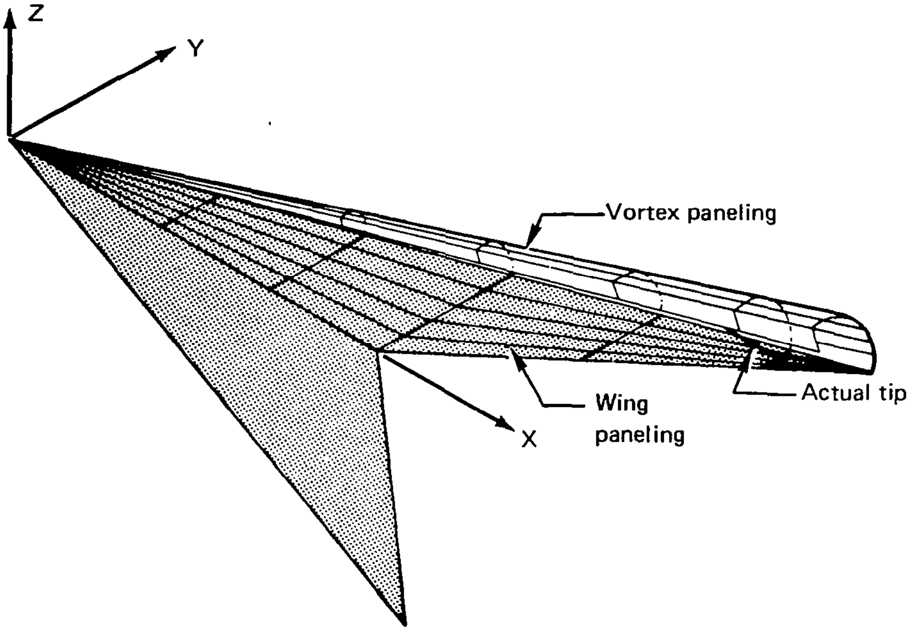

(a) Panel Model

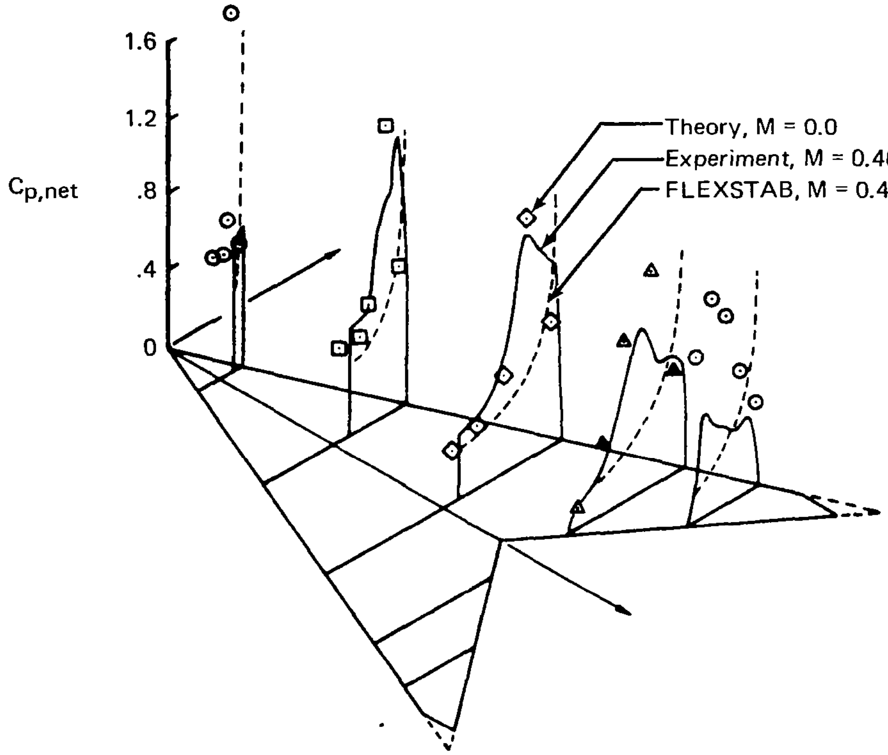

(b) Net Pressure Distributions

Figure 8.—Previous Evaluation of LEV Computer Code (ref. 4), Flat Wing, Zero Thickness, M = 0.0, α = 16°

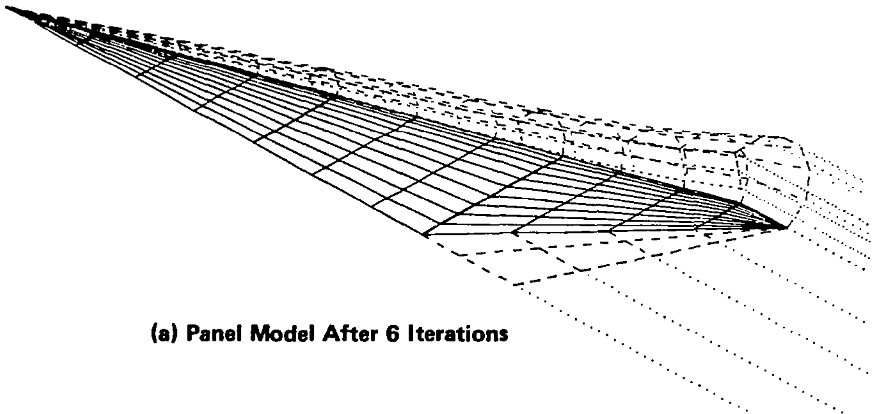

(a) Panel Model After 6 Iterations

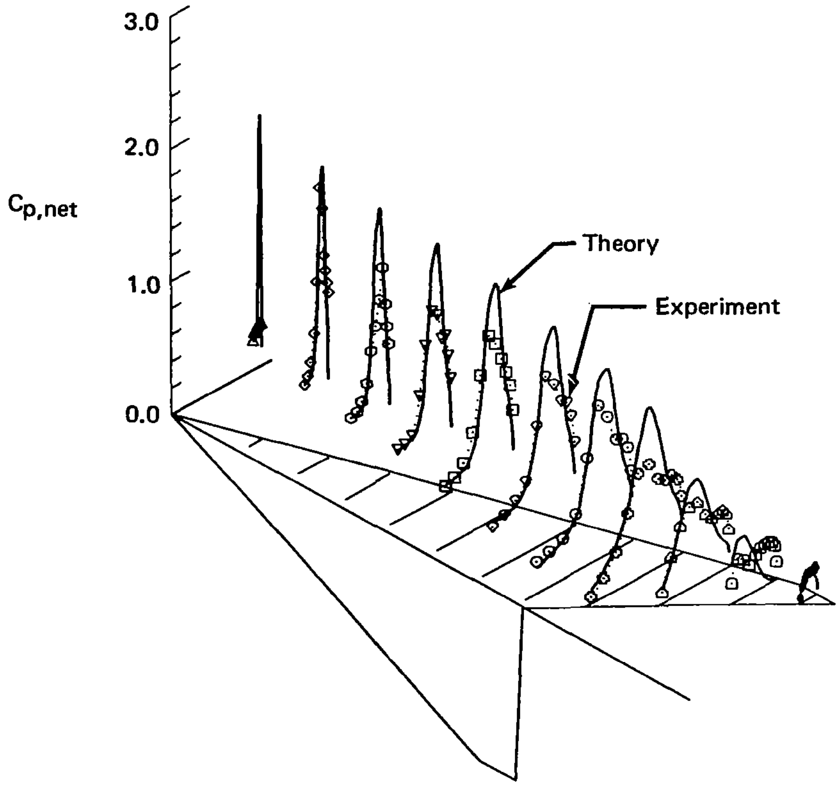

(b) Net Pressure Distributions

Figure 9.—Current Evaluation of LEV Computer Code, Flat Wing, Zero Thickness, $M = 0.40$, $\alpha = 16°$

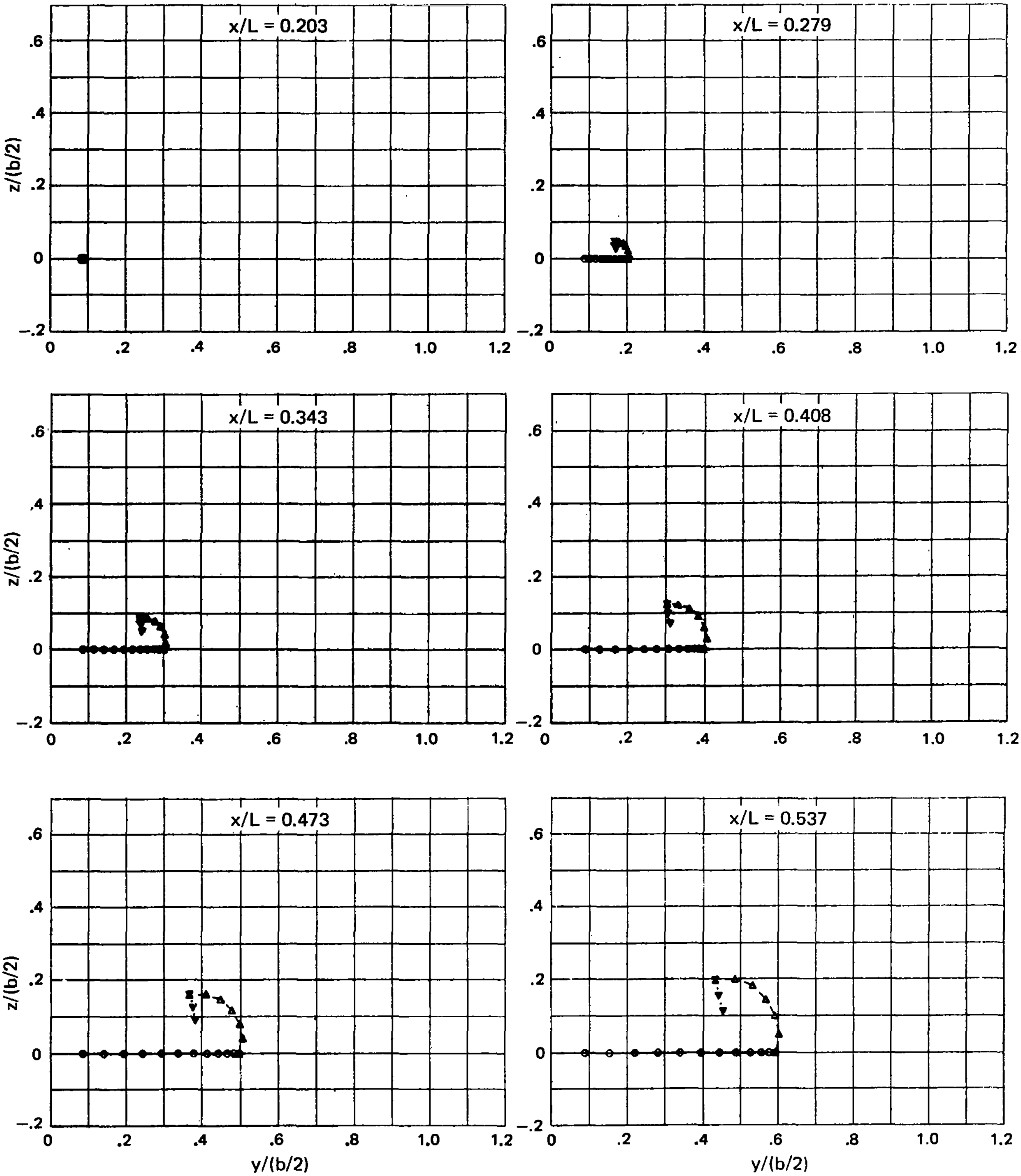

Figure 10.—Geometry of Panel Edges at Constant Body Stations, Flat Wing, Zero Thickness, Δa = 0.0, M = 0.40, α = 16°, Cycle 6

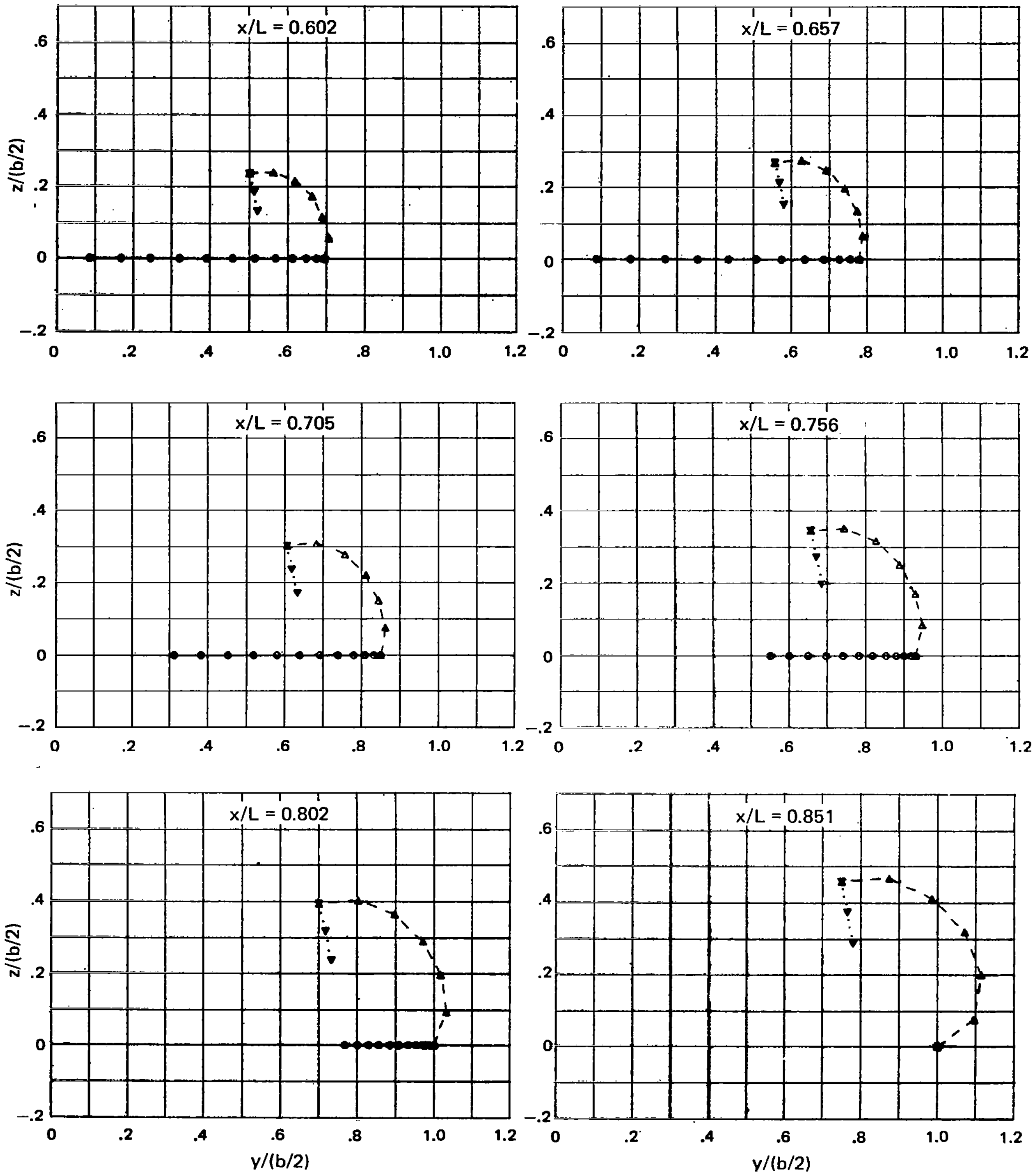

Figure 10.—(Concluded)

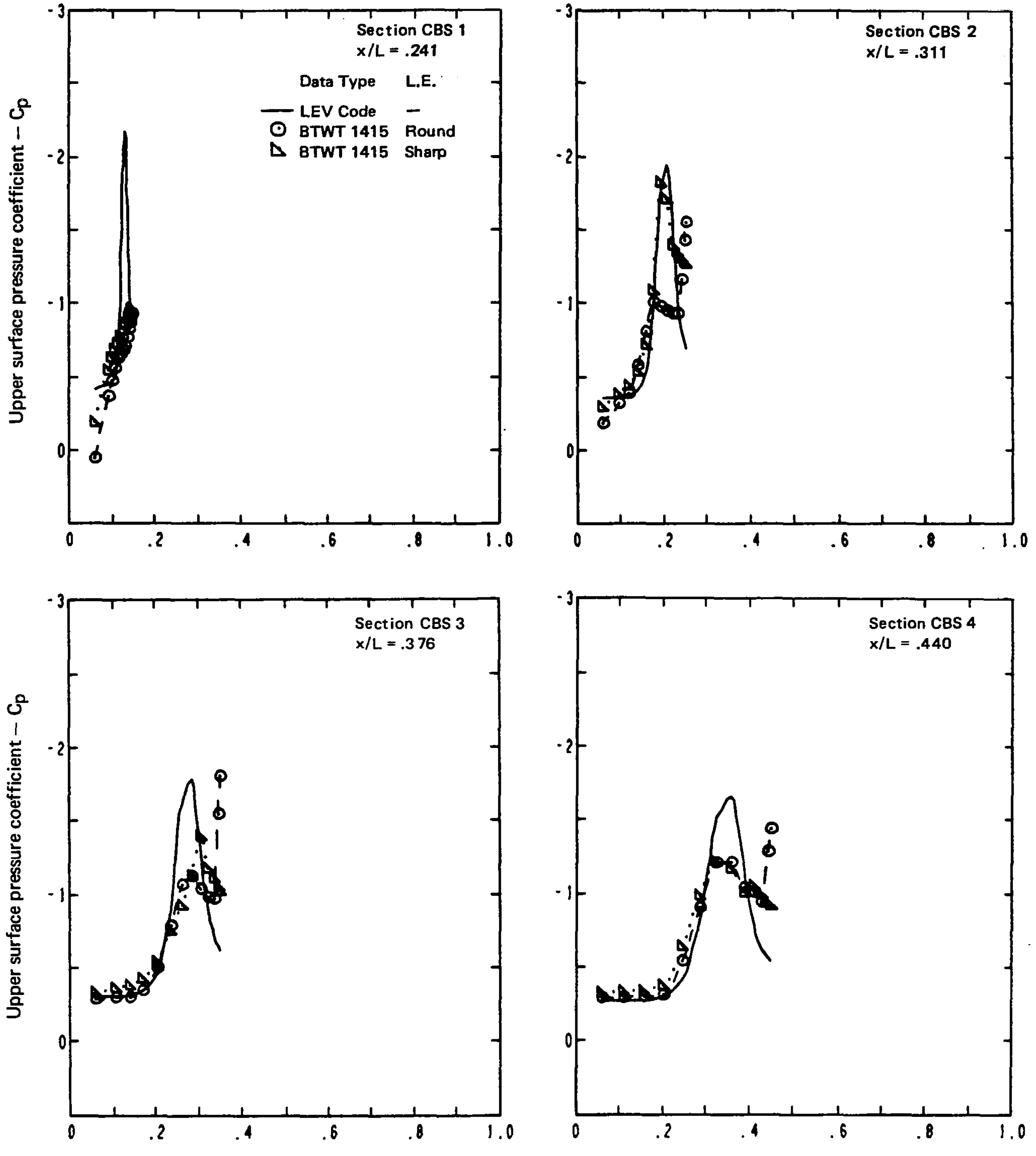

(a) Upper Surface Chordwise Pressure Distributions

Figure 11.—Pressure Distributions, Flat Wing, Zero Thickness, $\Delta a = 0.0$, $M = 0.40$, $\alpha = 16°$

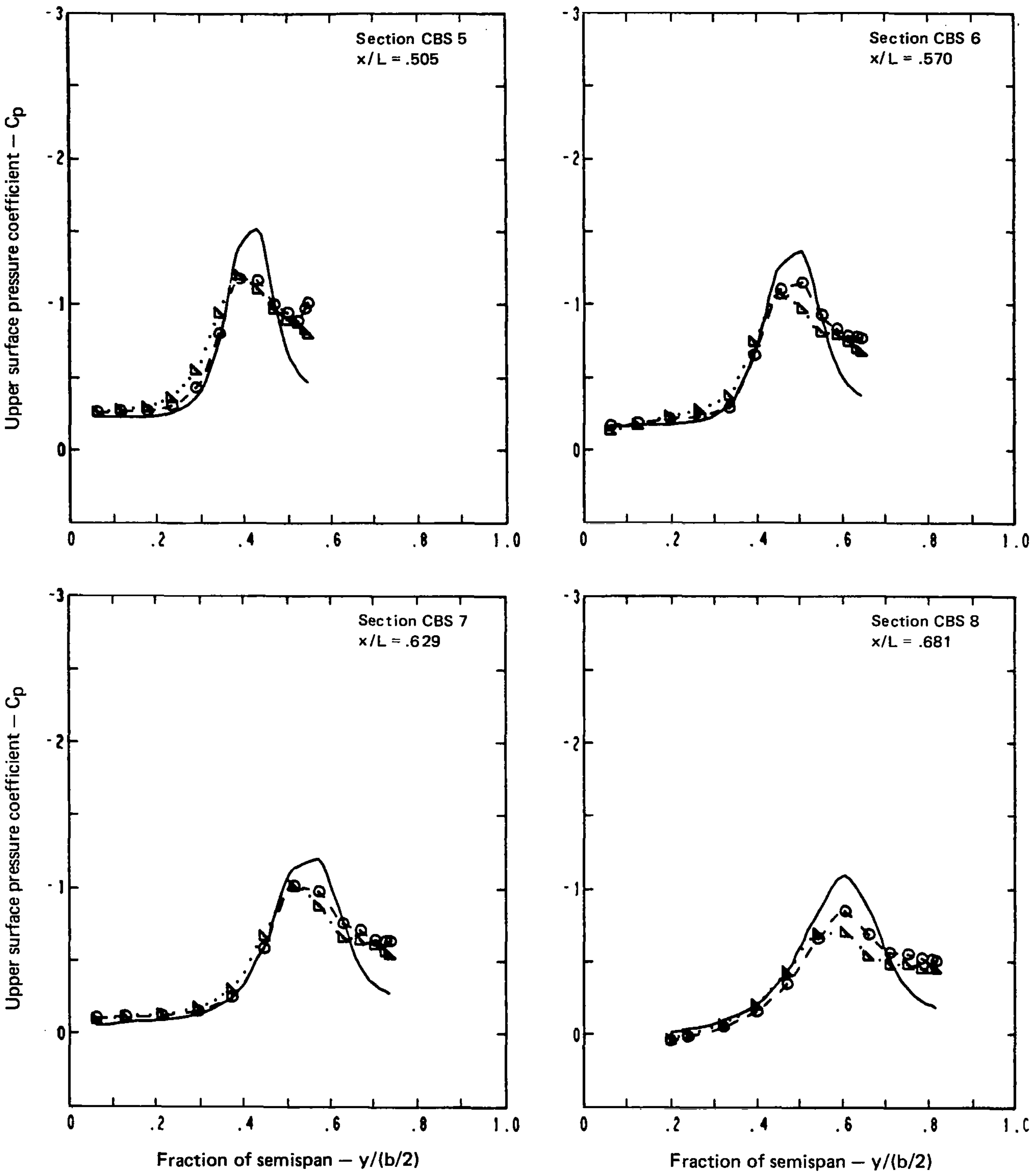

(a) (Continued)

Figure 11.—(Continued)

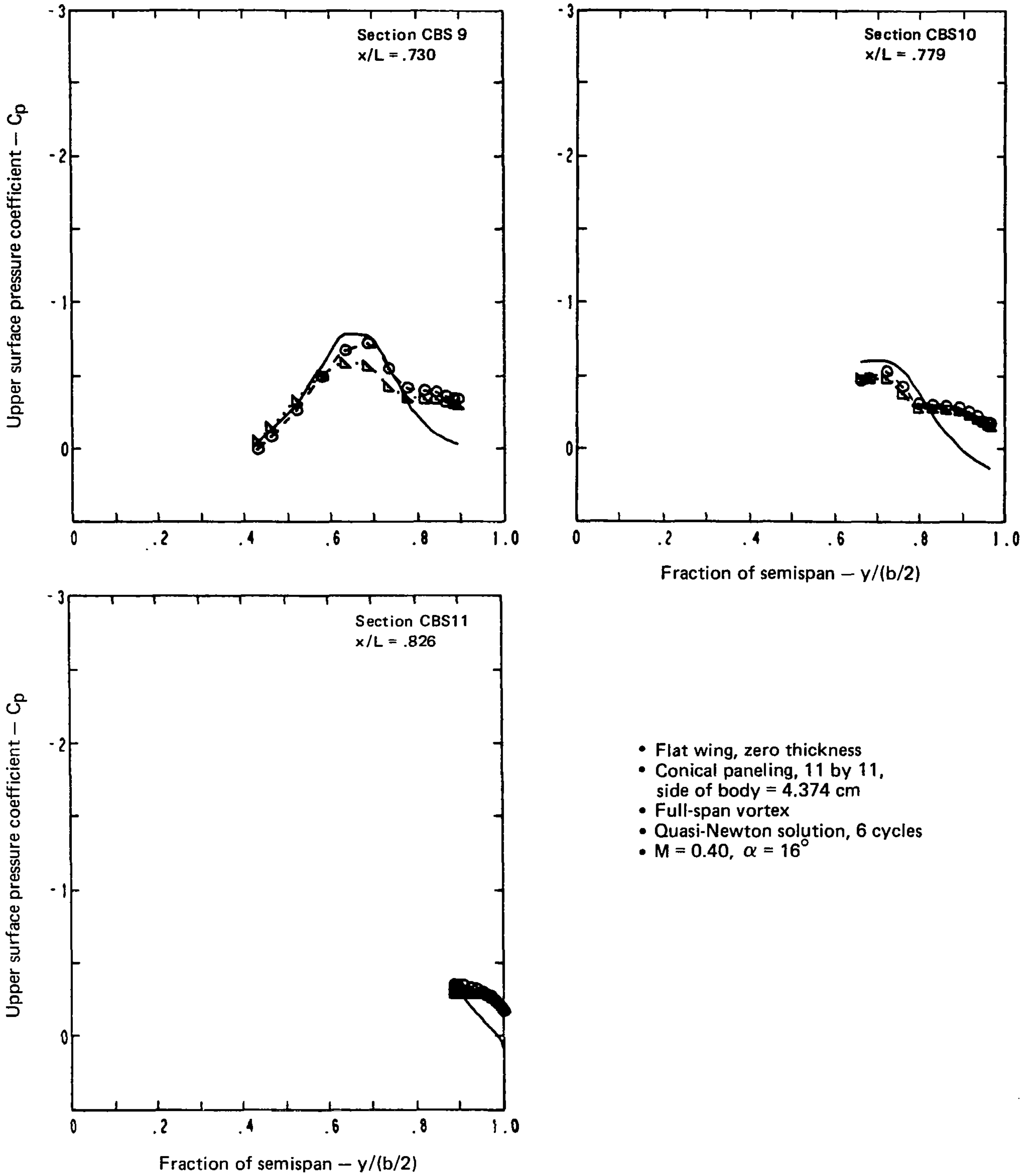

- Flat wing, zero thickness
- Conical paneling, 11 by 11, side of body = 4.374 cm
- Full-span vortex
- Quasi-Newton solution, 6 cycles
- M = 0.40, α = 16°

(a) (Concluded)

Figure 11.—(Continued)

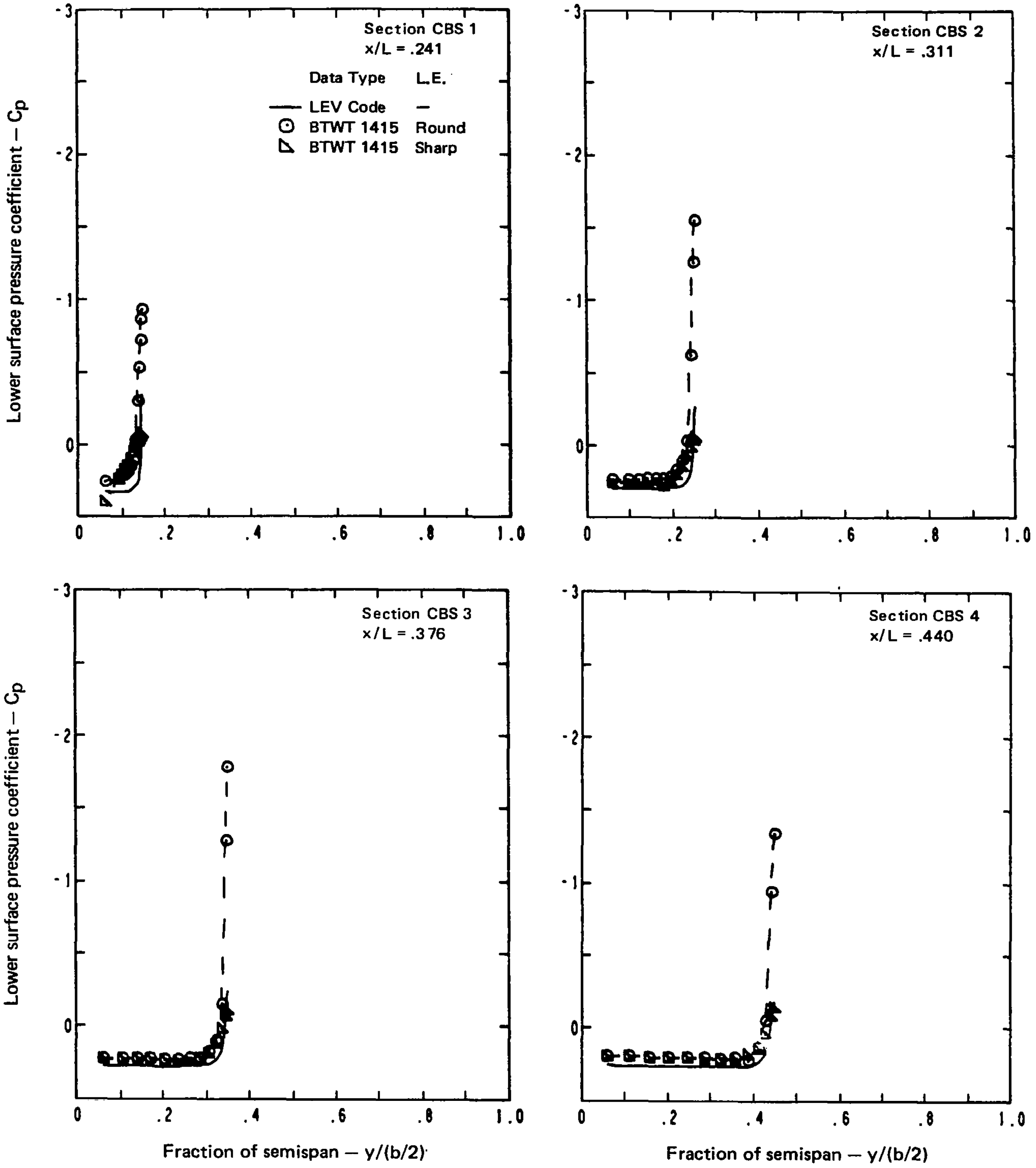

(b) Lower Surface Chordwise Pressure Distributions

Figure 11.—(Continued)

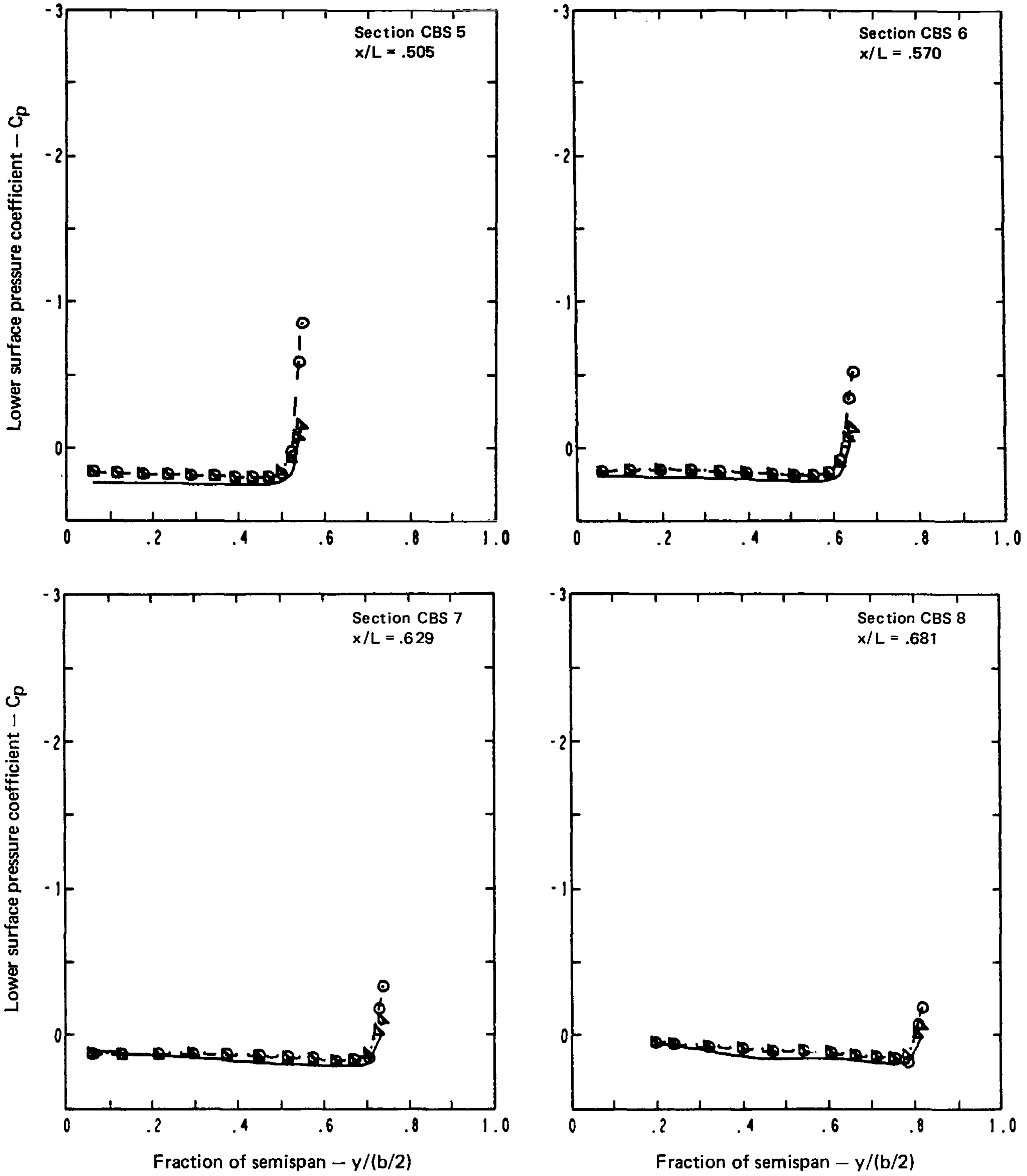

(b) (Continued)

Figure 11.–(Continued)

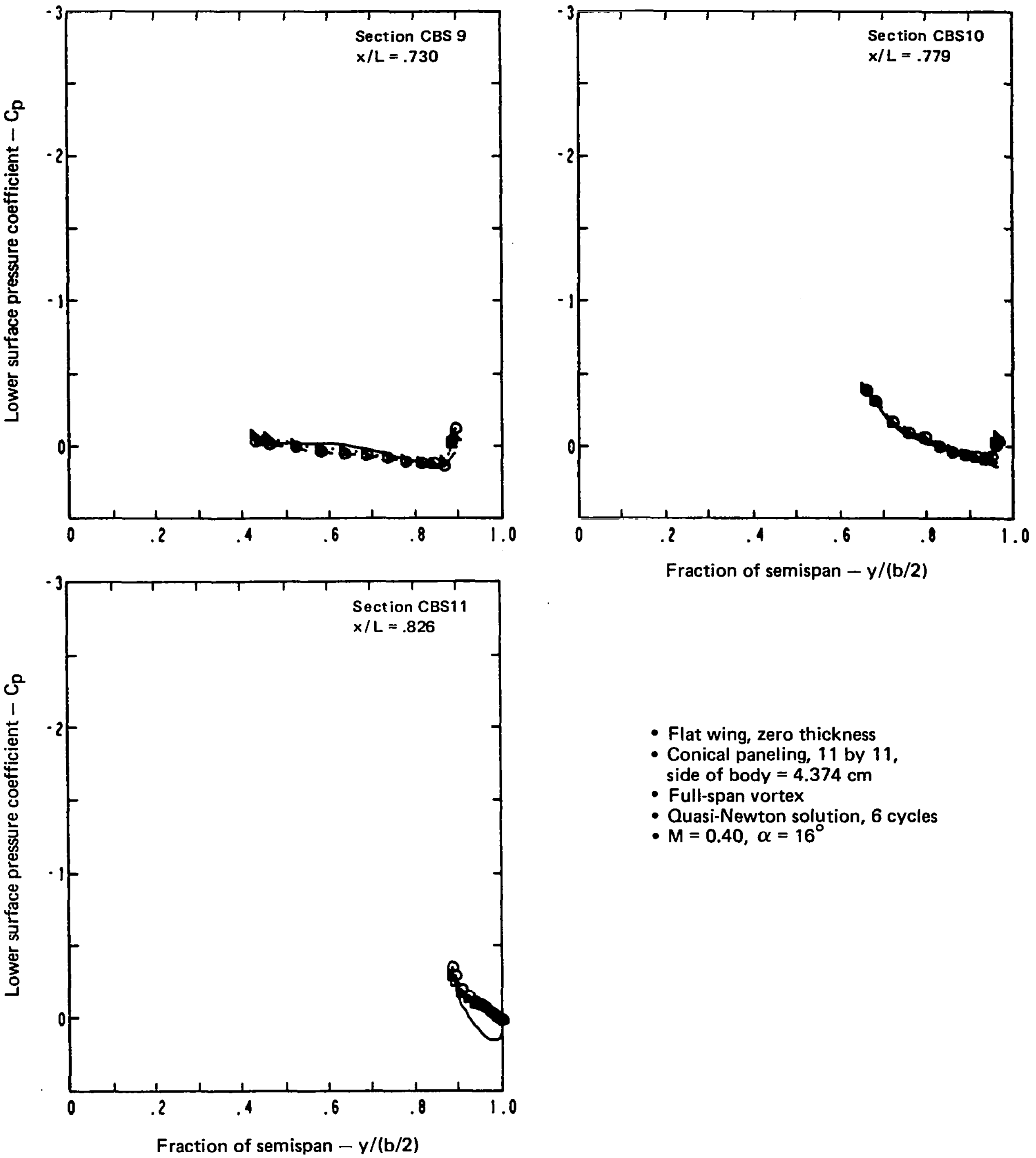

- Flat wing, zero thickness
- Conical paneling, 11 by 11, side of body = 4.374 cm
- Full-span vortex
- Quasi-Newton solution, 6 cycles
- M = 0.40, α = 16°

(b) (Concluded)

Figure 11.—(Continued)

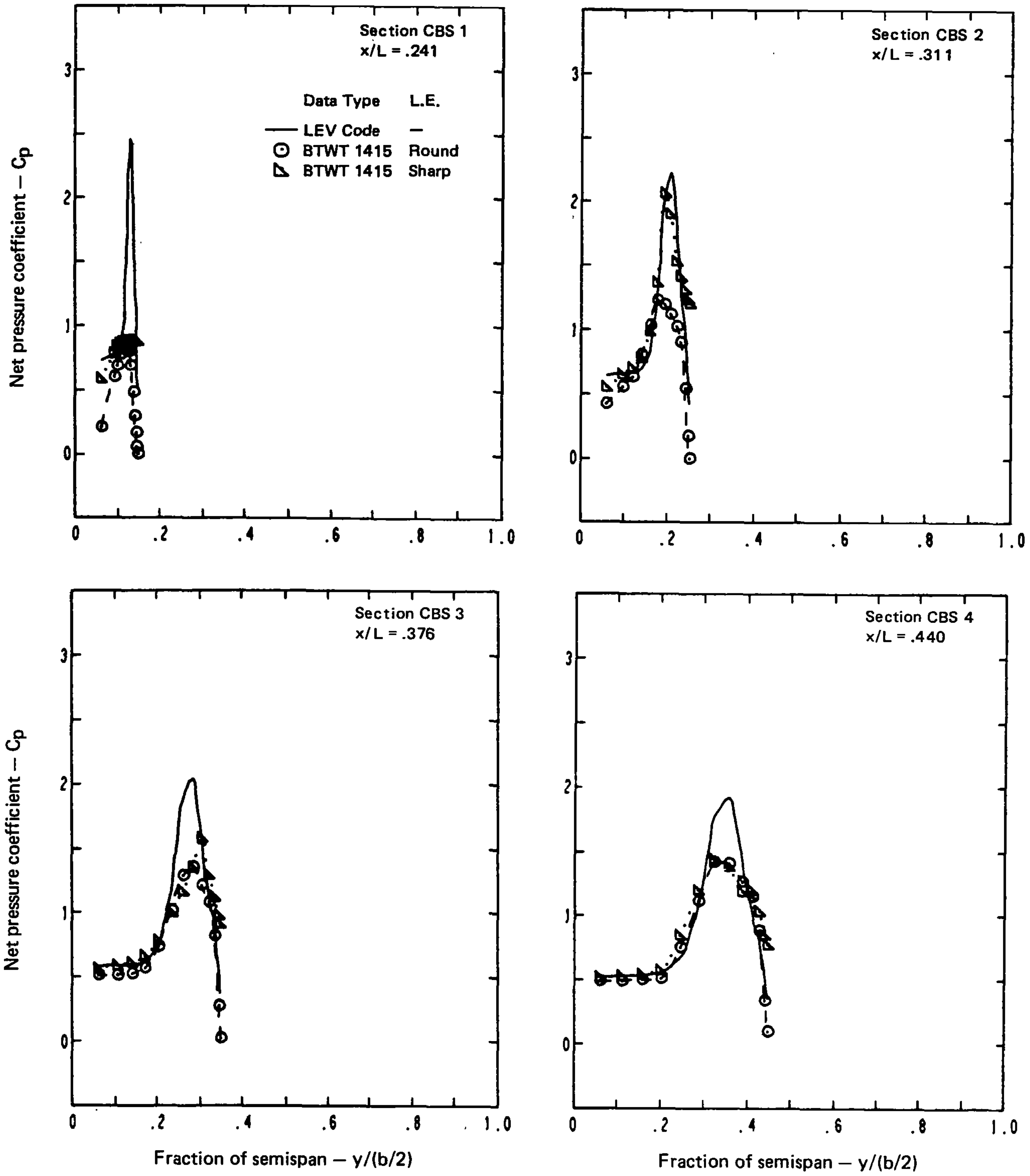

(c) Net Chordwise Pressure Distributions

Figure 11.—(Continued)

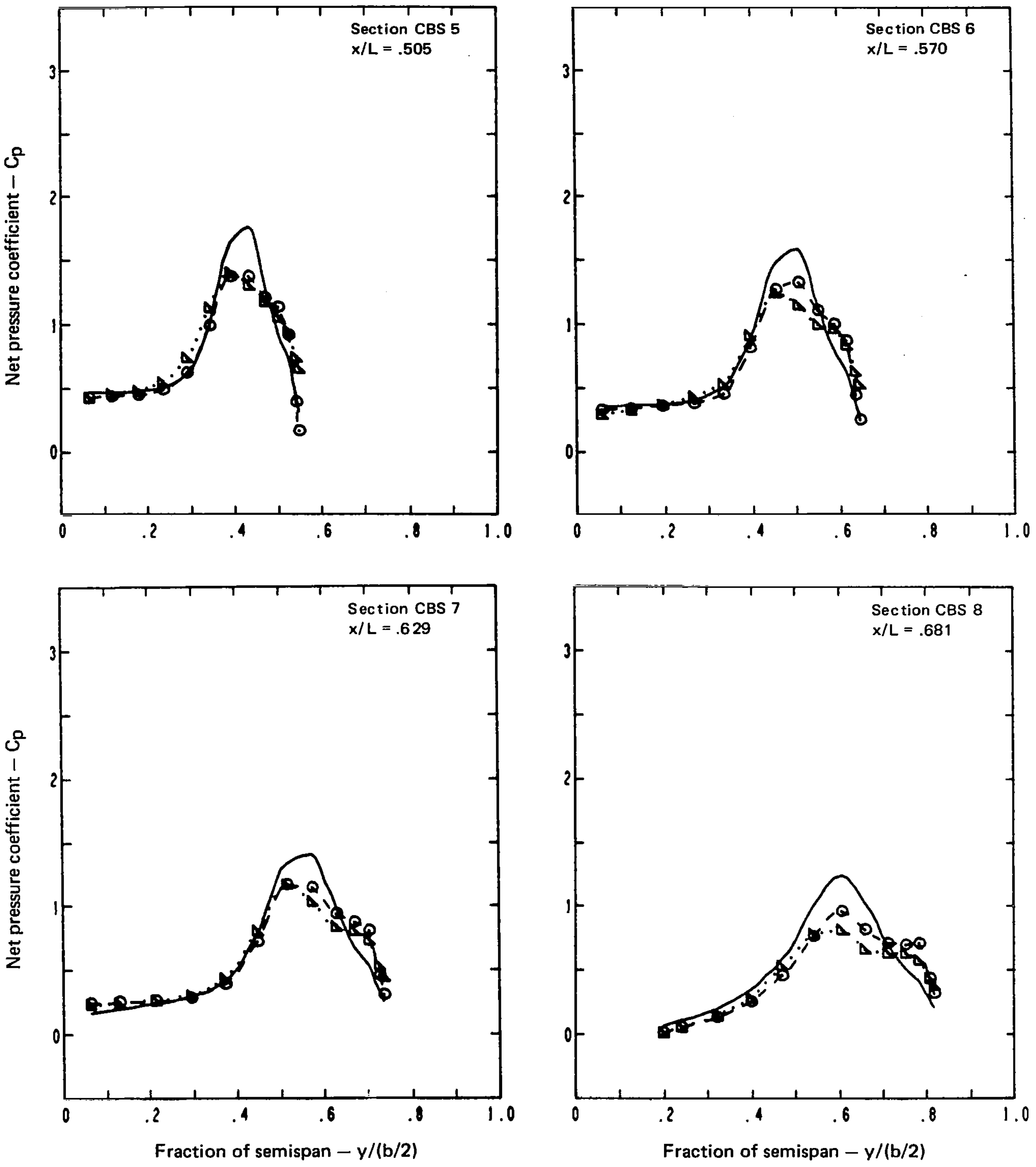

(c) (Continued)

Figure 11.—(Continued)

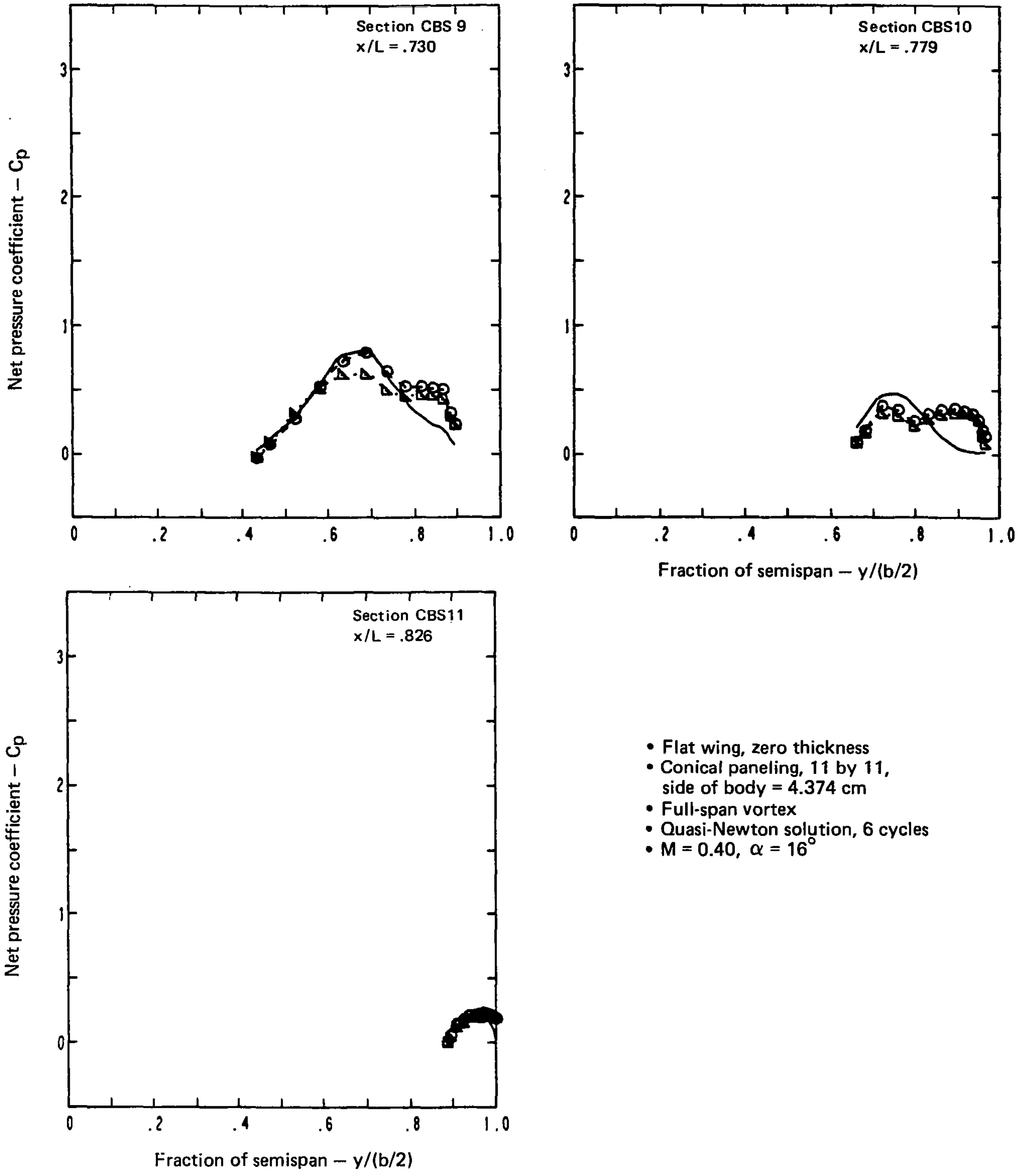

- Flat wing, zero thickness
- Conical paneling, 11 by 11, side of body = 4.374 cm
- Full-span vortex
- Quasi-Newton solution, 6 cycles
- M = 0.40, α = 16°

(c) (Concluded)

Figure 11.—(Concluded)

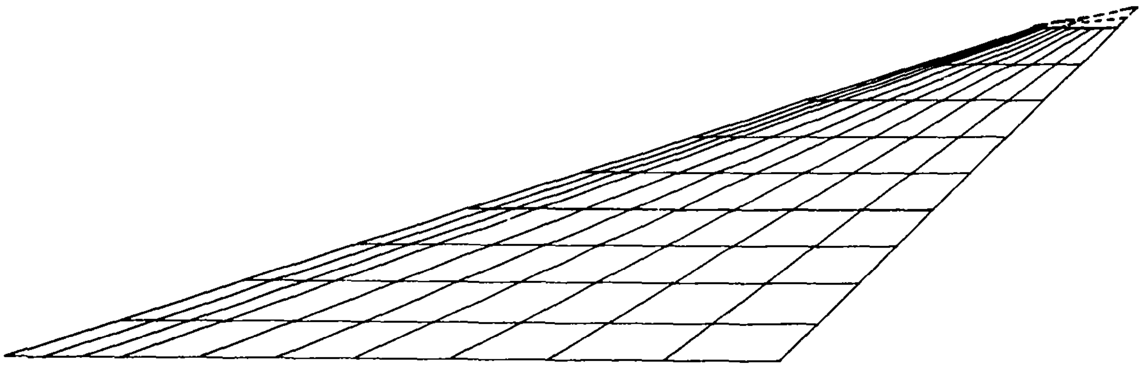

9 X 10 (90 panels)

Side of body = 4.374 cm (1.722 in.)

Figure 12.—Planform View of Streamwise Wing Paneling

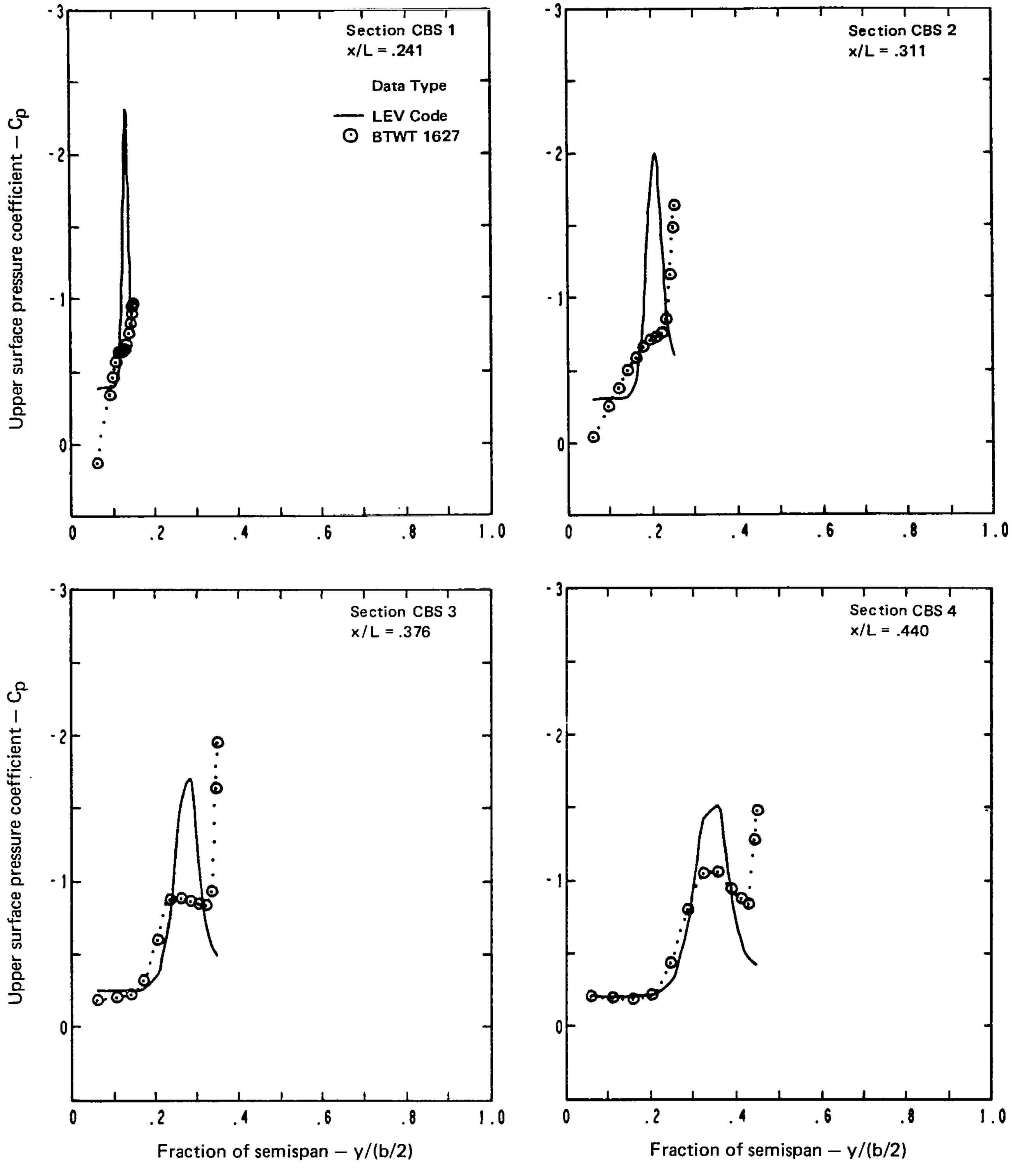

Figure 13.—Upper Surface Pressure Distributions, Twisted Wing, Zero Thickness, $\Delta a = 0.0$, $M = 0.40$, $\alpha = 16°$

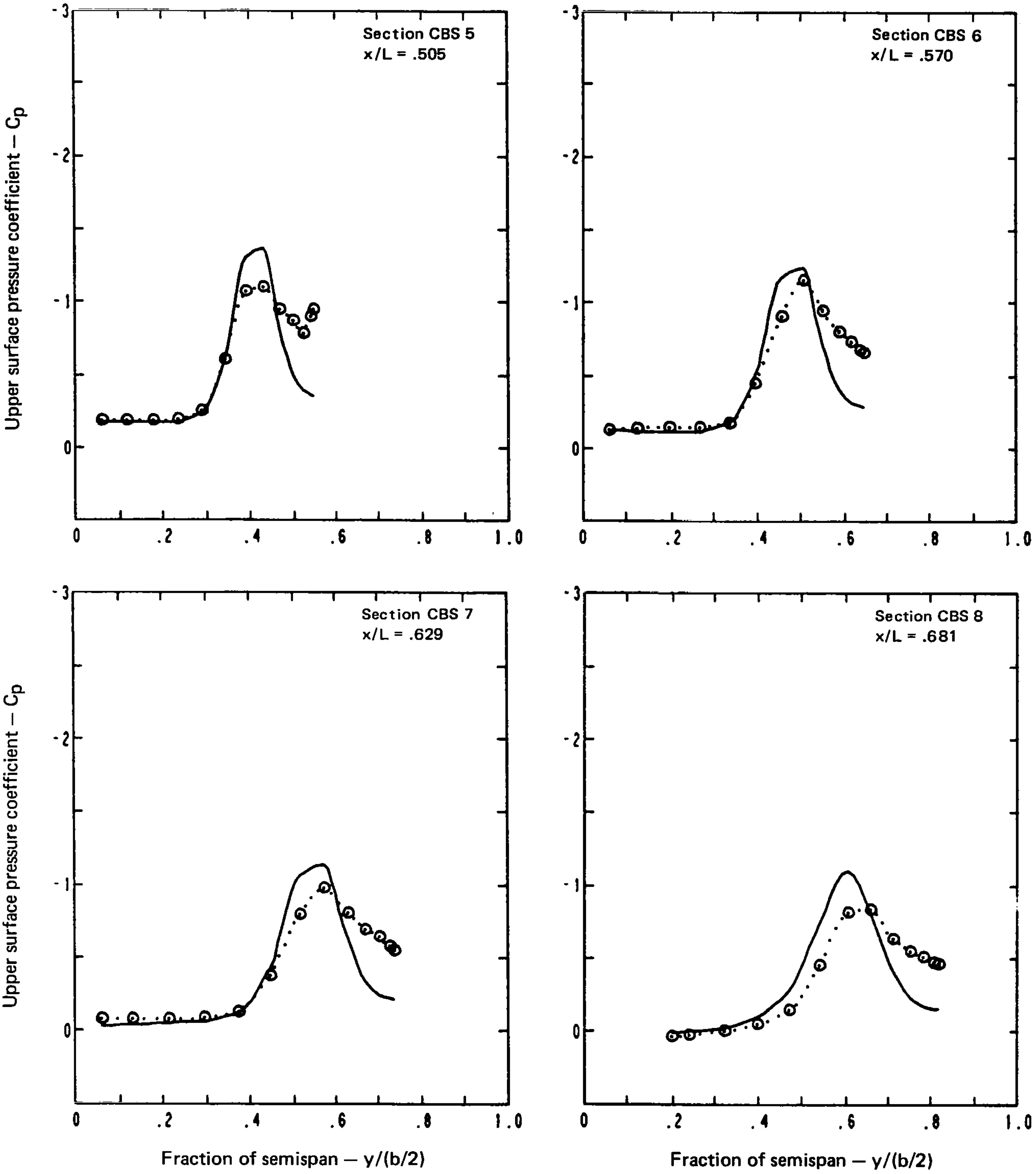

Figure 13.—(Continued)

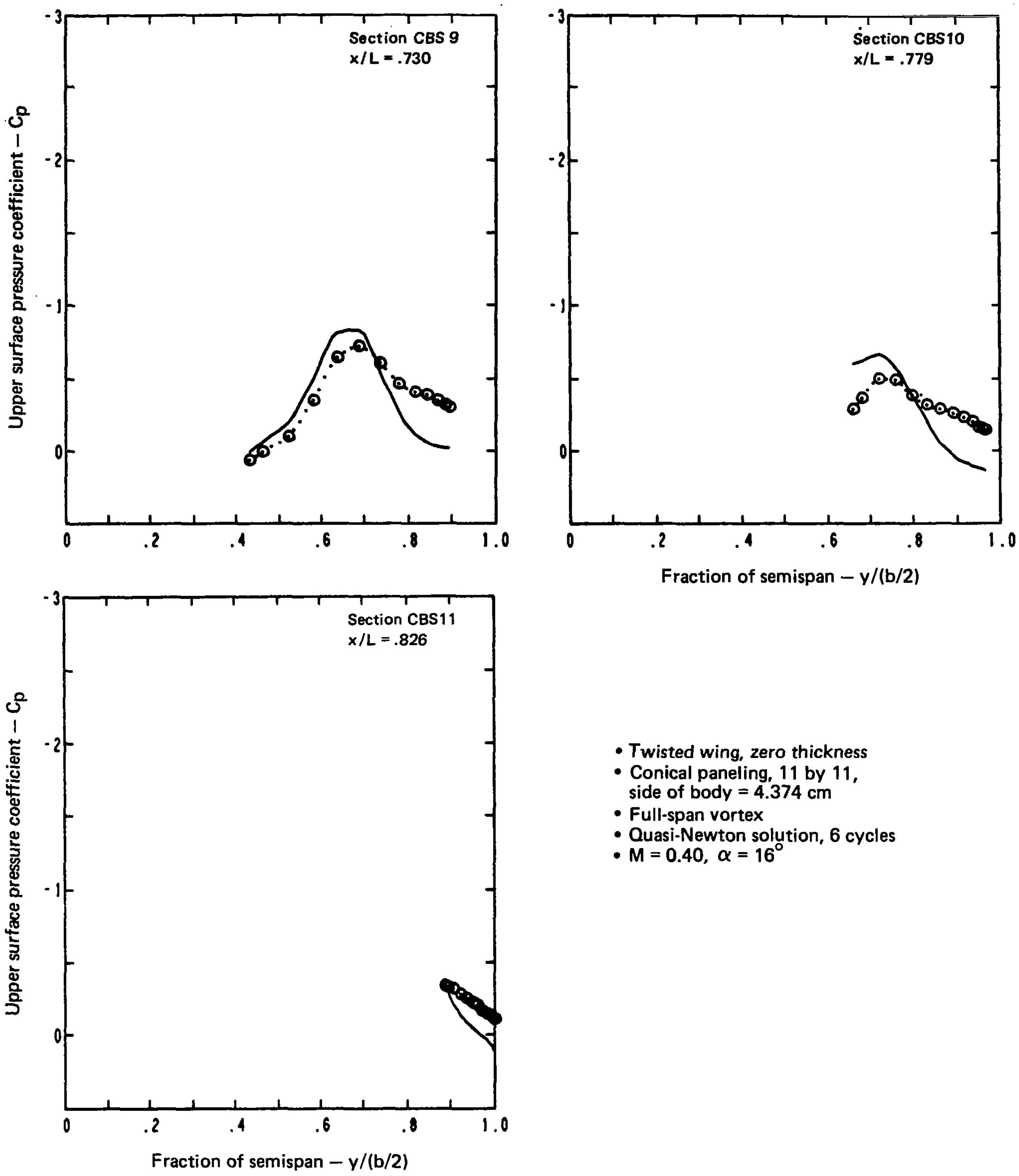

- Twisted wing, zero thickness
- Conical paneling, 11 by 11, side of body = 4.374 cm
- Full-span vortex
- Quasi-Newton solution, 6 cycles
- M = 0.40, α = 16°

Figure 13.–(Concluded)

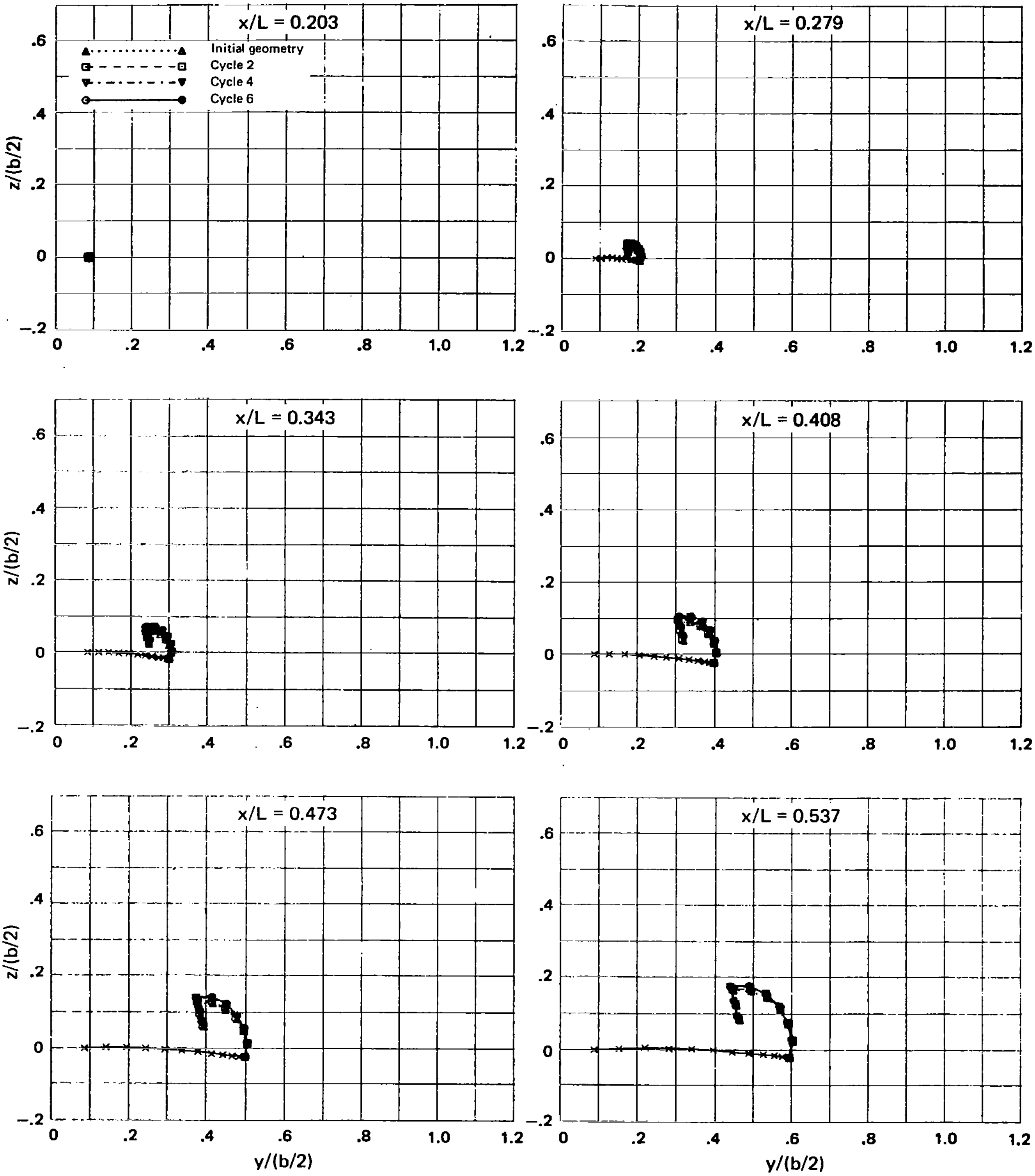

(a) Geometry of Panel Edges at Constant Body Stations

Figure 14.—Panel Geometry, Twisted Wing, Zero Thickness, $\Delta a = 0.0$, $M = 0.40$, $\alpha = 16°$, Several Cycles

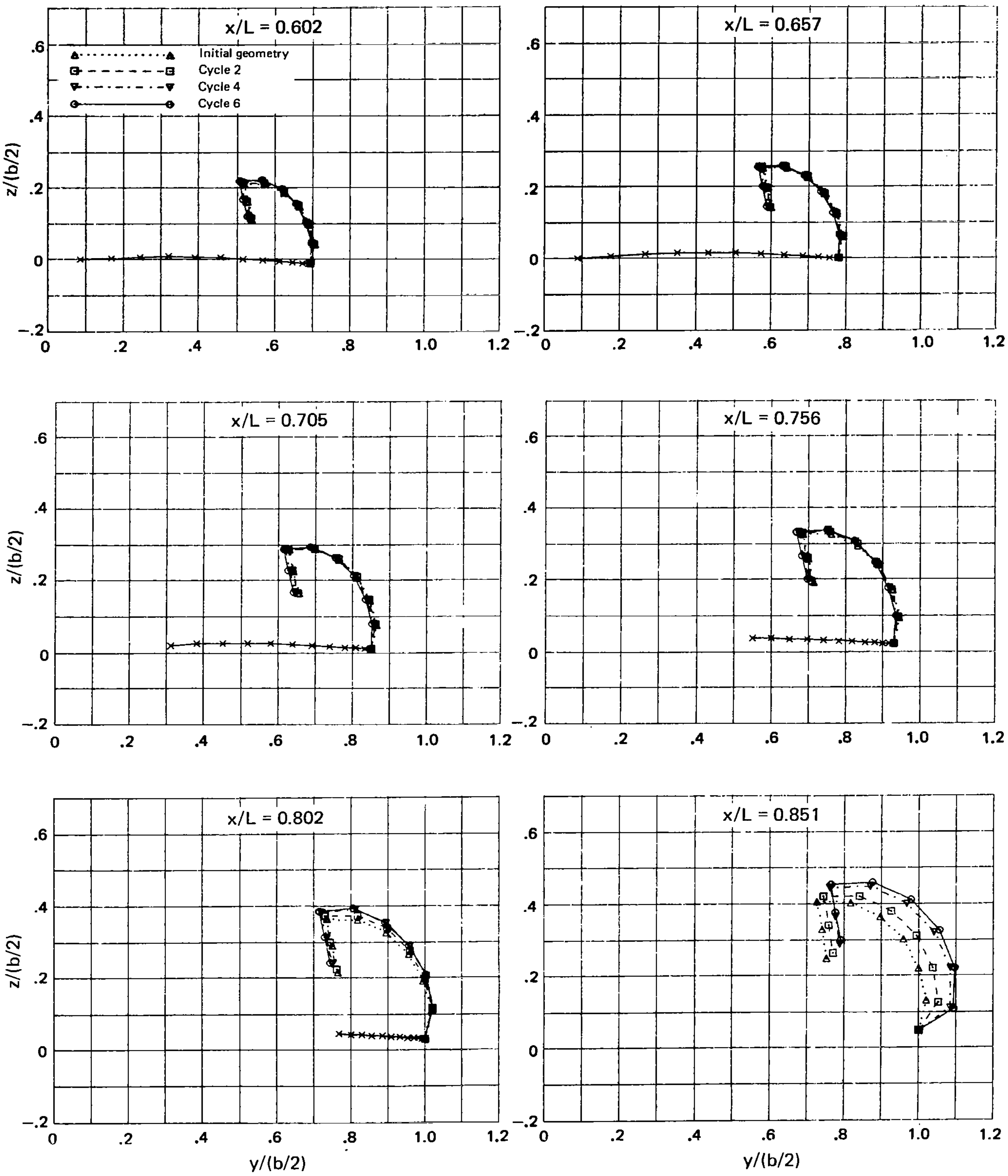

(a) Concluded

Figure 14.—(Continued)

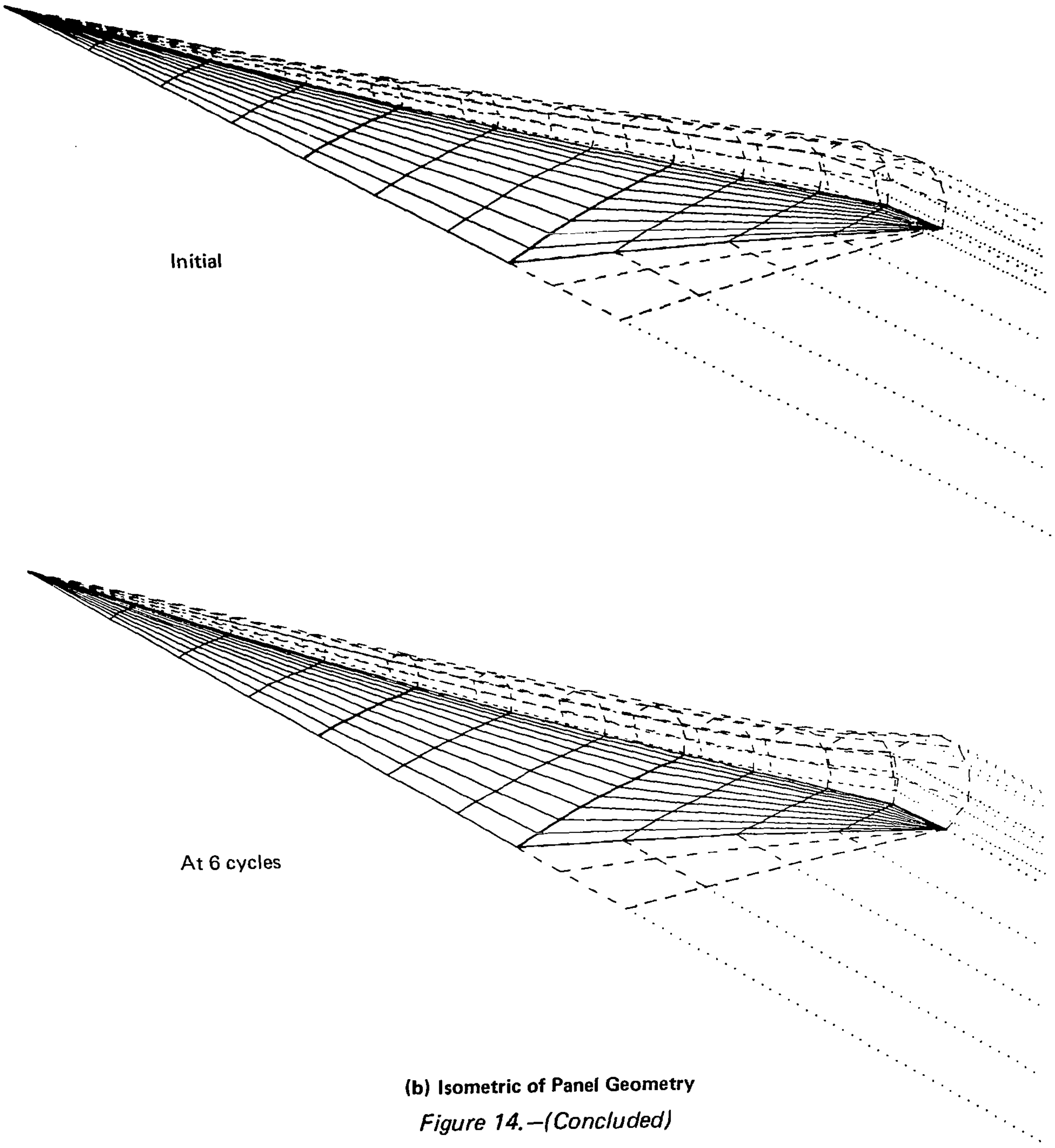

(b) Isometric of Panel Geometry

Figure 14.–(Concluded)

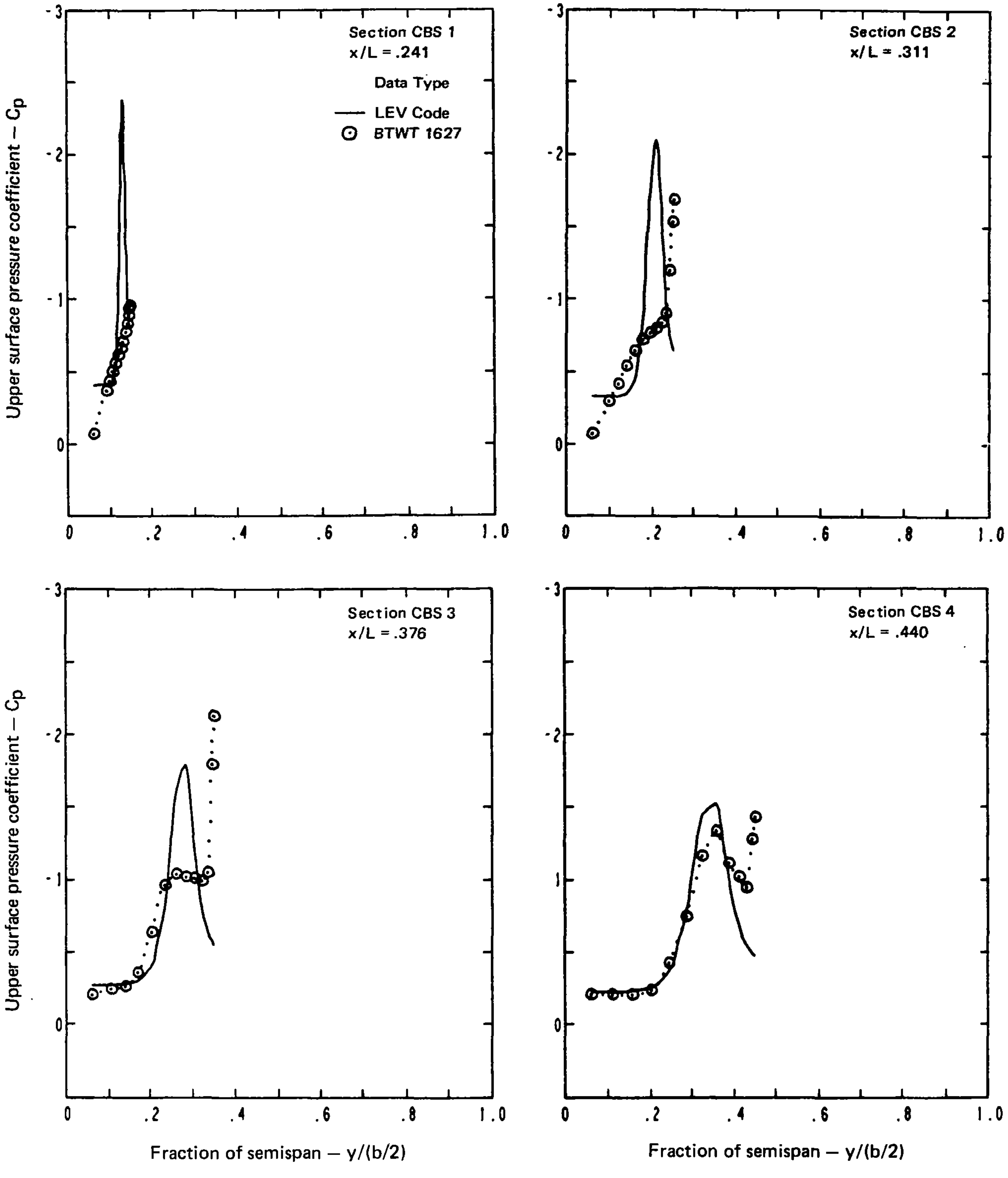

Figure 15.—Upper Surface Pressure Distributions, Cambered-Twisted Wing, Zero Thickness, $\Delta a = 0.0$, $M = 0.40$, $\alpha = 16°$

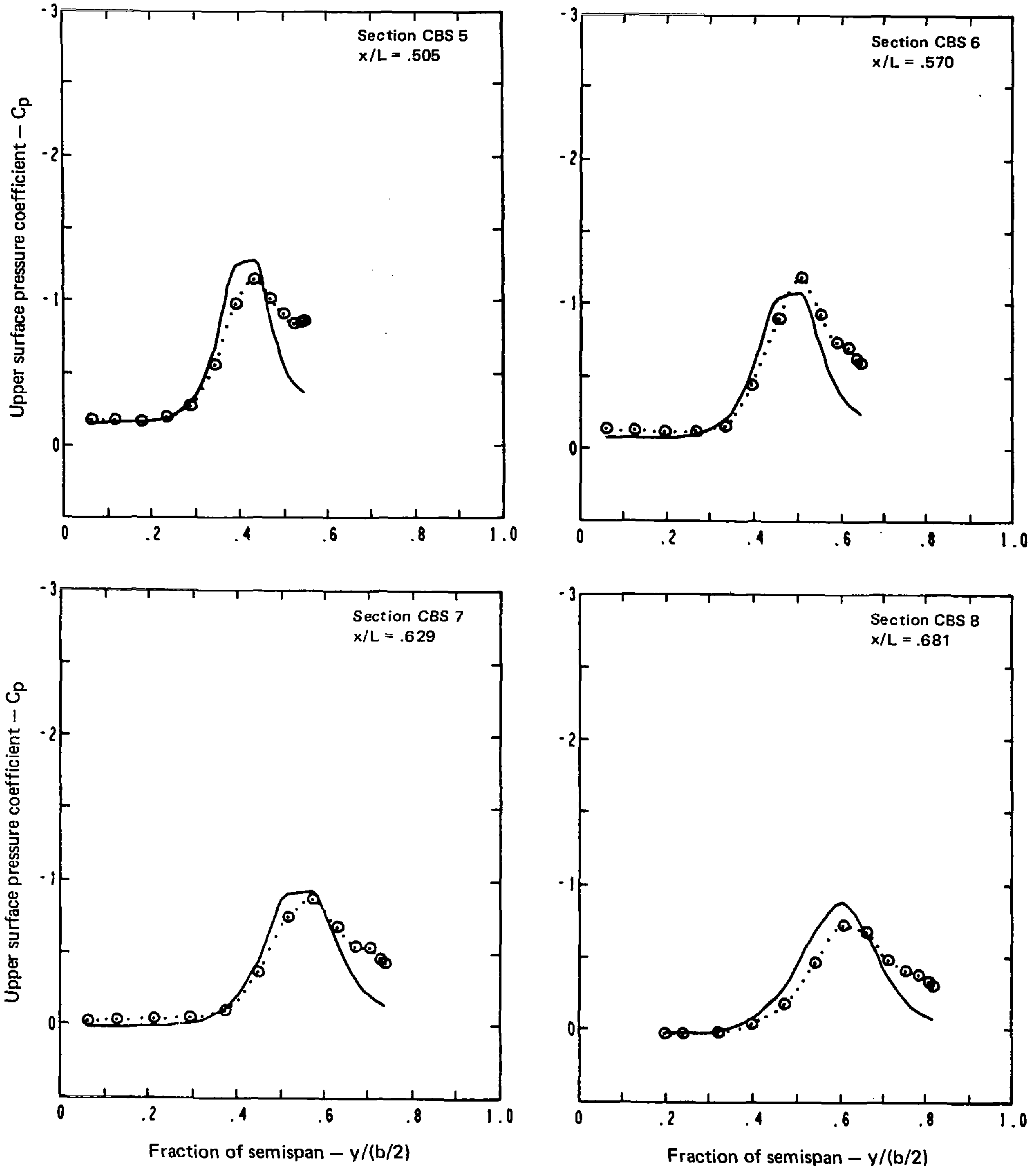

Figure 15.—(Continued)

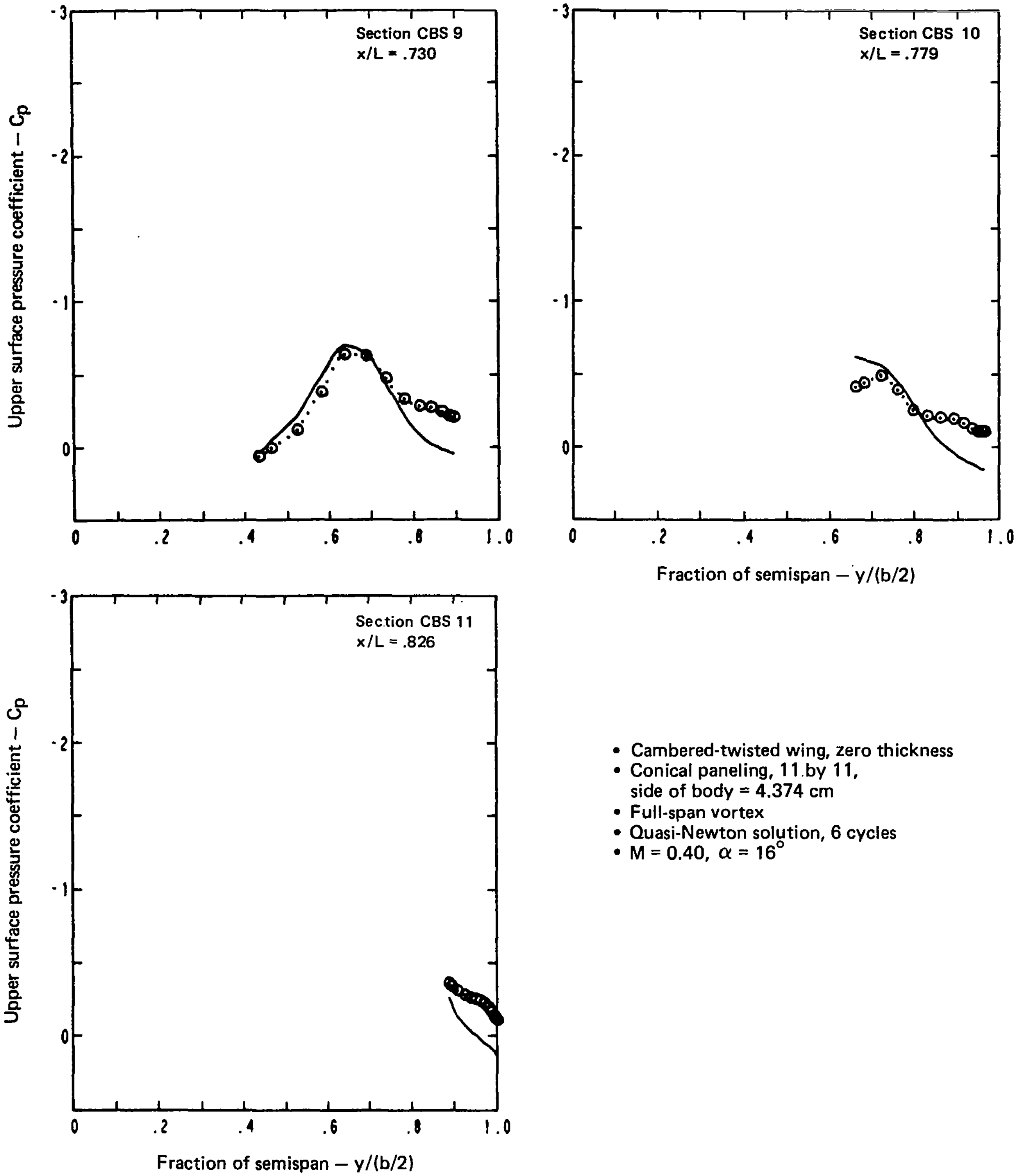

- Cambered-twisted wing, zero thickness
- Conical paneling, 11 by 11, side of body = 4.374 cm
- Full-span vortex
- Quasi-Newton solution, 6 cycles
- $M = 0.40$, $\alpha = 16^\circ$

Figure 15.—(Concluded)

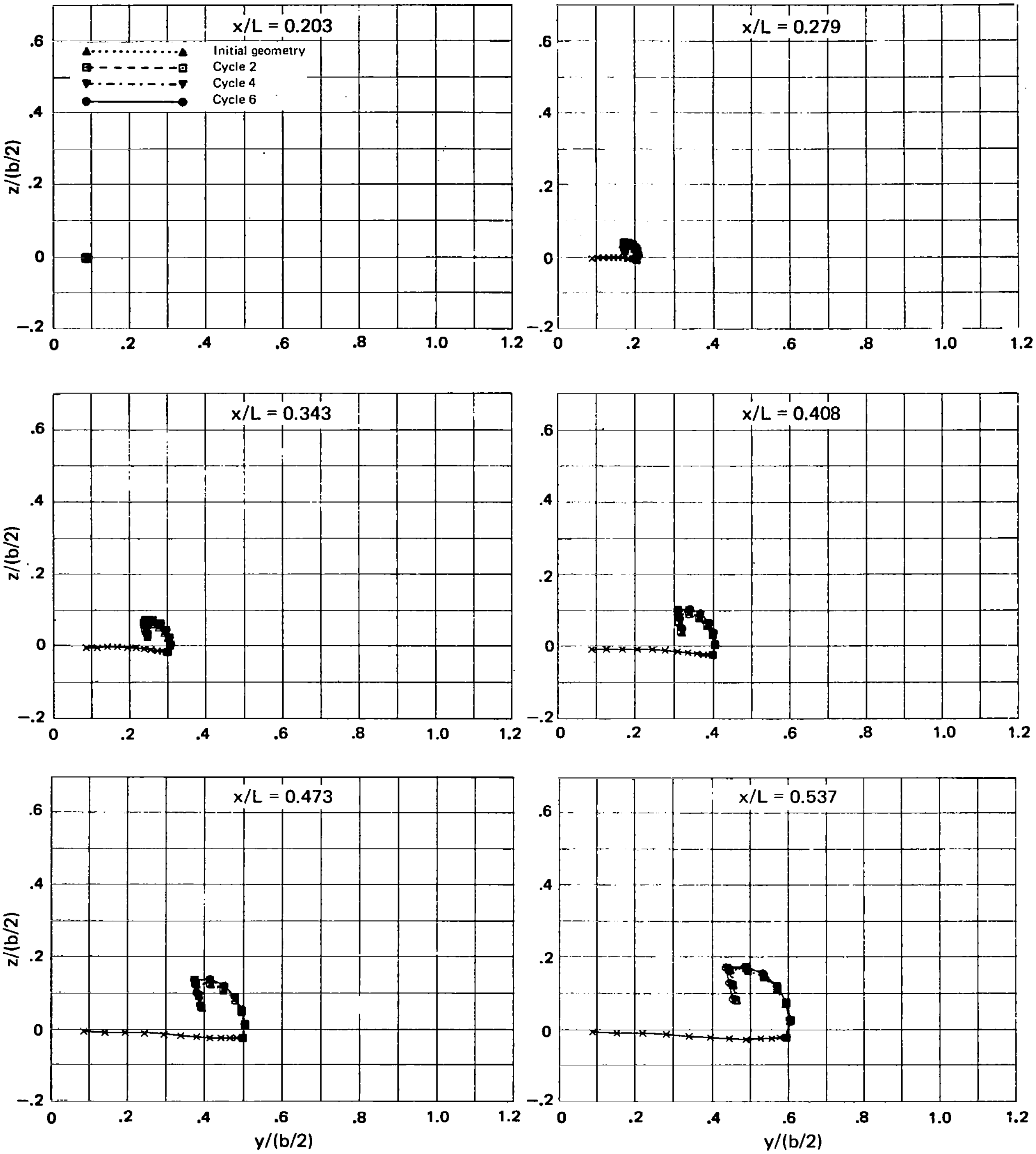

(a) Geometry of Panel Edges at Constant Body Station

Figure 16.—Panel Geometry, Cambered-Twisted Wing, Zero Thickness, Δa = 0.0, M = 0.40, α = 16°, Several Cycles

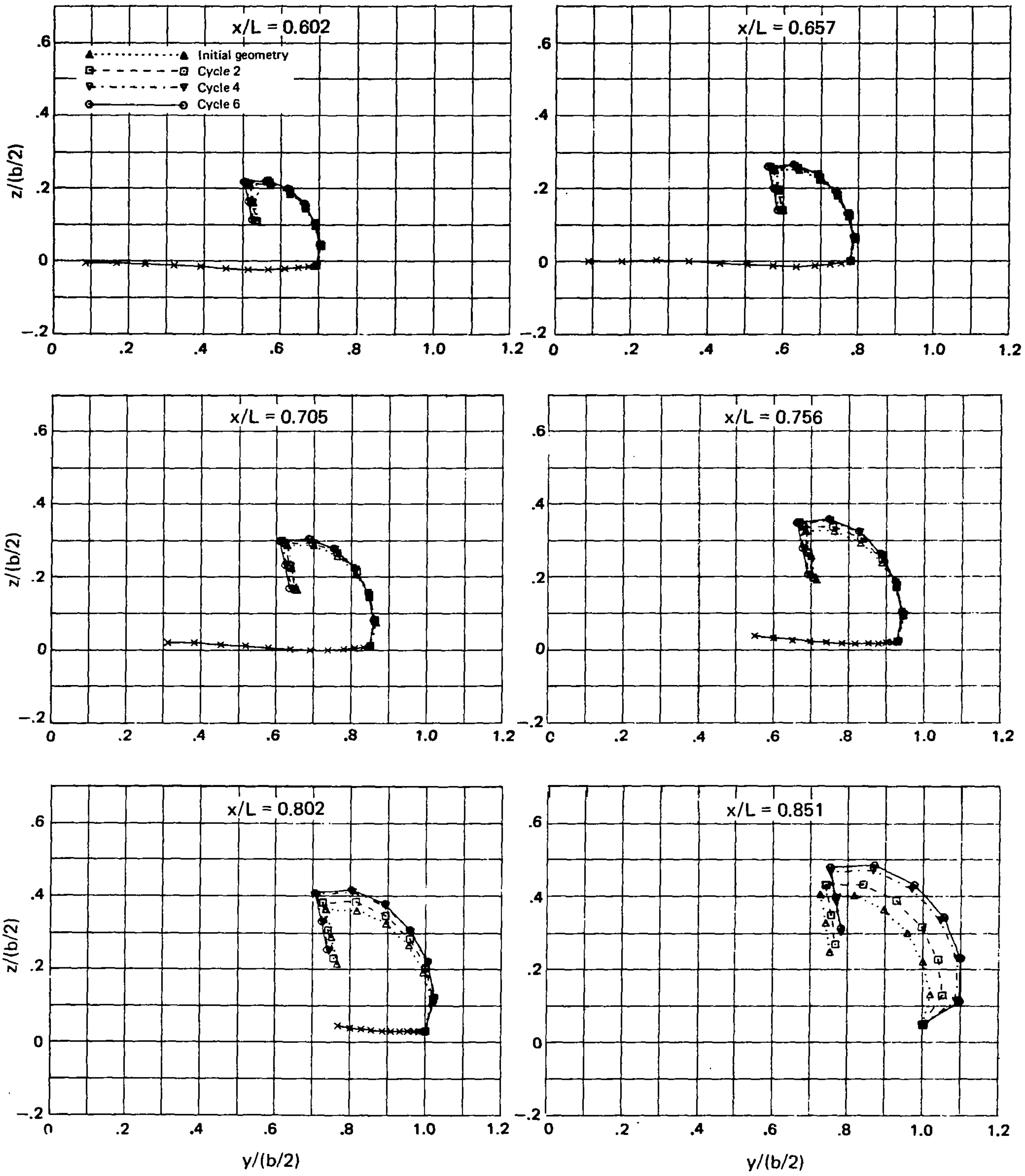

(a) Concluded

Figure 16.—(Continued)

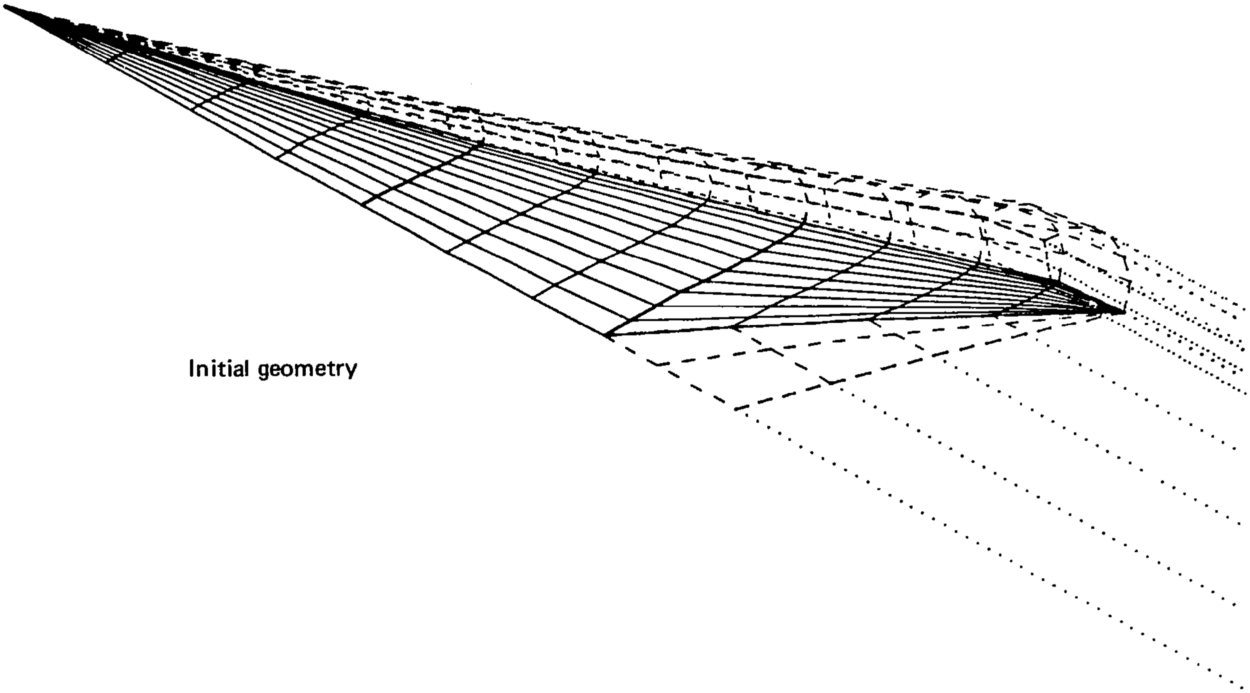

Initial geometry

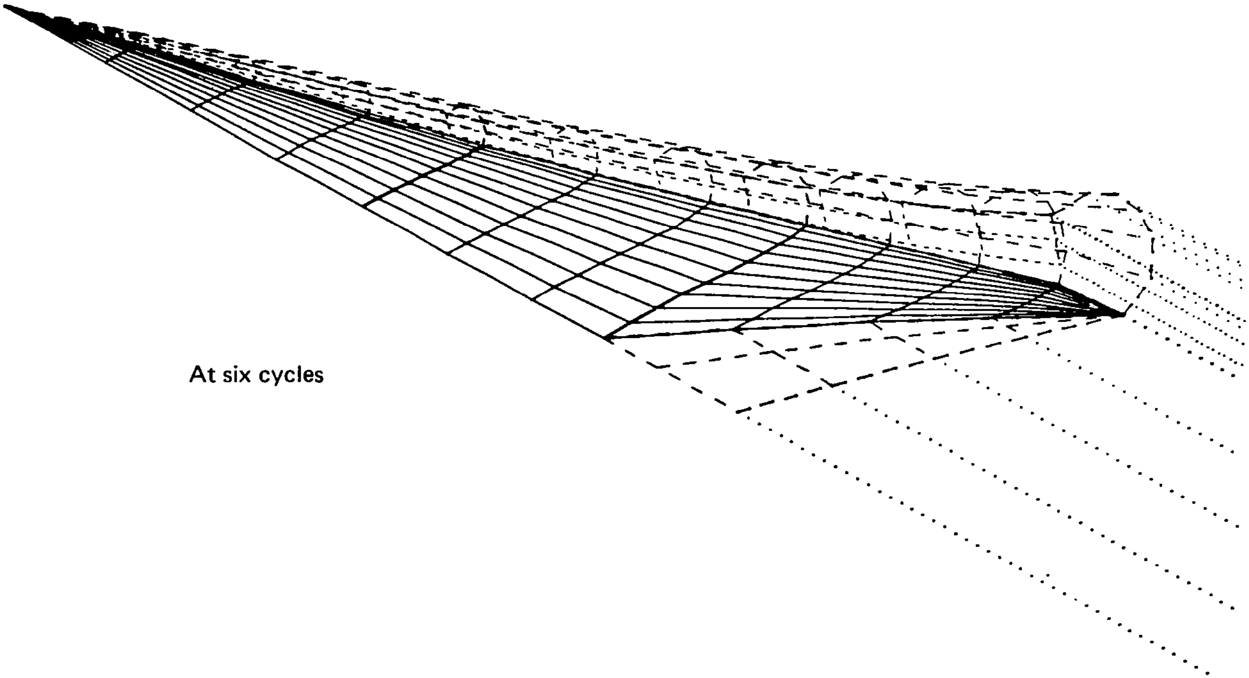

At six cycles

(b) Isometric of Panel Geometry

Figure 16.—(Concluded)

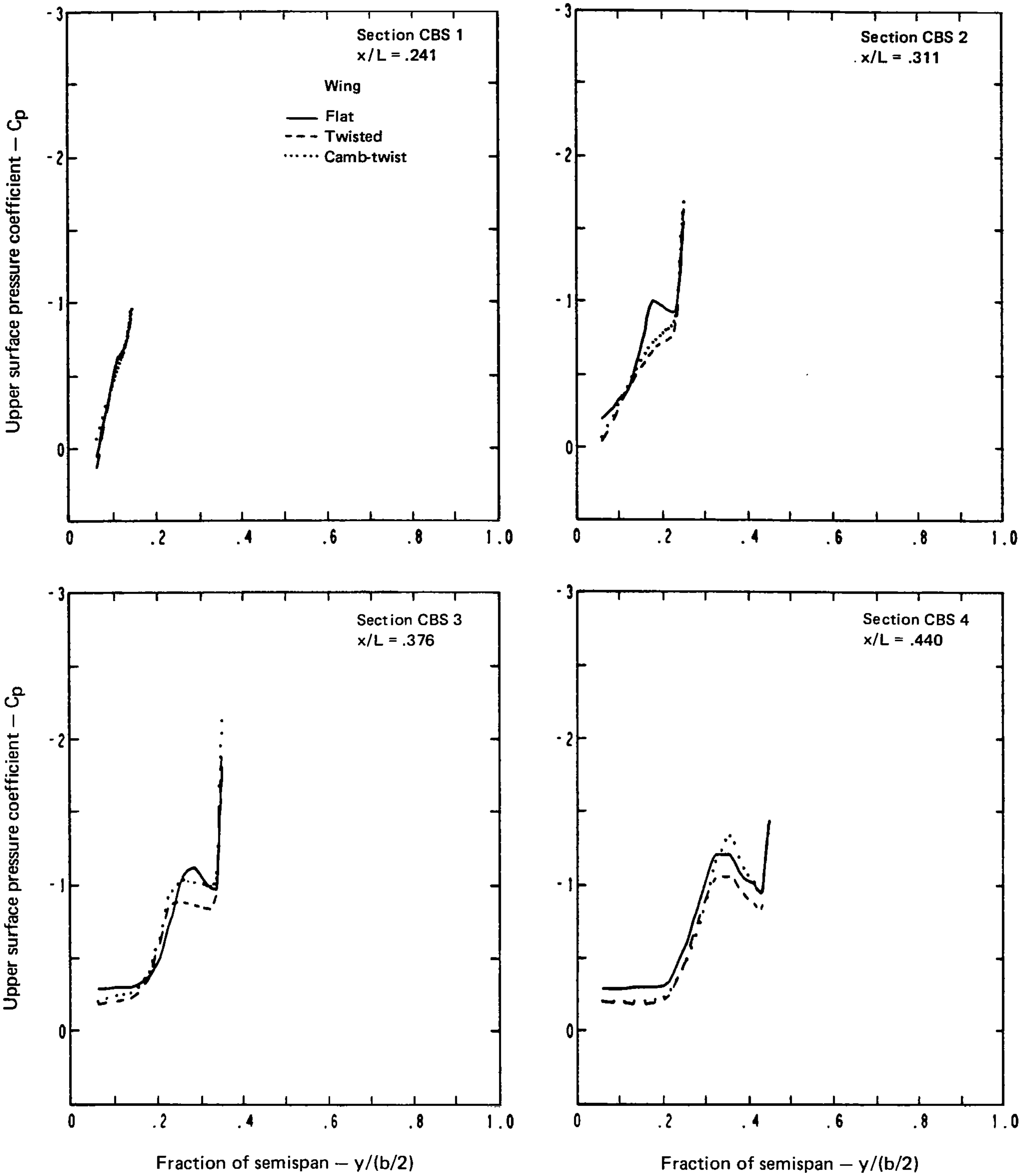

(a) Experimental Data

Figure 17.—Comparison of Upper Surface Pressure Distributions for Three Wing Shapes, Zero Thickness, Δ a = 0.0, M = 0.40, α = 16°

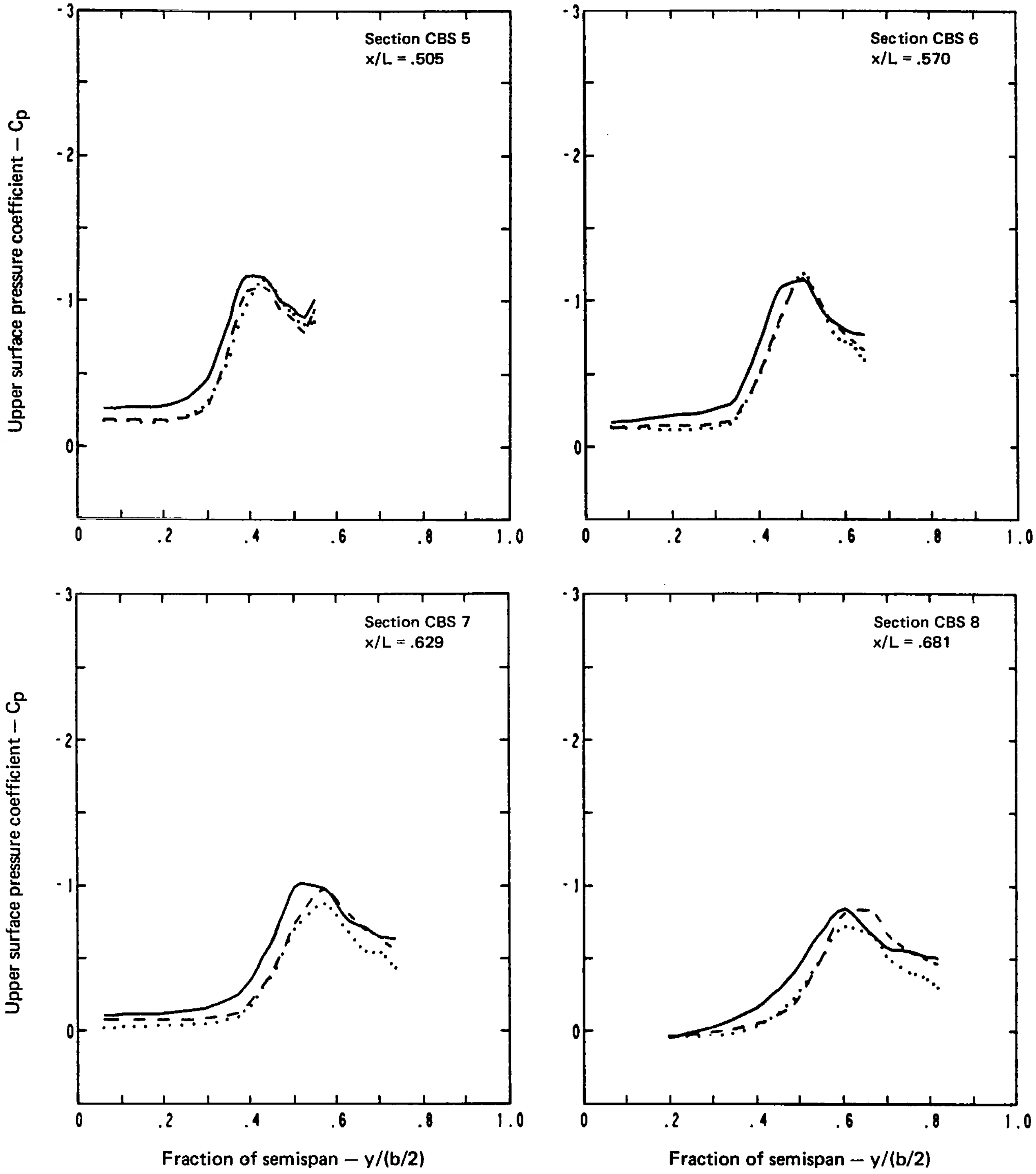

(a) (Continued)

Figure 17.—(Continued)

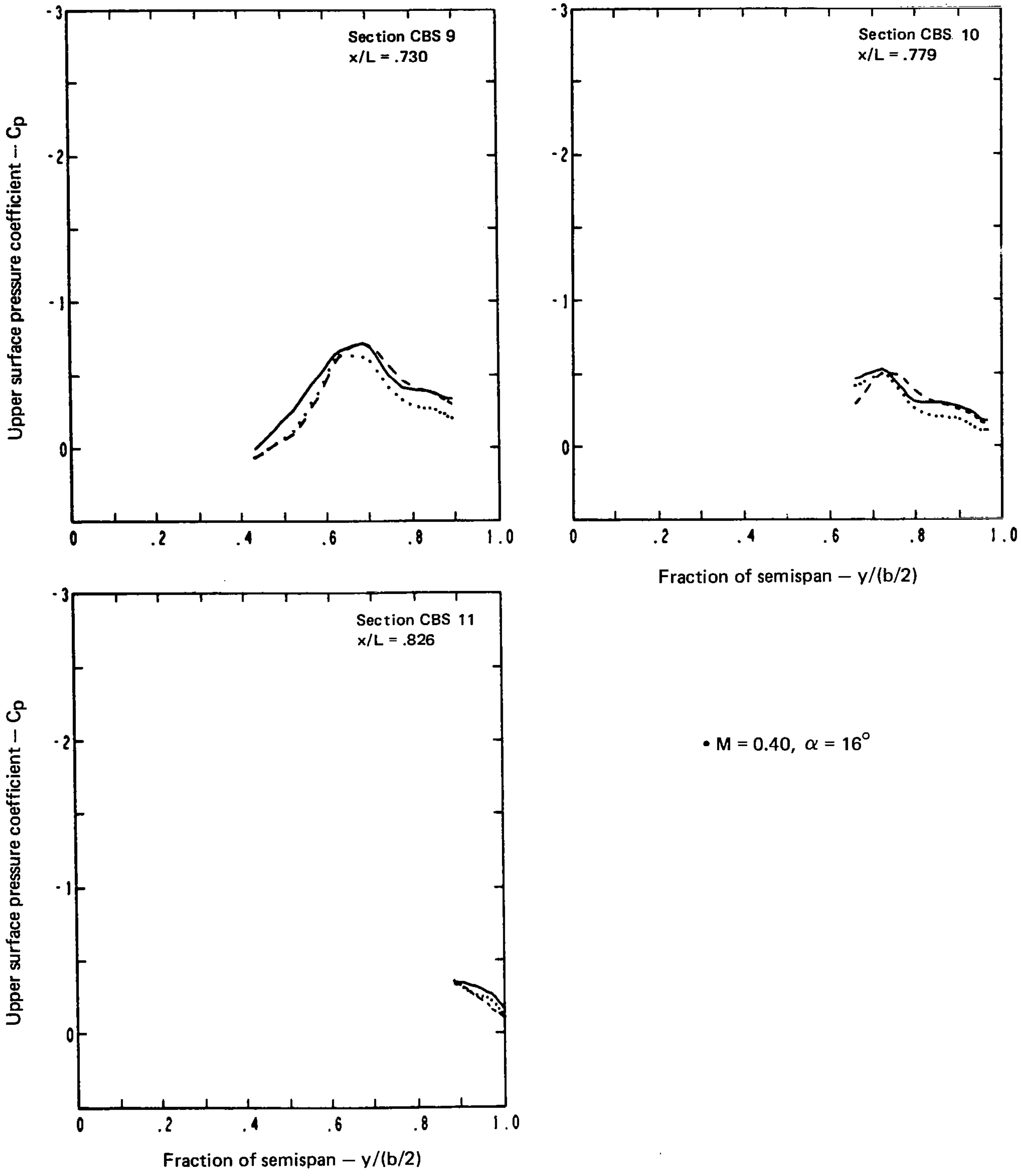

(a) (Concluded)

Figure 17.—Continued)

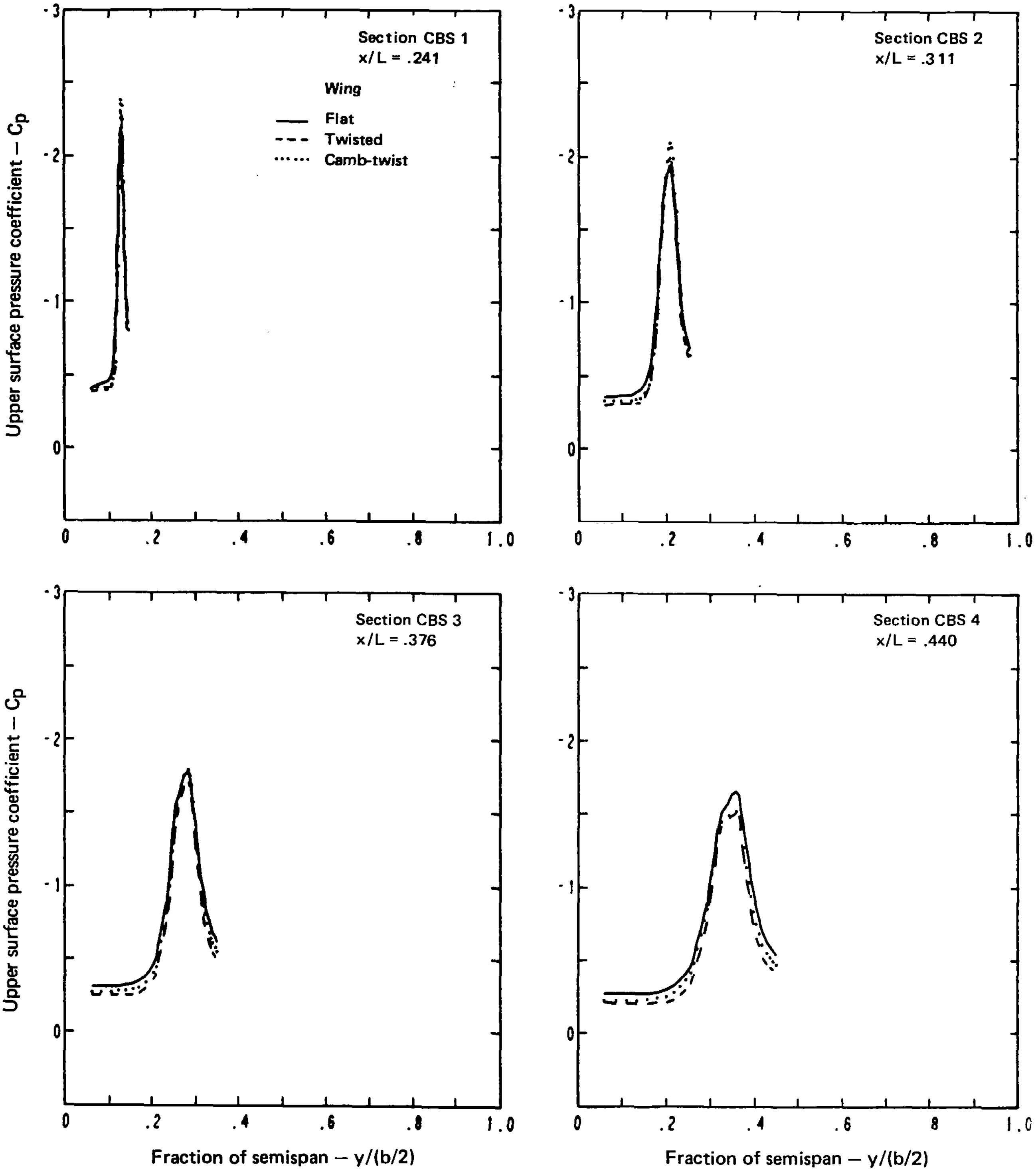

(b) Theoretical Predictions

Figure 17.—(Continued)

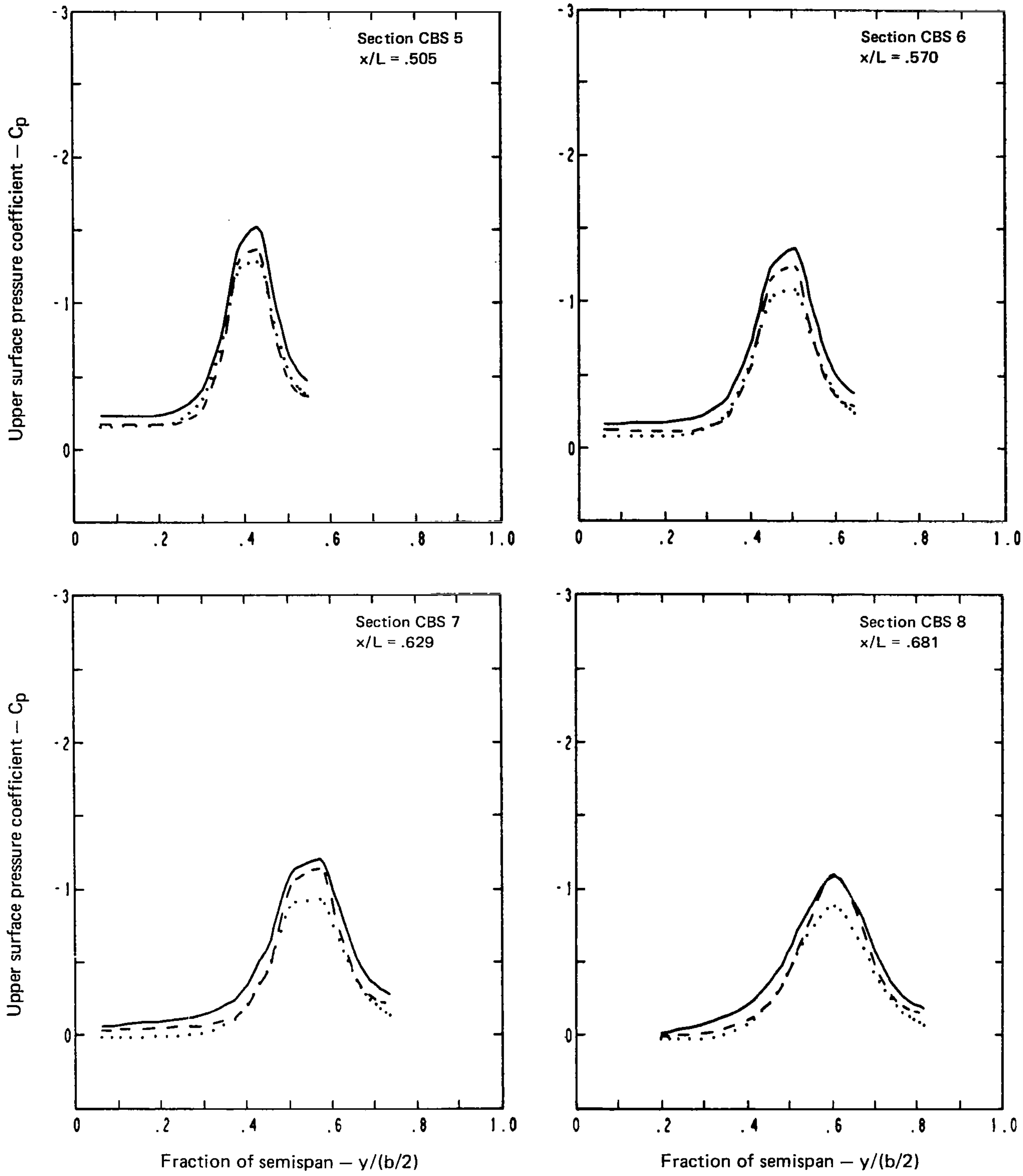

(b) (Continued)

Figure 17.—(Continued)

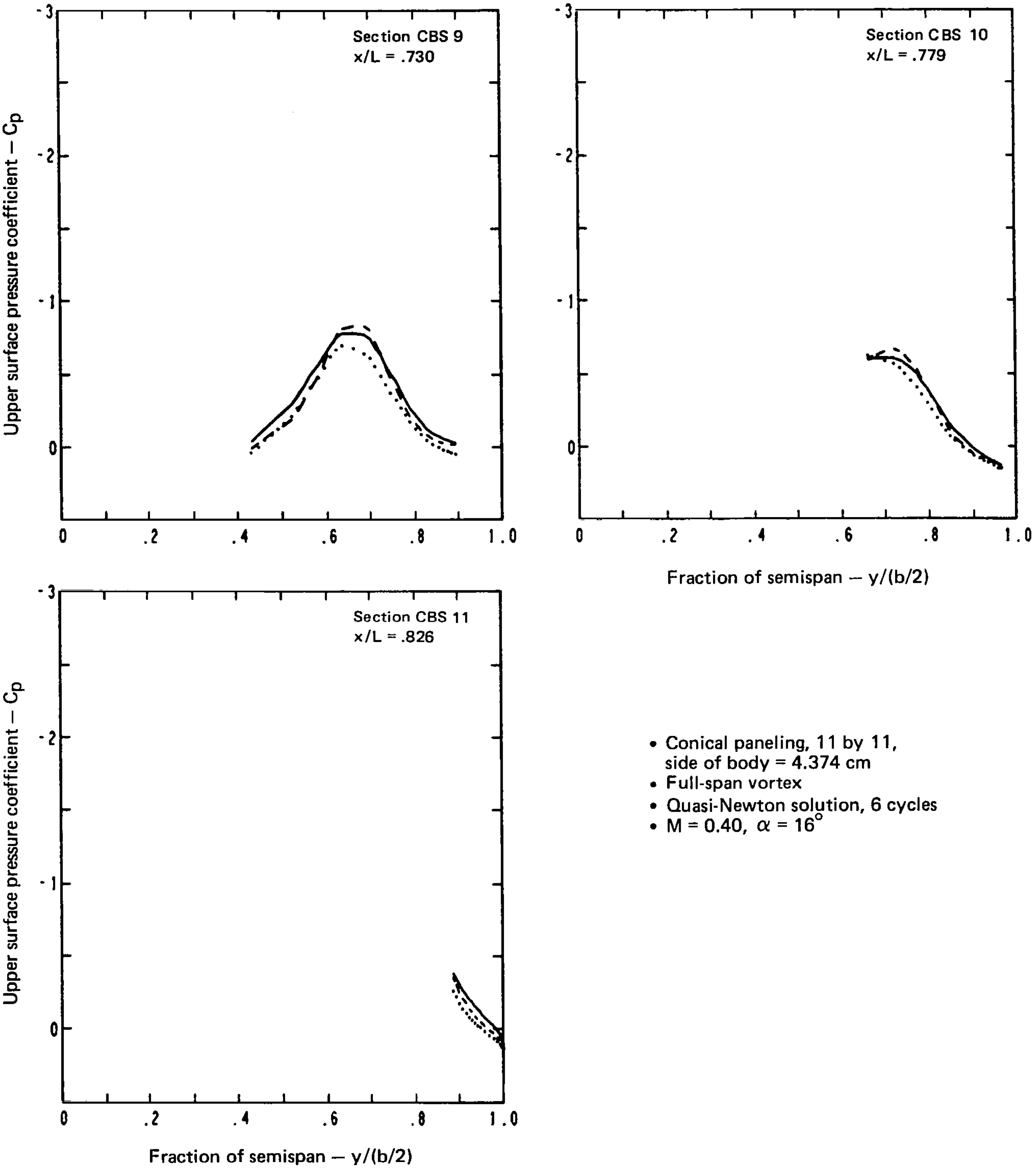

- Conical paneling, 11 by 11, side of body = 4.374 cm
- Full-span vortex
- Quasi-Newton solution, 6 cycles
- M = 0.40, $\alpha = 16^\circ$

(b) (Concluded)

Figure 17.—(Concluded)

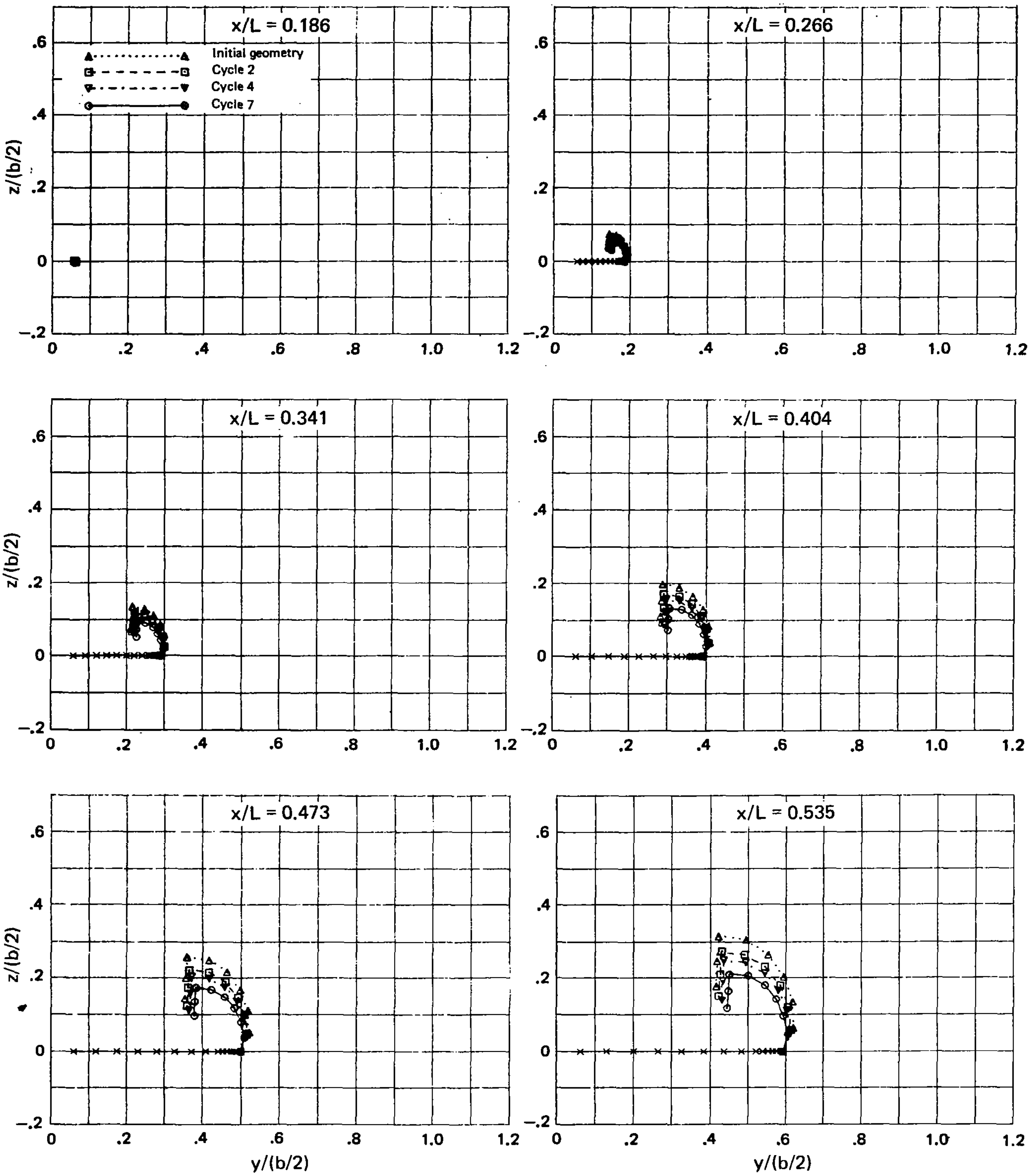

Figure 18.—Geometry of Panel Edges at Constant Body Stations, Flat Wing, Zero Thickness, Revised Side of Body Definition, Denser Wing Paneling, $\Delta a = 0.6$, $M = 0.40$, $\alpha = 16°$, Several Cycles

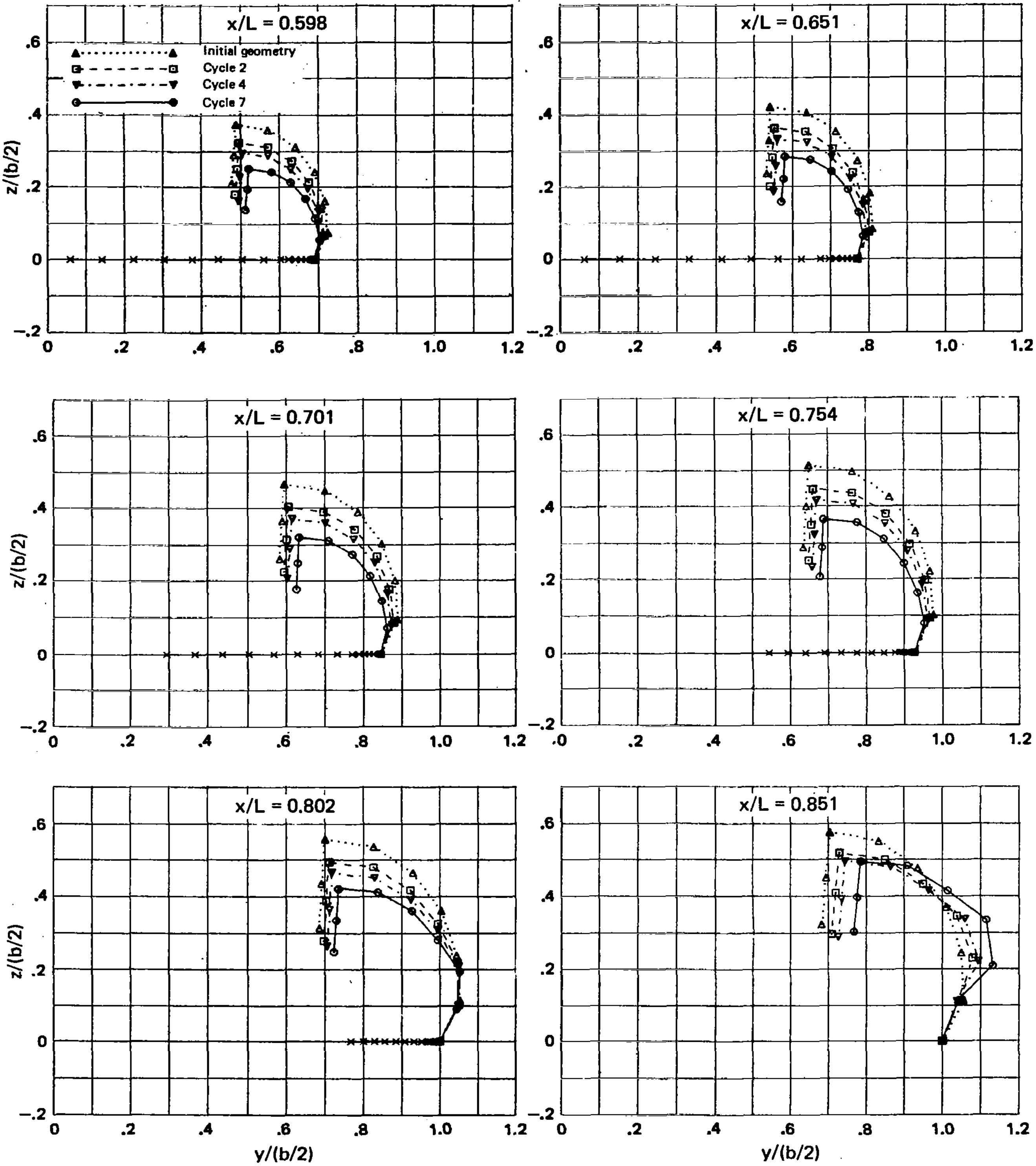

Figure 18.—(Concluded)

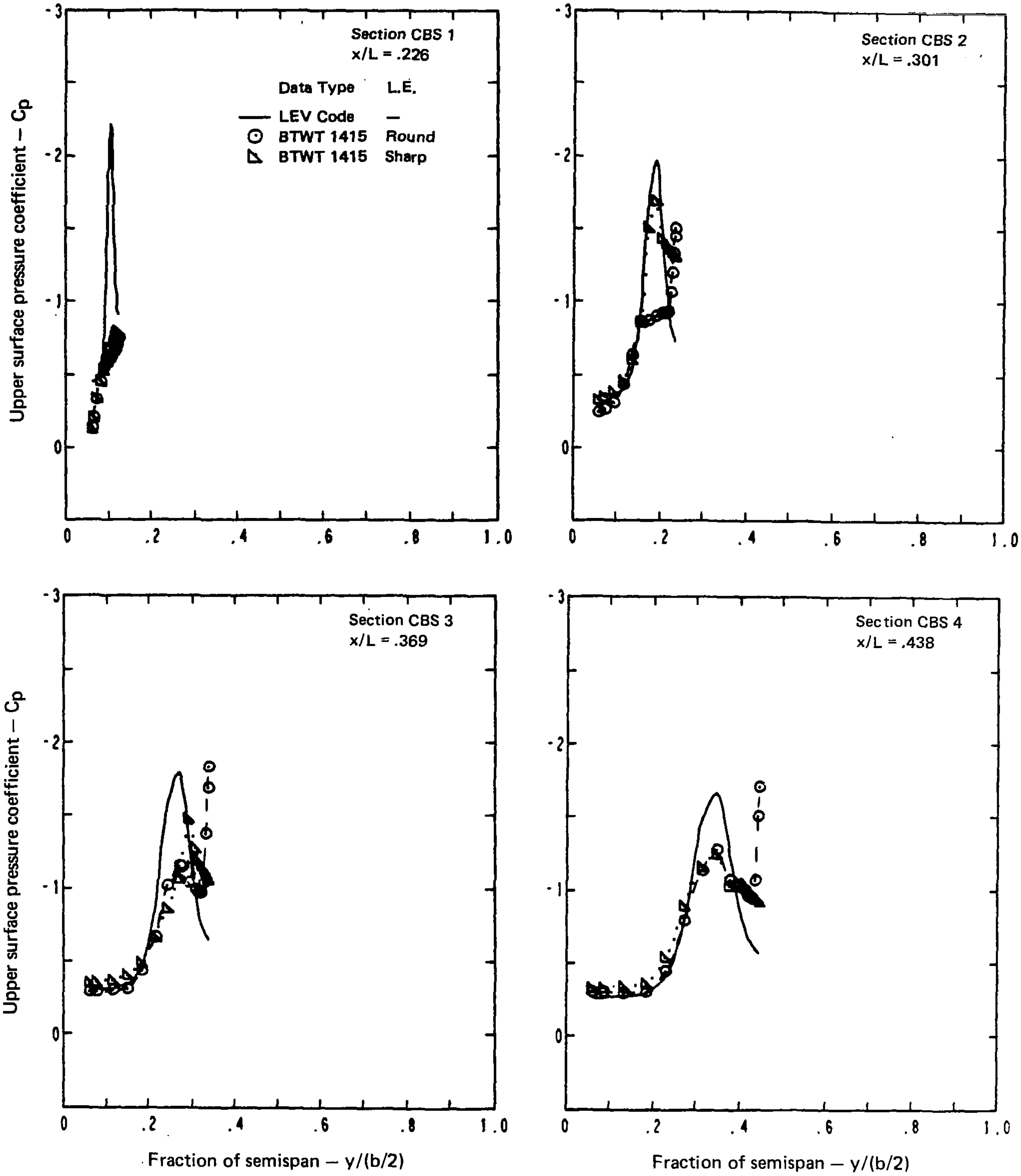

(a) Upper Surface Chordwise Pressure Distributions

Figure 19.—Pressure Distributions, Flat Wing, Zero Thickness, Revised Side of Body Definition, Denser Wing Paneling, Δ a = 0.6, M = 0.40, α = 16°

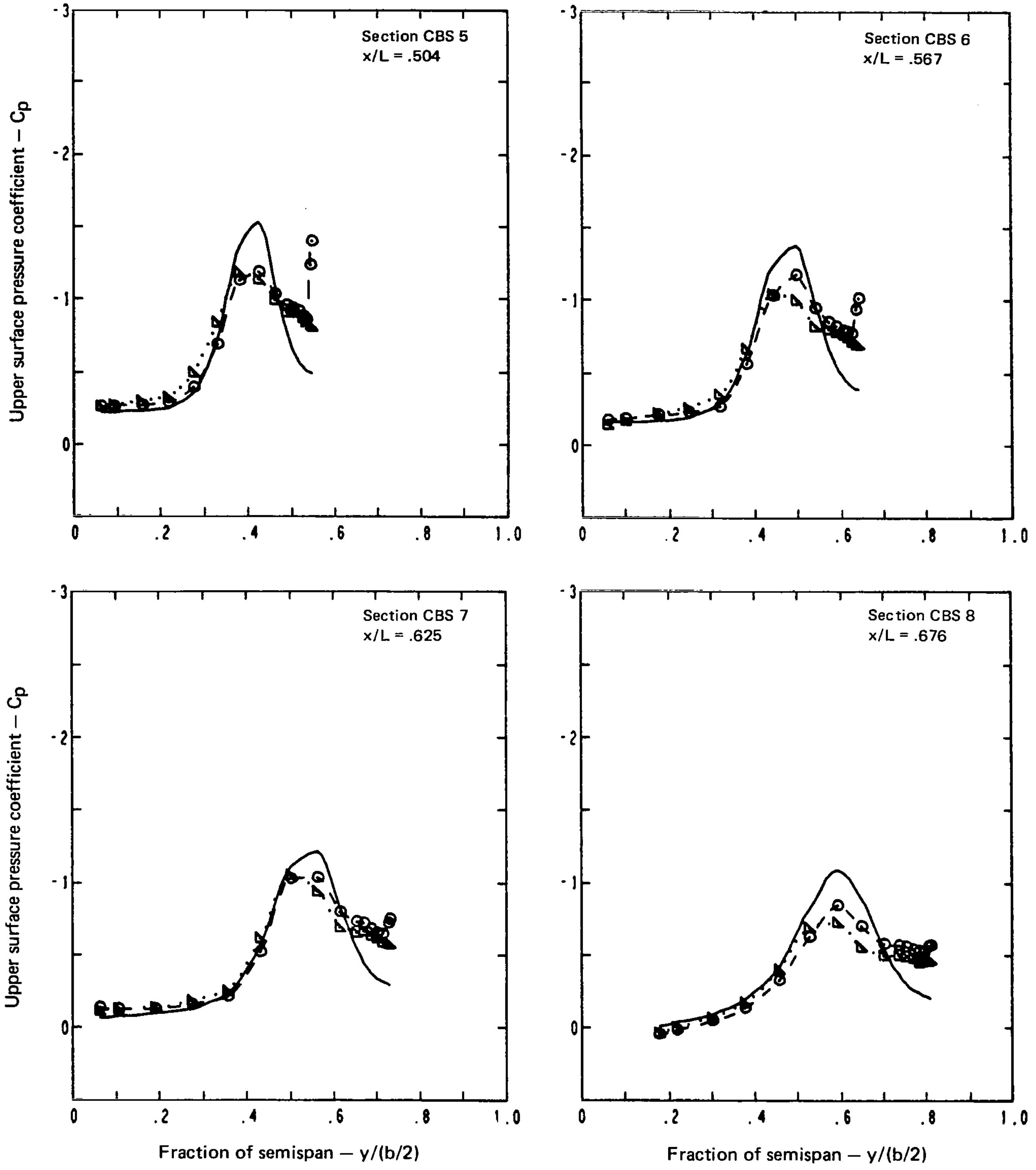

(a) (Continued)

Figure 19.—(Continued)

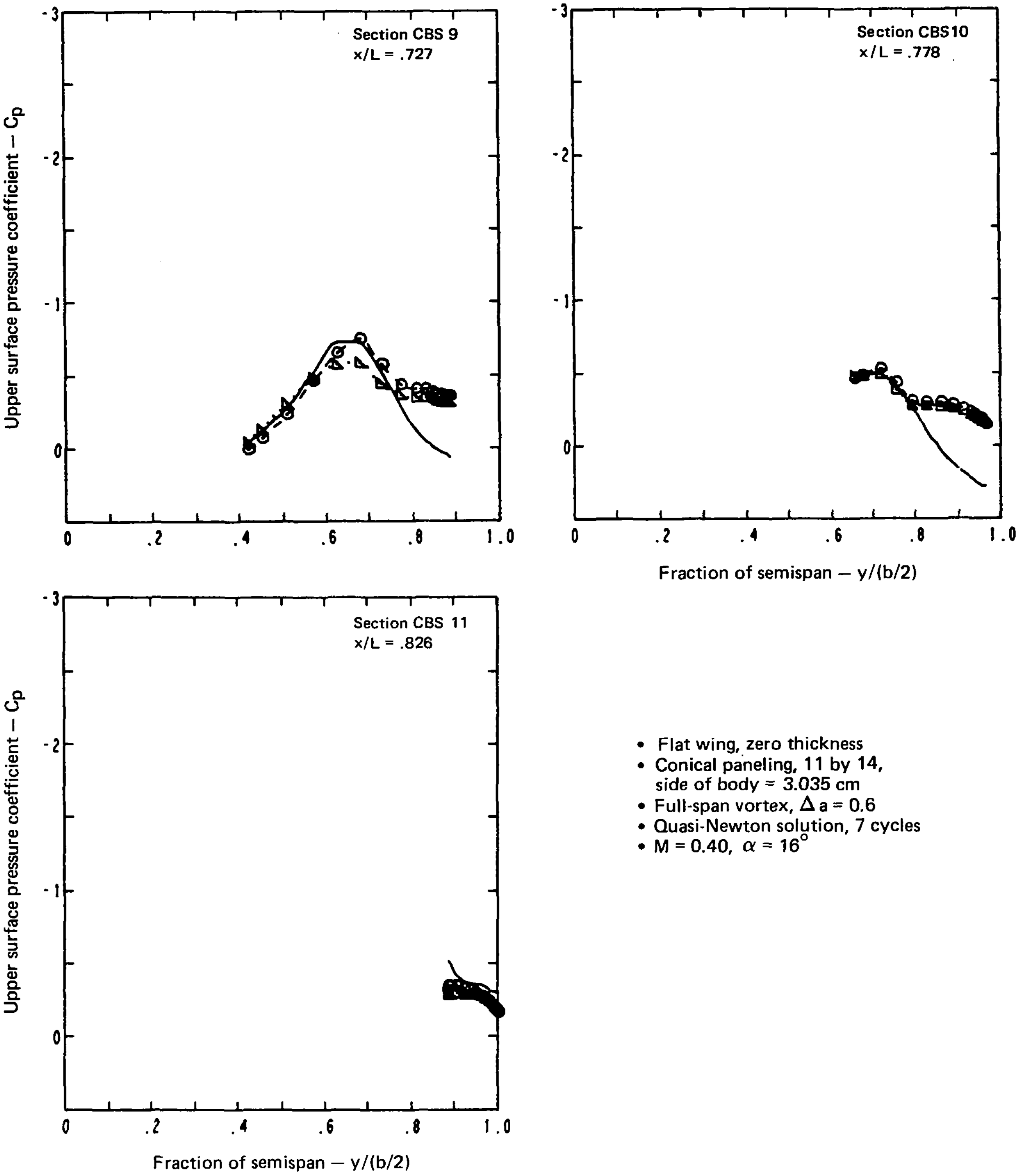

- Flat wing, zero thickness
- Conical paneling, 11 by 14, side of body = 3.035 cm
- Full-span vortex, $\Delta a = 0.6$
- Quasi-Newton solution, 7 cycles
- $M = 0.40$, $\alpha = 16^{\circ}$

(a) (Concluded)

Figure 19.—(Continued)

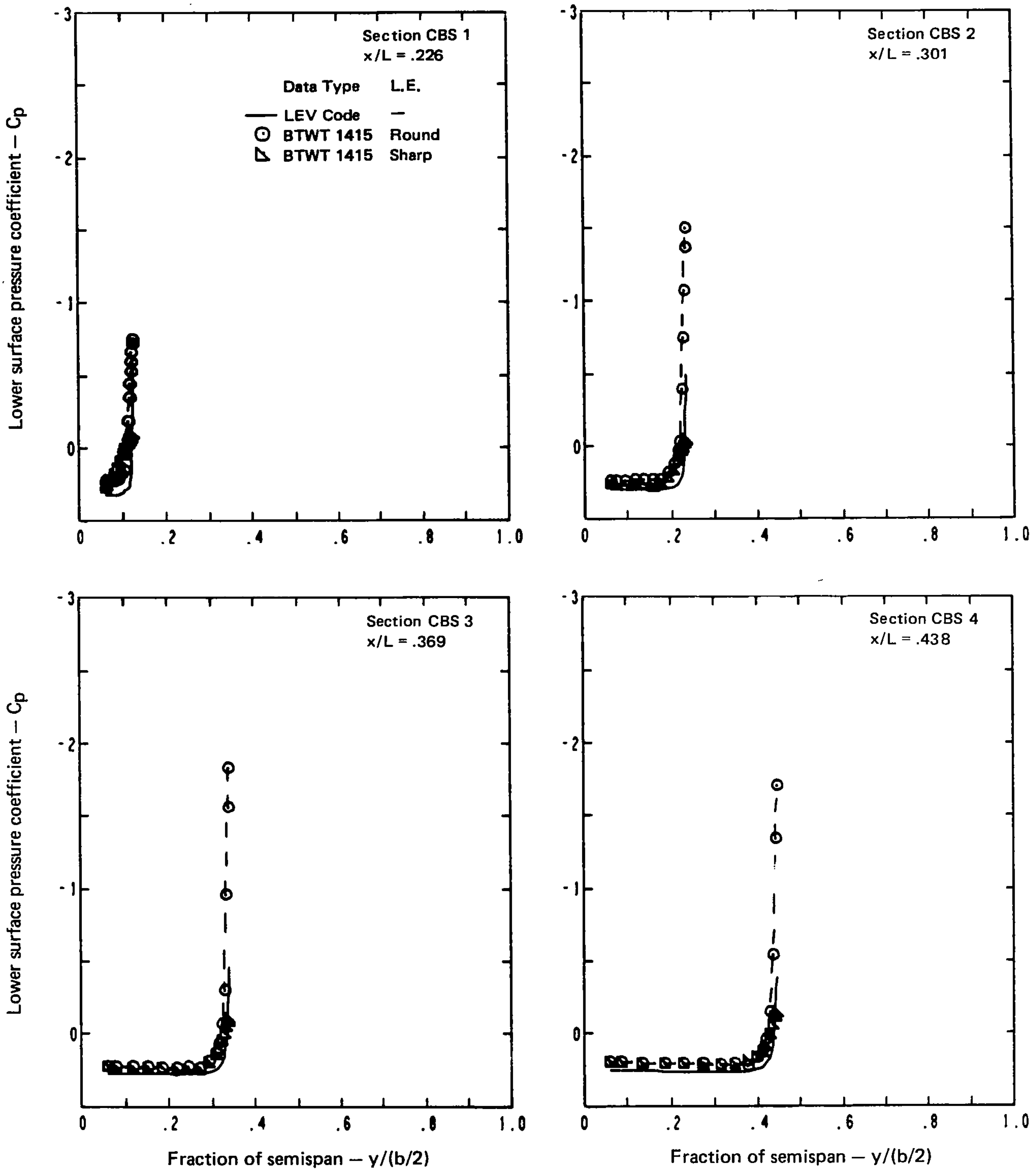

(b) Lower Surface Chordwise Pressure Distributions

Figure 19.—(Continued)

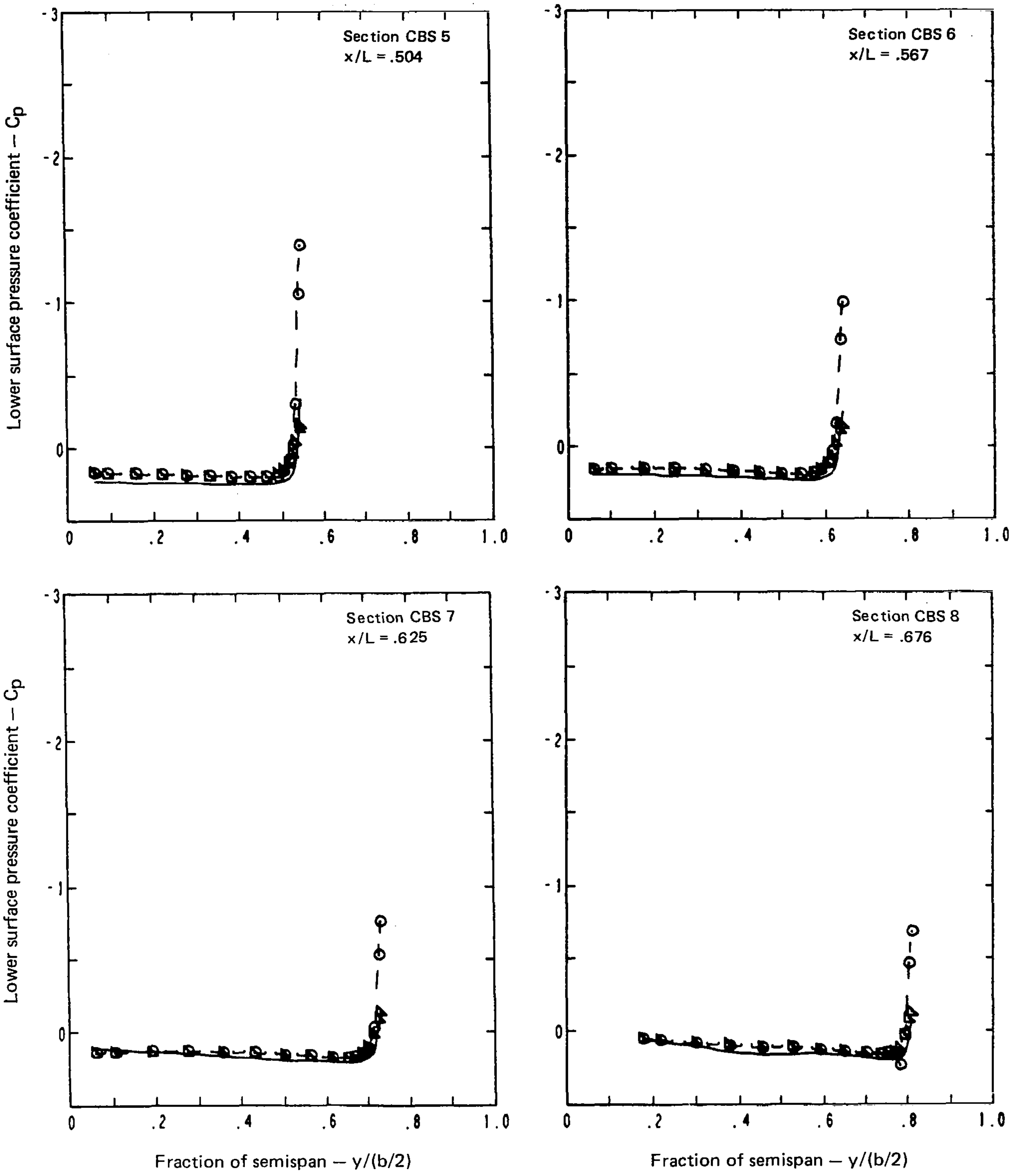

(b) (Continued)

Figure 19.—(Continued)

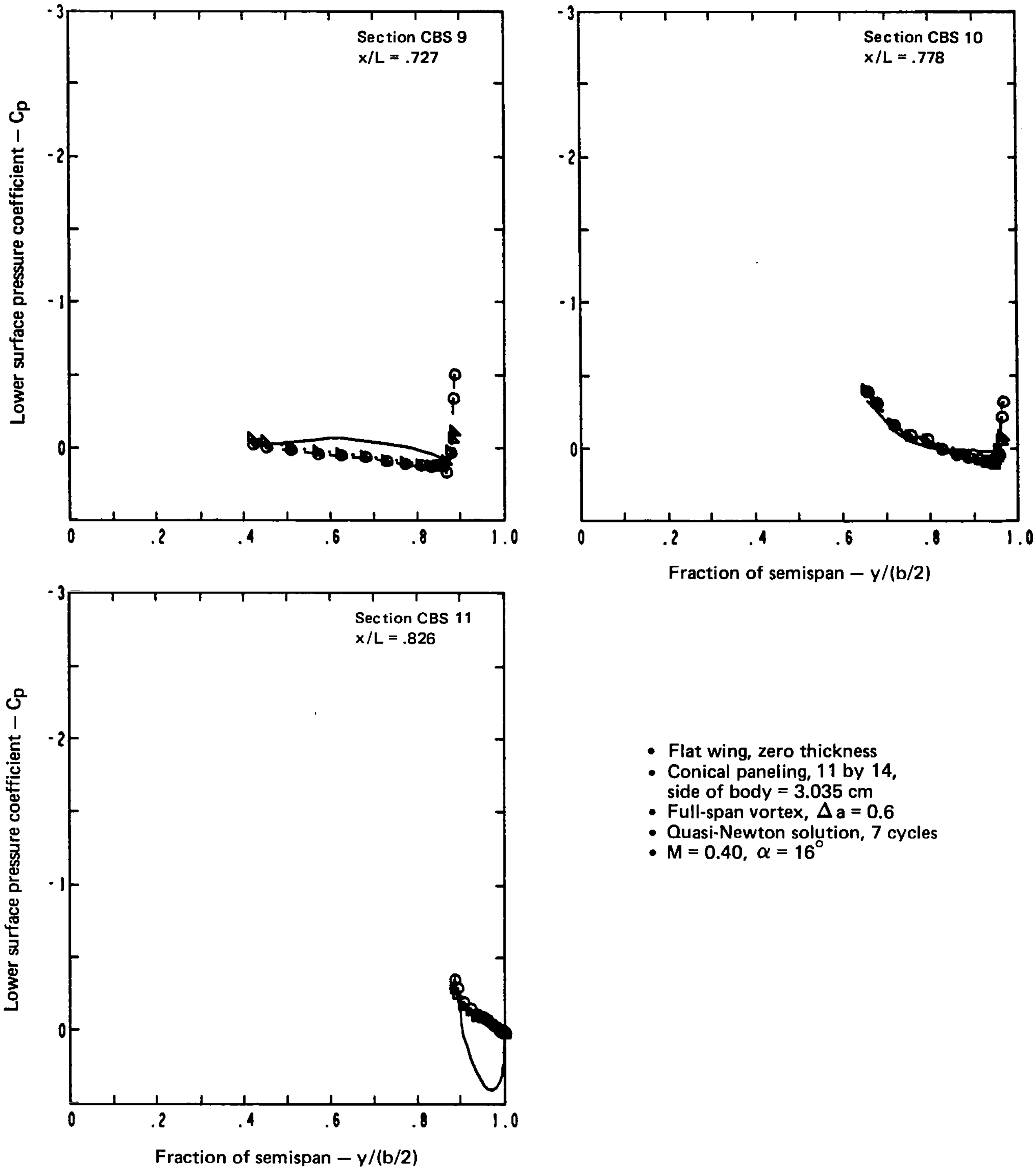

- Flat wing, zero thickness
- Conical paneling, 11 by 14, side of body = 3.035 cm
- Full-span vortex, $\Delta a = 0.6$
- Quasi-Newton solution, 7 cycles
- $M = 0.40$, $\alpha = 16^{\circ}$

(b) (Concluded)

Figure 19.—(Continued)

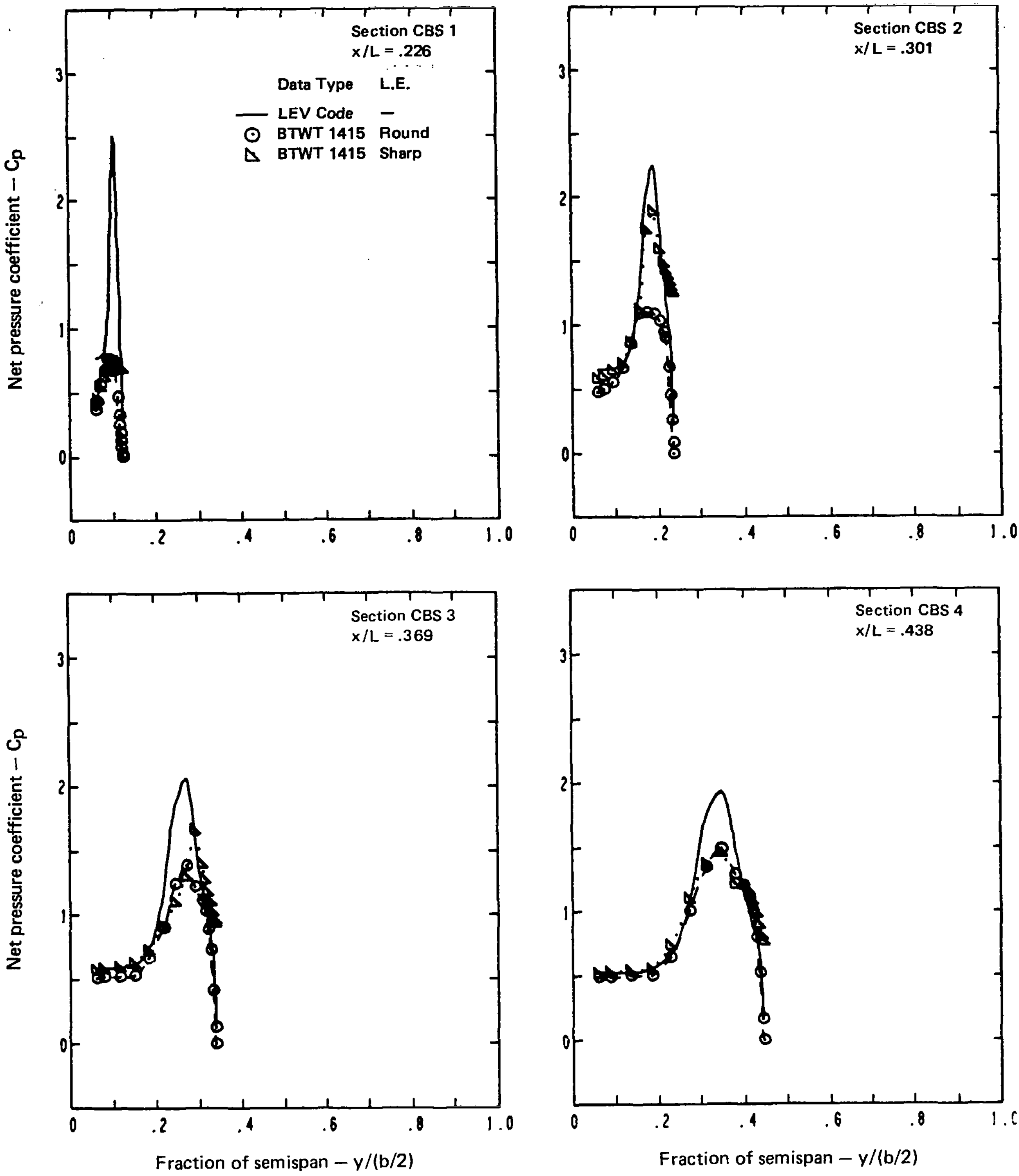

(c) Net Chordwise Pressure Distributions

Figure 19.—(Continued)

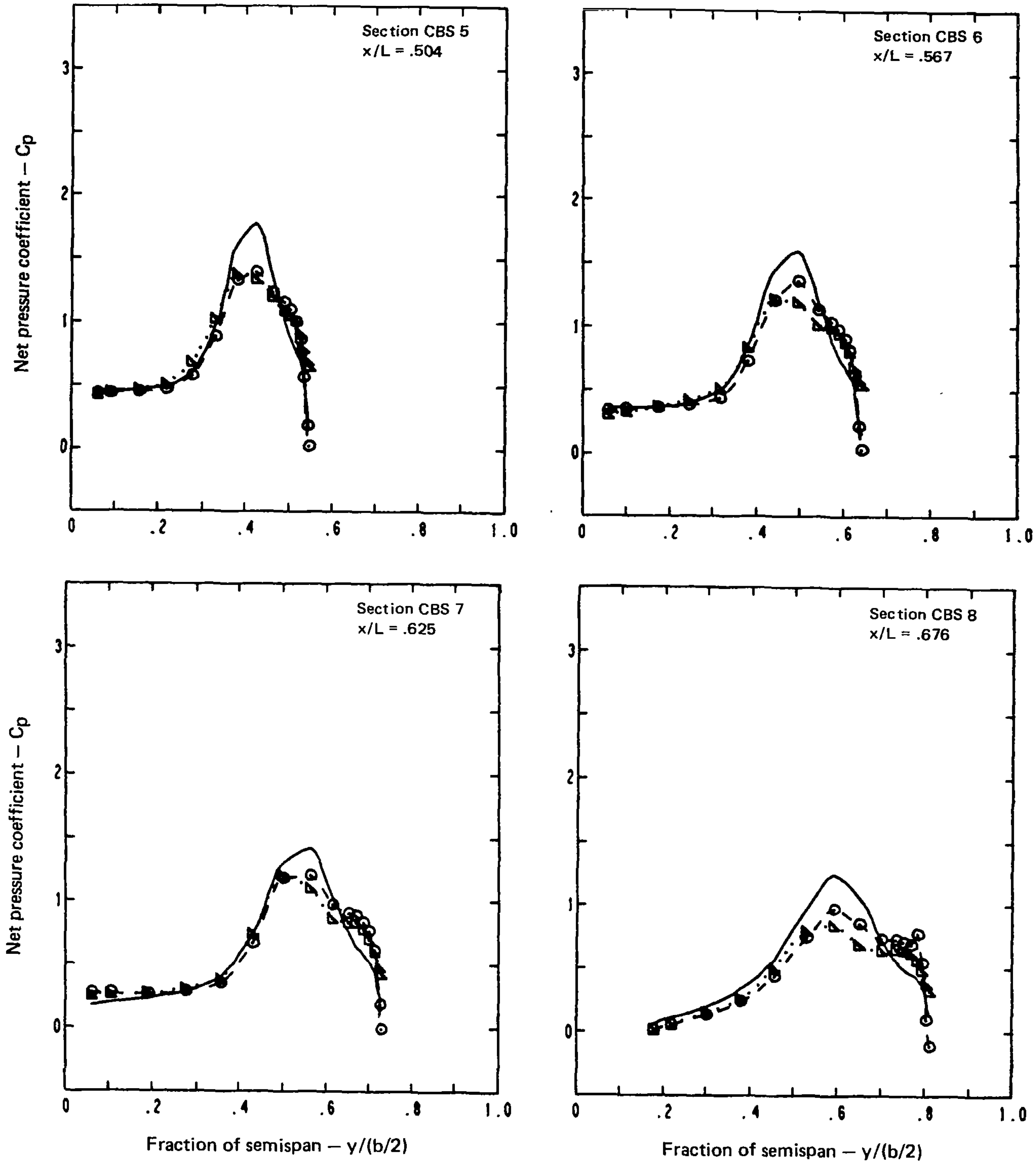

(c) (Continued)

Figure 19.—(Continued)

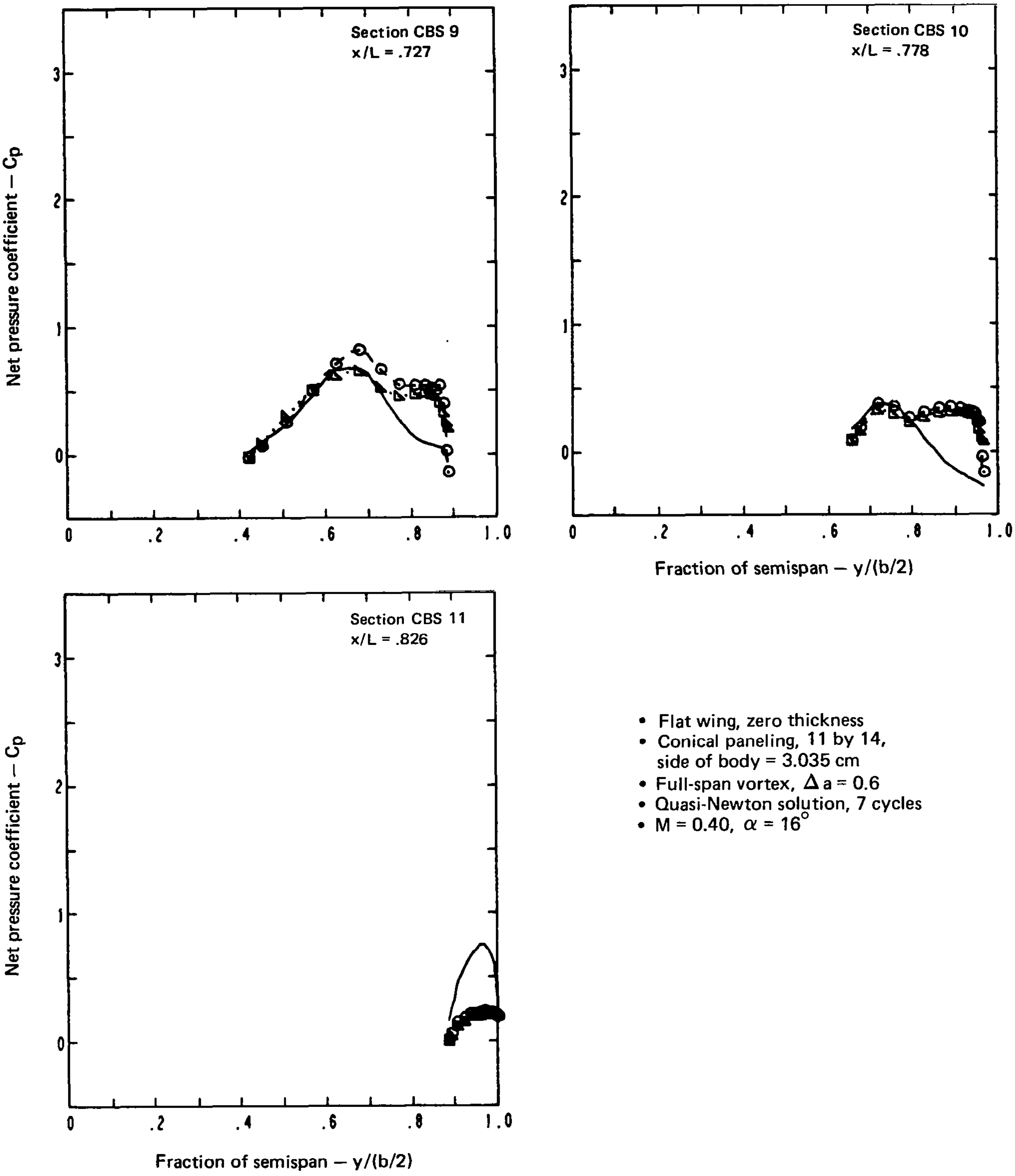

- Flat wing, zero thickness
- Conical paneling, 11 by 14, side of body = 3.035 cm
- Full-span vortex, Δa = 0.6
- Quasi-Newton solution, 7 cycles
- M = 0.40, $\alpha = 16^{\circ}$

(c) (Concluded)

Figure 19.–(Concluded)

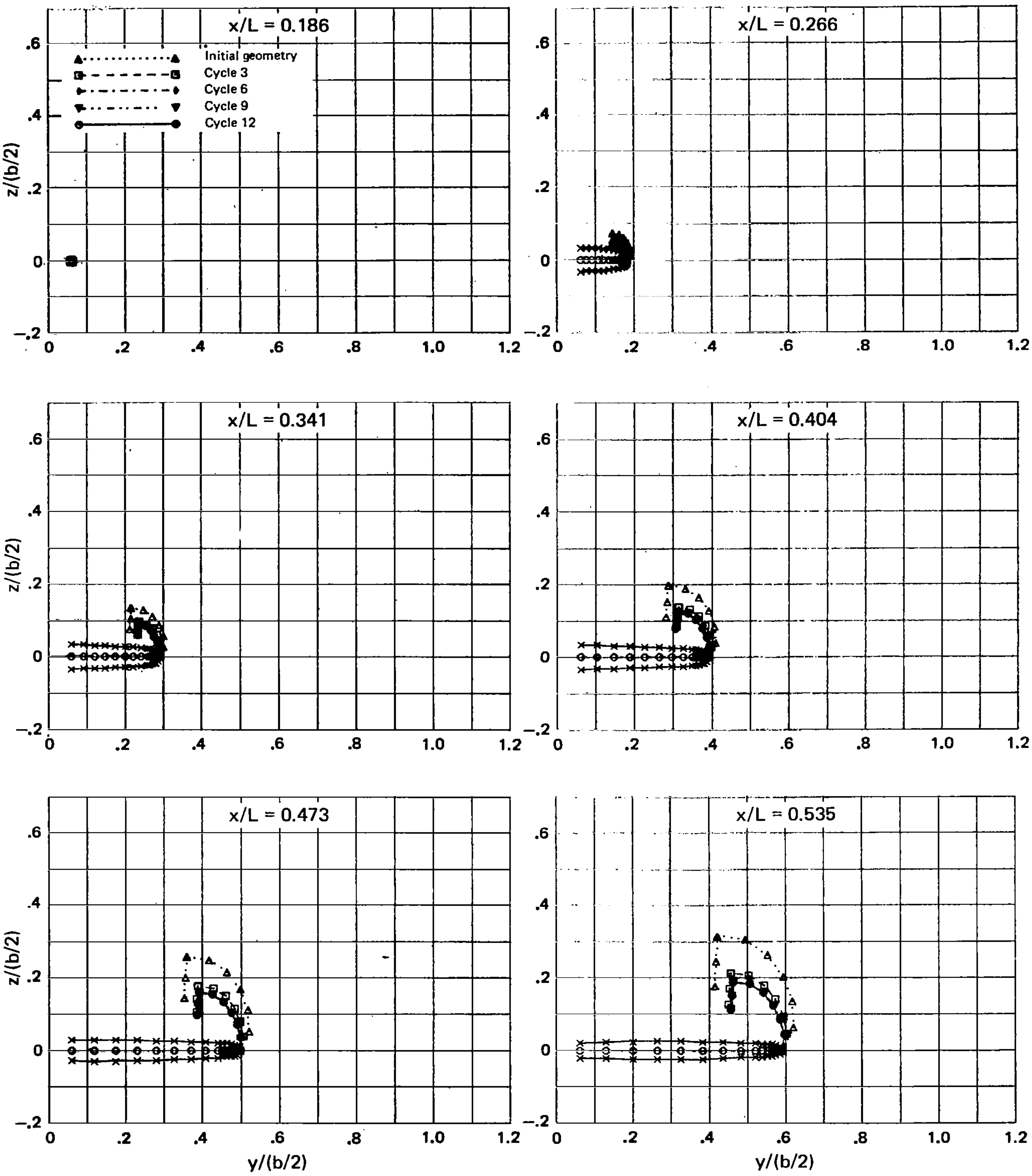

(a) All Sections at One Scale

Figure 20.—Geometry of Panel Edges at Constant Body Stations, Flat Wing With Thickness, $\Delta a = 0.6$, $M = 0.40$, $\alpha = 16°$, Several Cycles

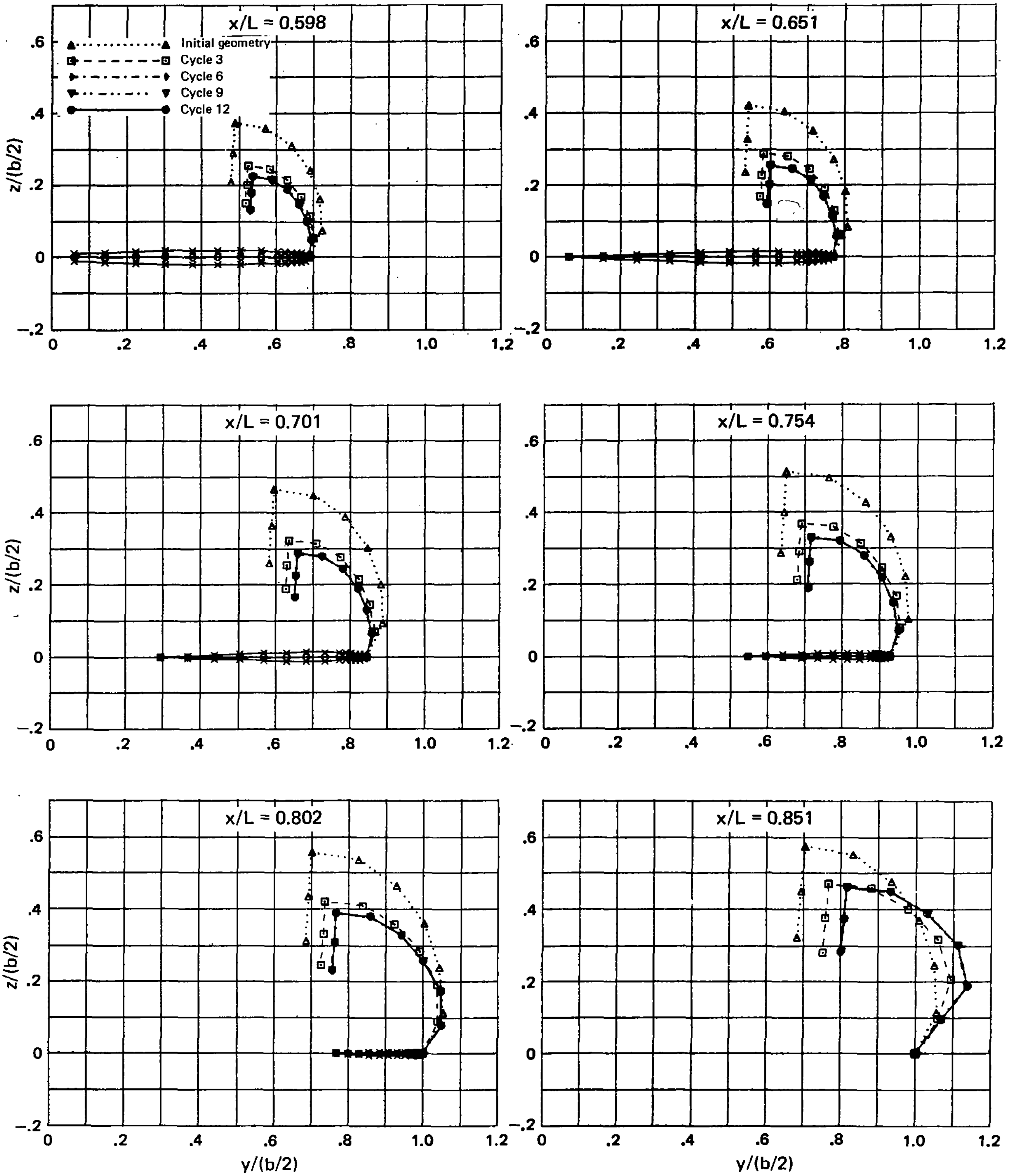

(a) Concluded

Figure 20.—(Continued)

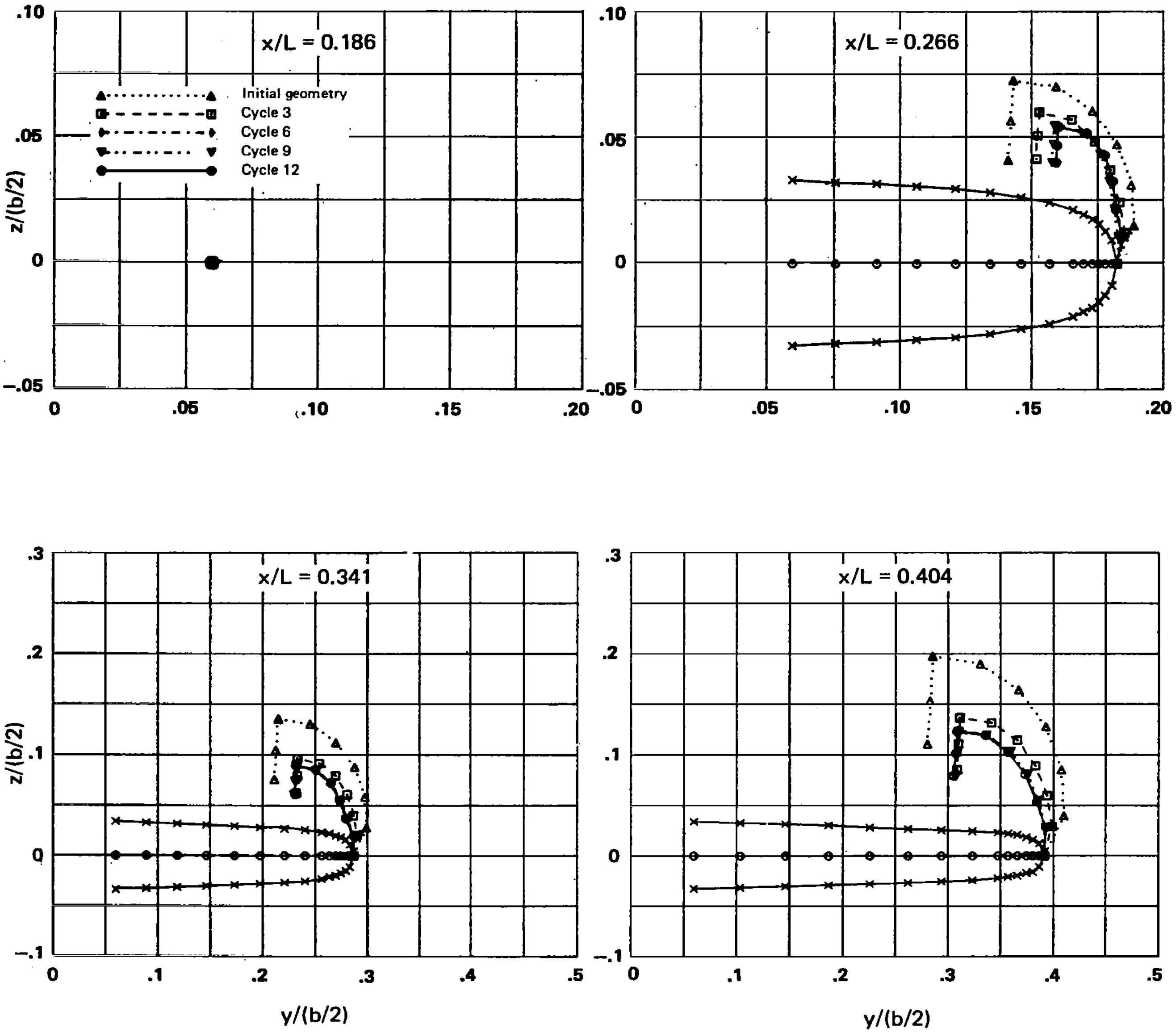

(b) Selected Enlarged Sections

Figure 20.—(Concluded)

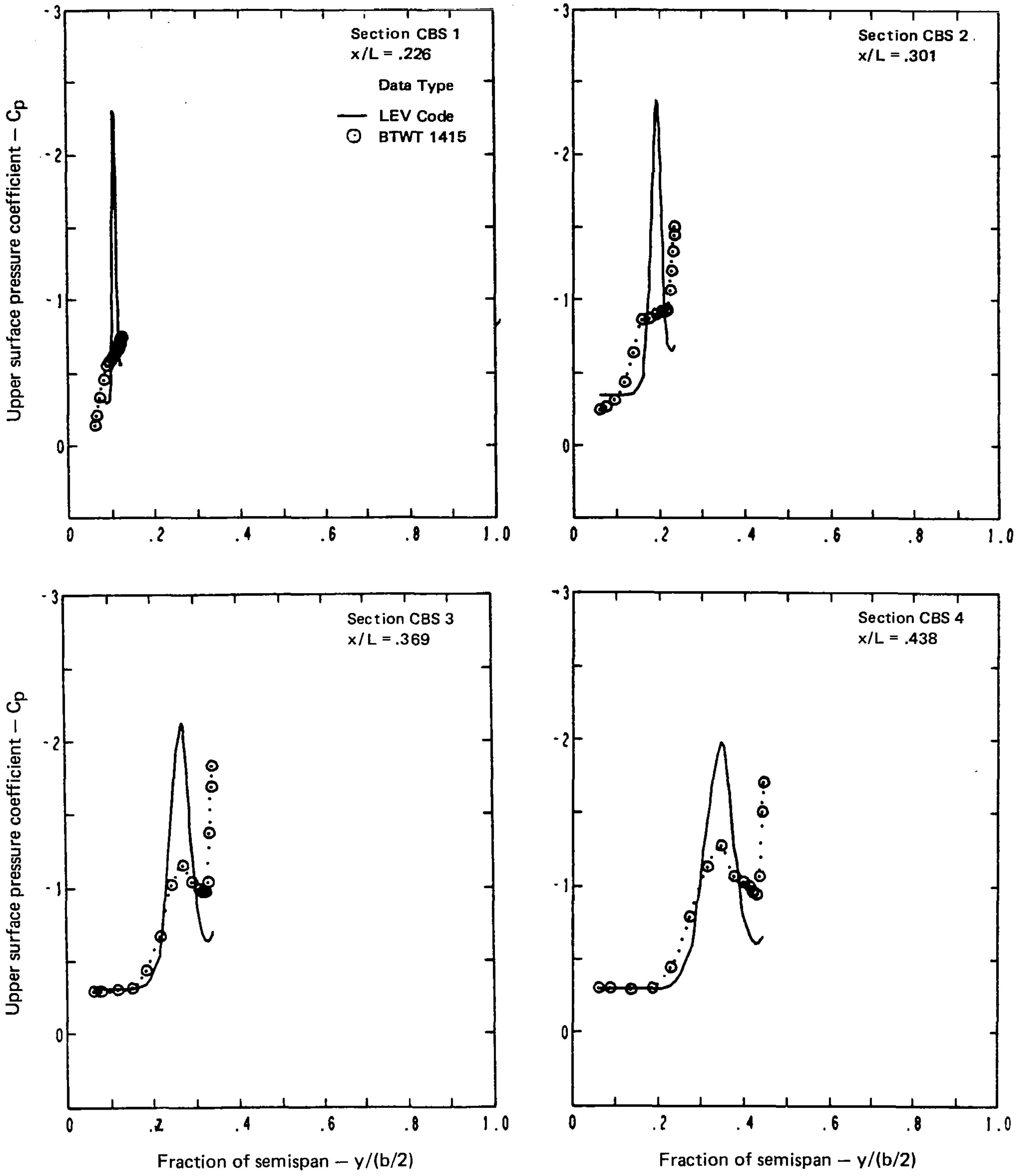

(a) Upper Surface Spanwise Pressure Distributions

Figure 21.—Upper Surface Pressure Distributions, Flat Wing With Thickness,
$\Delta a = 0.6$, $M = 0.40$, $\alpha = 16^\circ$

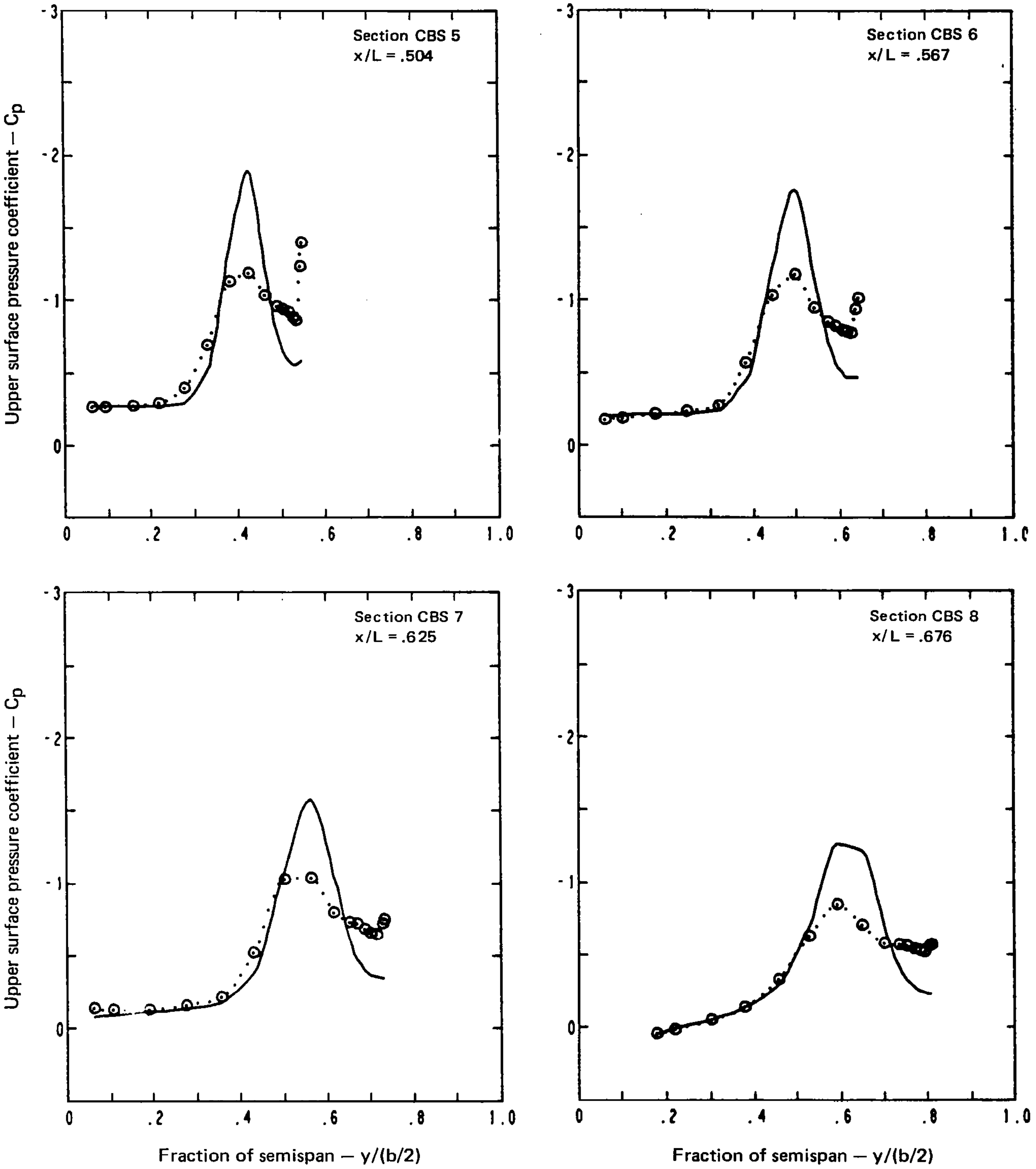

(a) (Continued)

Figure 21.—(Continued)

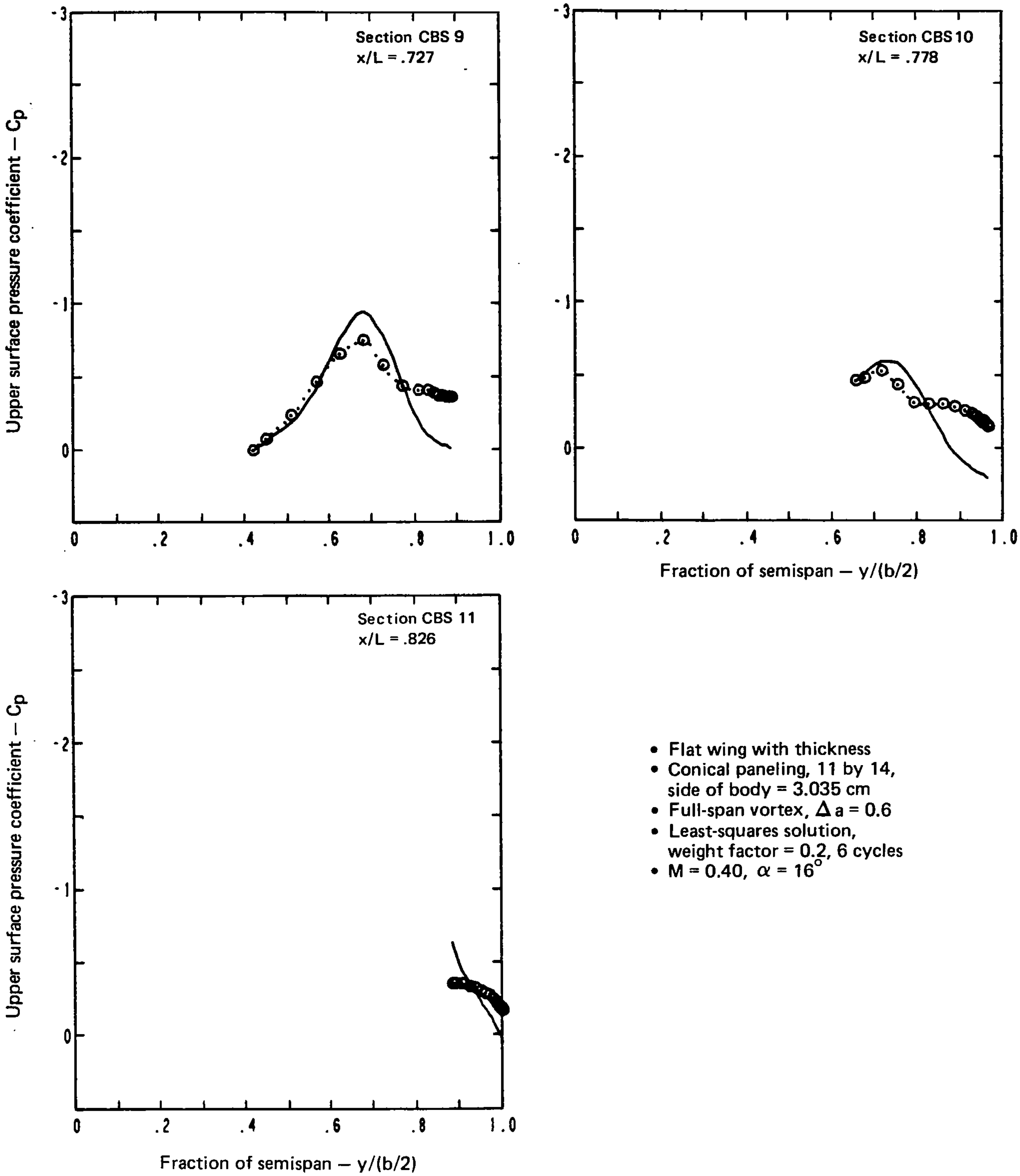

(a) (Concluded)

Figure 21.—(Continued)

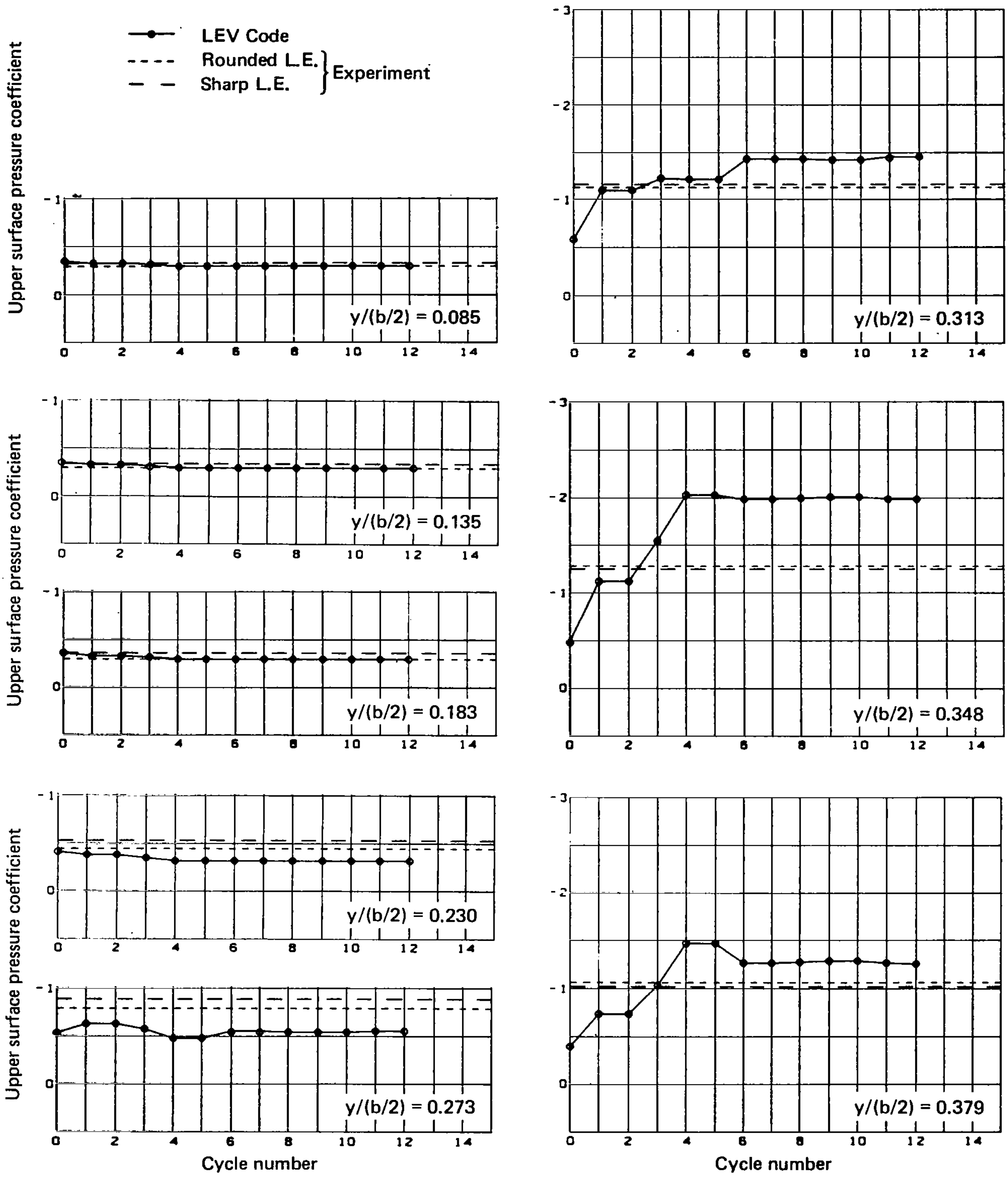

(b) Upper Surface Pressure Coefficients as a Function of Cycle, x/L = 0.438

Figure 21.—(Continued)

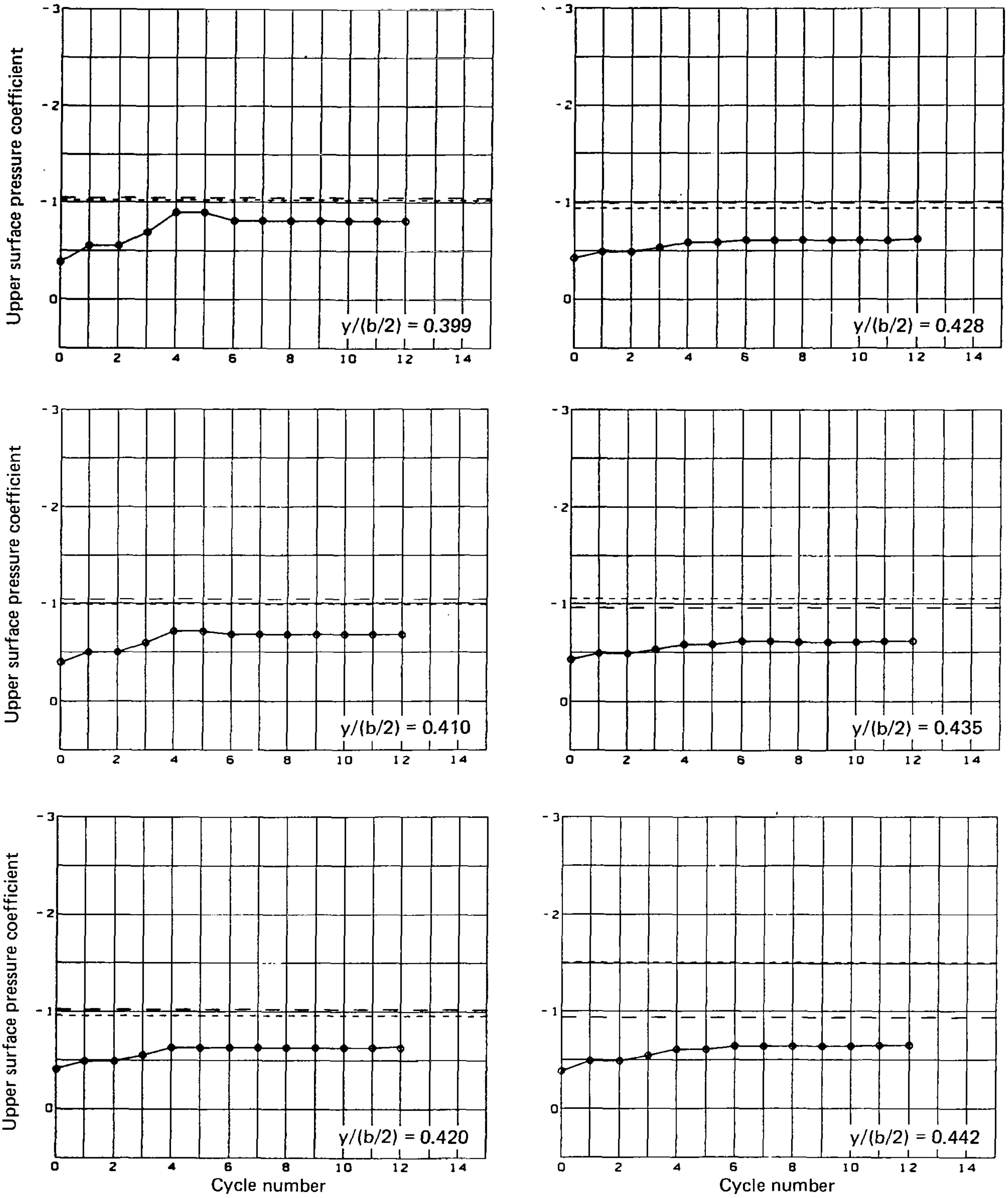

(b) (Concluded)

Figure 21.—(Concluded)

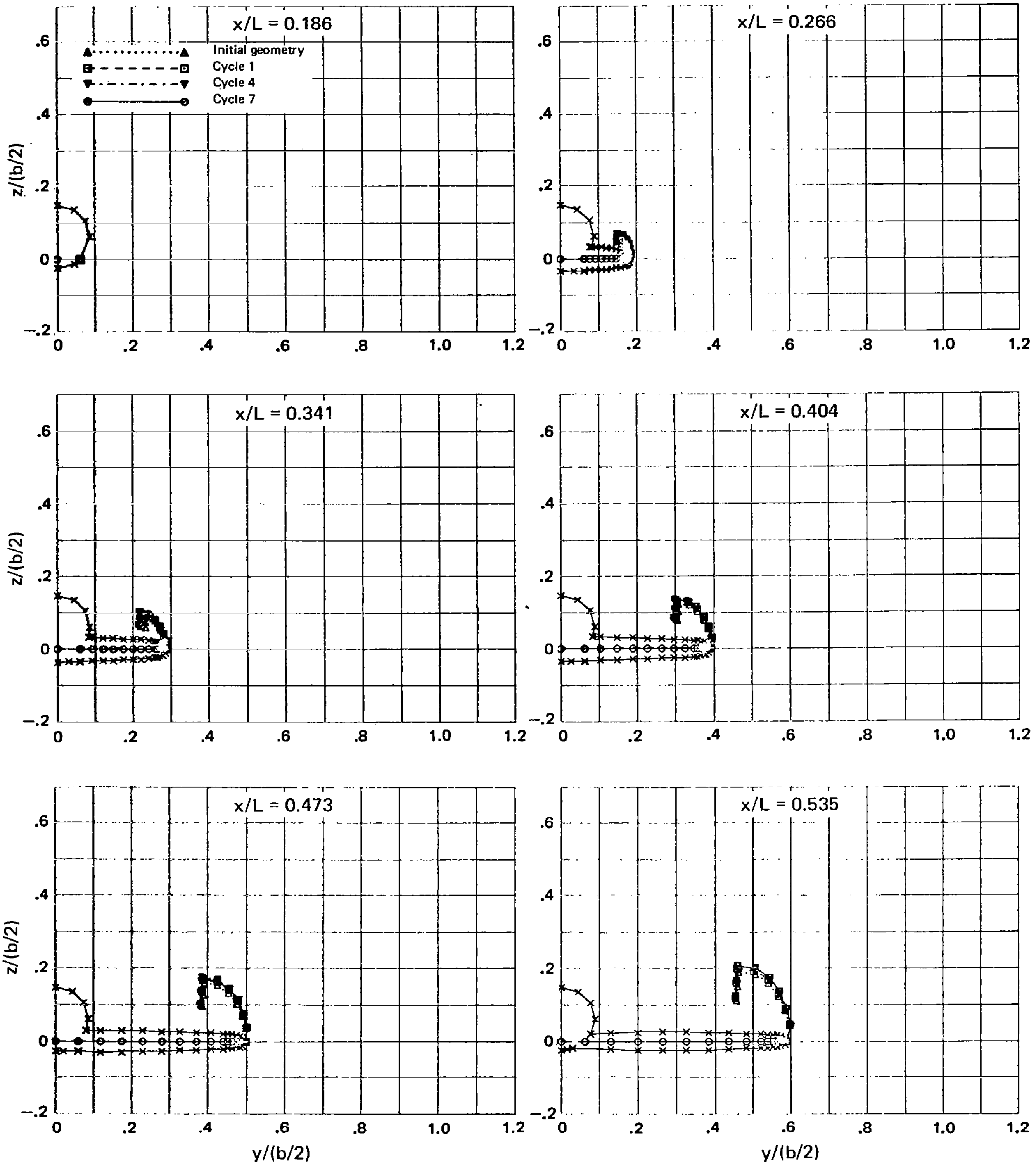

Figure 22.—Geometry of Panel Edges at Constant Body Stations, Flat Wing With Thickness and Fuselage, M = 0.40, α = 16°, Several Cycles

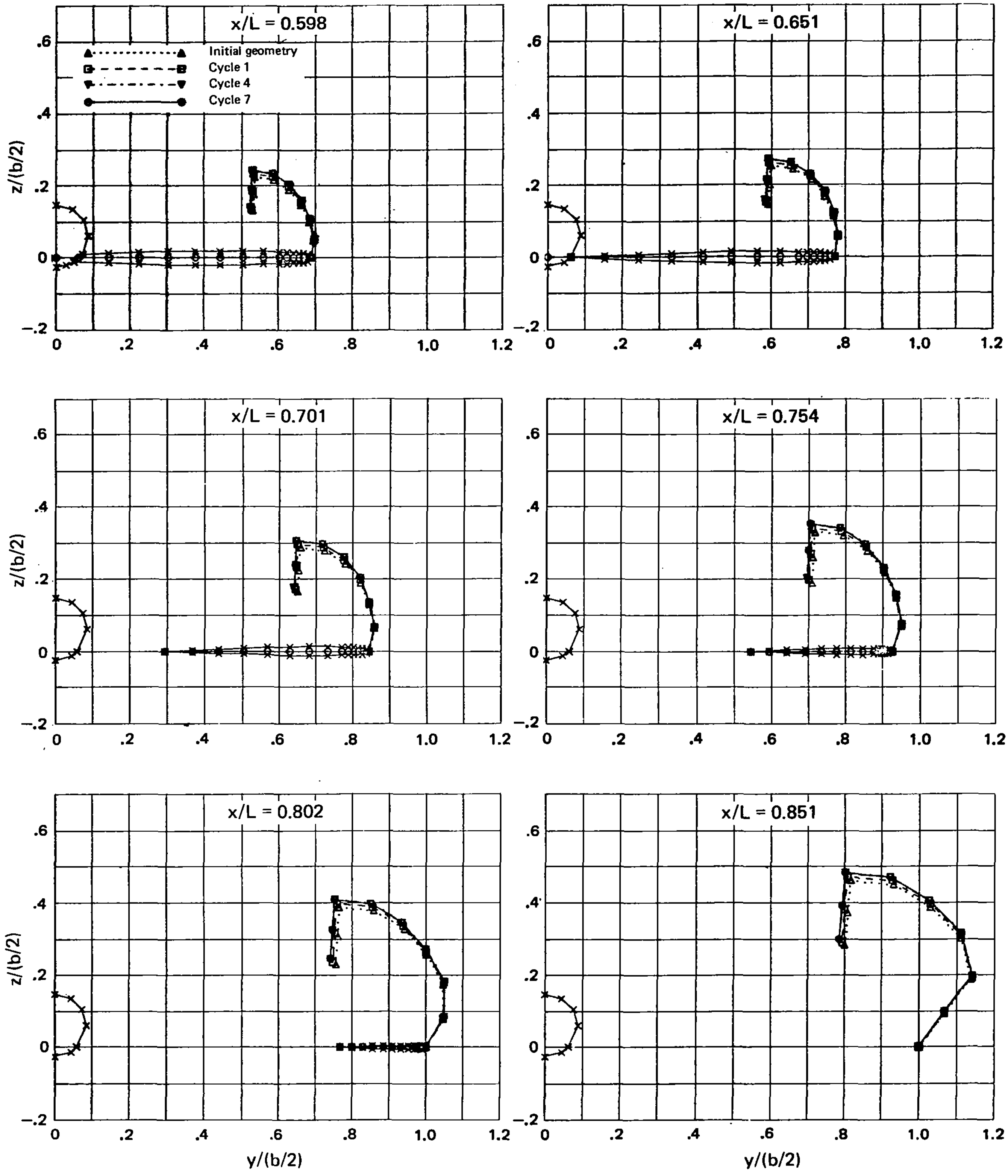

Figure 22.—(Concluded)

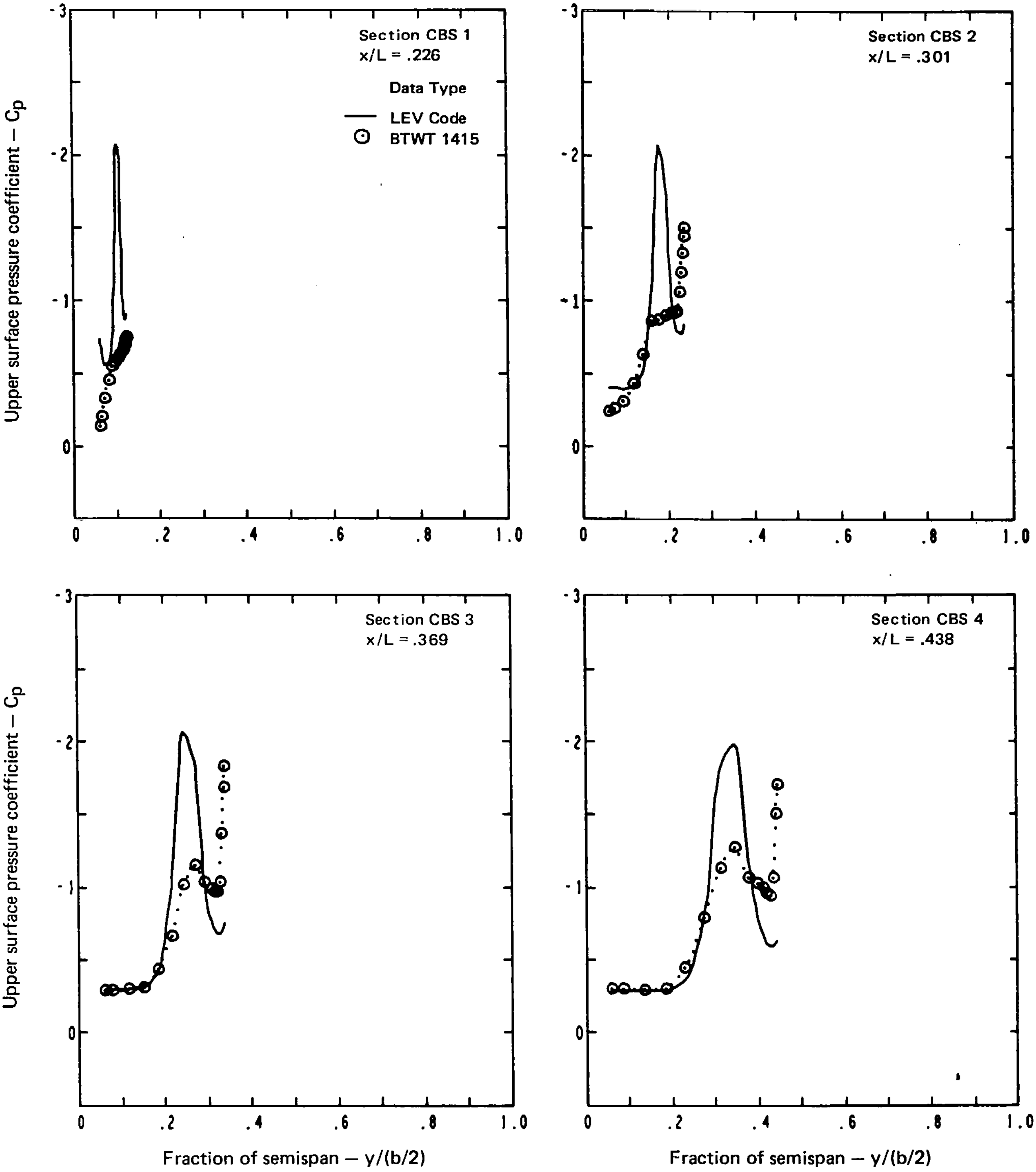

Figure 23.—Upper Surface Pressure Distributions, Flat Wing With Thickness and Fuselage, $M = 0.40$, $\alpha = 16°$

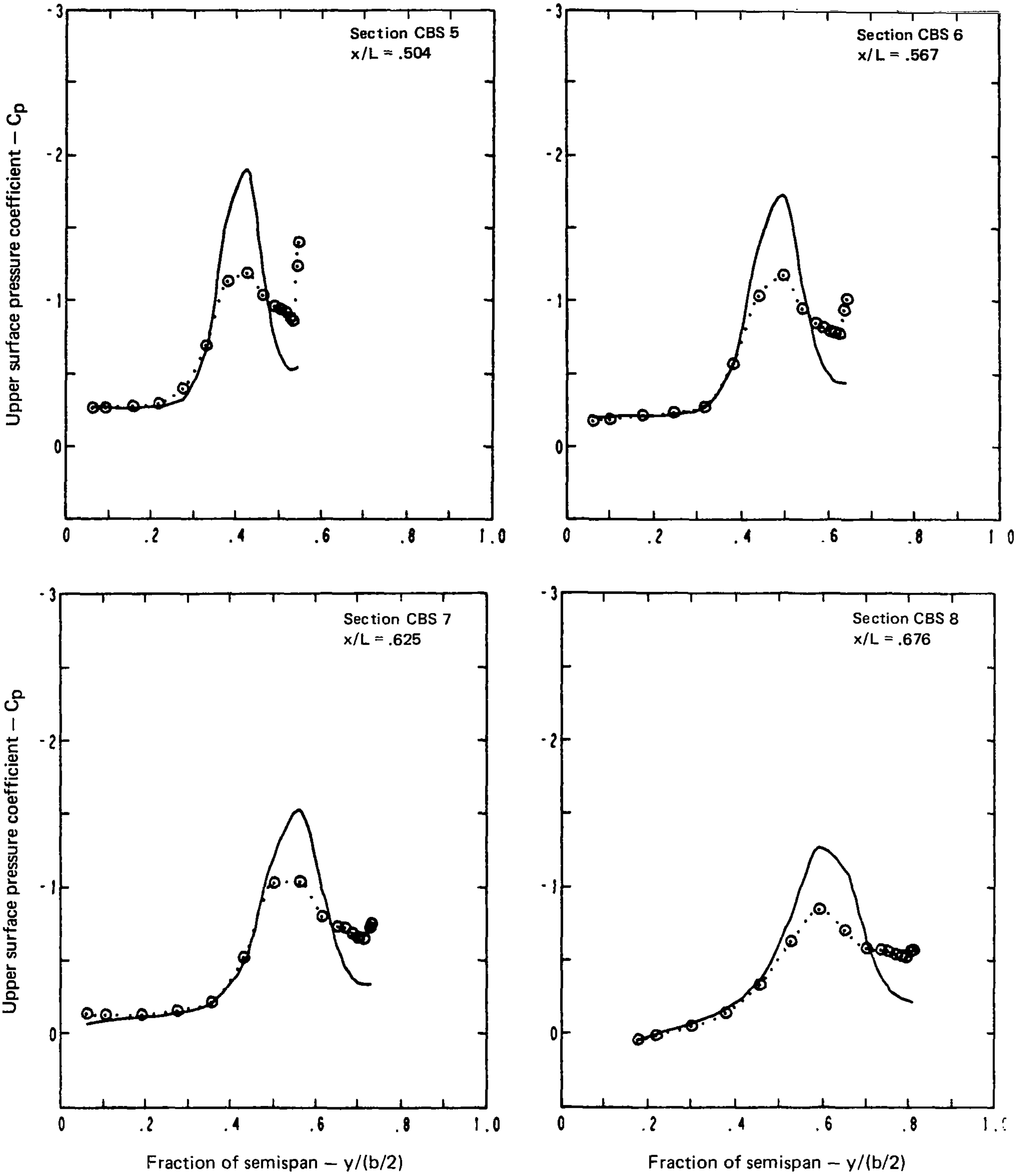

Figure 23.—(Continued)

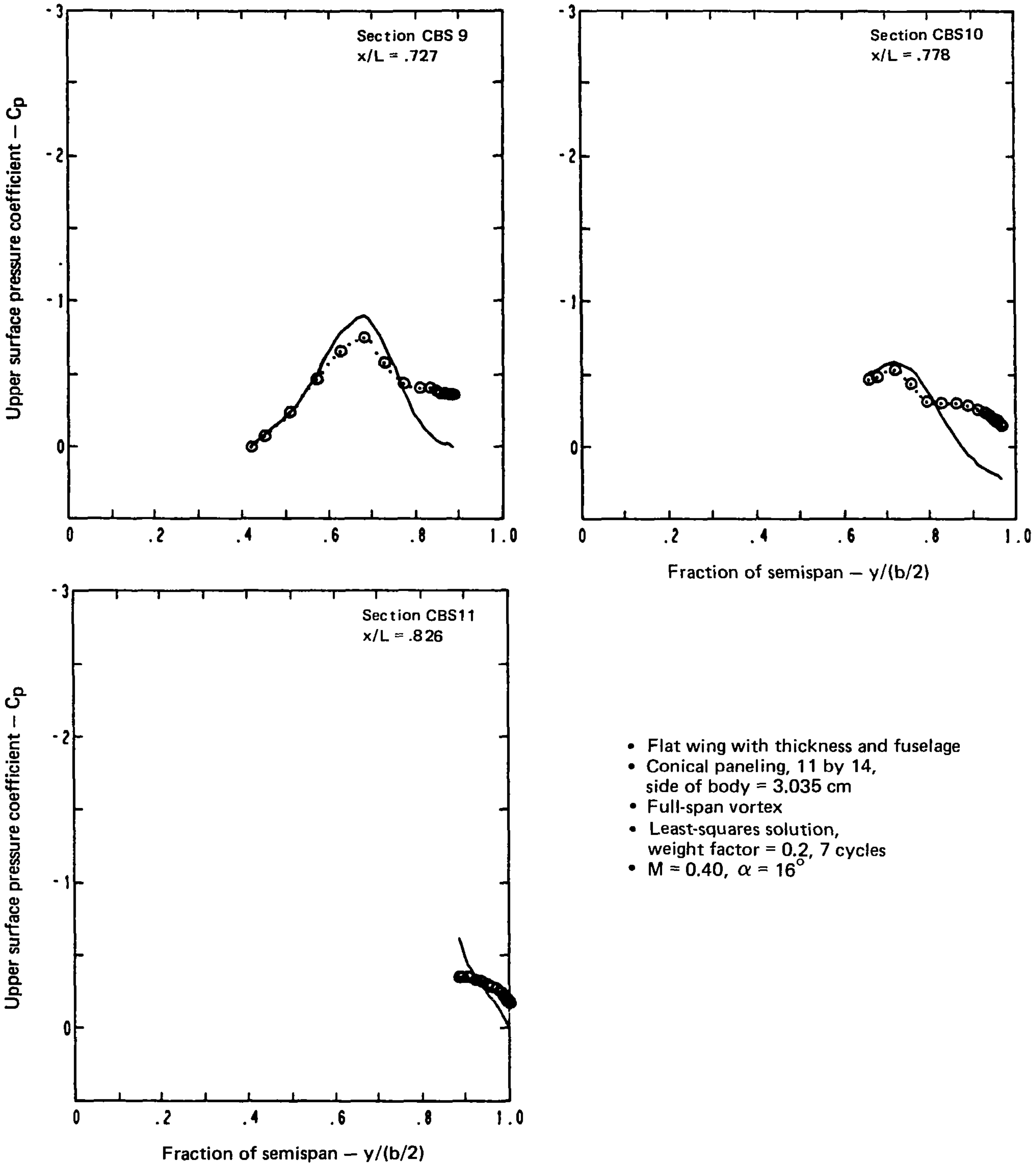

- Flat wing with thickness and fuselage
- Conical paneling, 11 by 14,
  side of body = 3.035 cm
- Full-span vortex
- Least-squares solution,
  weight factor = 0.2, 7 cycles
- $M = 0.40$, $\alpha = 16^\circ$

Figure 23.—(Concluded)

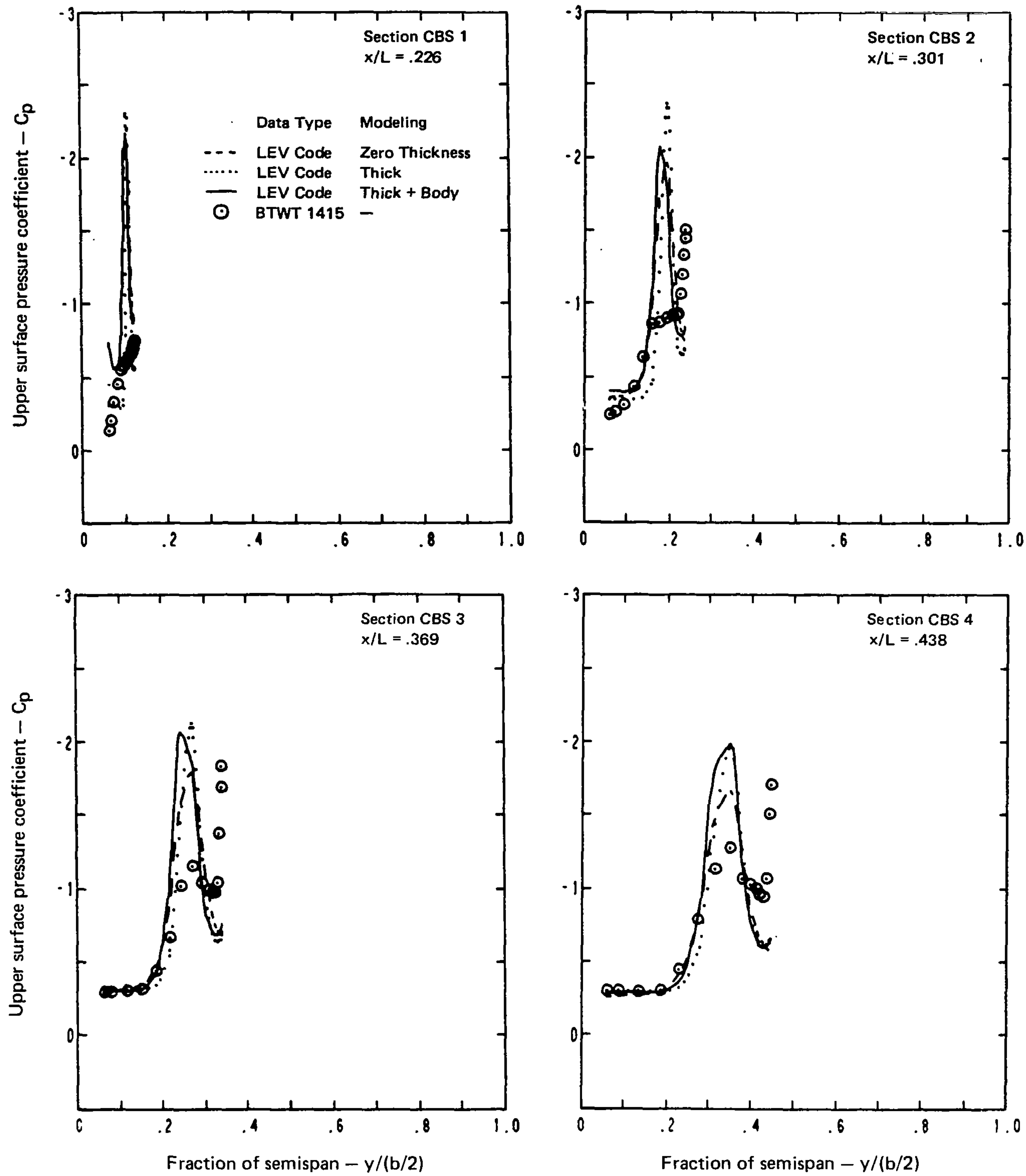

(a) Upper Surface Chordwise Pressure Distributions

Figure 24.—Effect of Wing Thickness and Fuselage Representation on Pressure Distributions, Flat Wing, $M = 0.40$, $\alpha = 16°$

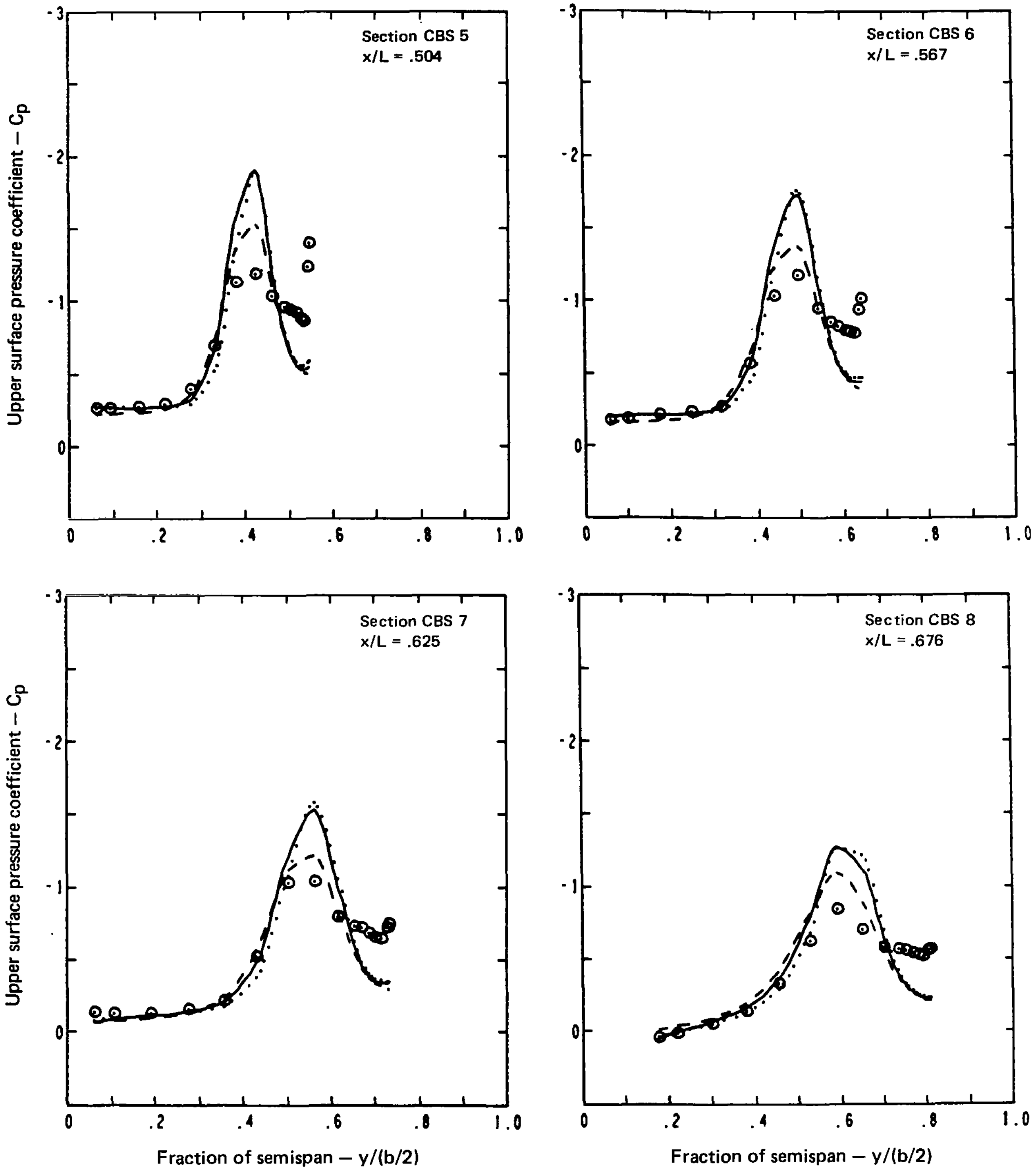

(a) (Continued)

Figure 24.—(Continued)

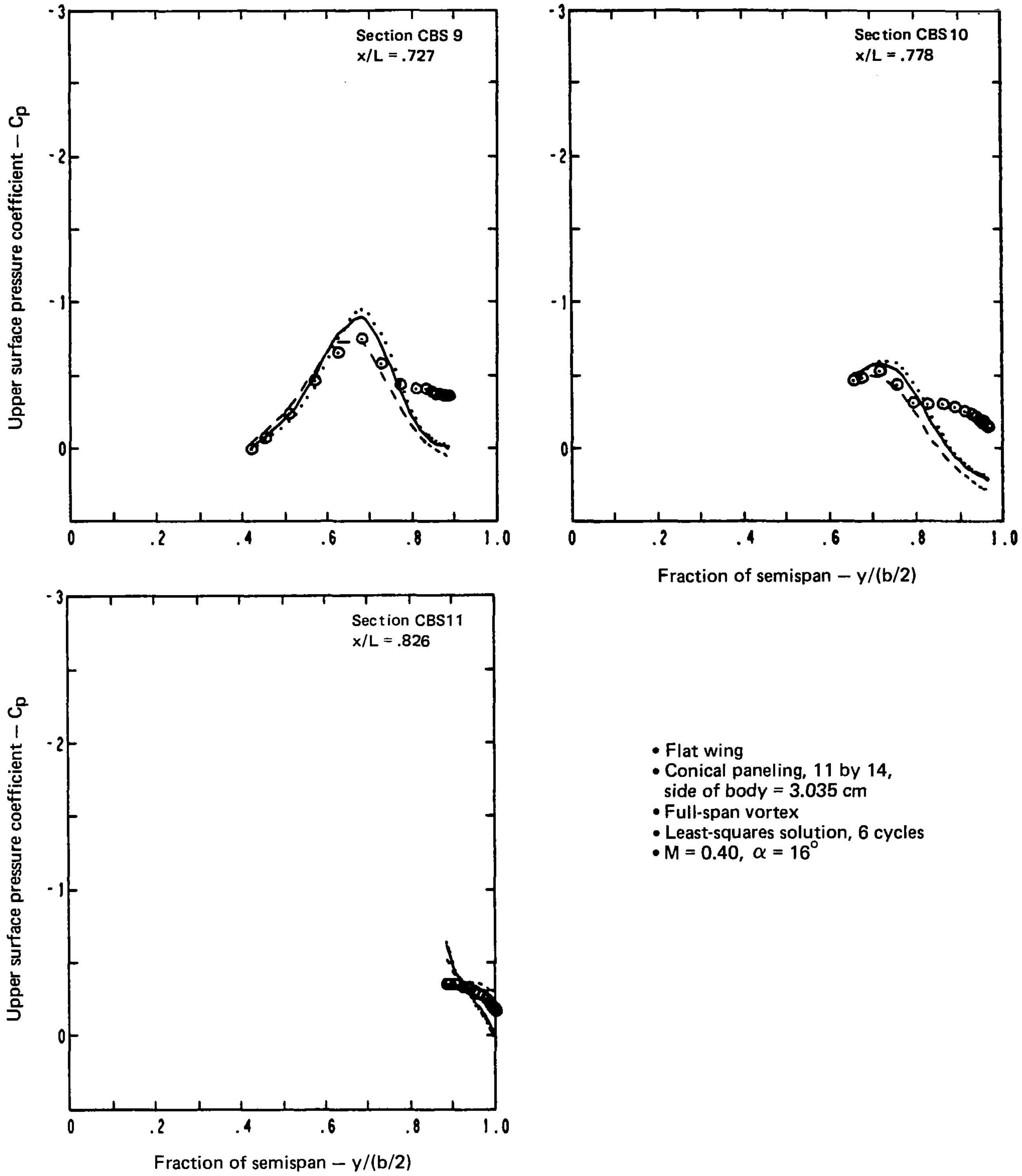

(a) (Concluded)

Figure 24.—(Continued)

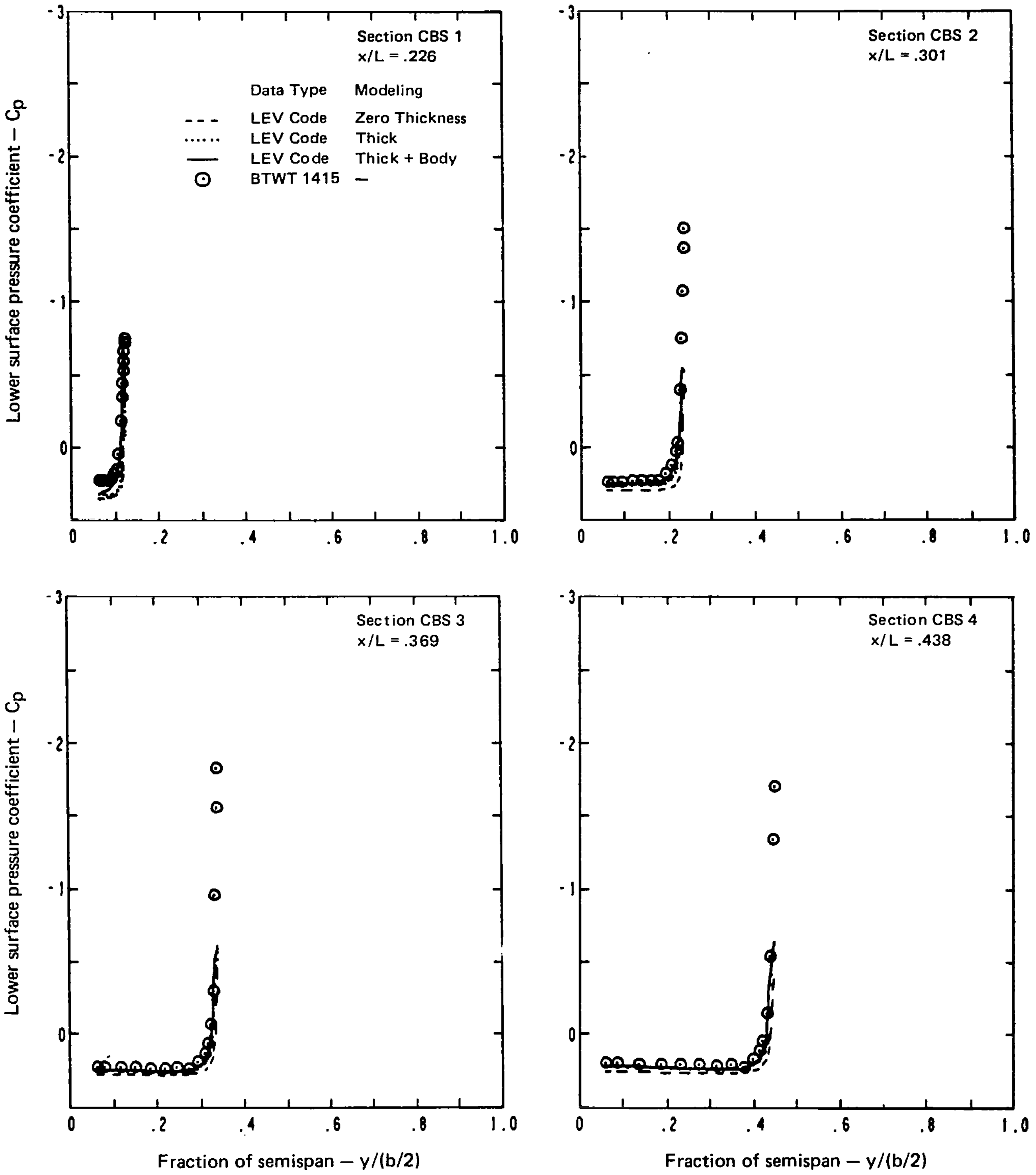

(b) Lower Surface Chordwise Pressure Distributions

Figure 24.—(Continued)

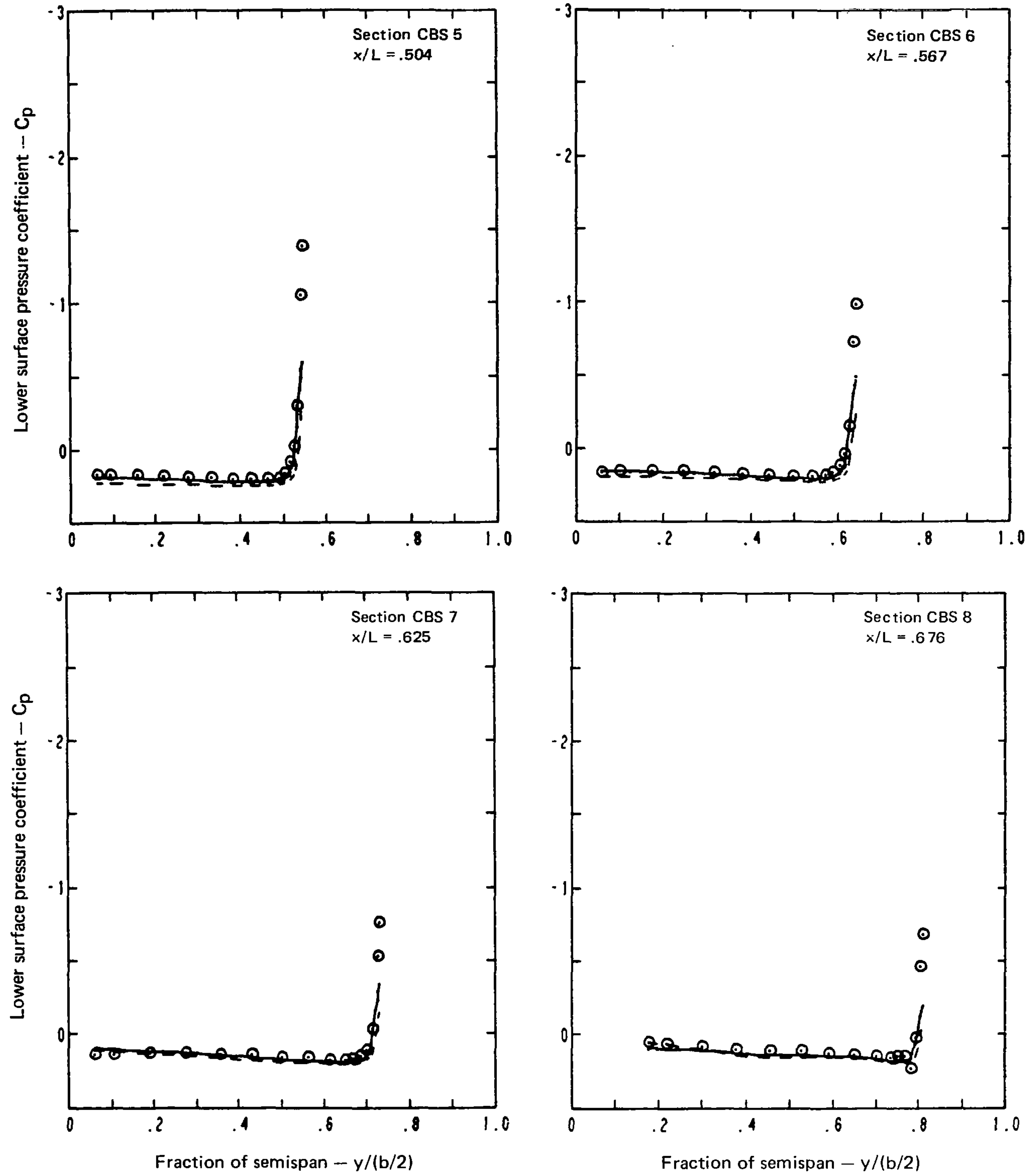

(b) (Continued)

Figure 24.—(Continued)

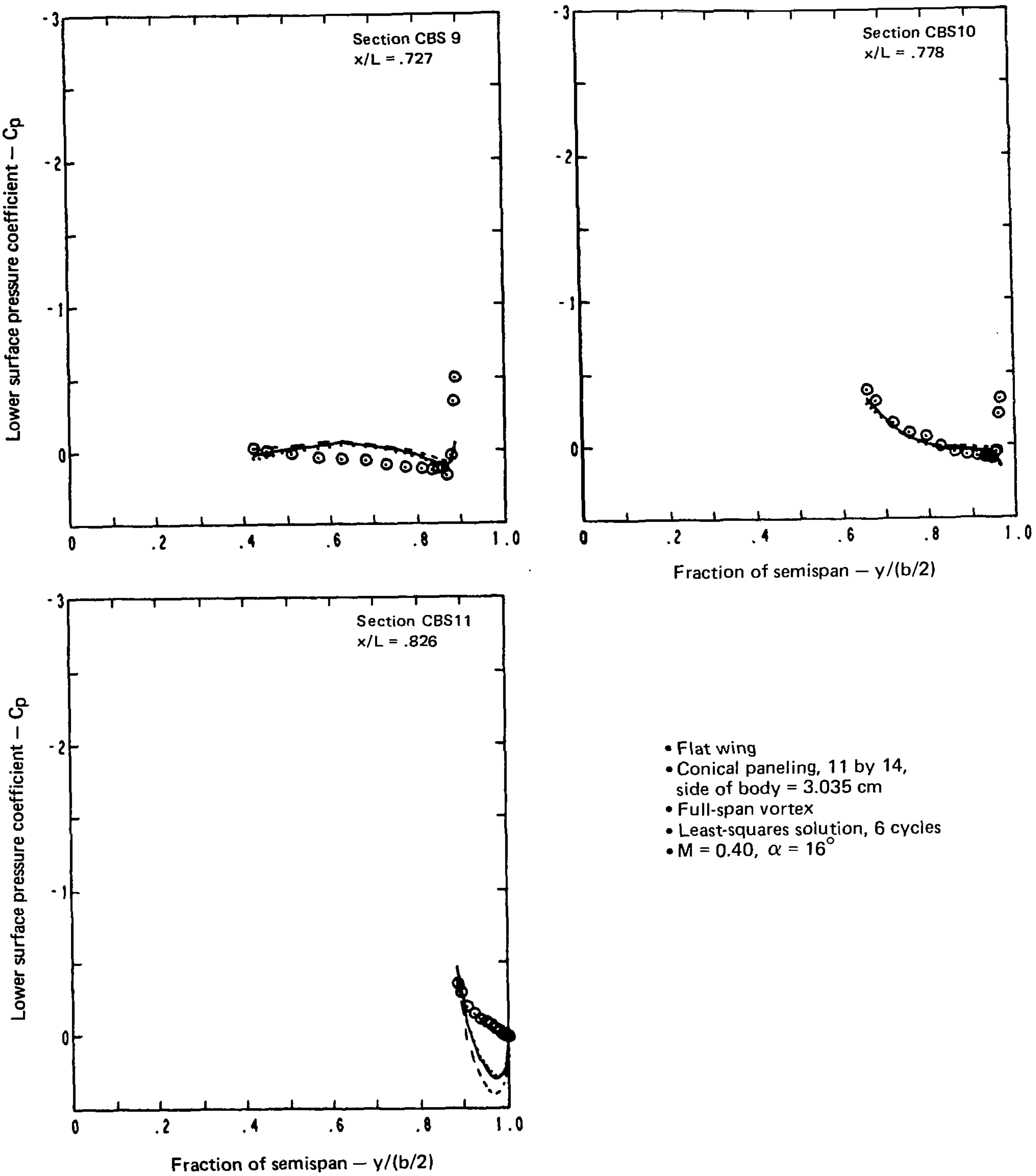

- Flat wing
- Conical paneling, 11 by 14, side of body = 3.035 cm
- Full-span vortex
- Least-squares solution, 6 cycles
- M = 0.40, α = 16°

(b) (Concluded)

Figure 24.—(Continued)

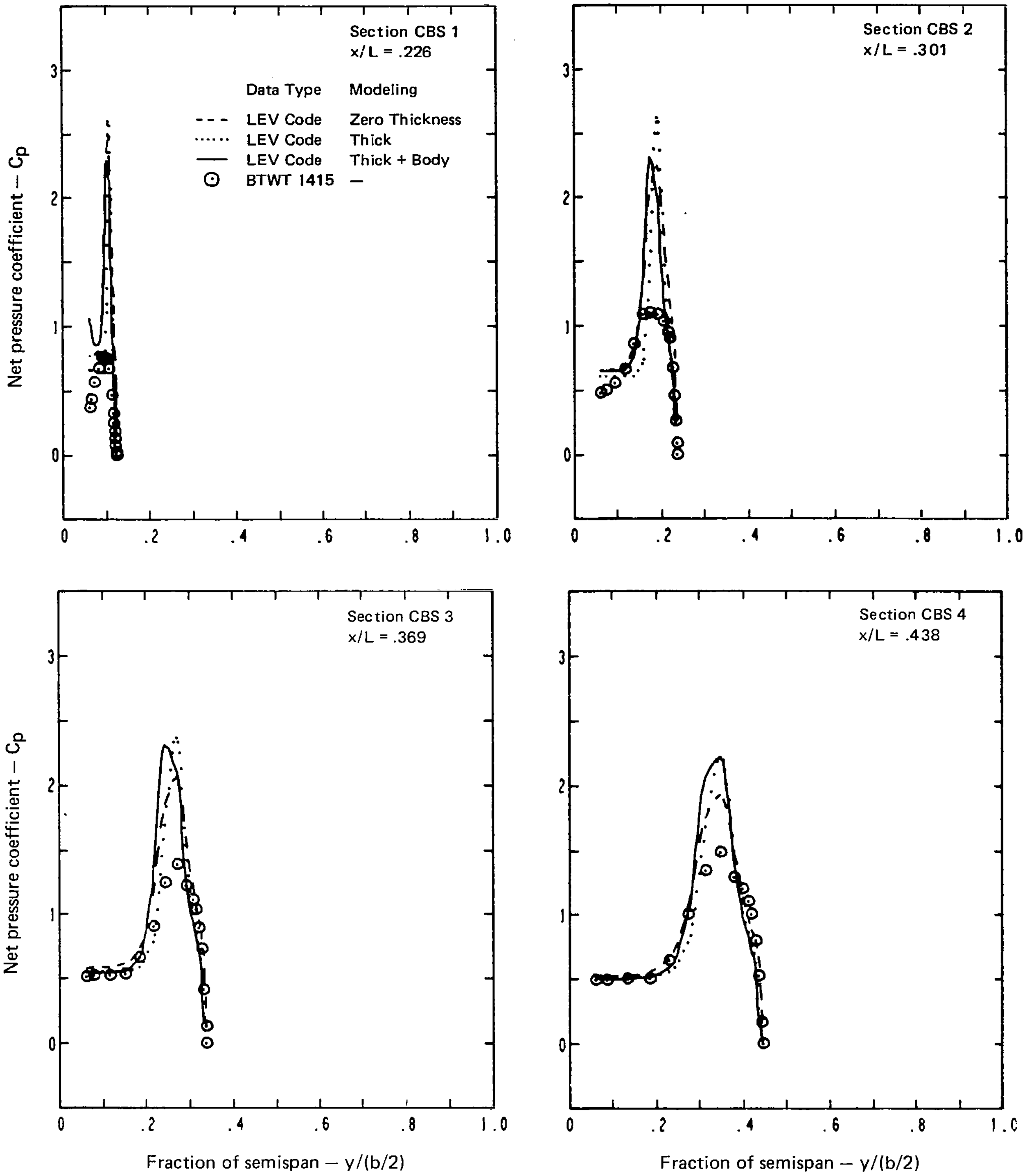

(c) Net Chordwise Pressure Distributions

Figure 24.—(Continued)

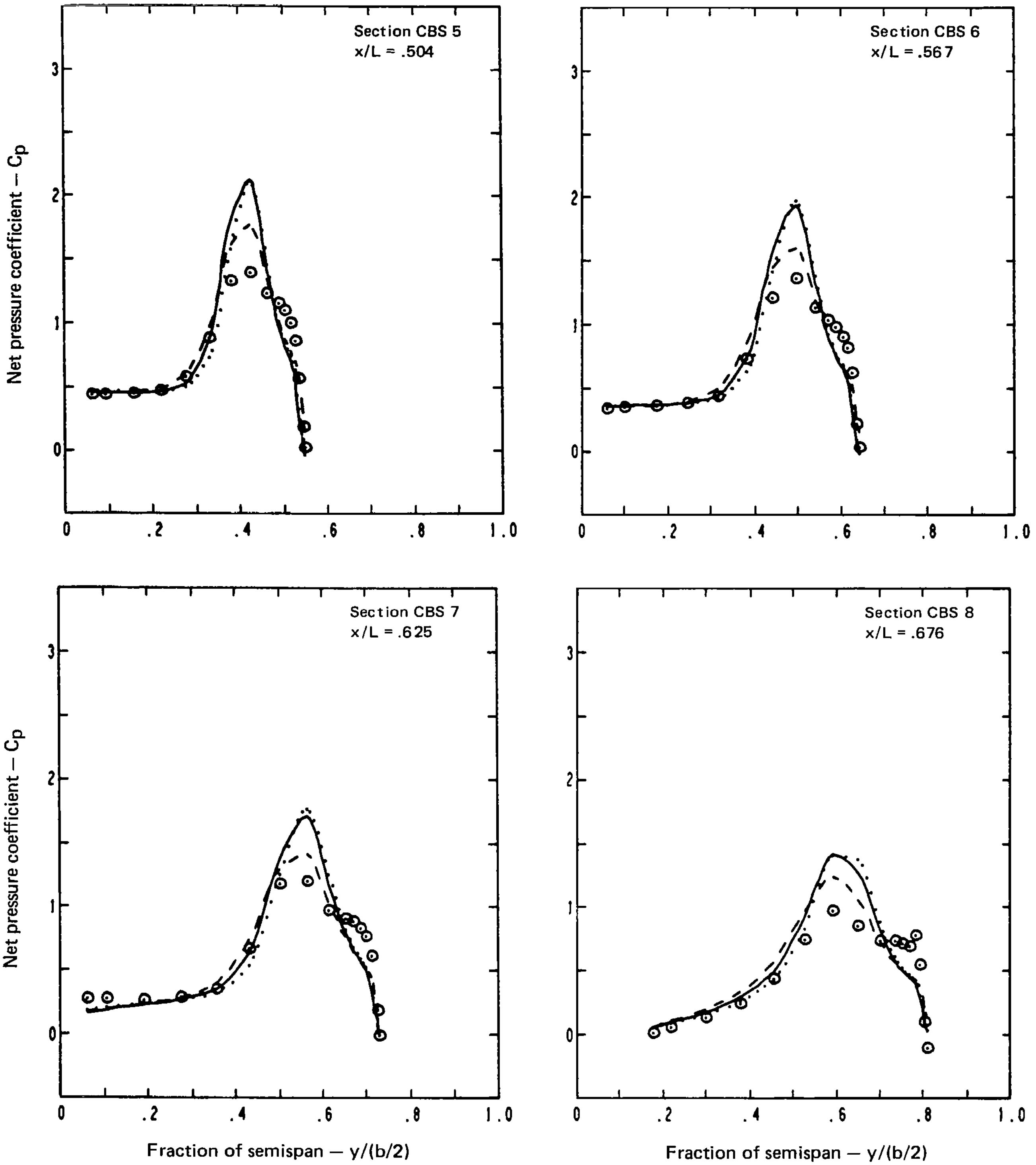

(c) (Continued)

Figure 24.—(Continued)

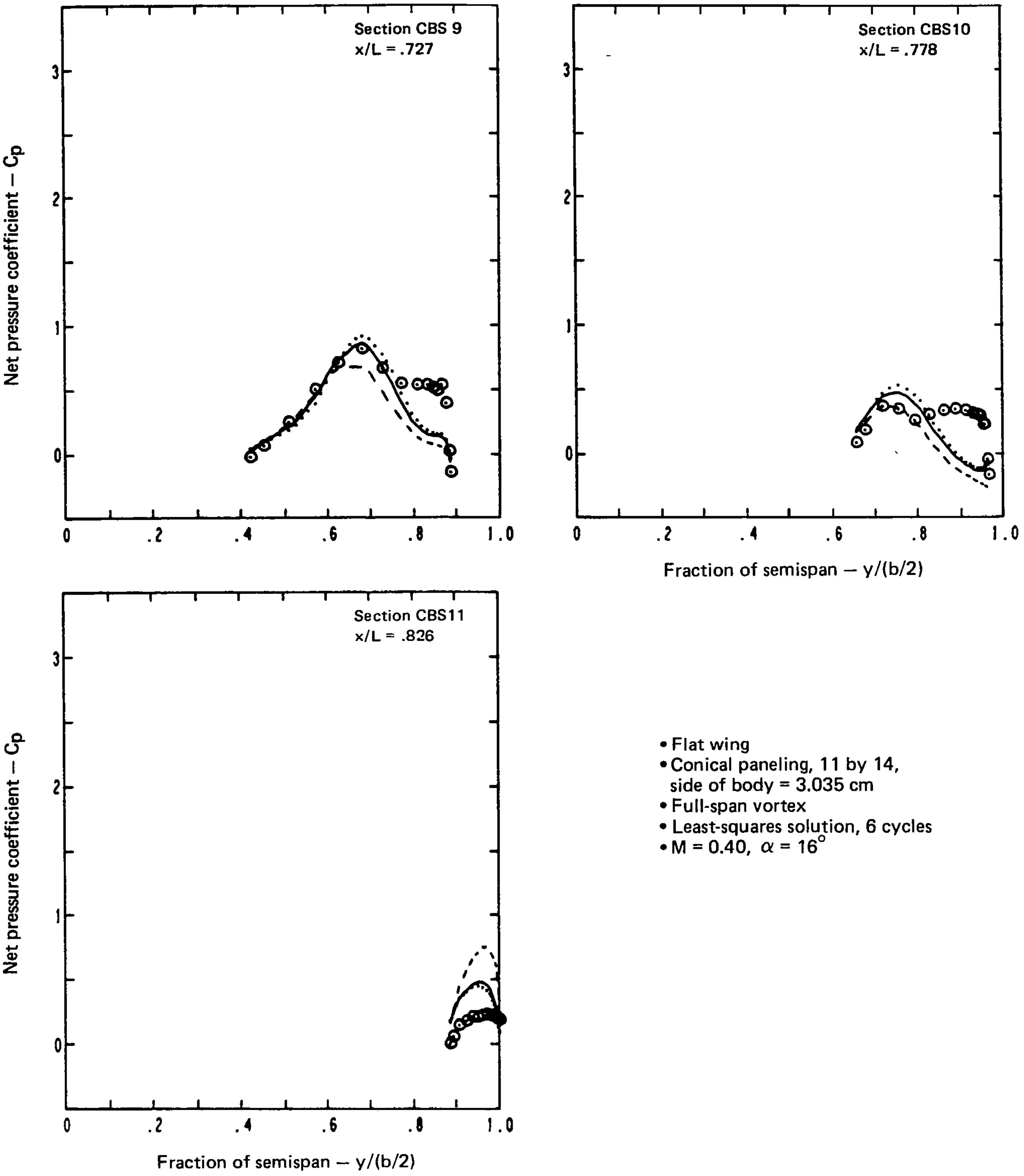

- Flat wing
- Conical paneling, 11 by 14, side of body = 3.035 cm
- Full-span vortex
- Least-squares solution, 6 cycles
- M = 0.40, α = 16°

(c) (Concluded)

Figure 24.—(Concluded)

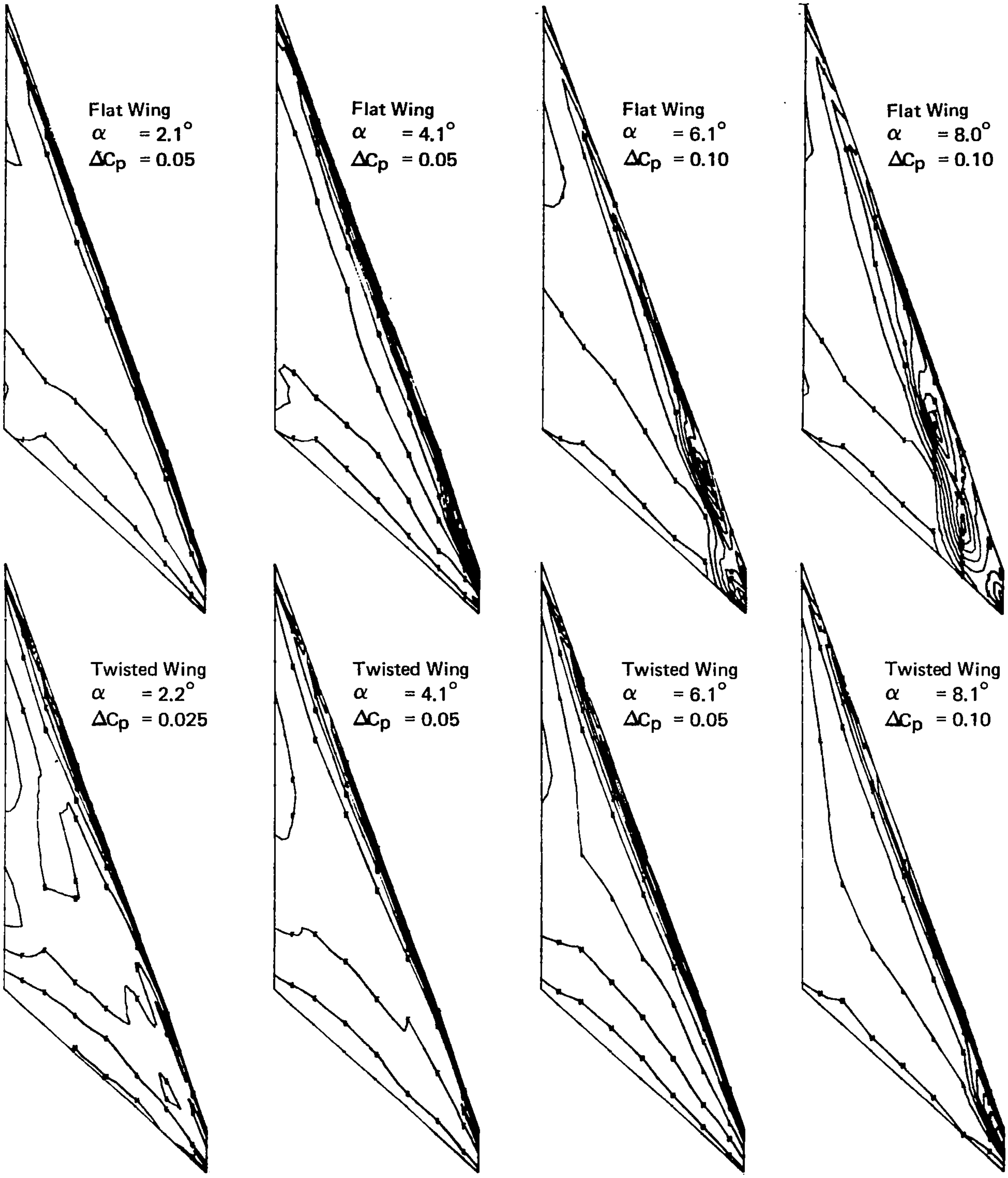

Note: ΔC_p = increment between adjacent isobars

Figure 25.—Experimental Upper Surface Isobars, Flat and Twisted Wings, M = 0.40

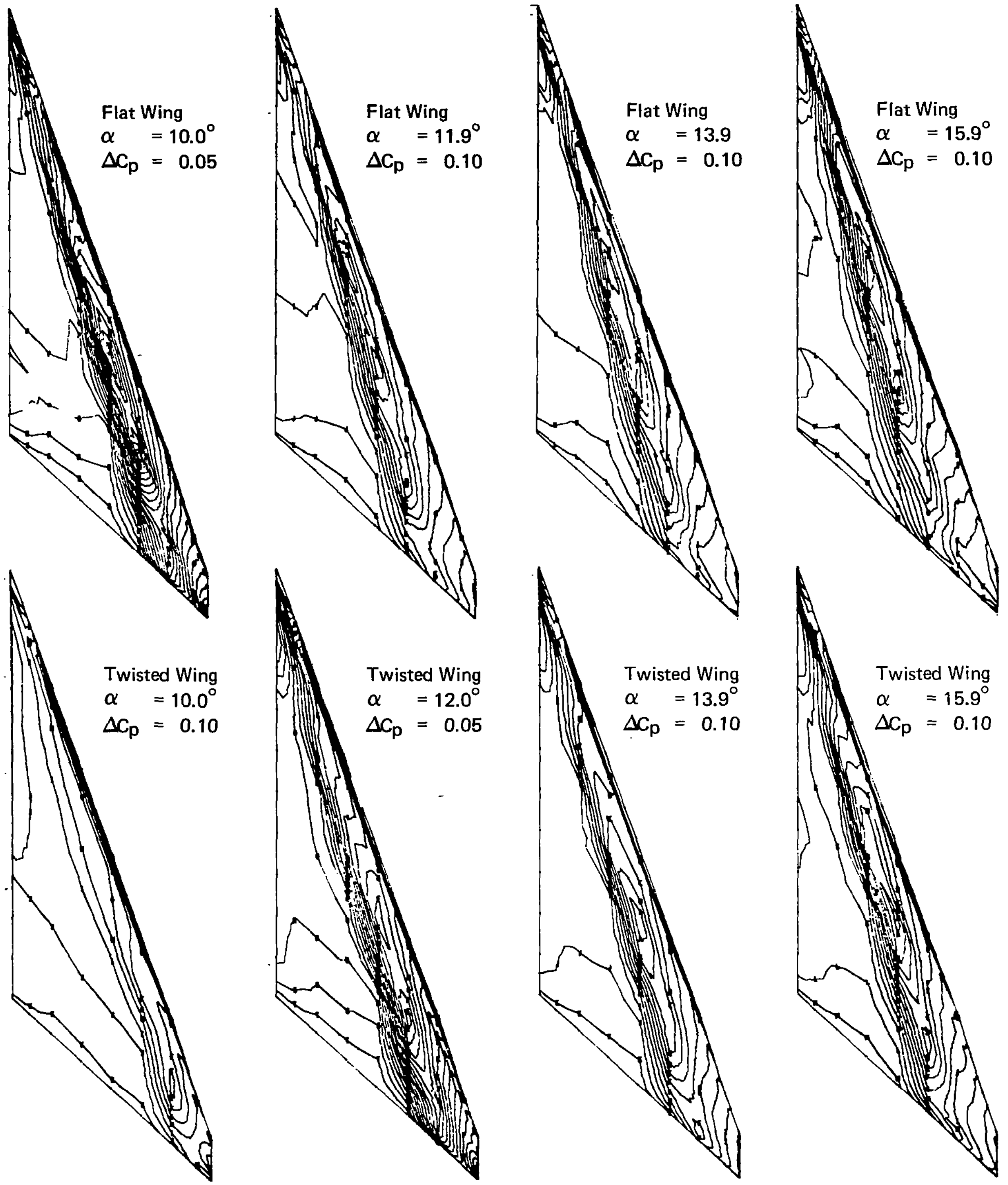

Note: ΔC_p = increment between adjacent isobars

Figure 25.—(Concluded)

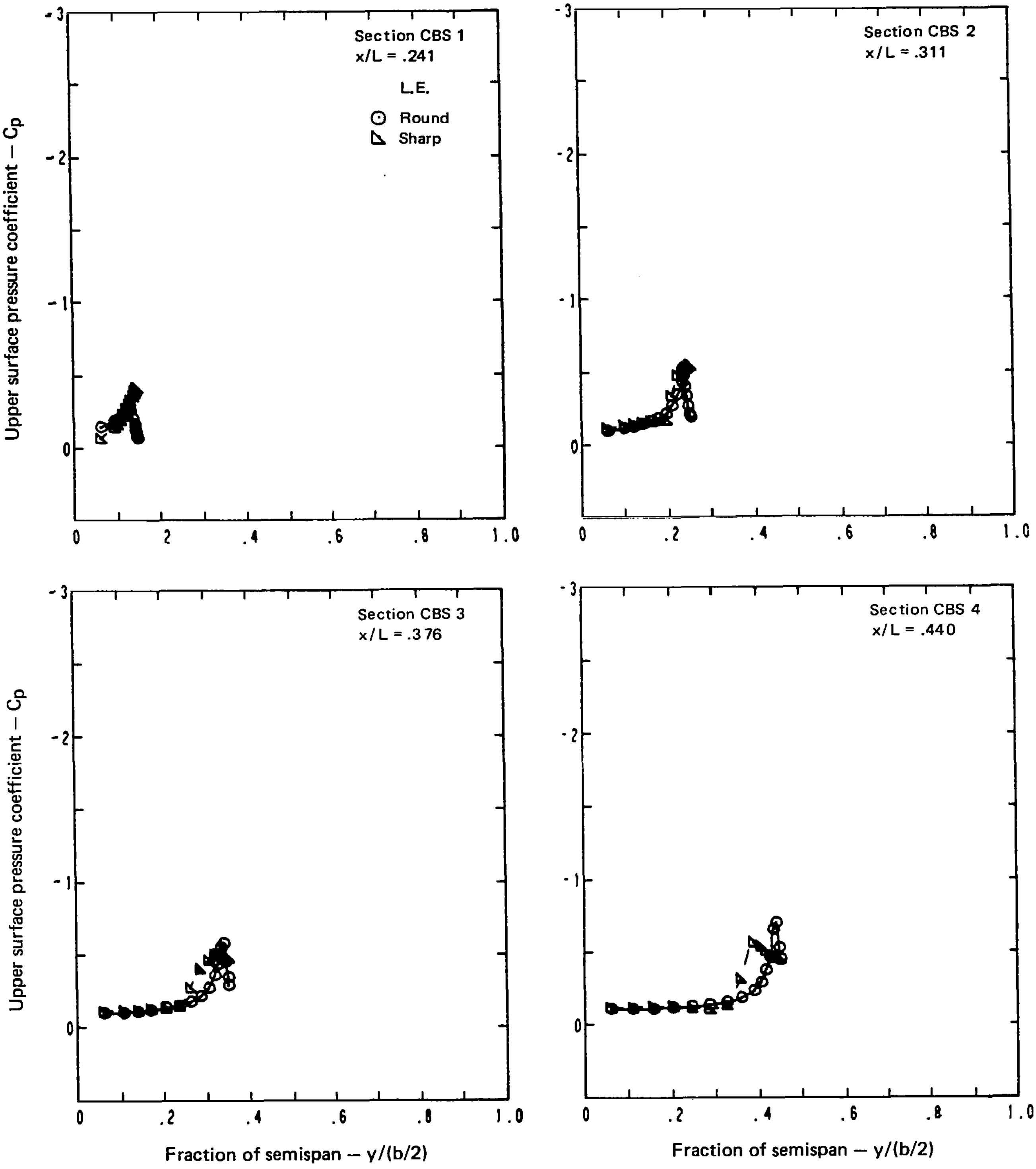

(a) Angle of Attack = 6°

Figure 26.—Experimental Upper Surface Pressure Distributions, Flat Wing, M = 0.40

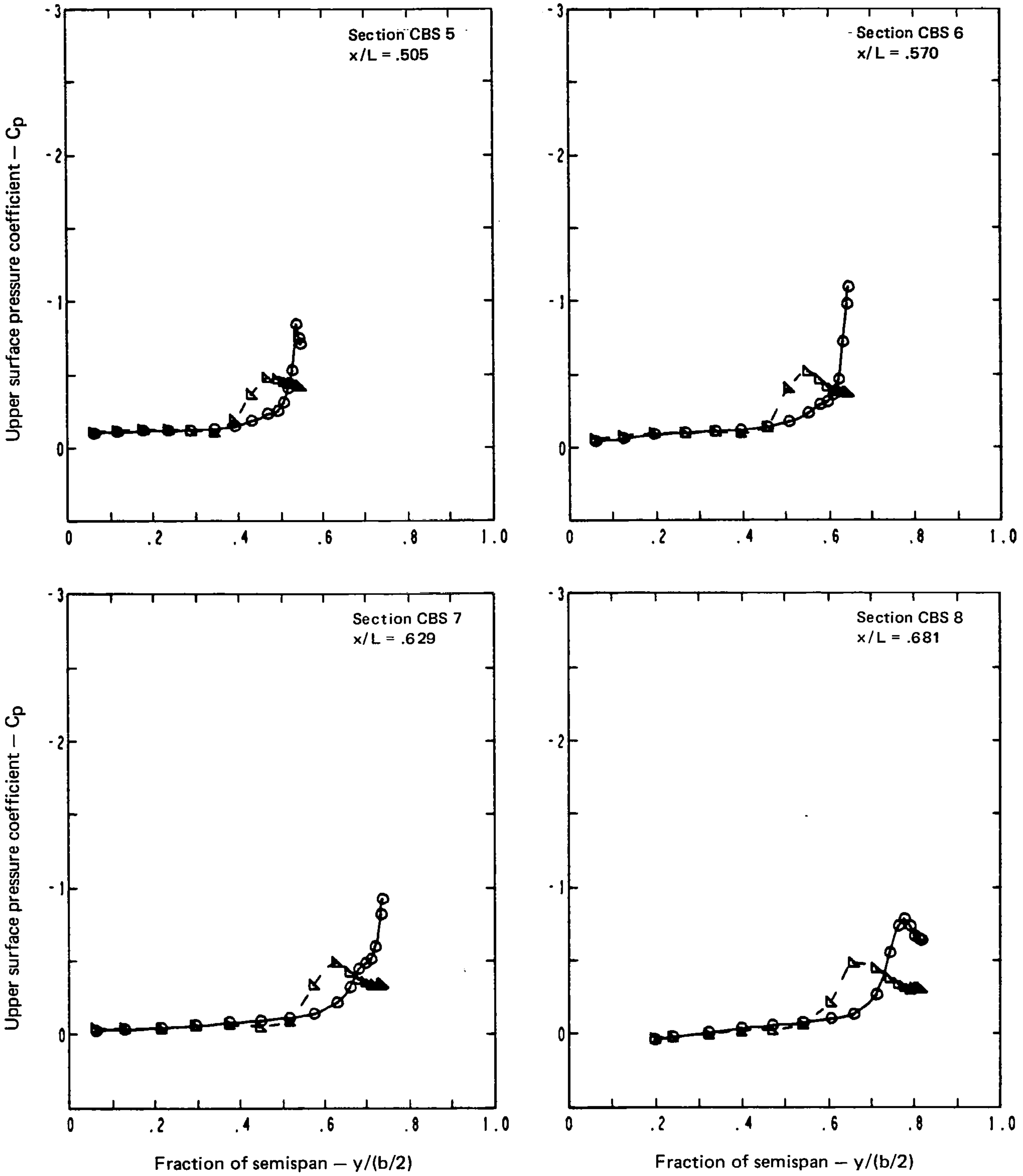

(a) (Continued)

Figure 26.—(Continued)

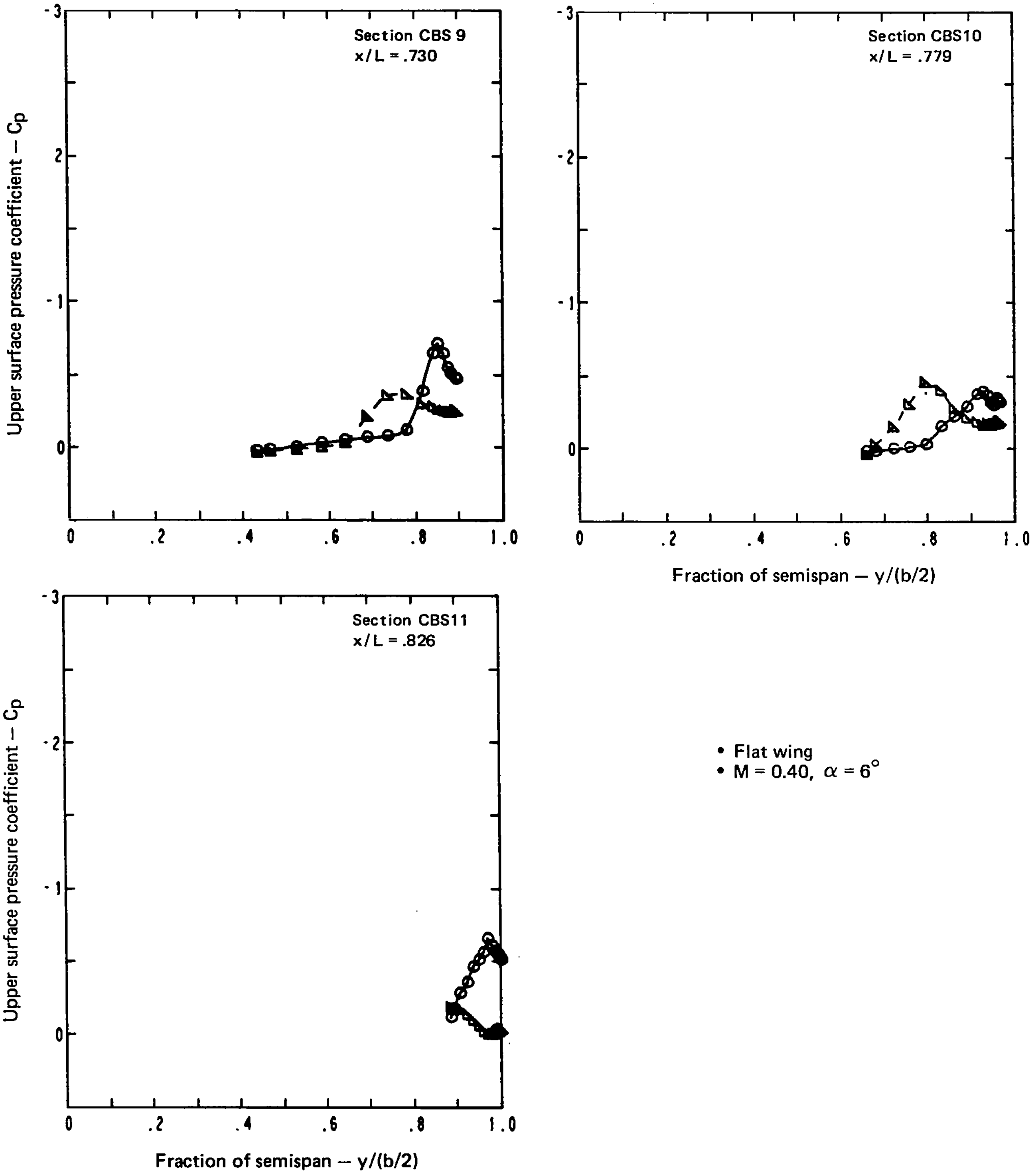

(a) (Concluded)

Figure 26.—(Continued)

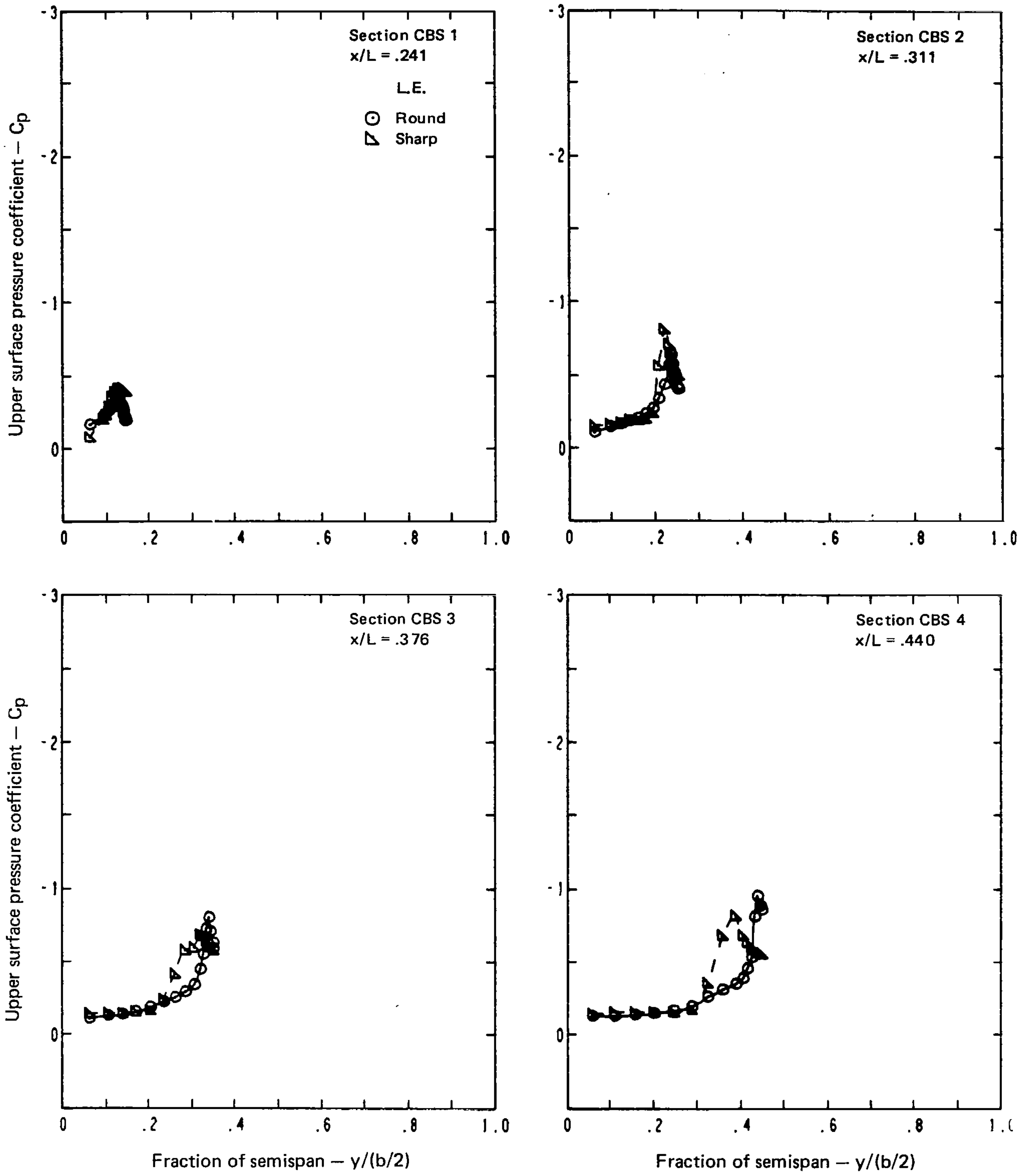

(b) Angle of Attack = 8°

Figure 26.—(Continued)

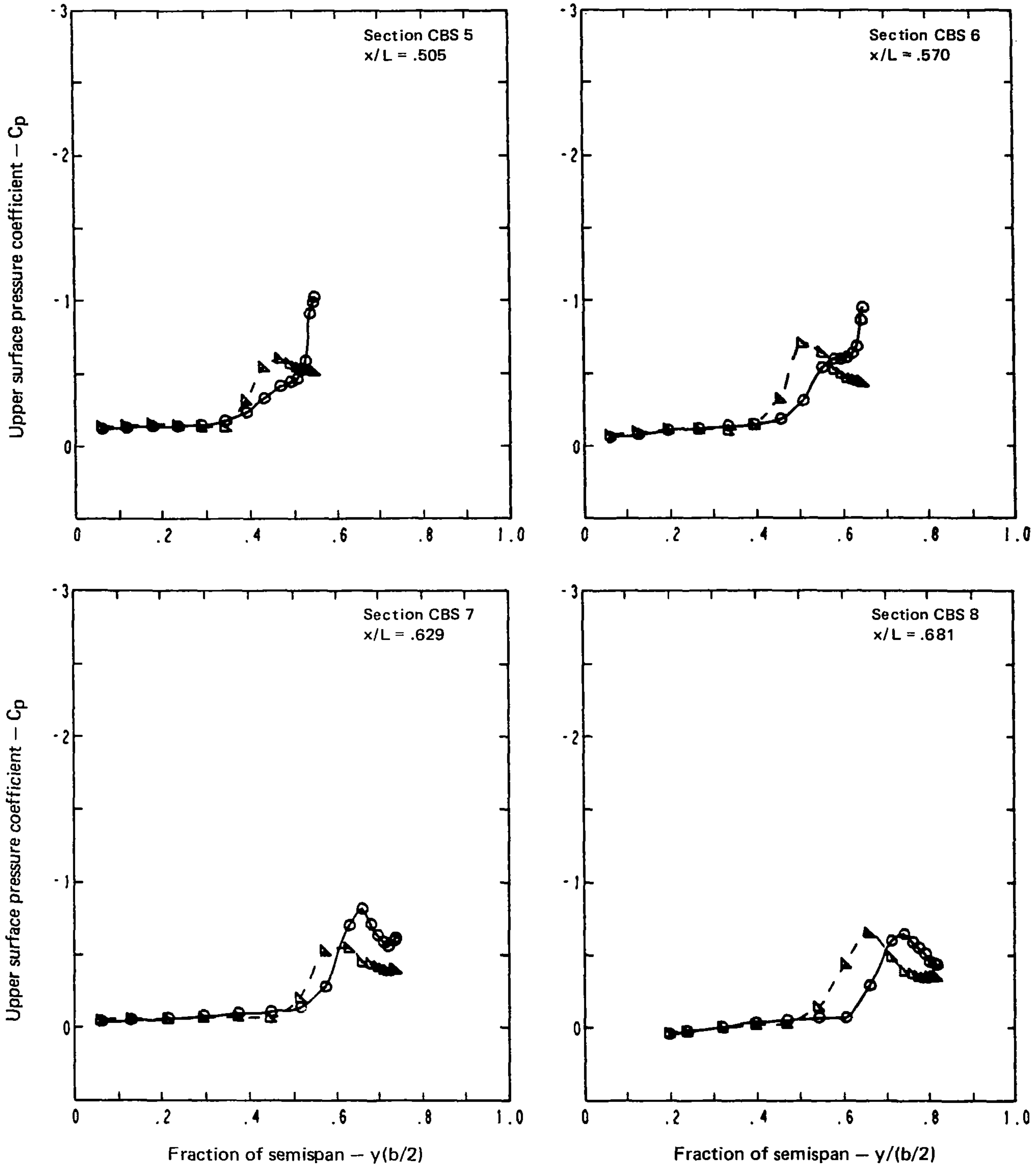

(b) (Continued)

Figure 26.—(Continued)

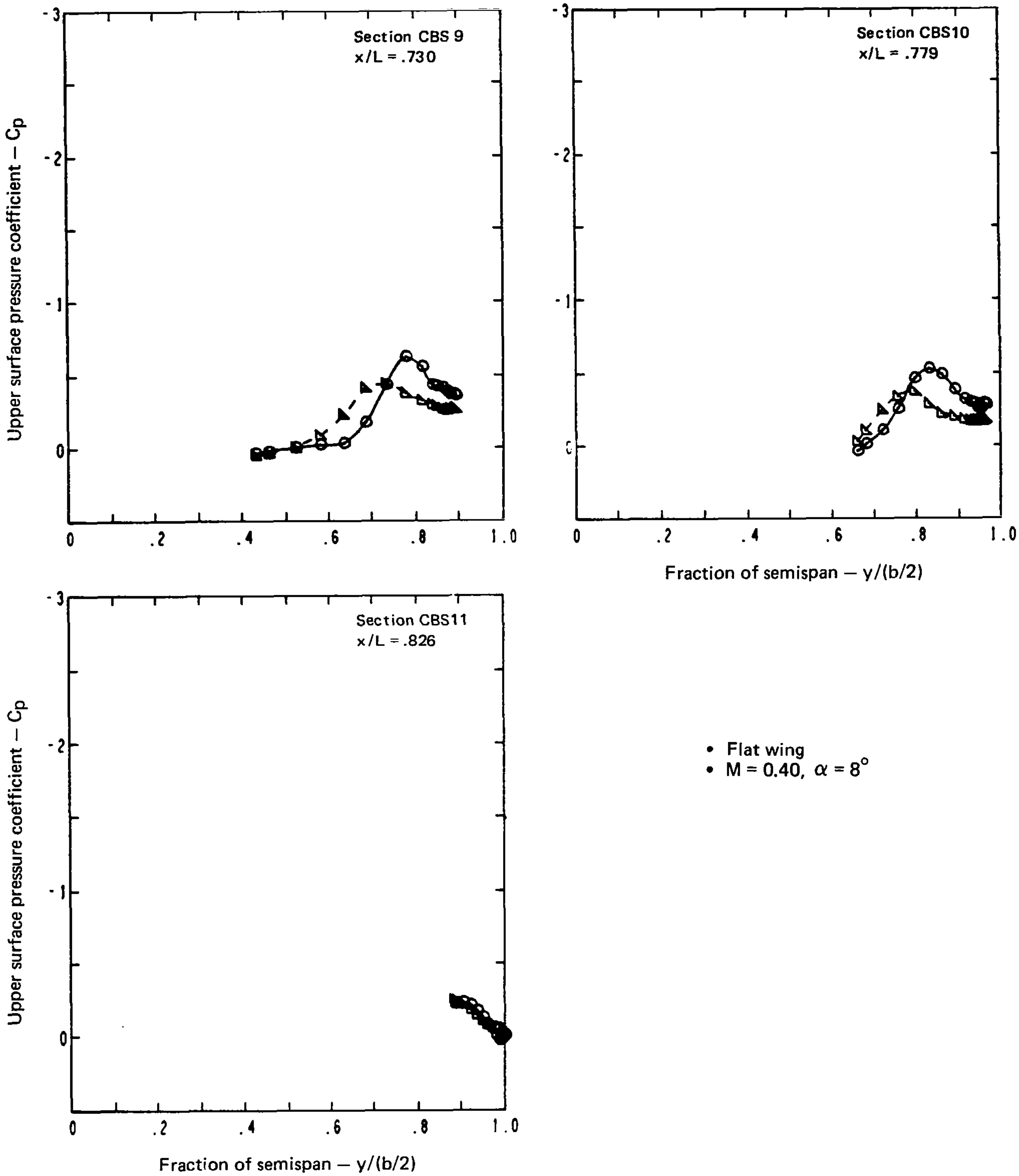

- Flat wing
- M = 0.40, $\alpha = 8^\circ$

(b) (Concluded)

Figure 26.—(Concluded)

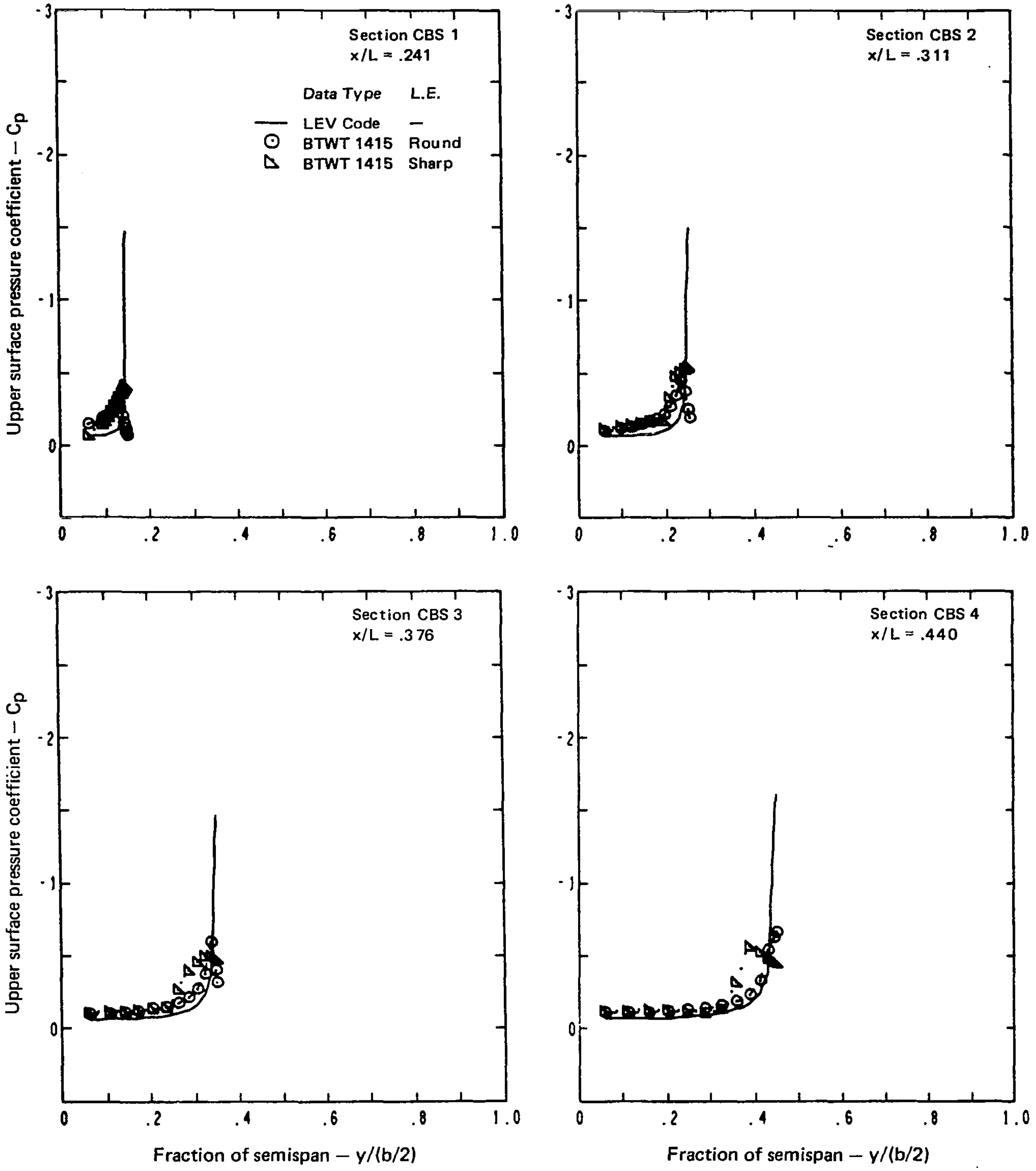

Figure 27.—Upper Surface Pressure Distributions, Flat Wing, Zero Thickness, $\Delta a = 0.0$, $M = 0.40$, $\alpha = 6°$

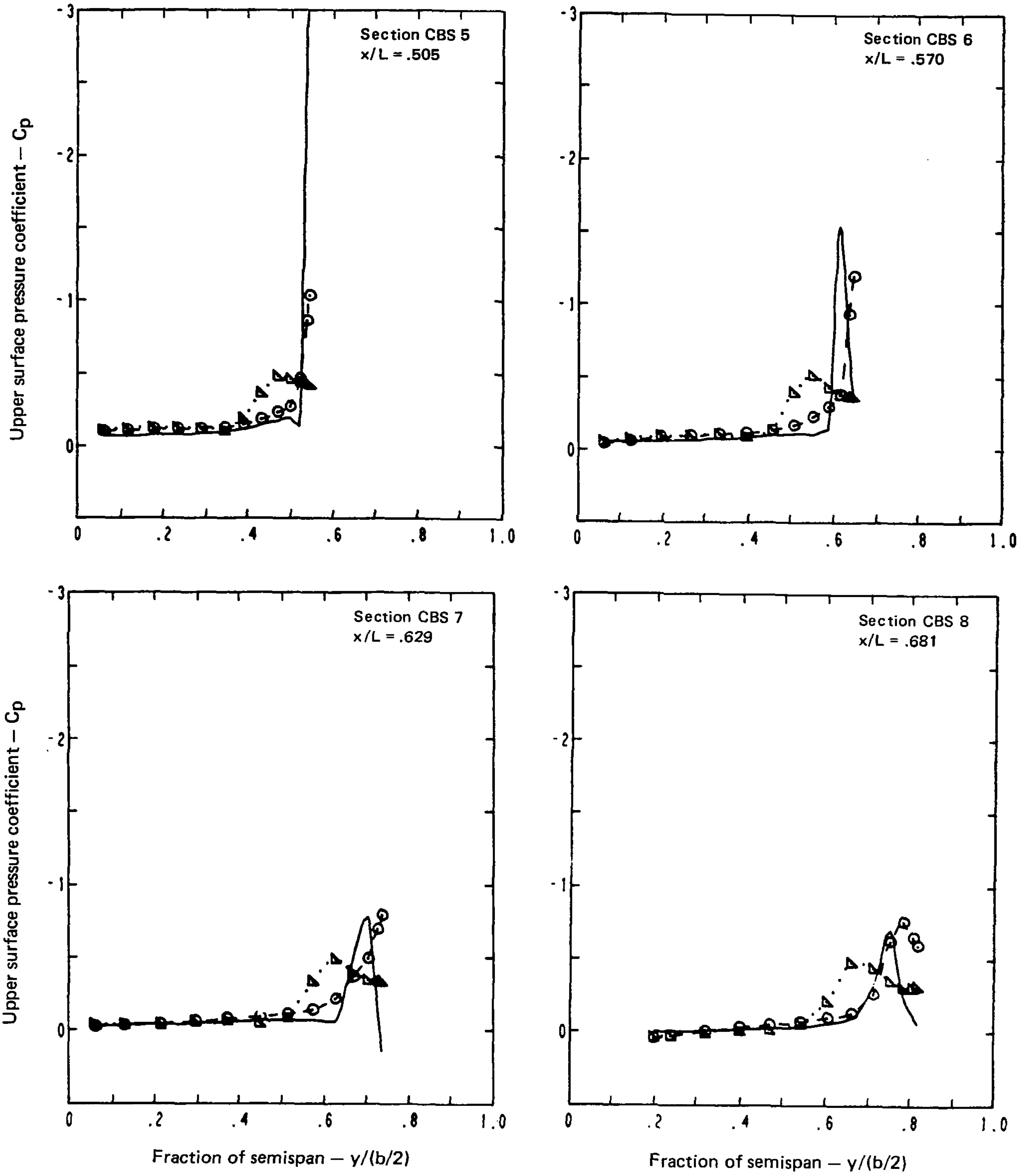

Figure 27.—(Continued)

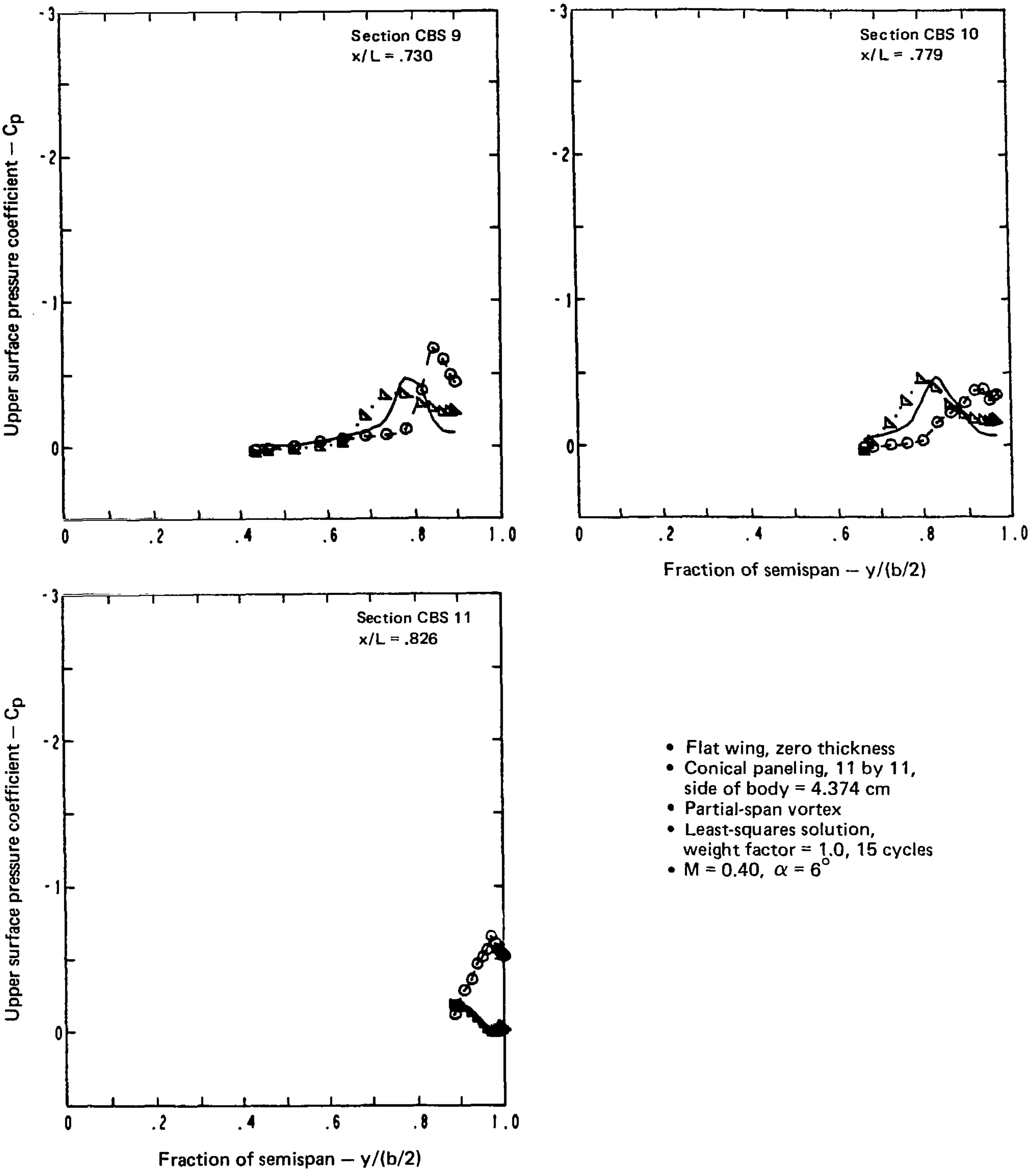

- Flat wing, zero thickness
- Conical paneling, 11 by 11, side of body = 4.374 cm
- Partial-span vortex
- Least-squares solution, weight factor = 1.0, 15 cycles
- M = 0.40, $\alpha = 6^\circ$

Figure 27.—(Concluded)

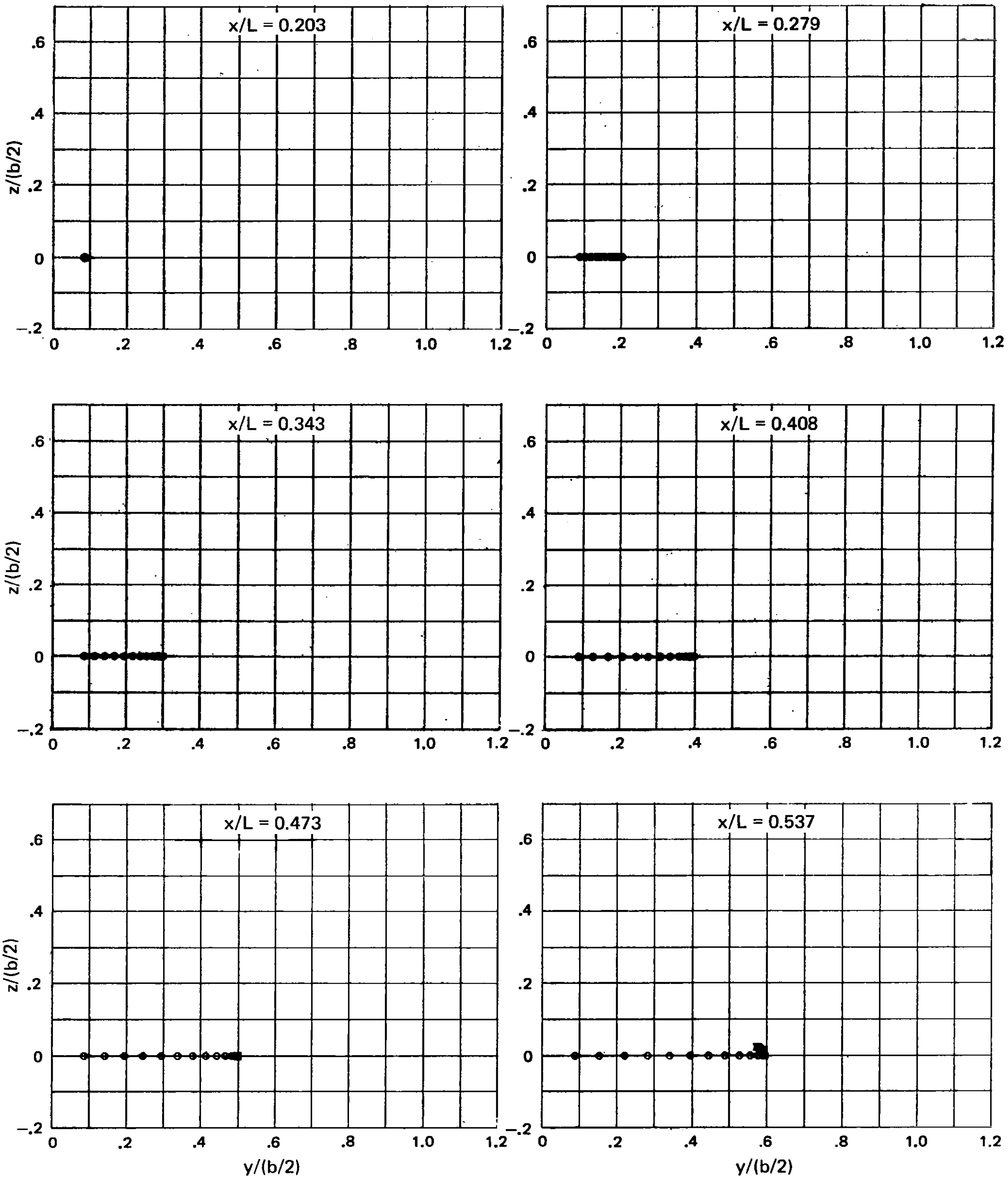

Figure 28.—Geometry of Panel Edges at Constant Body Stations, Flat Wing, Zero Thickness, $\Delta a = 0.0$, $M = 0.40$, $\alpha = 6°$, Cycle 15

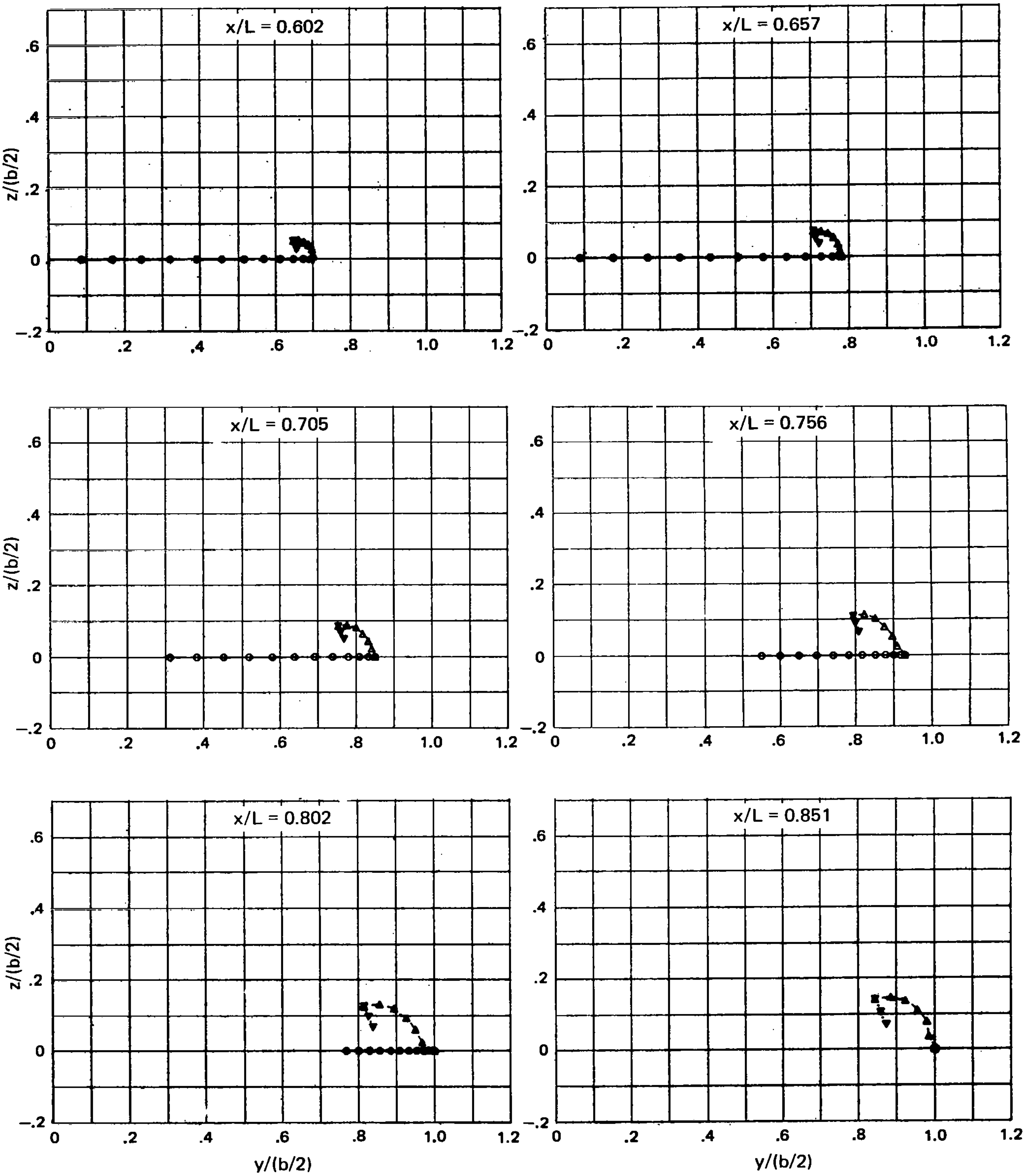

Figure 28.—(Concluded)

11 X 11 (121 panels)

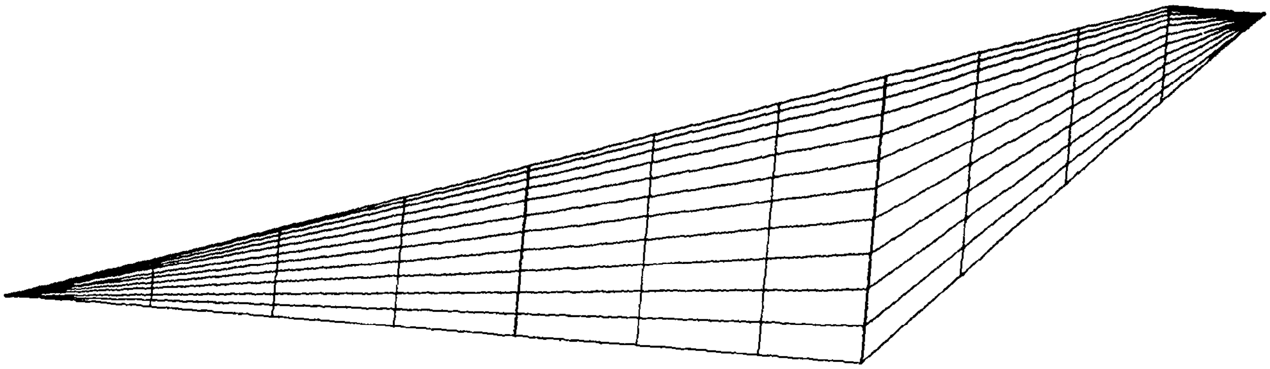

11 X 14 (154 panels)

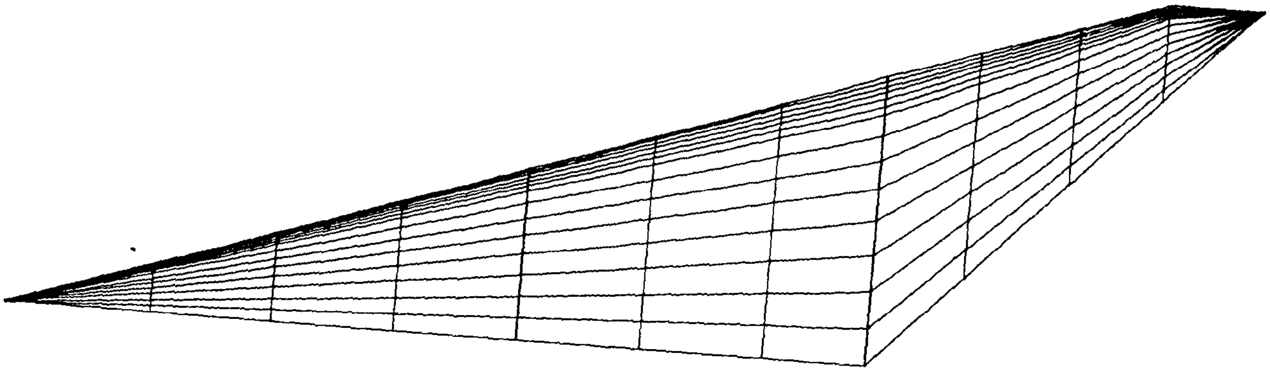

Figure 29.—Planform View of Conical Wing Paneling

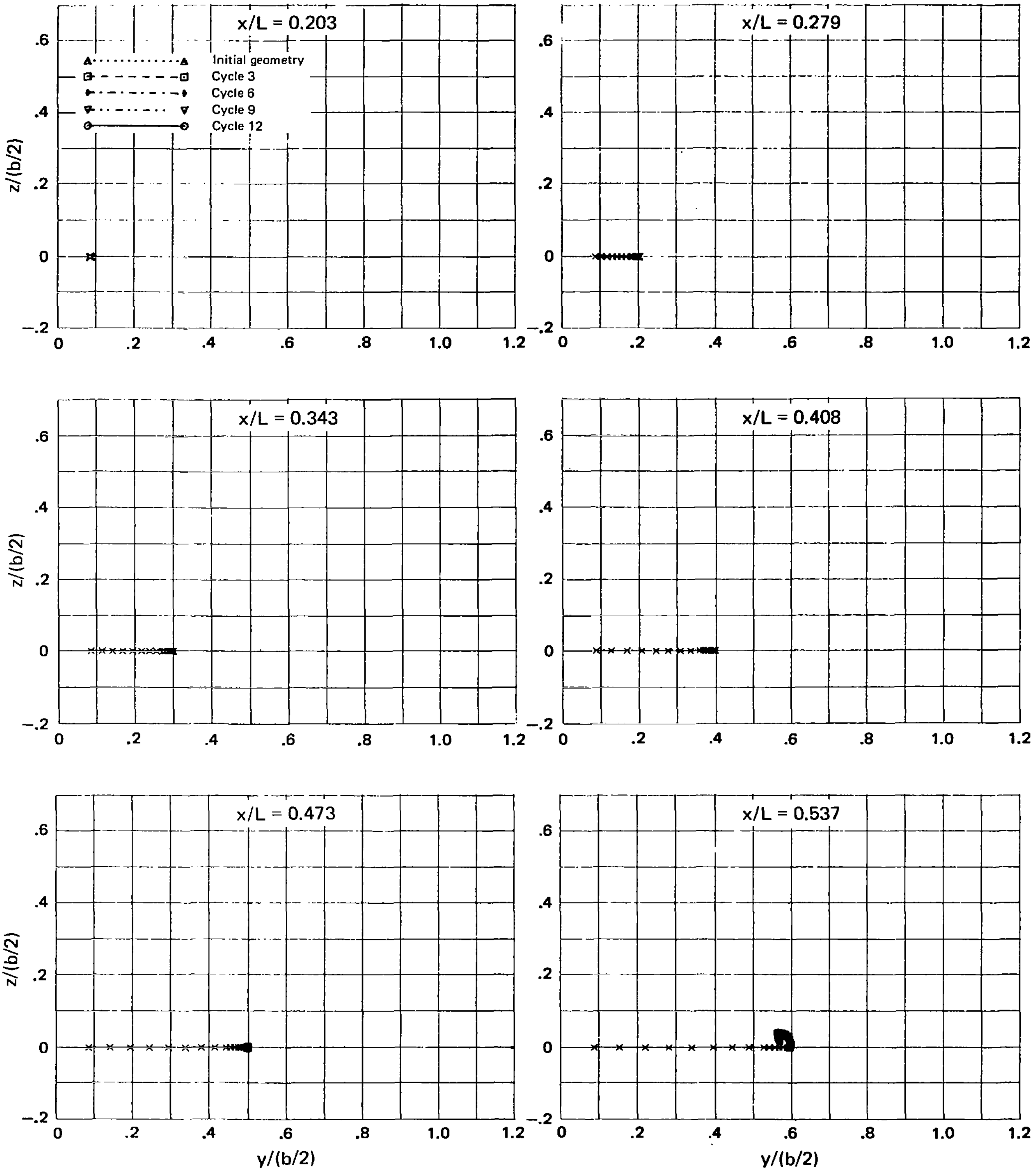

Figure 30.—Geometry of Panel Edges at Constant Body Stations, Flat Wing, Zero Thickness, Denser Wing Paneling, Δ a = 0.6, M = 0.40, α = 6°, Several Cycles

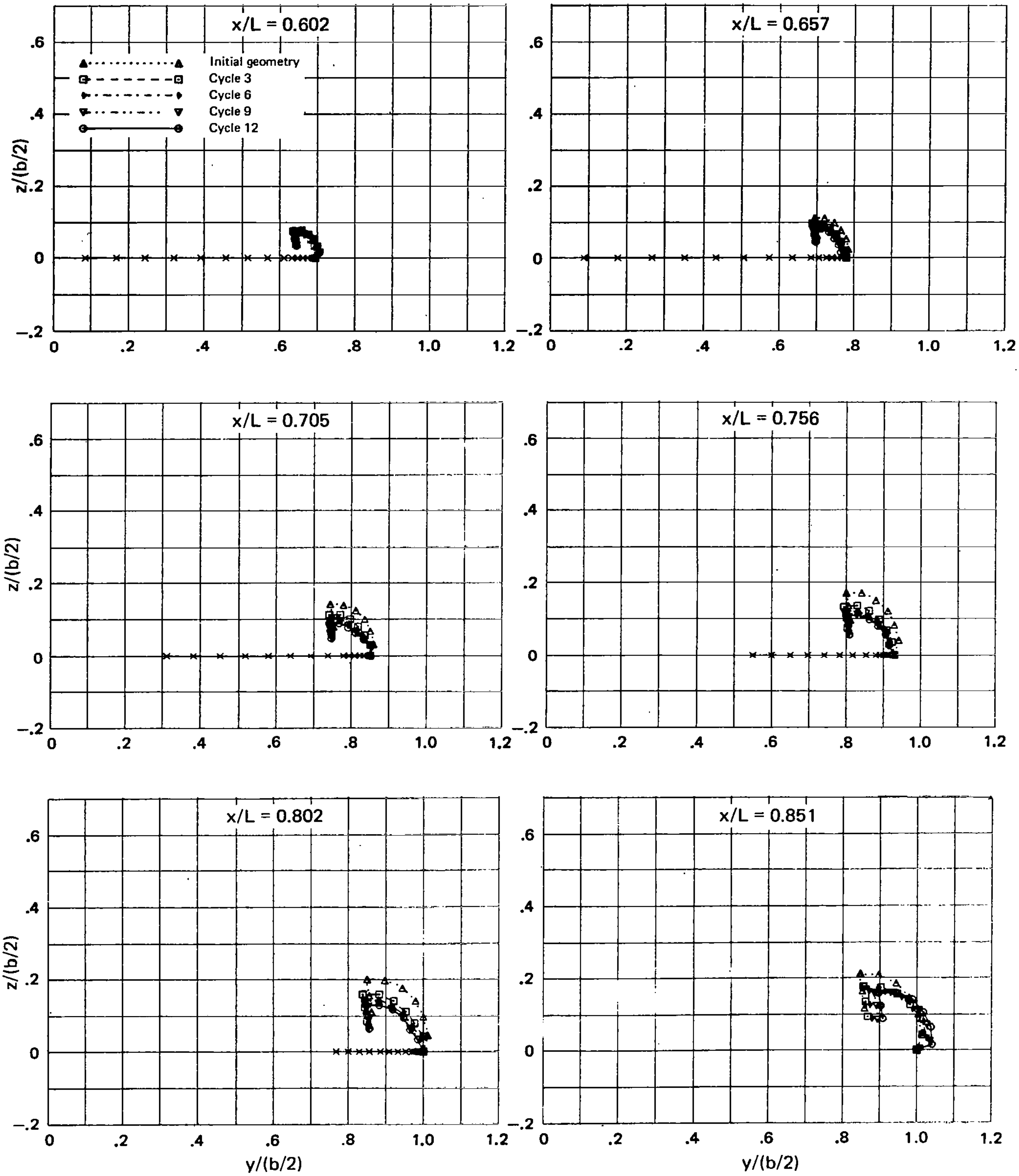

Figure 30.—(Concluded)

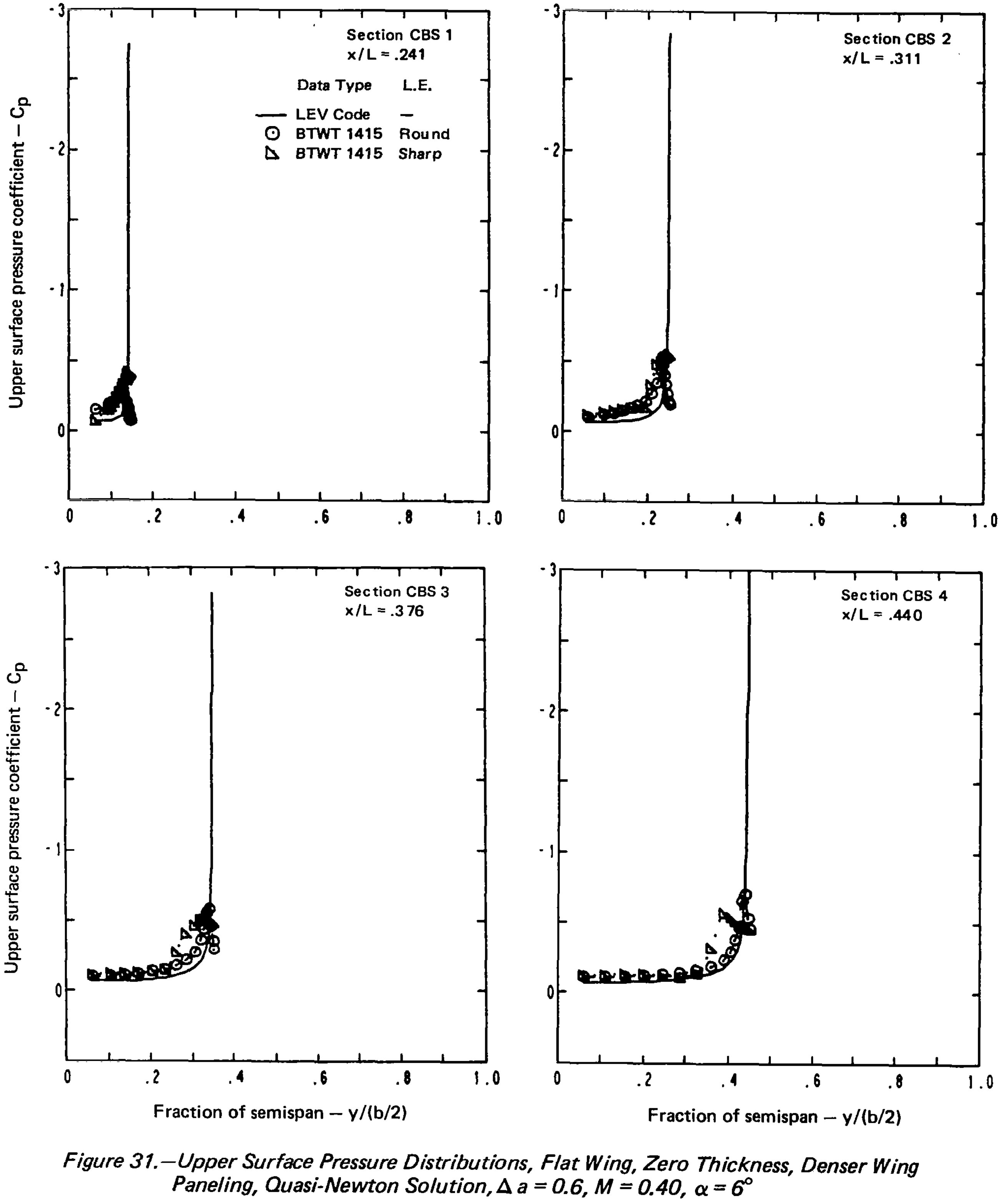

Figure 31.—Upper Surface Pressure Distributions, Flat Wing, Zero Thickness, Denser Wing Paneling, Quasi-Newton Solution, $\Delta a = 0.6$, $M = 0.40$, $\alpha = 6°$

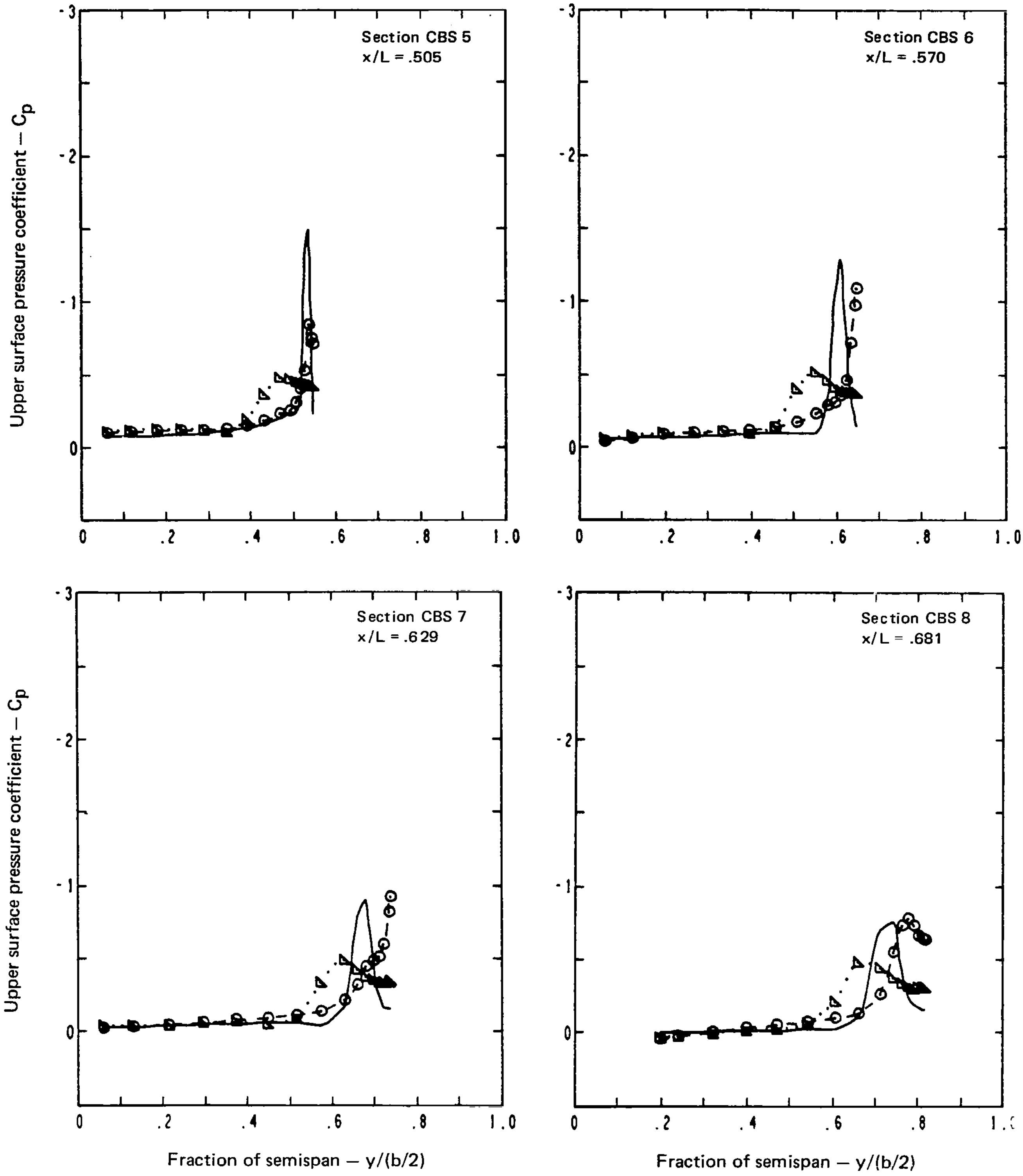

Figure 31.—(Continued)

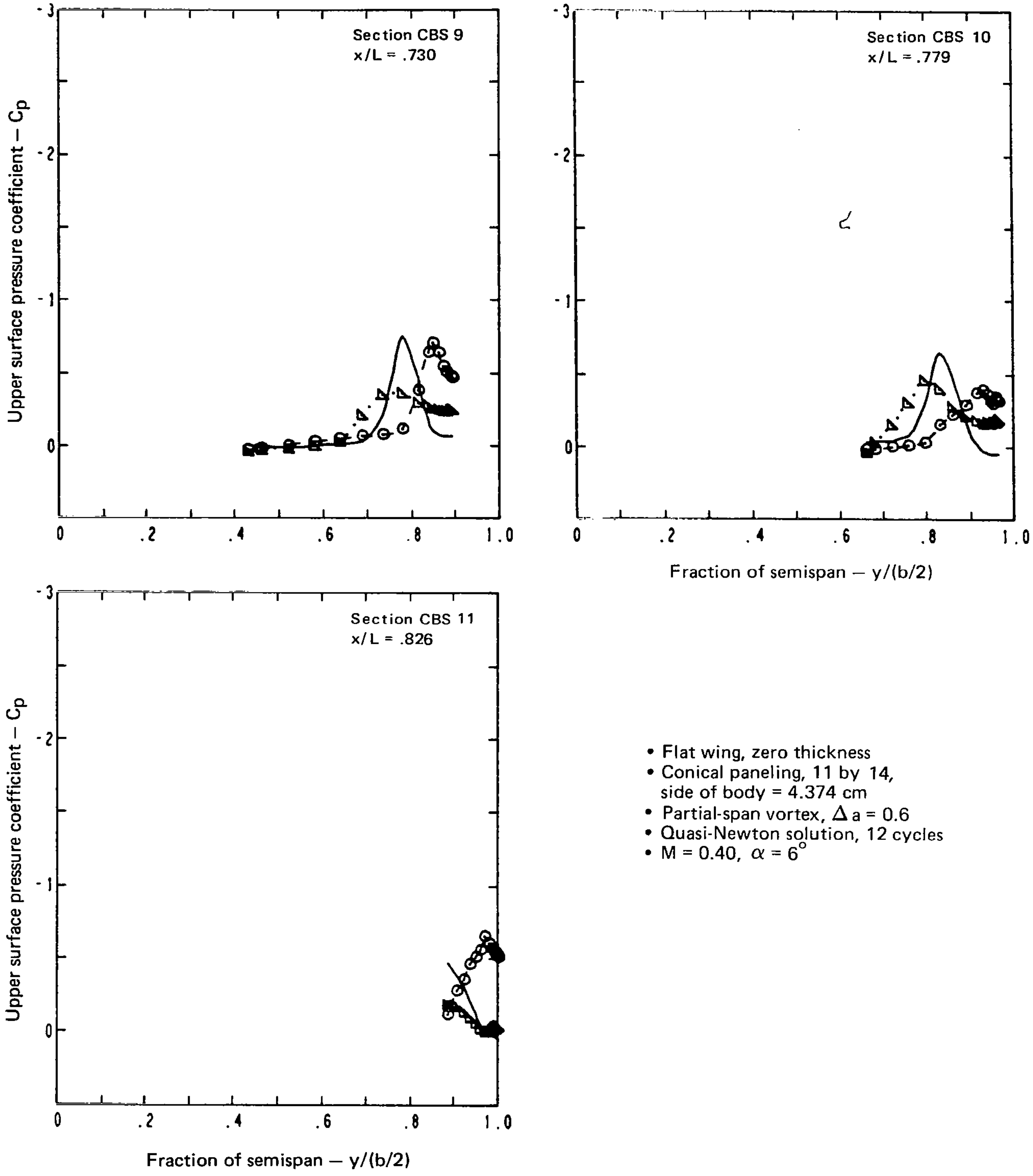

- Flat wing, zero thickness
- Conical paneling, 11 by 14,
  side of body = 4.374 cm
- Partial-span vortex, $\Delta a = 0.6$
- Quasi-Newton solution, 12 cycles
- $M = 0.40$, $\alpha = 6^\circ$

Figure 31.—(Concluded)

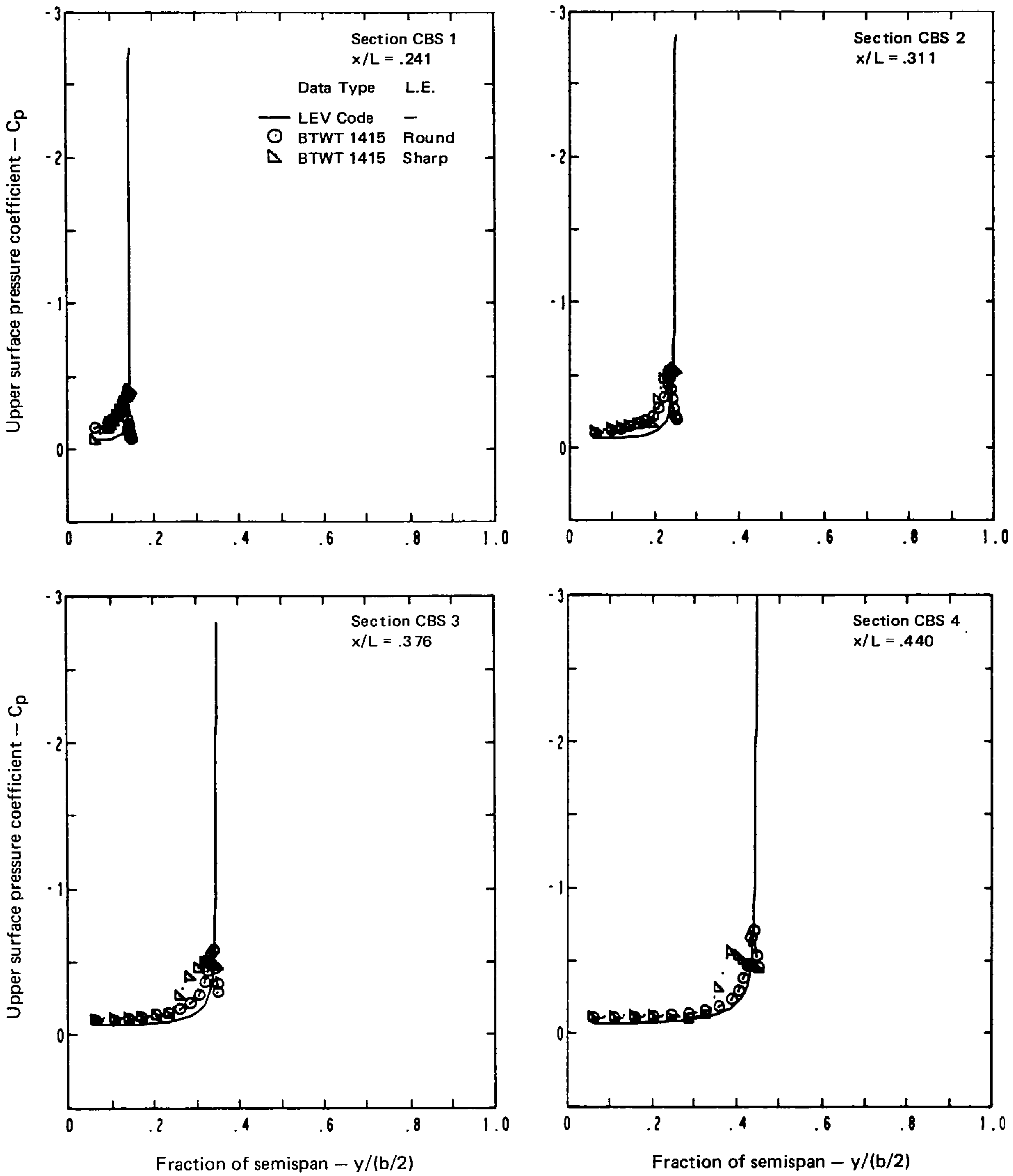

Figure 32.—Upper Surface Pressure Distributions, Flat Wing, Zero Thickness, Denser Wing Paneling, Least-Squares Solution, Weight Factor = 1.0, Δ a = 0.6, M = 0.40, α = 6°

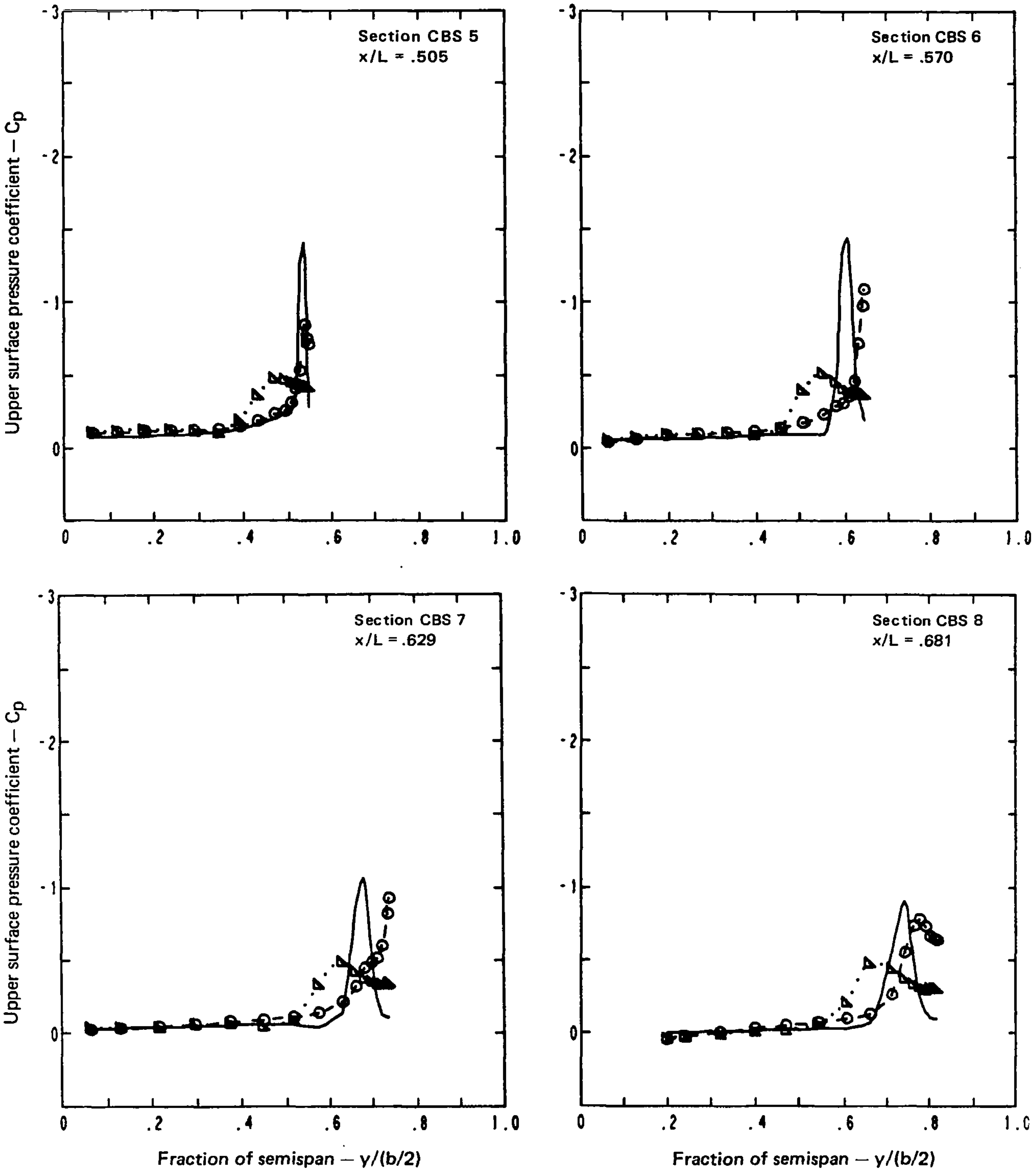

Figure 32.—(Continued)

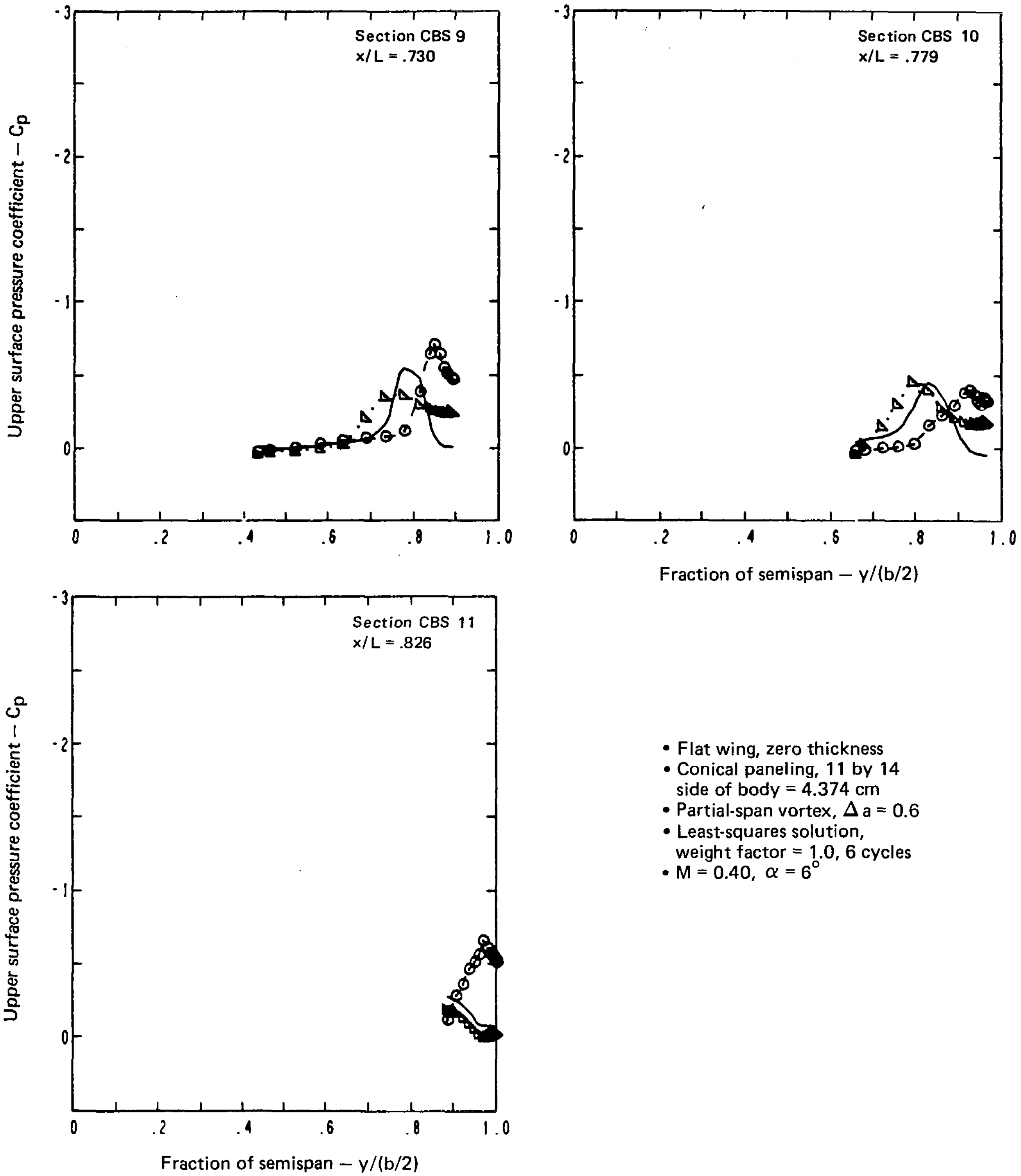

- Flat wing, zero thickness
- Conical paneling, 11 by 14
  side of body = 4.374 cm
- Partial-span vortex, $\Delta a = 0.6$
- Least-squares solution,
  weight factor = 1.0, 6 cycles
- $M = 0.40$, $\alpha = 6^{\circ}$

Figure 32.—(Concluded)

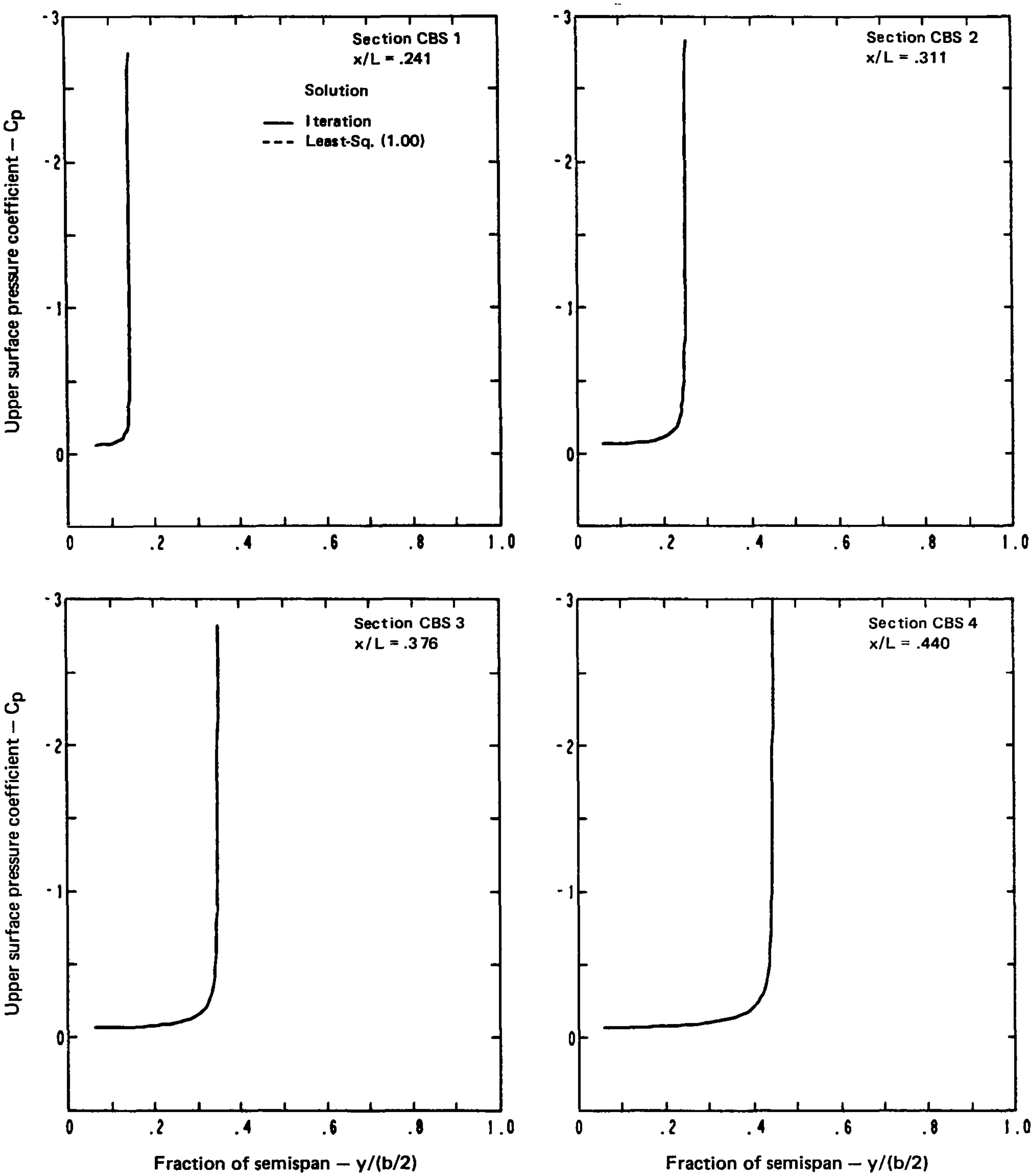

Figure 33.—Effect of Solution Method on Upper Surface Pressure Distribution, Flat Wing, Zero Thickness, $\Delta a = 0.6$, $M = 0.40$, $\alpha = 6°$

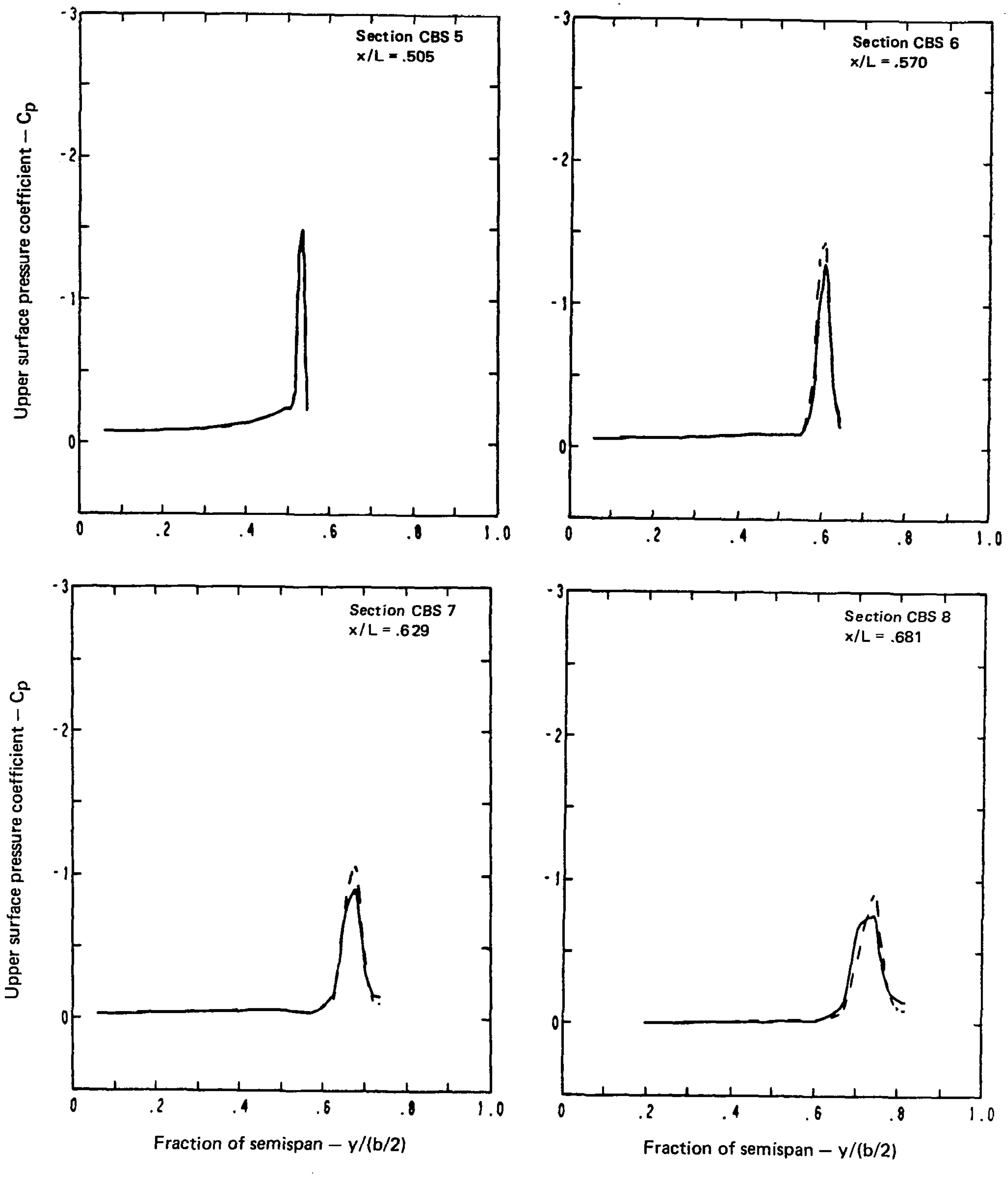

Figure 33.—(Continued)

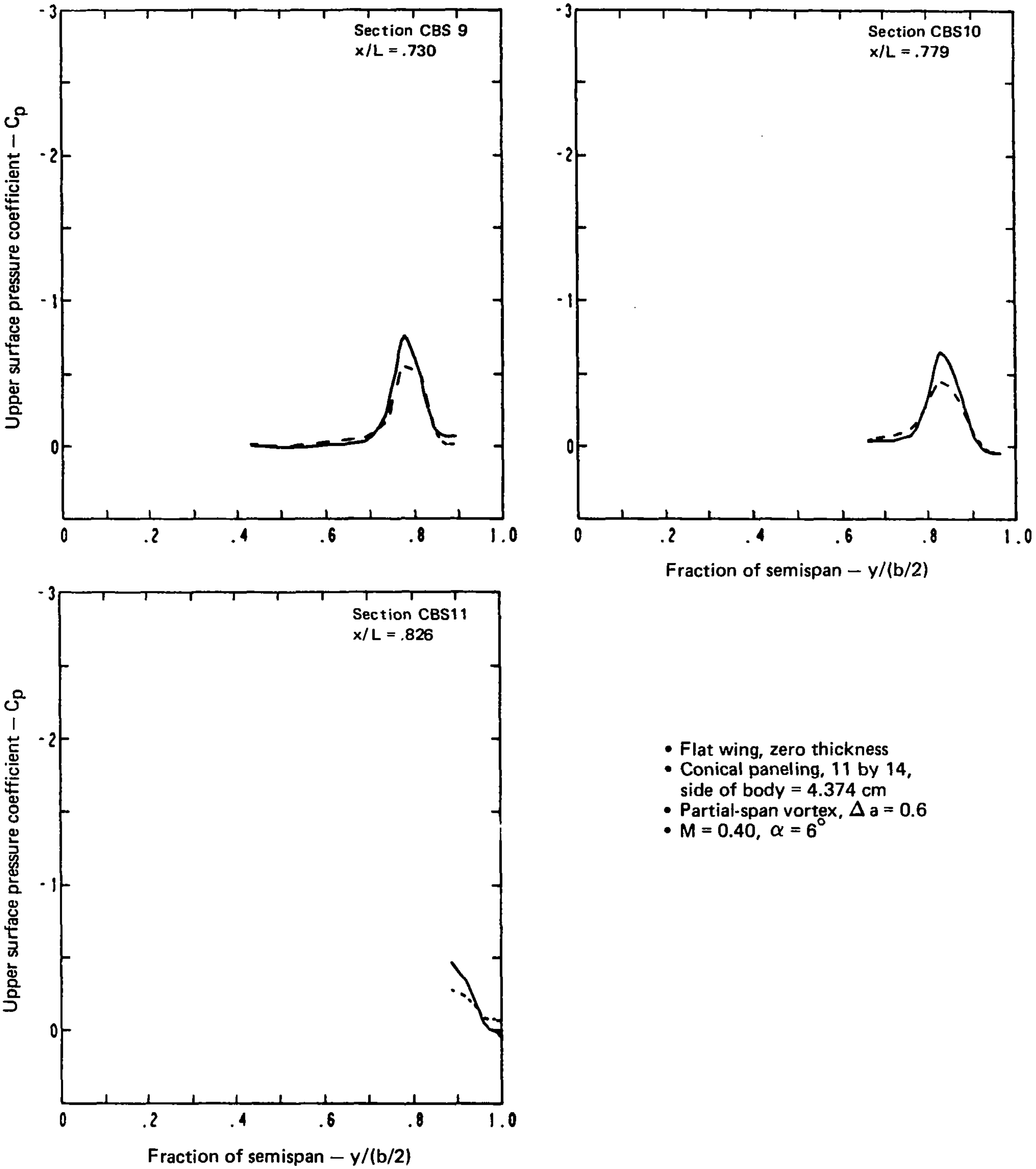

- Flat wing, zero thickness
- Conical paneling, 11 by 14, side of body = 4.374 cm
- Partial-span vortex, Δ a = 0.6
- M = 0.40, $\alpha = 6^\circ$

Figure 33.—(Concluded)

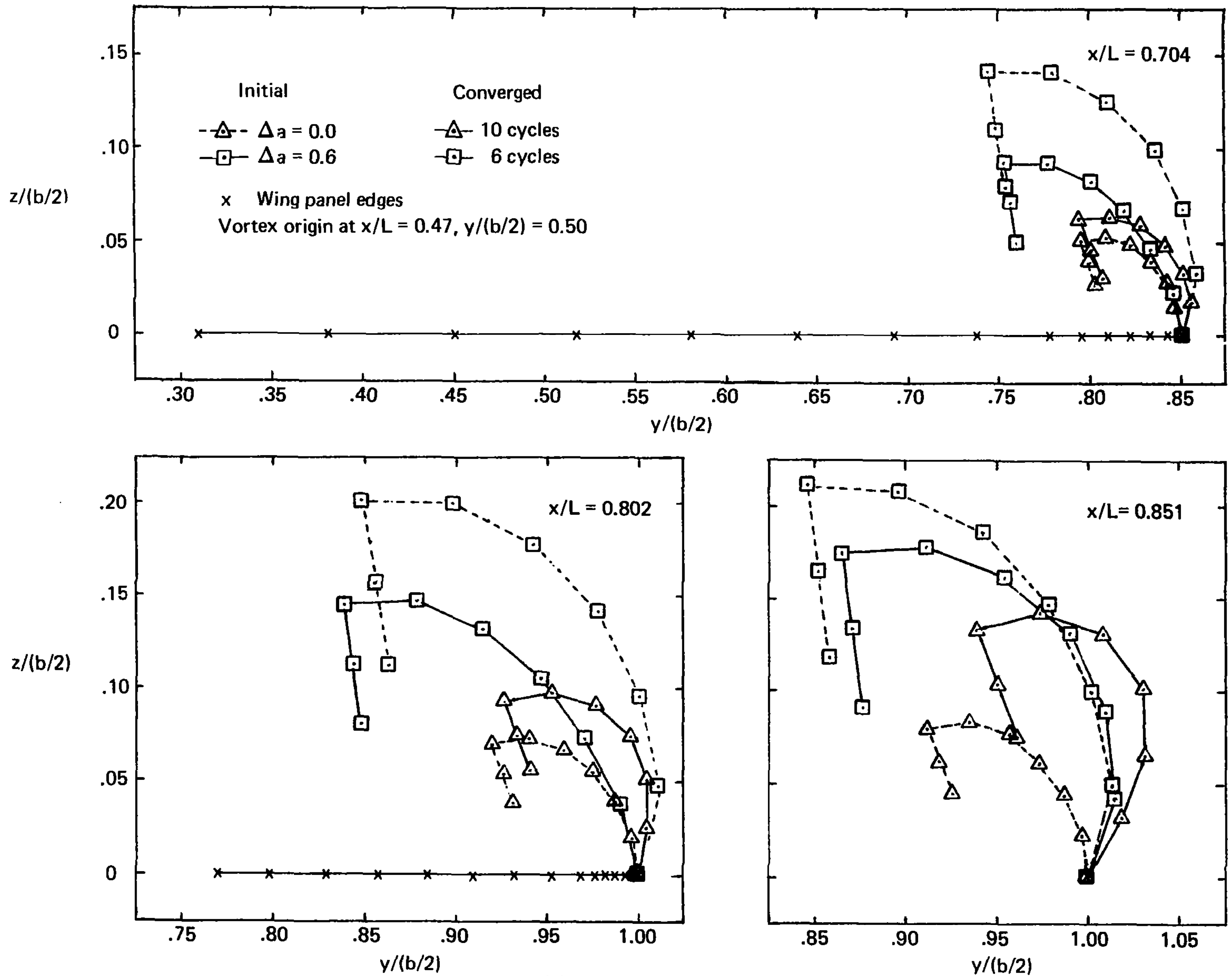

(a) Effect of Initial Vortex Size

Figure 34.—Geometry of Panel Edges at Constant Body Stations, Effect of Initial Vortex Size and Solution Method on Converged Vortex Shape, Flat Wing, Zero Thickness, $M = 0.40$, $\alpha = 6°$

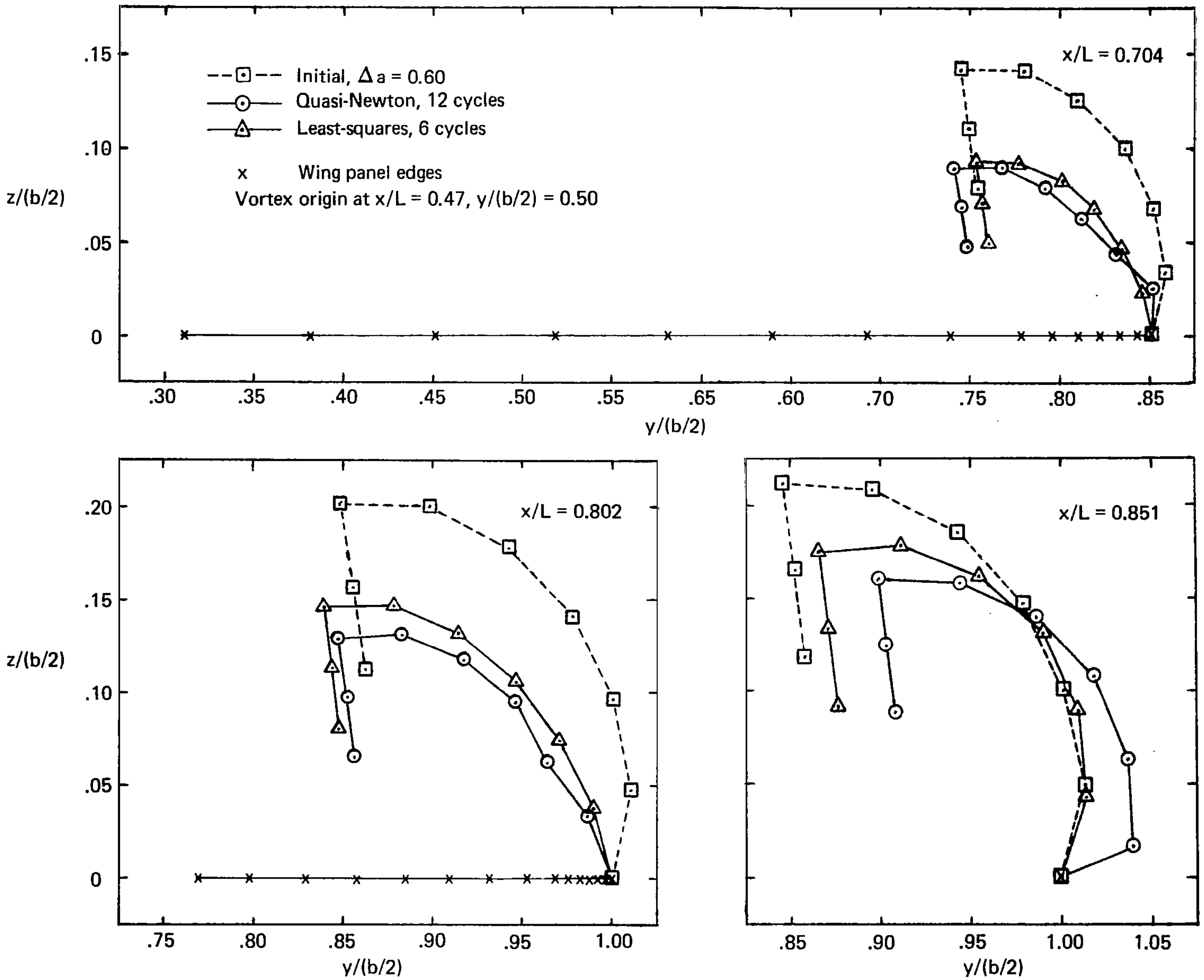

(b) Effect of Solution Type

Figure 34.—(Concluded)

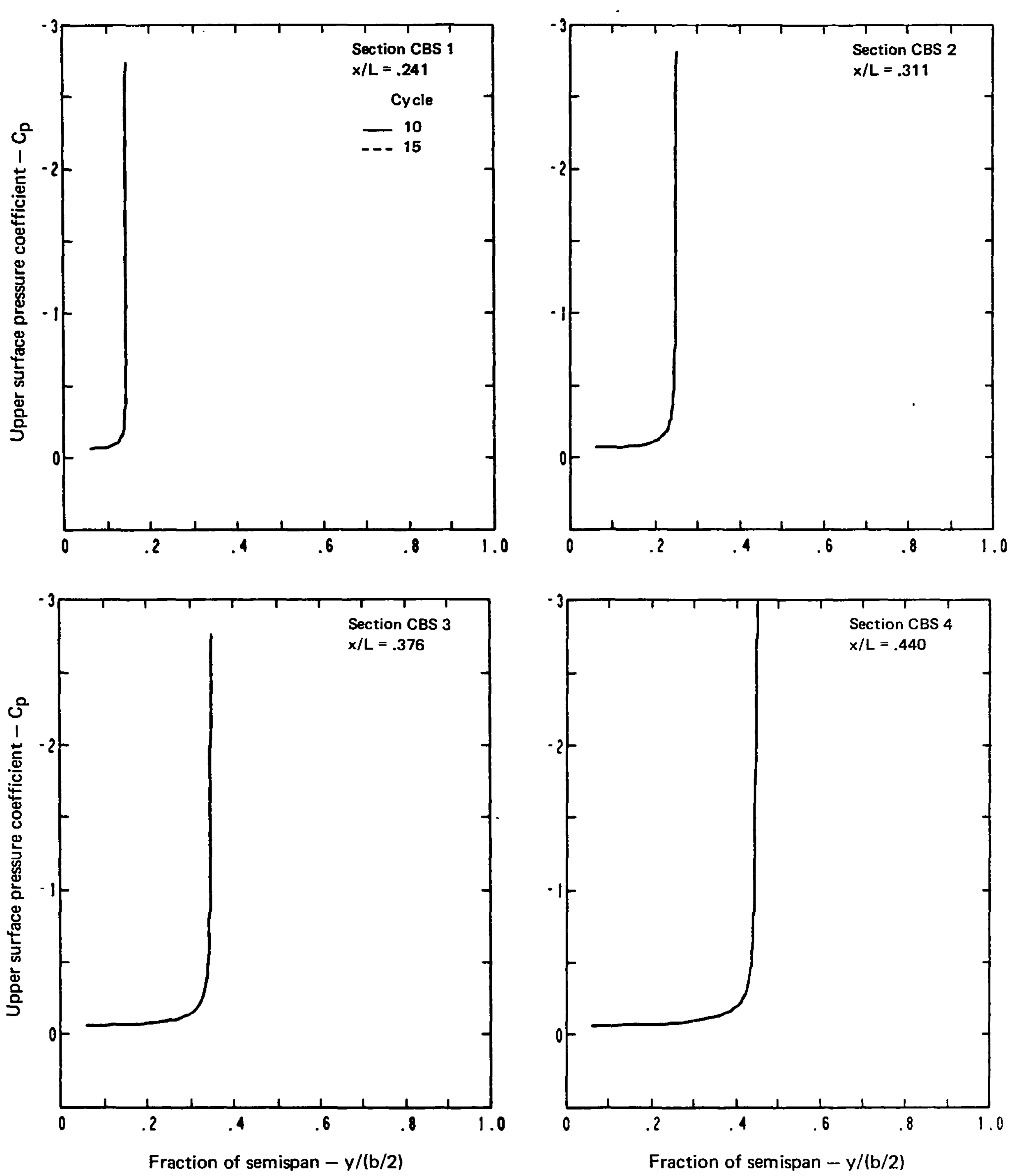

Figure 35.—Comparison of Upper Surface Pressure Distributions for Two Cycles, Flat Wing, Zero Thickness, $\Delta a = 0.0$, $M = 0.40$, $\alpha = 6°$

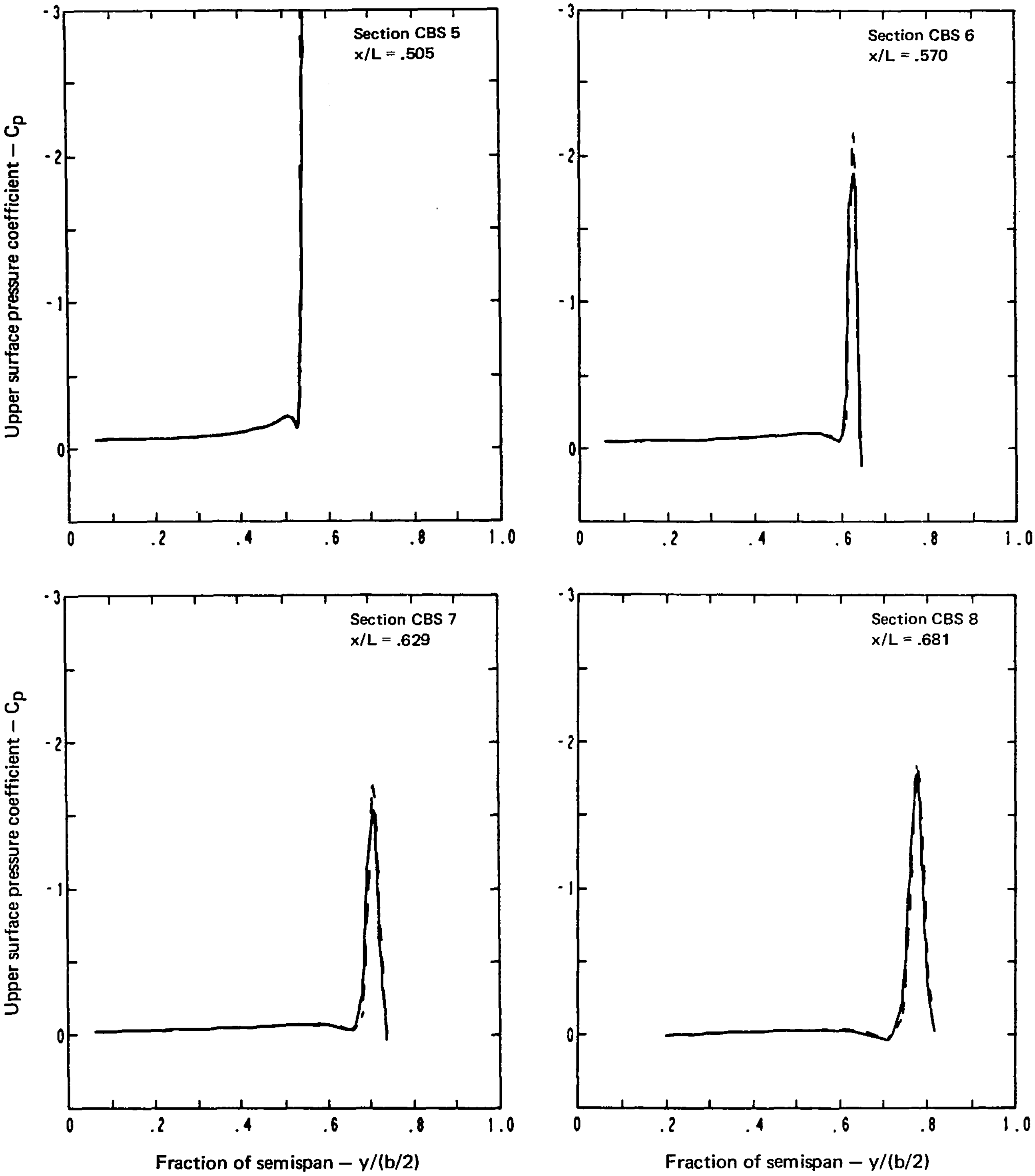

Figure 35.–(Continued)

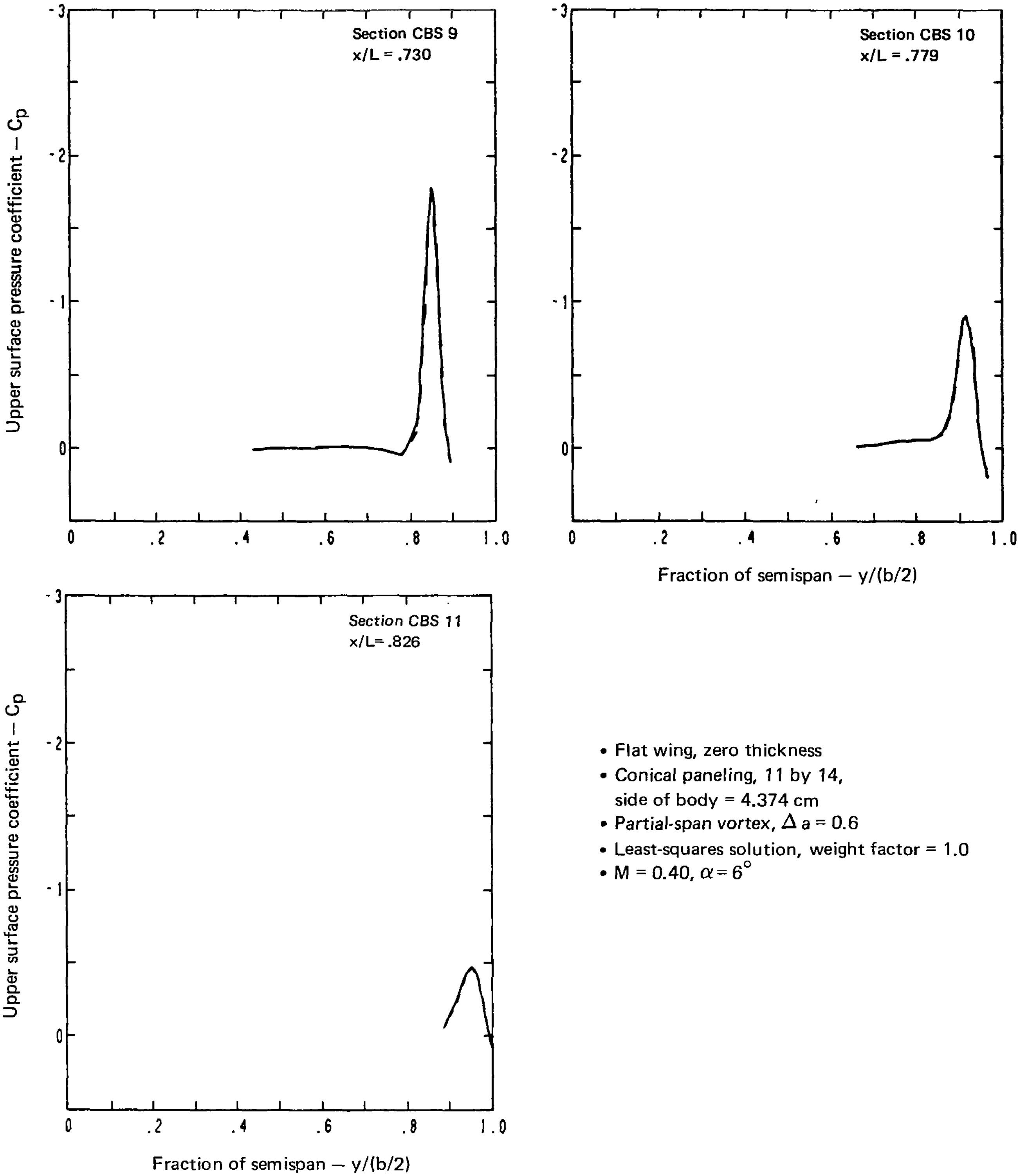

- Flat wing, zero thickness
- Conical paneling, 11 by 14,
  side of body = 4.374 cm
- Partial-span vortex, $\Delta a = 0.6$
- Least-squares solution, weight factor = 1.0
- $M = 0.40$, $\alpha = 6^\circ$

Figure 35.—(Concluded)

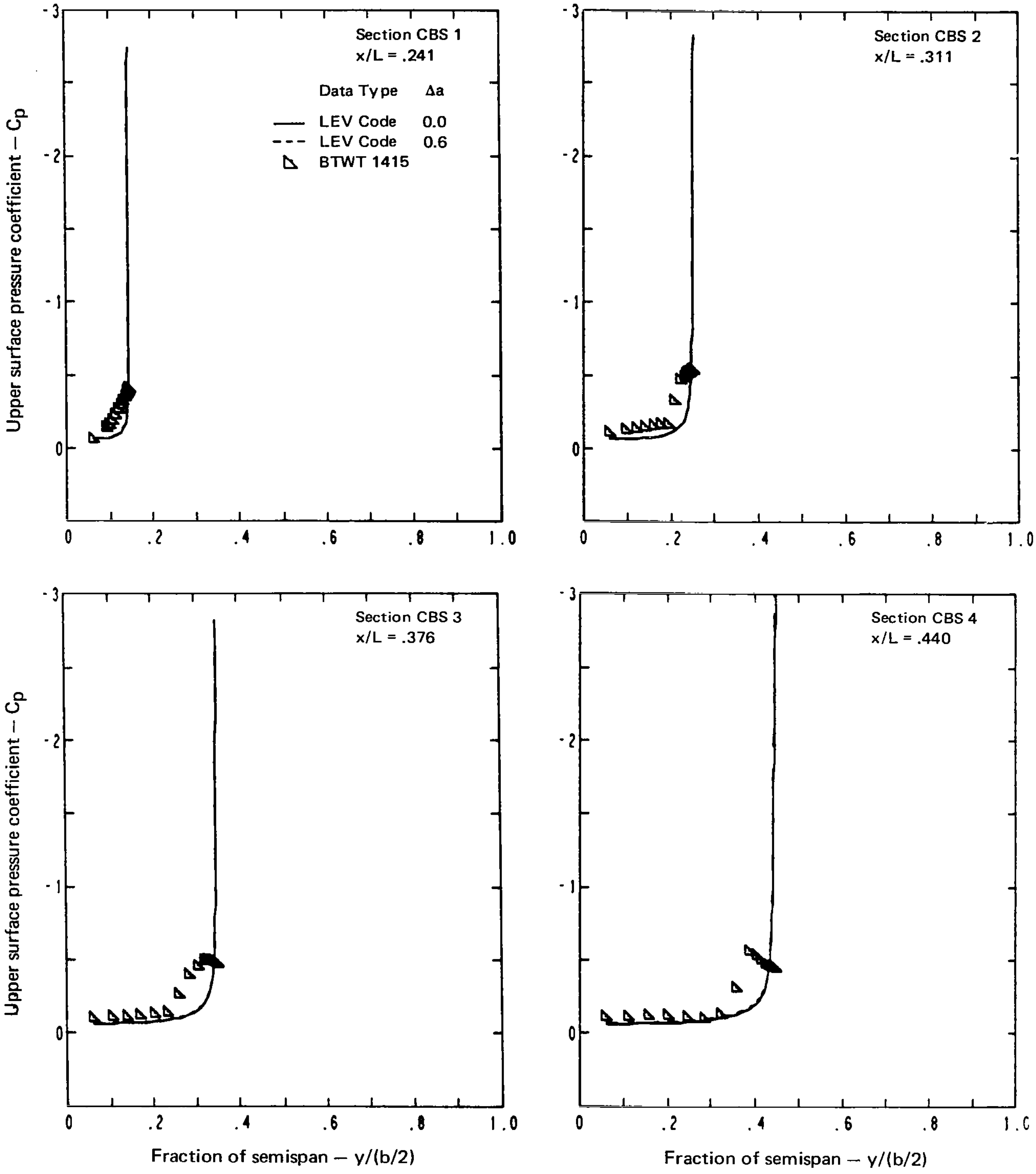

Figure 36.—Effect of Initial Vortex Size, Upper Surface Pressure Distributions, Flat Wing, Zero Thickness, Least-Squares Solution, M = 0.40, α = 6°

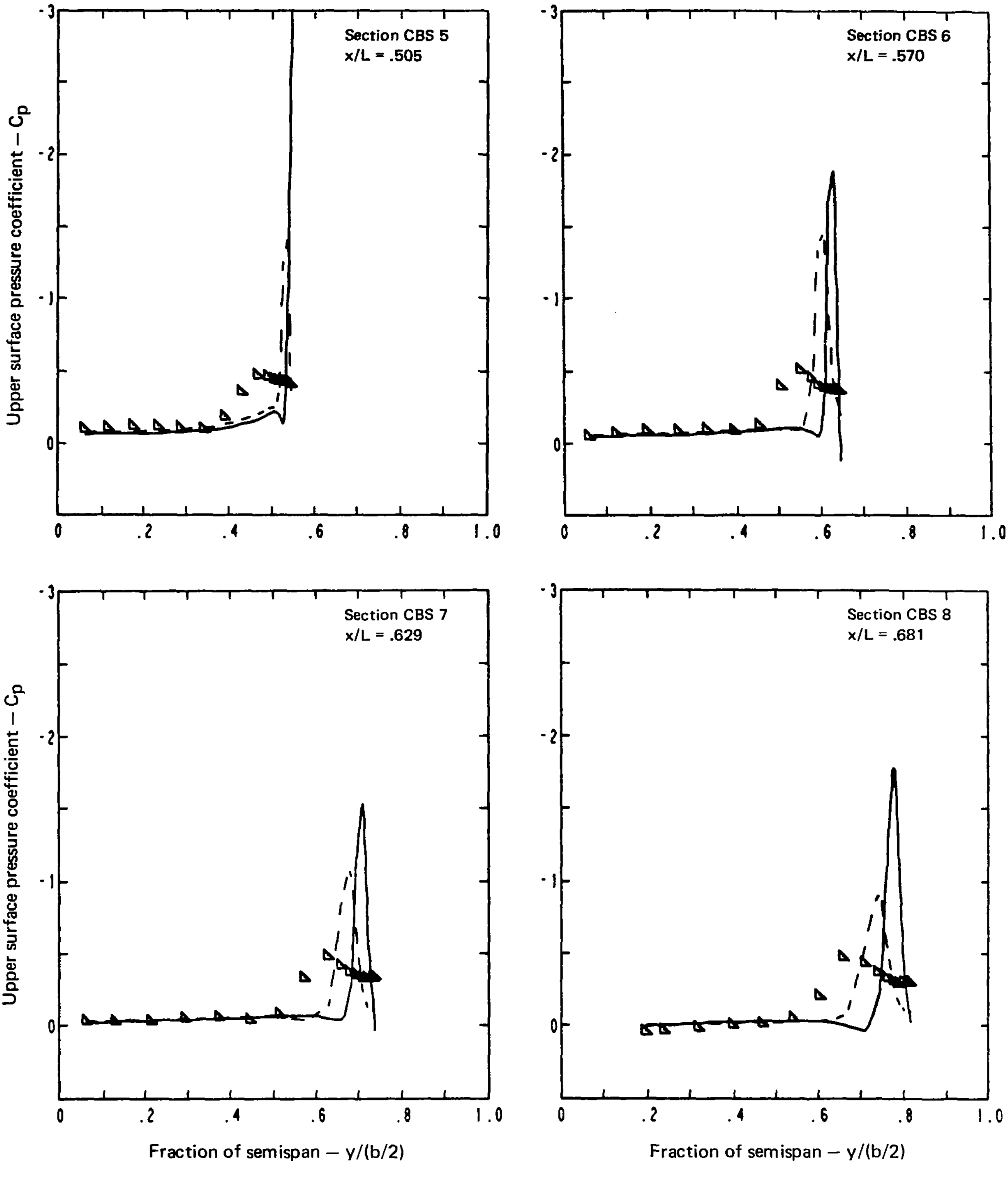

Figure 36.—(Continued)

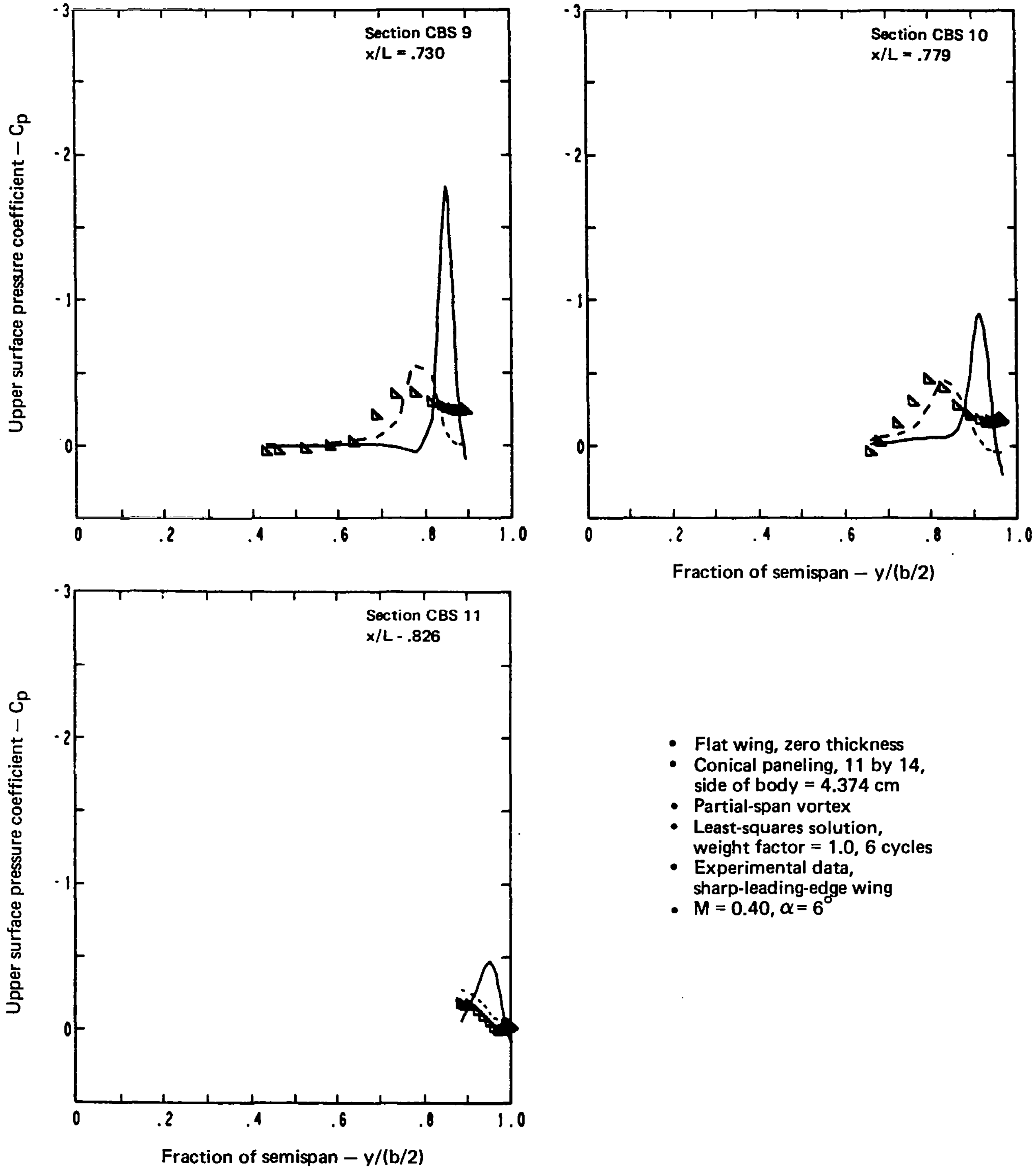

Figure 36.—(Concluded).

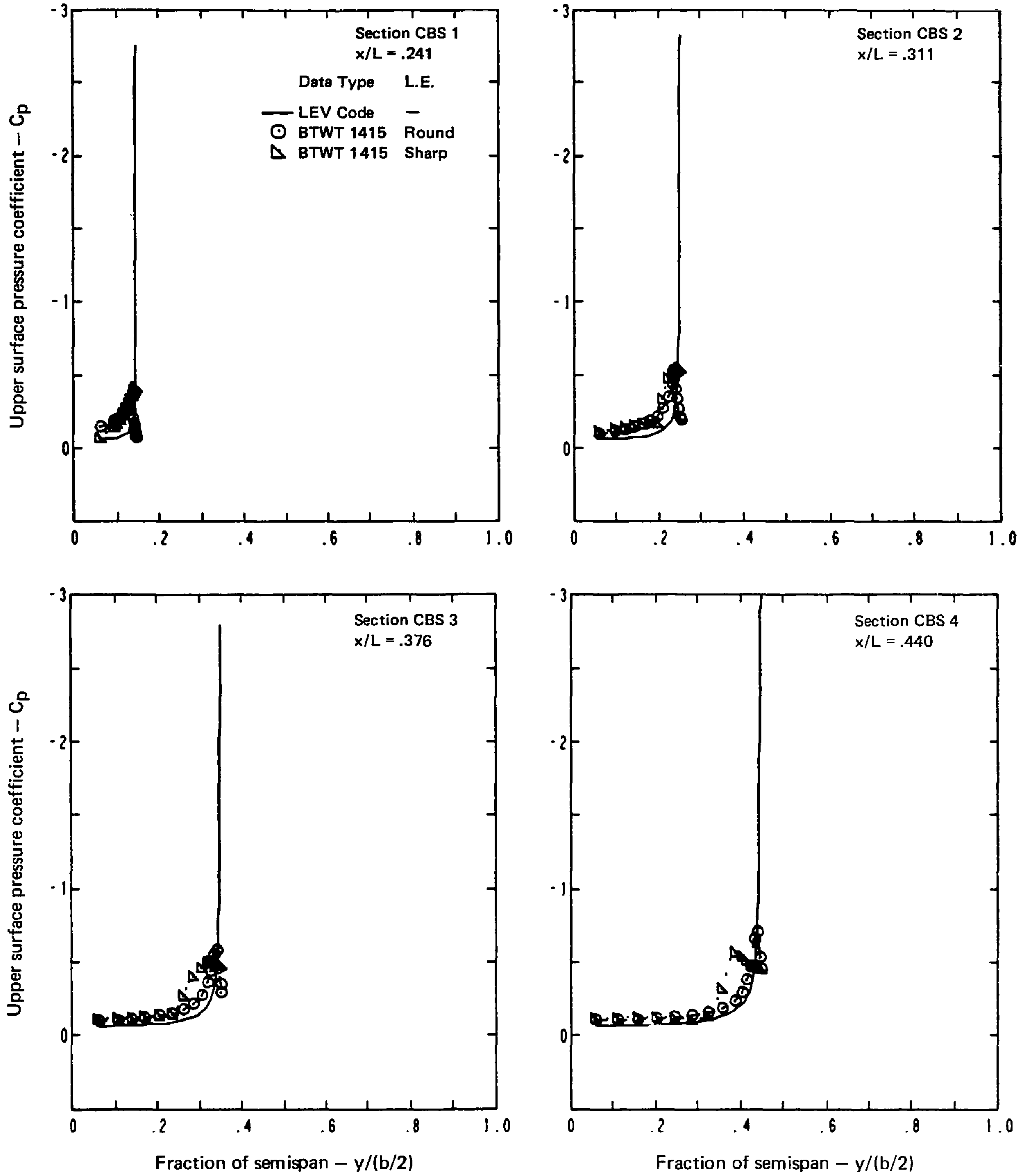

Figure 37.—Upper Surface Pressure Distributions, Flat Wing, Zero Thickness, Denser Wing Paneling, Least-Squares Solution, Weight Factor = 5.0, $\Delta a = 0.6$, $M = 0.40$, $\alpha = 6^\circ$

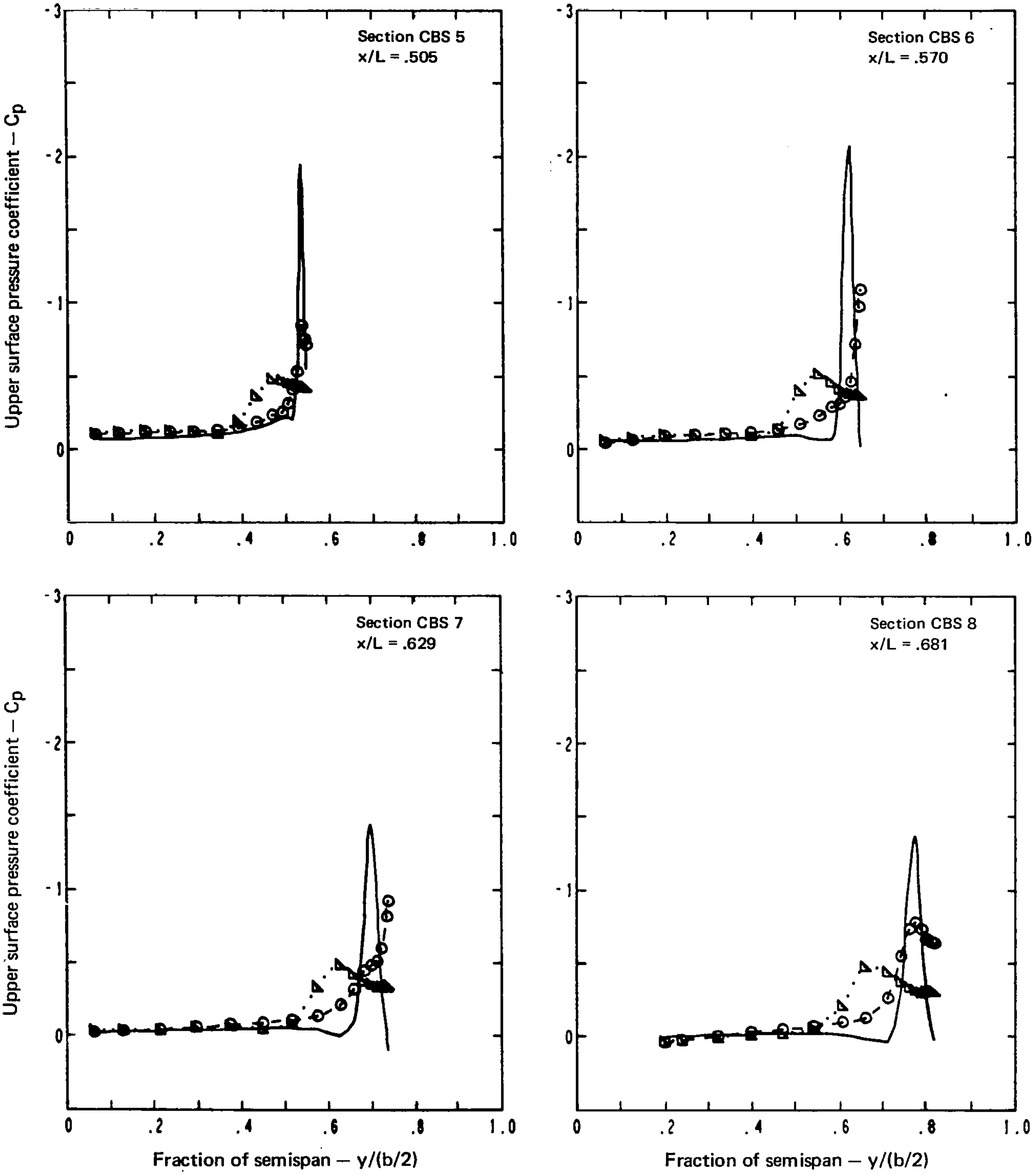

Figure 37.—(Continued)

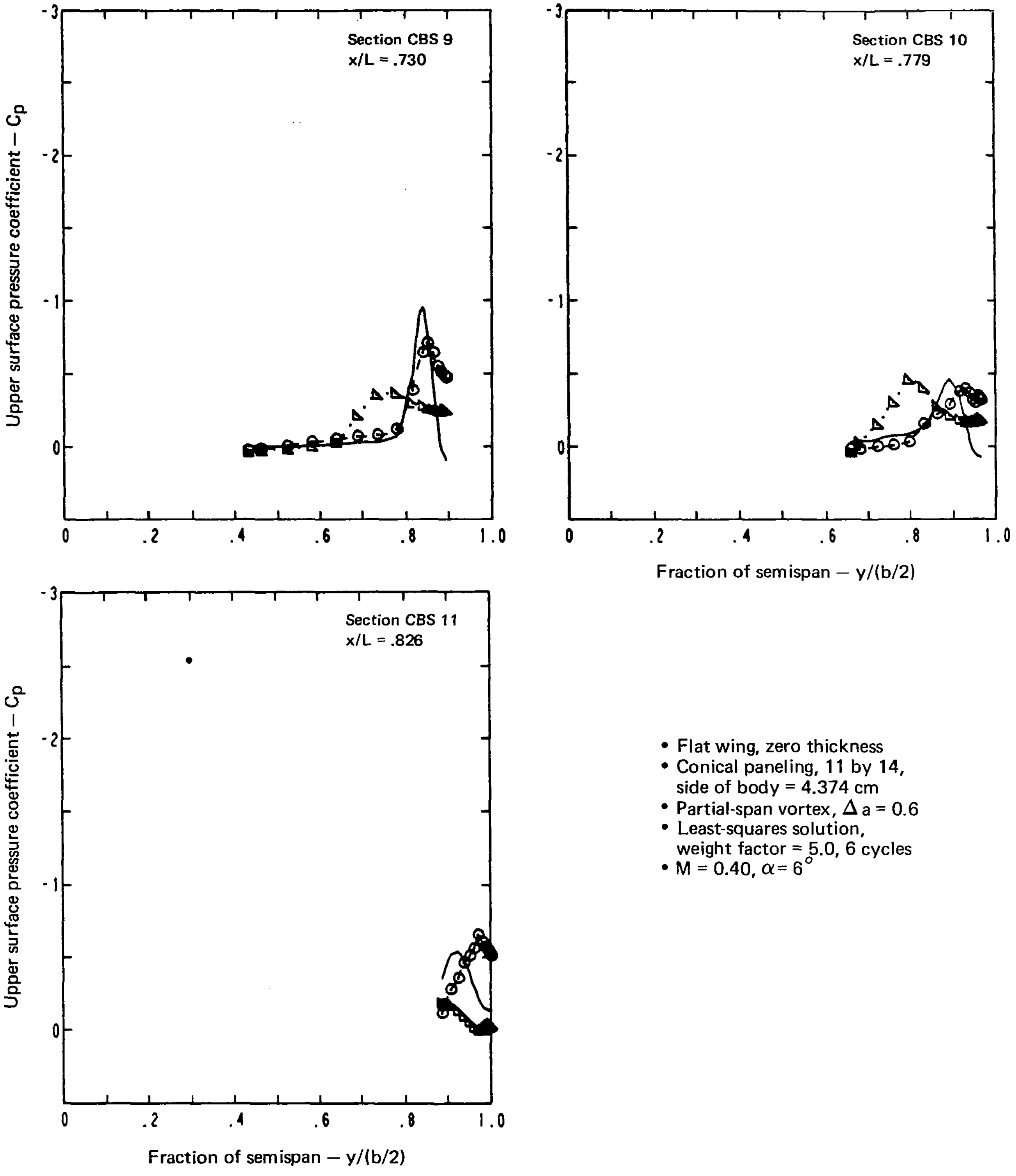

- Flat wing, zero thickness
- Conical paneling, 11 by 14, side of body = 4.374 cm
- Partial-span vortex, Δa = 0.6
- Least-squares solution, weight factor = 5.0, 6 cycles
- M = 0.40, α = 6°

Figure 37.—(Concluded)

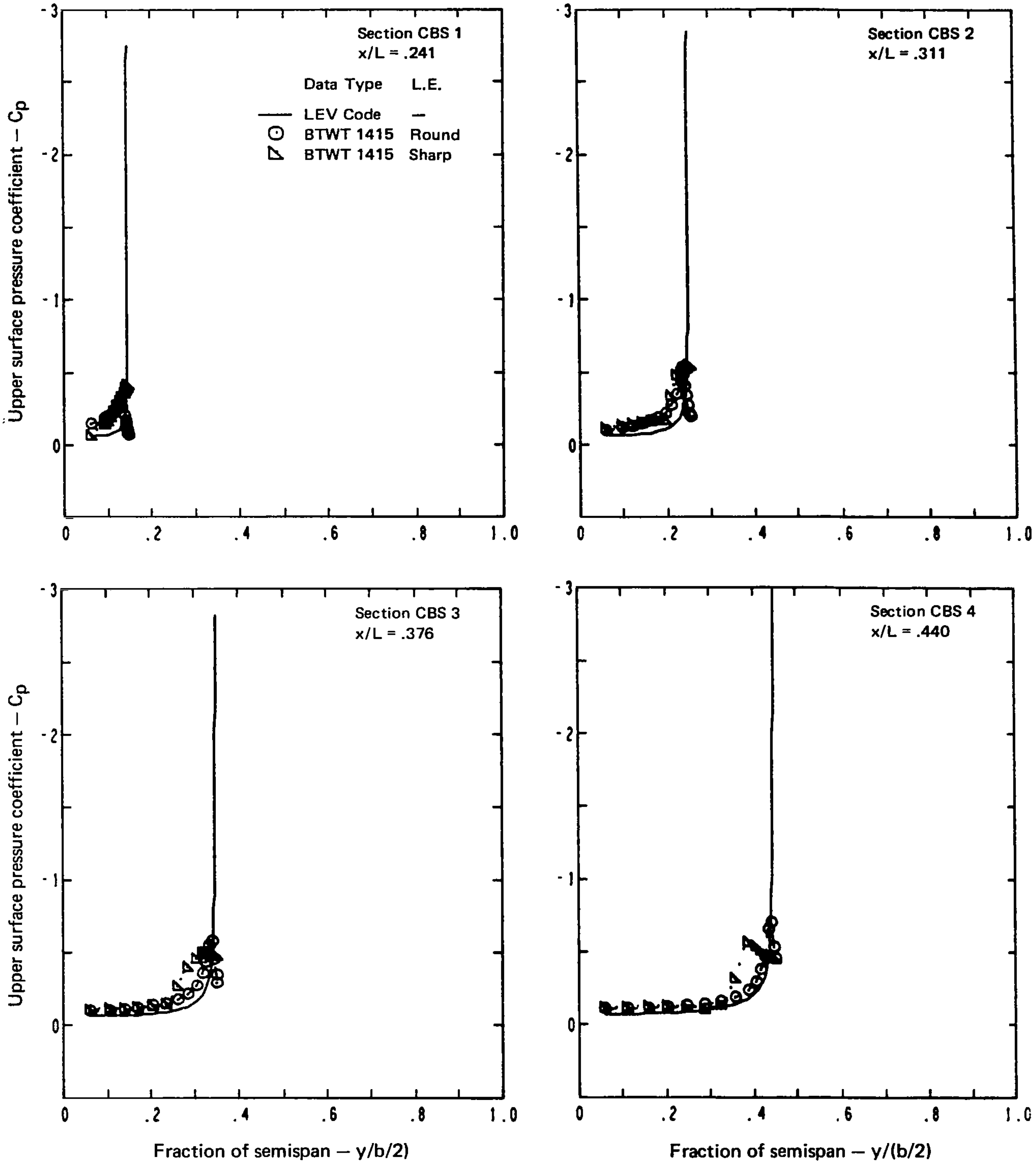

Figure 38.—Upper Surface Pressure Distributions, Flat Wing, Zero Thickness, Denser Wing Paneling, Least-Squares Solution, Weight Factor = 0.5, Δa = 0.6, M = 0.40, α = 6°

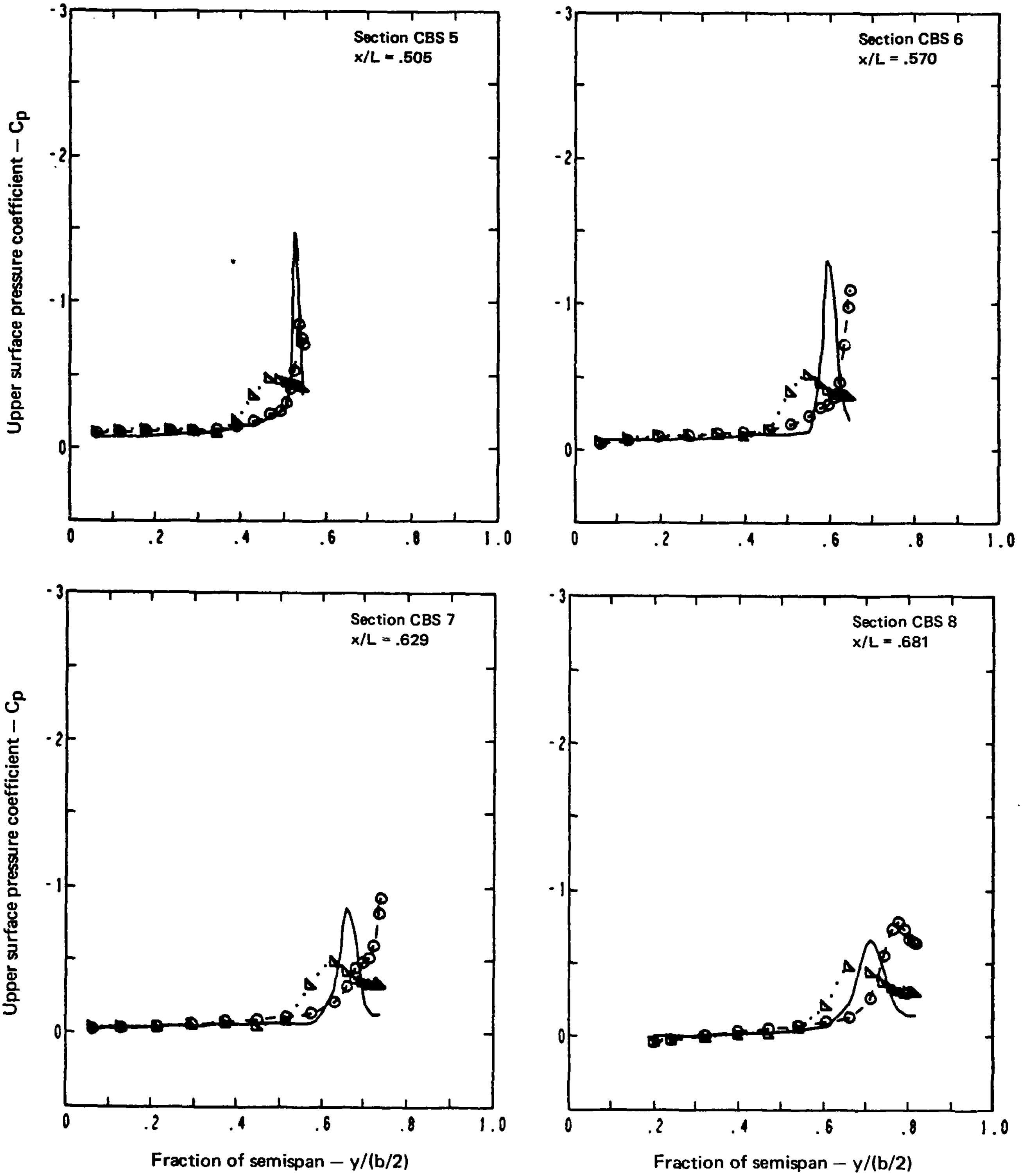

Figure 38.—(Continued)

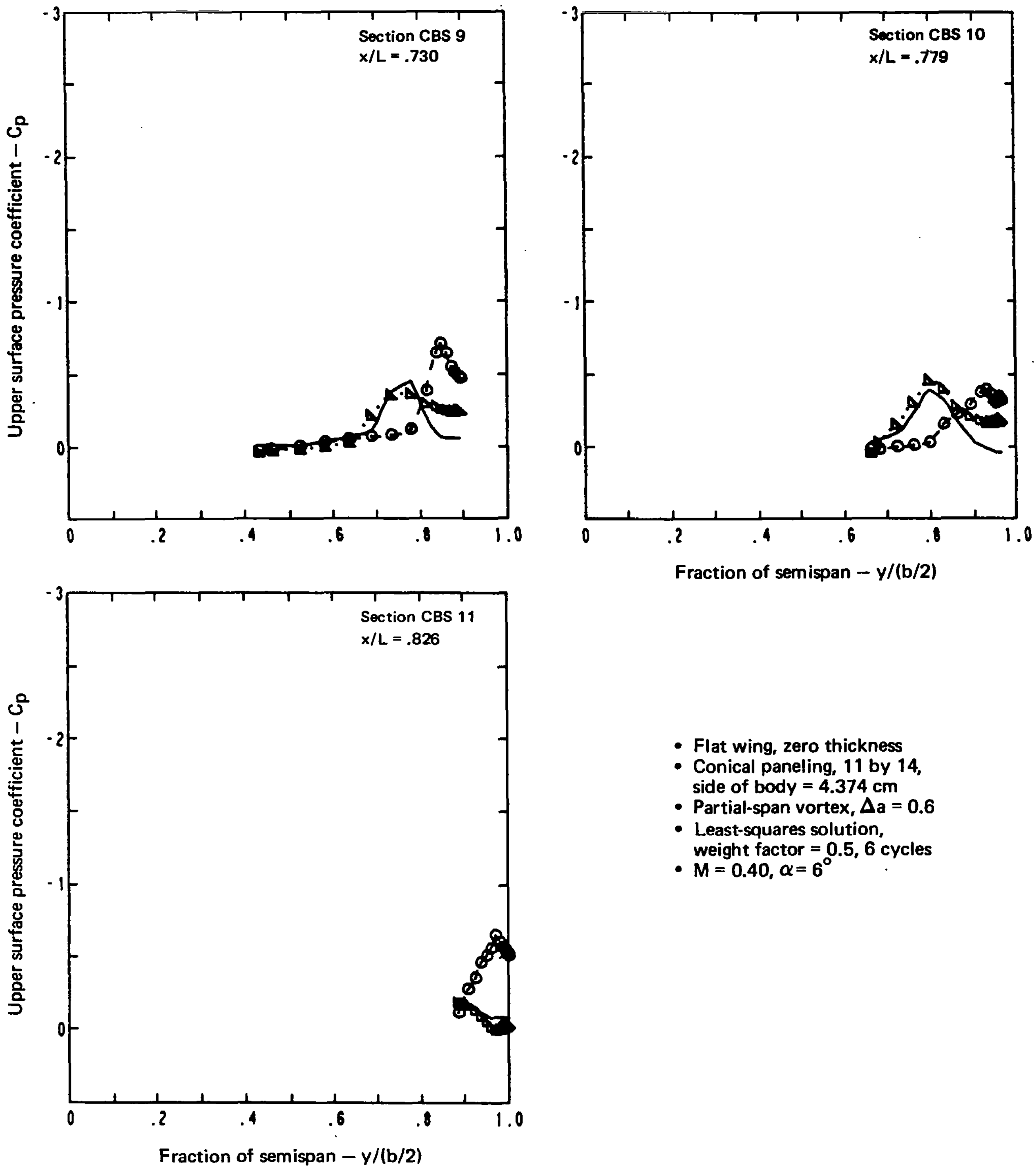

- Flat wing, zero thickness
- Conical paneling, 11 by 14, side of body = 4.374 cm
- Partial-span vortex, Δa = 0.6
- Least-squares solution, weight factor = 0.5, 6 cycles
- $M = 0.40$, $\alpha = 6^\circ$

Figure 38.—(Concluded)

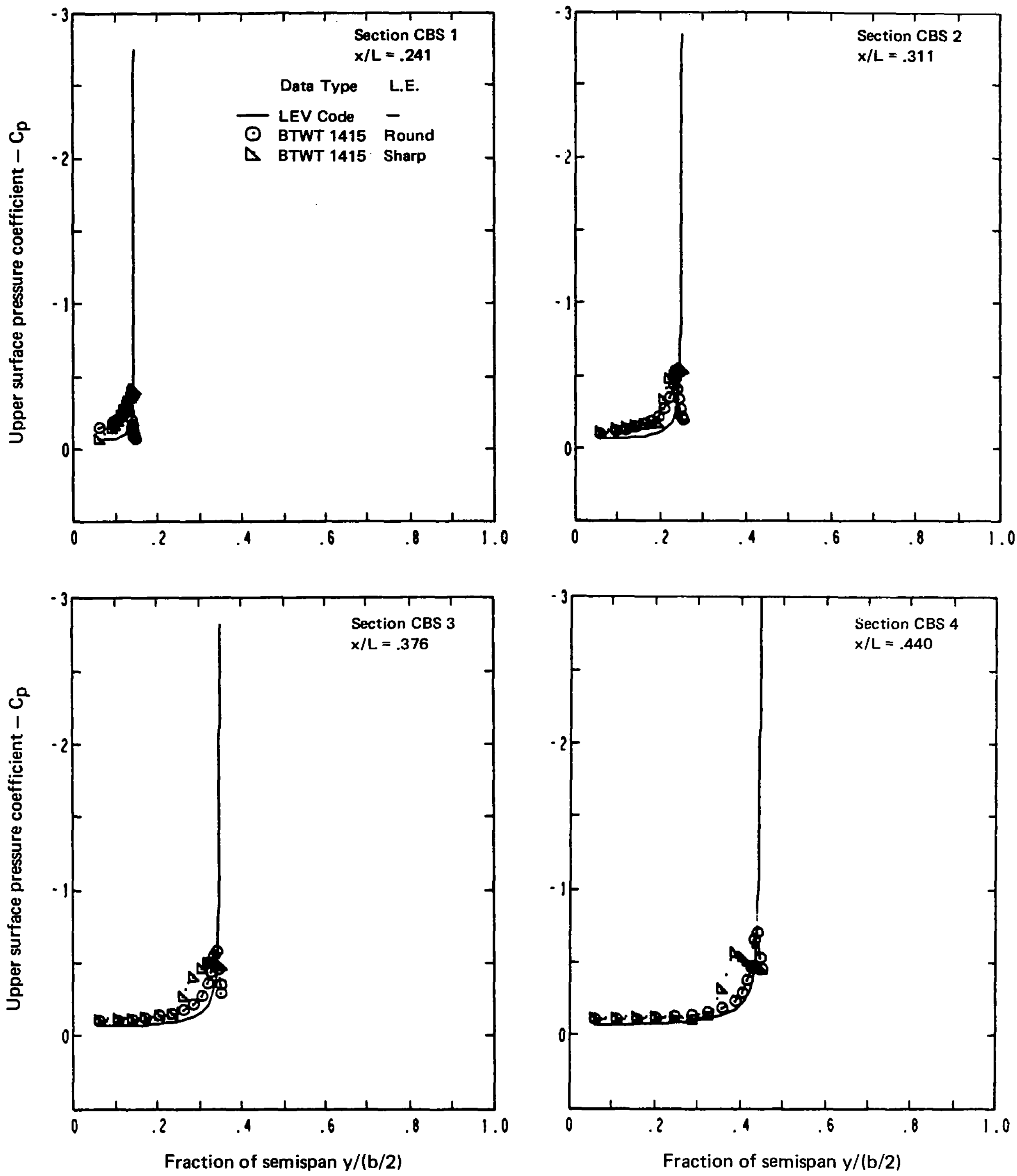

Figure 39.—Upper Surface Pressure Distributions, Flat Wing, Zero Thickness, Denser Wing Paneling, Least-Squares Solution, Weight Factor = 0.2, Δa = 0.6, M = 0.40, α = 6°

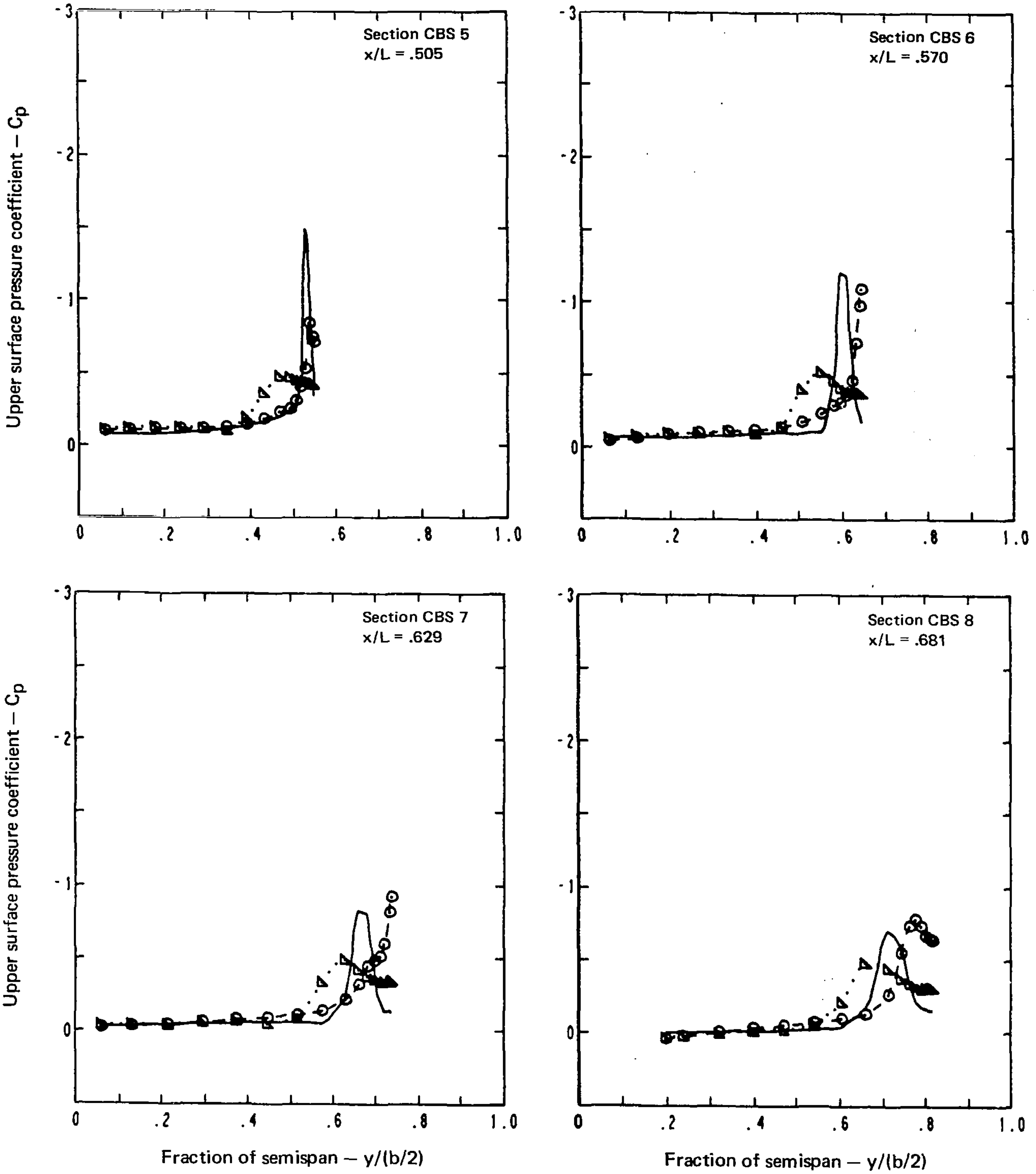

Figure 39.—(Continued)

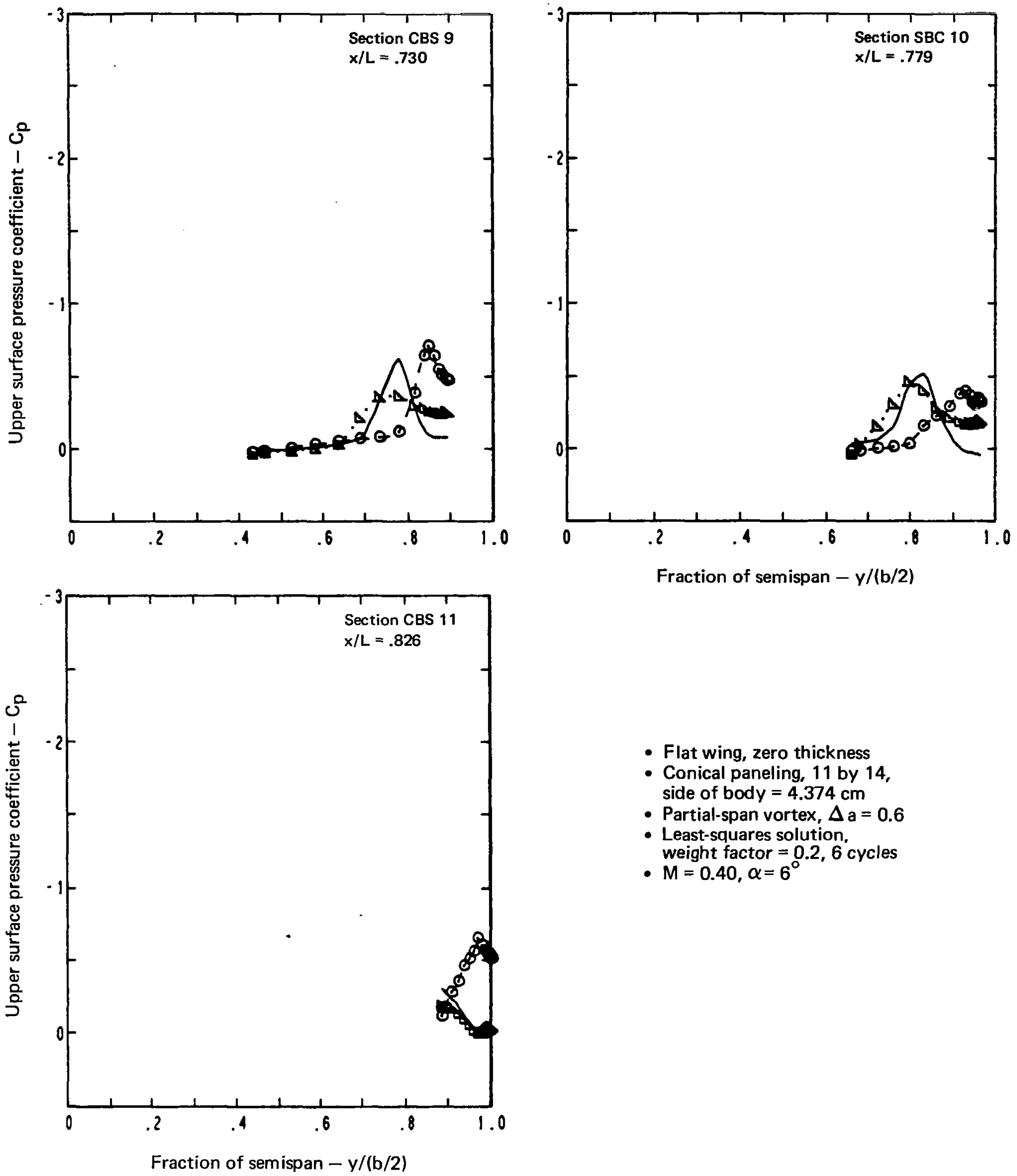

- Flat wing, zero thickness
- Conical paneling, 11 by 14, side of body = 4.374 cm
- Partial-span vortex, $\Delta a = 0.6$
- Least-squares solution, weight factor = 0.2, 6 cycles
- $M = 0.40$, $\alpha = 6^\circ$

Figure 39.—(Concluded)

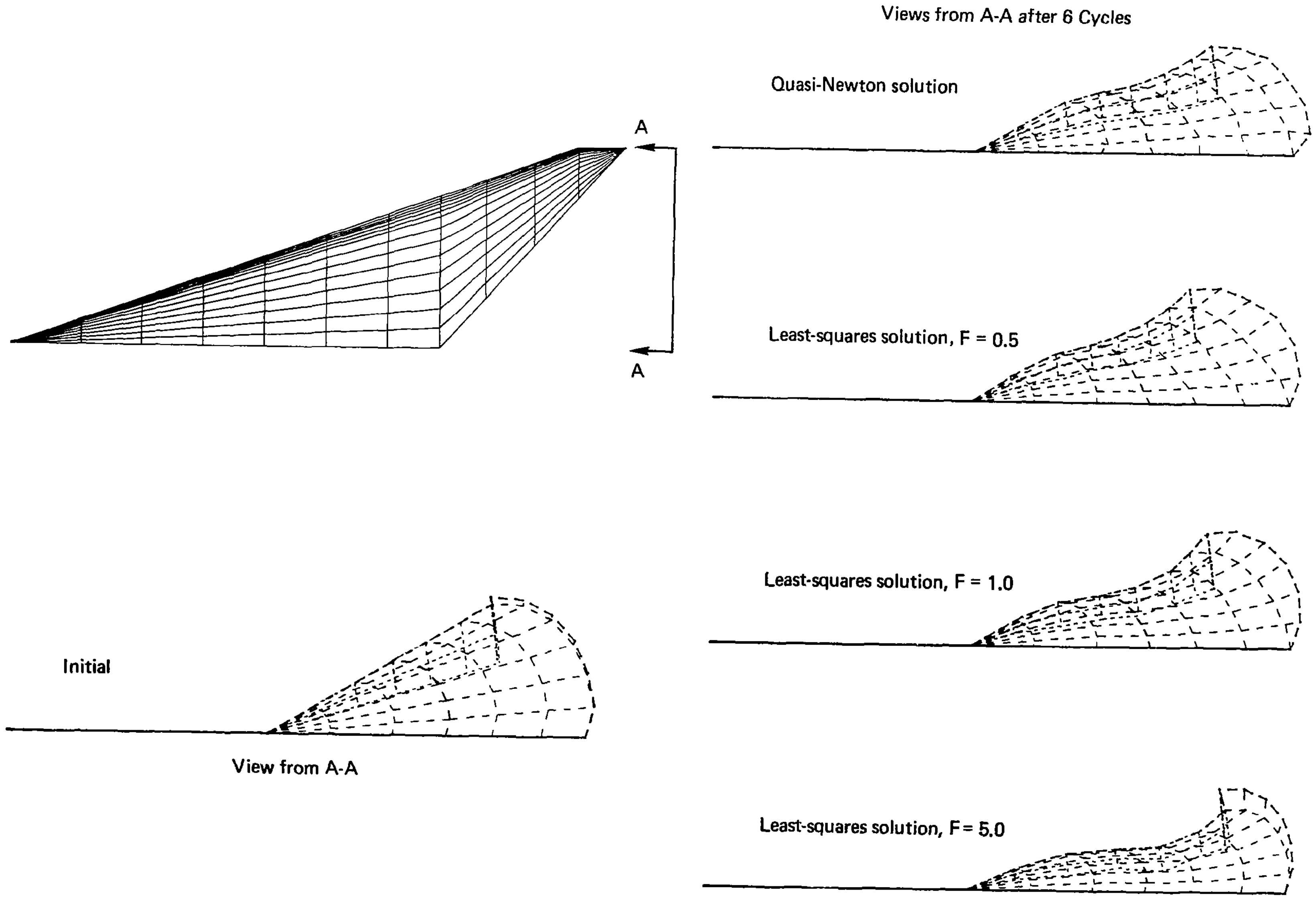

Figure 40.—Effect of Solution Type and Weight Factor (F) on Twist Function, Rear View of Vortex Geometry, Flat Wing, Zero Thickness, $\Delta a = 0.6$, $M = 0.40$, $\alpha = 6°$

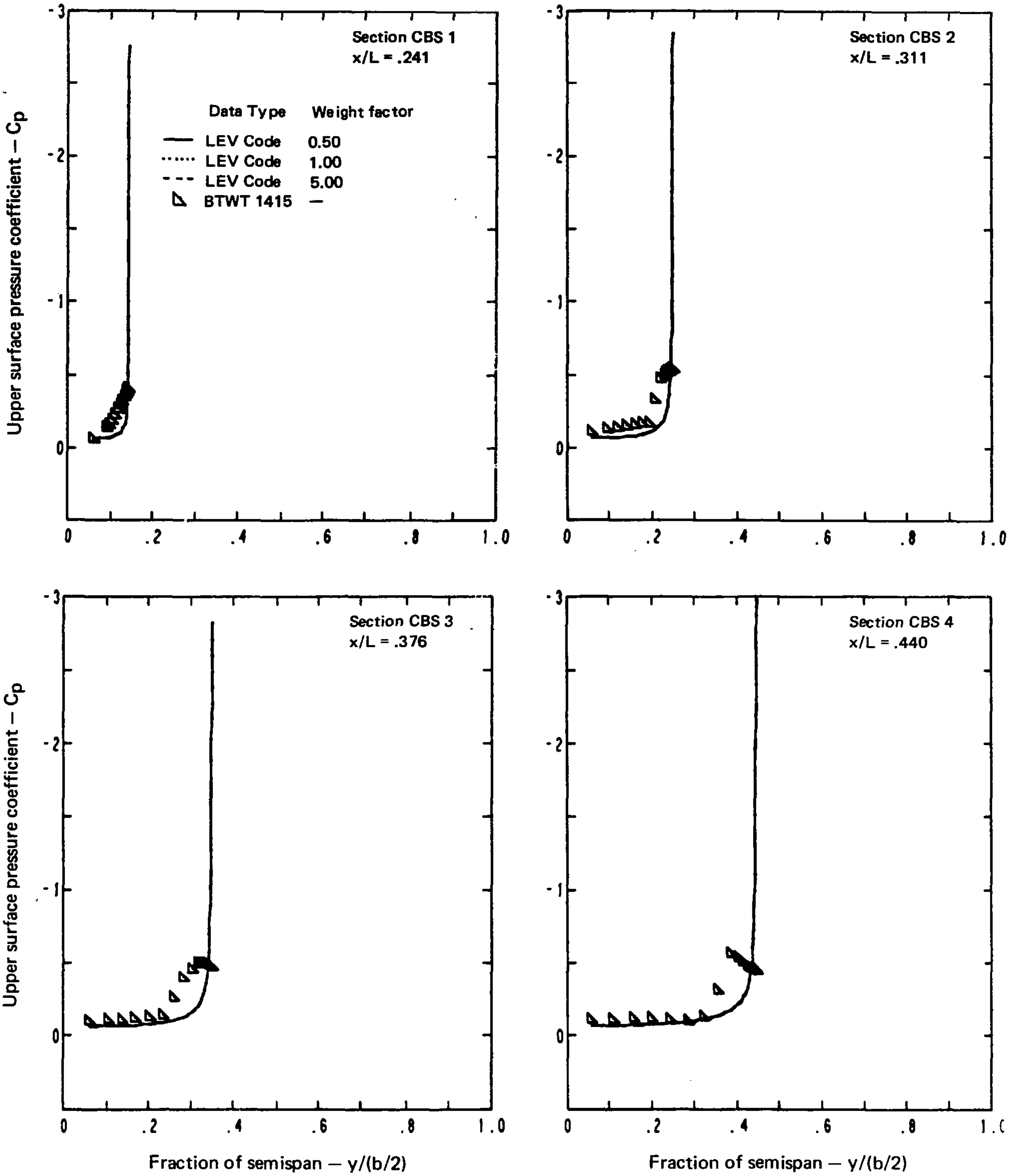

Figure 41.–Effect of Weight Factor on Twist Function, Upper Surface Pressure Distributions, Flat Wing, Zero Thickness, Least-Squares Solution, $\Delta a = 0.6$, $M = 0.40$, $\alpha = 6^0$

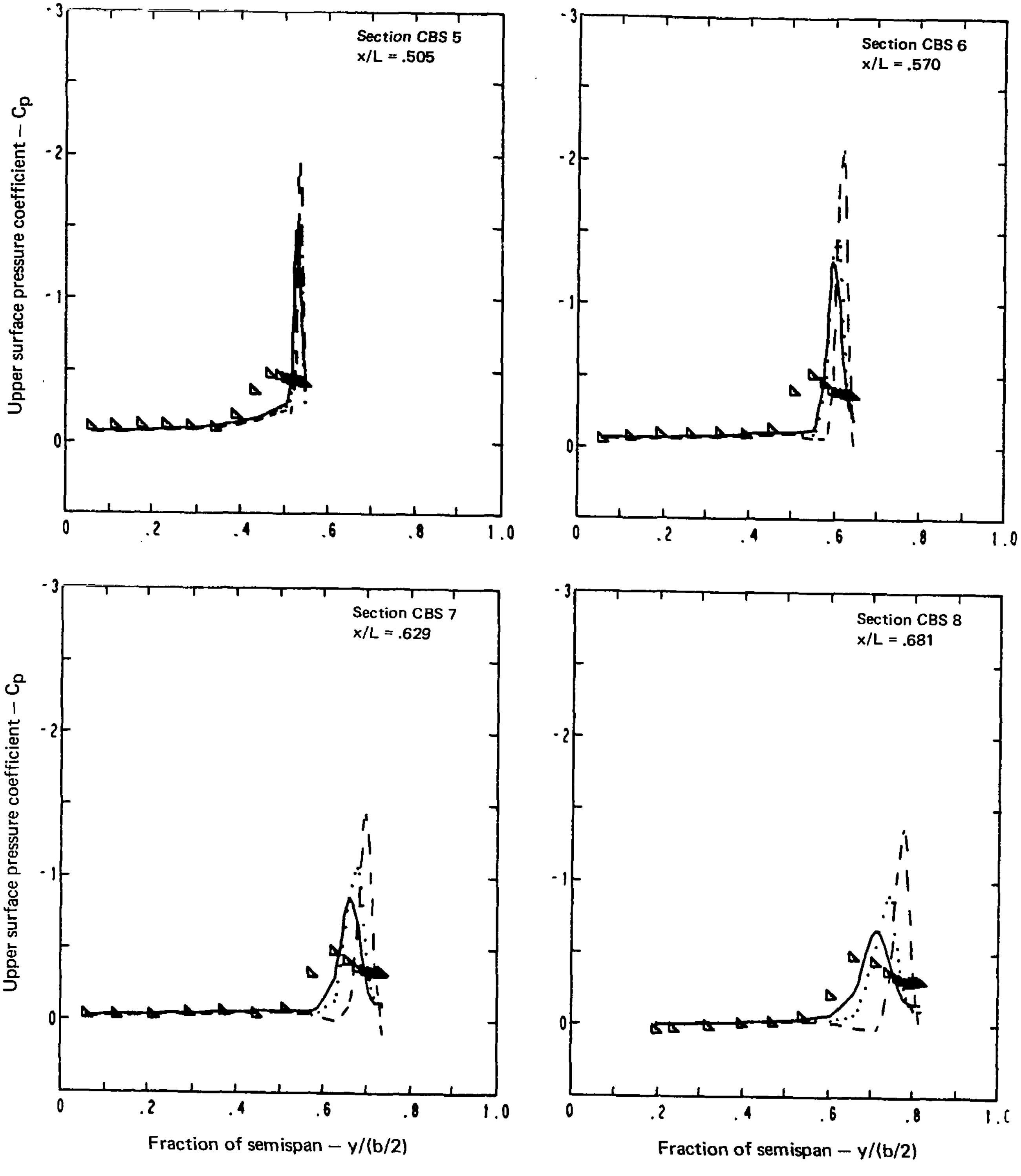

Figure 41.–(Continued)

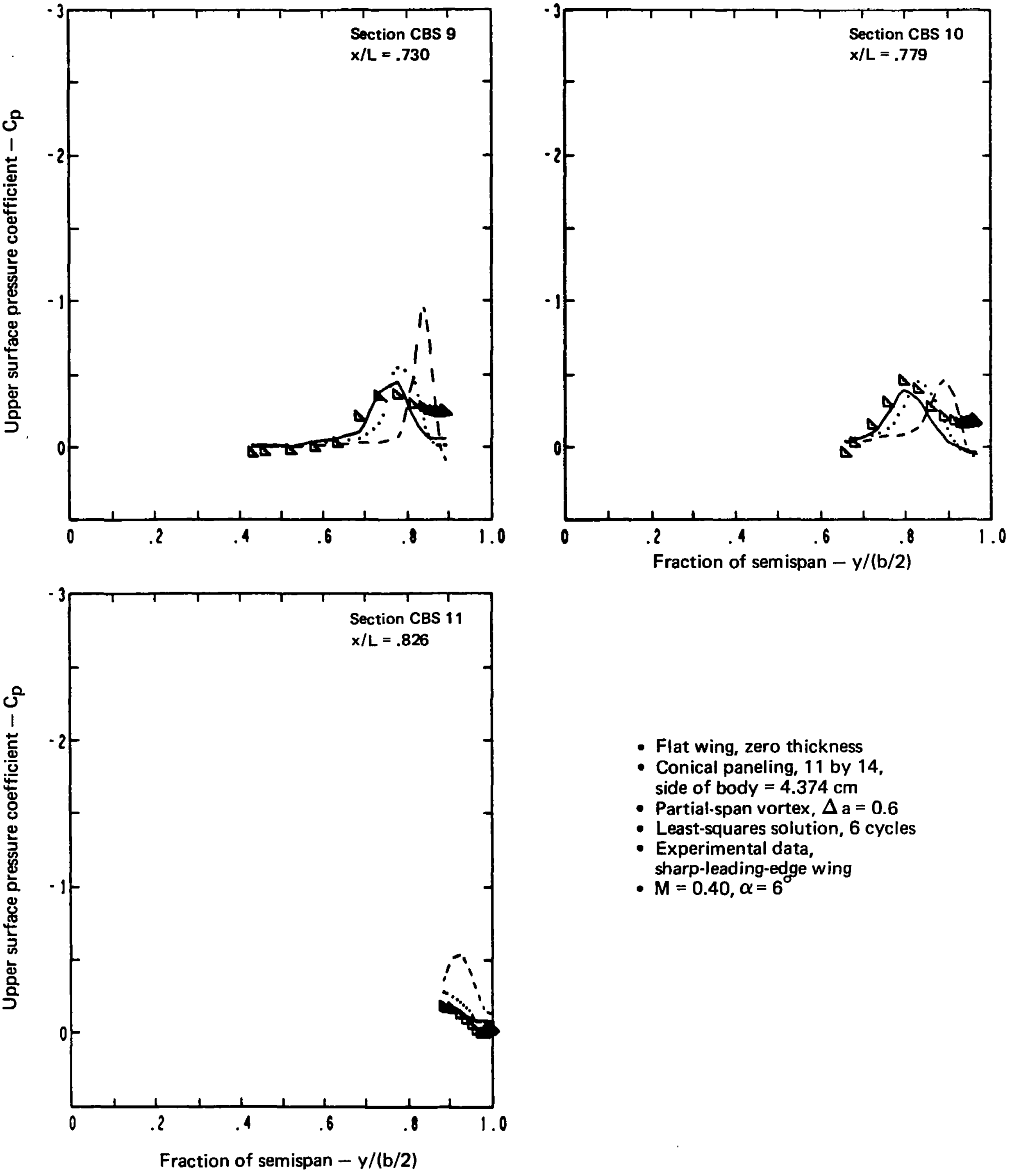

- Flat wing, zero thickness
- Conical paneling, 11 by 14, side of body = 4.374 cm
- Partial-span vortex, Δ a = 0.6
- Least-squares solution, 6 cycles
- Experimental data, sharp-leading-edge wing
- M = 0.40, α = 6°

Figure 41.—(Concluded)

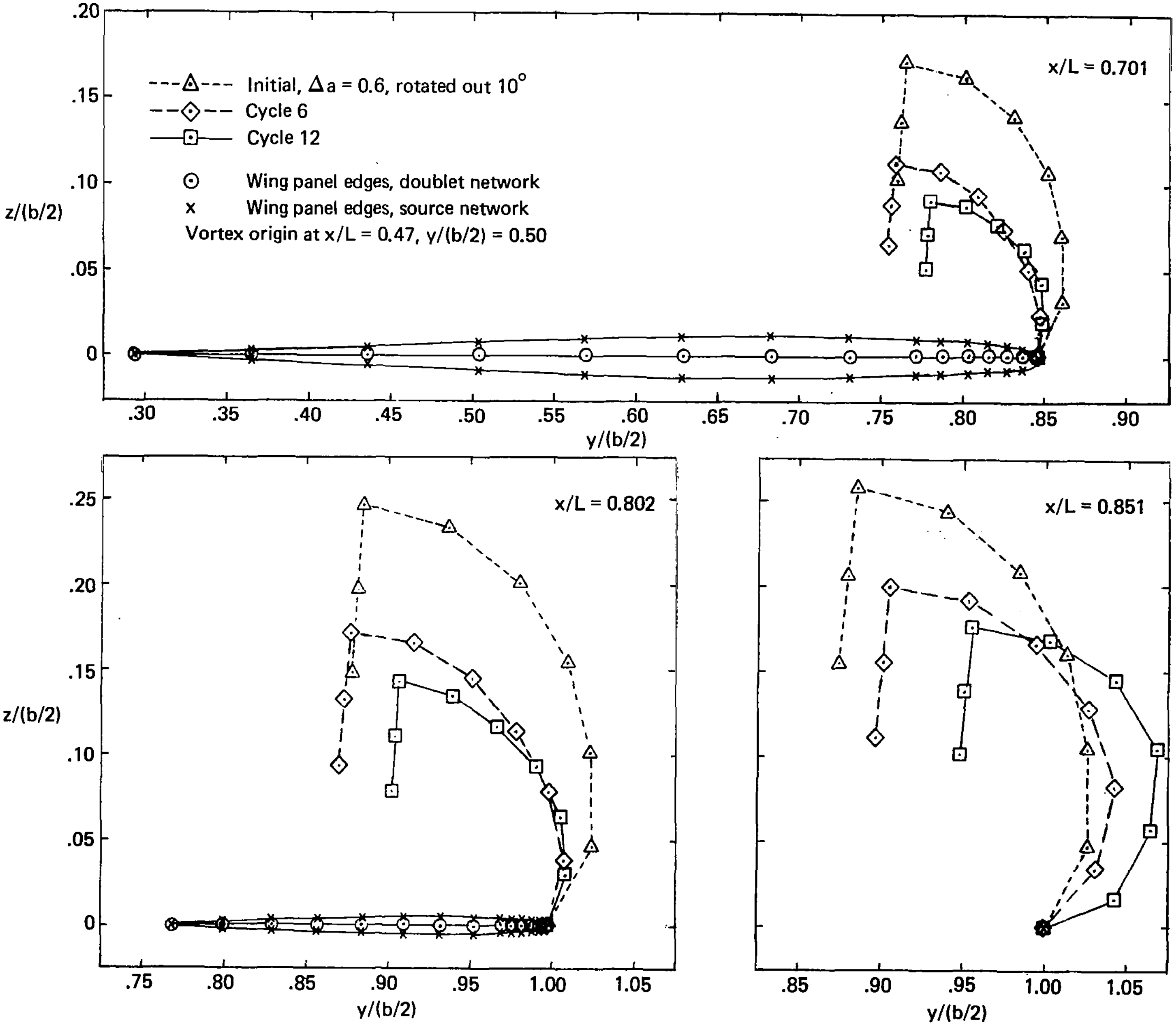

Figure 42.—Geometry of Panel Edges at Constant Body Stations, Flat Wing With Thickness, Δ a = 0.6, Initial Vortex Rotated Outward, M = 0.40, α = 8°, Several Cycles

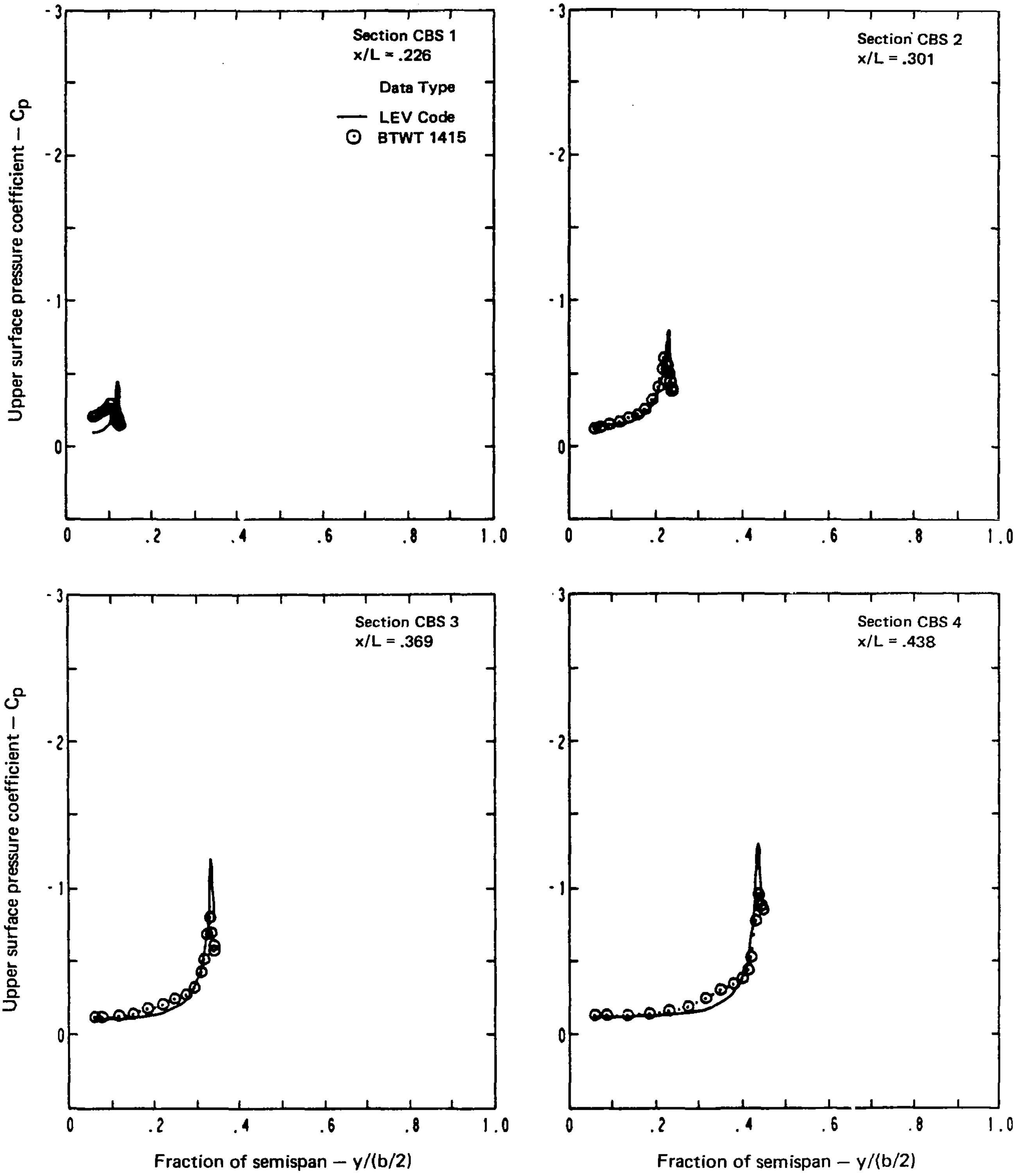

(a) Upper Surface Chordwise Pressure Distributions

Figure 43.—Pressure Distributions, Flat Wing With Thickness, $\Delta a = 0.6$, Initial Vortex Rotated Outward, $M = 0.40$, $\alpha = 8°$

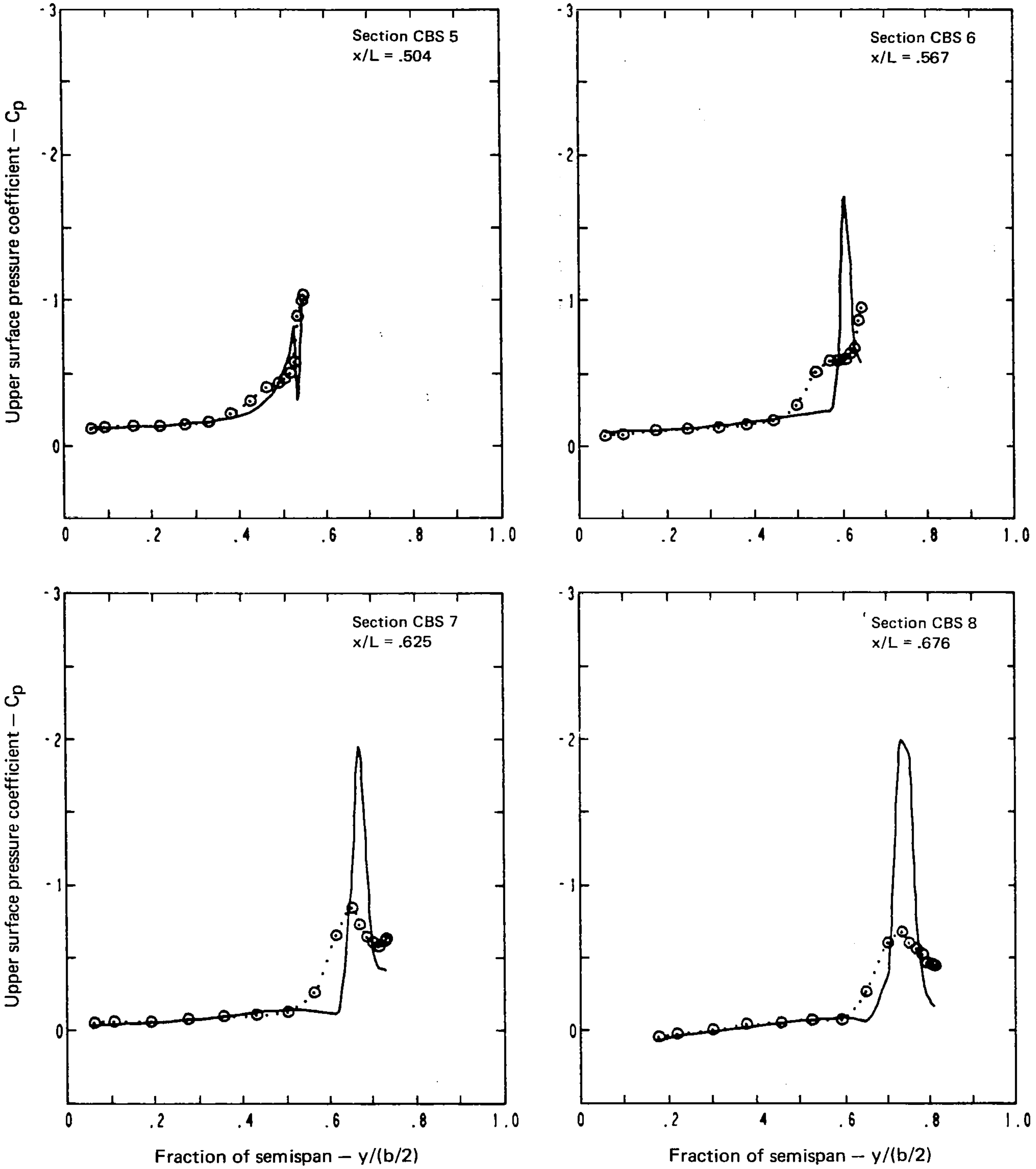

(a) (Continued)

Figure 43.—(Continued)

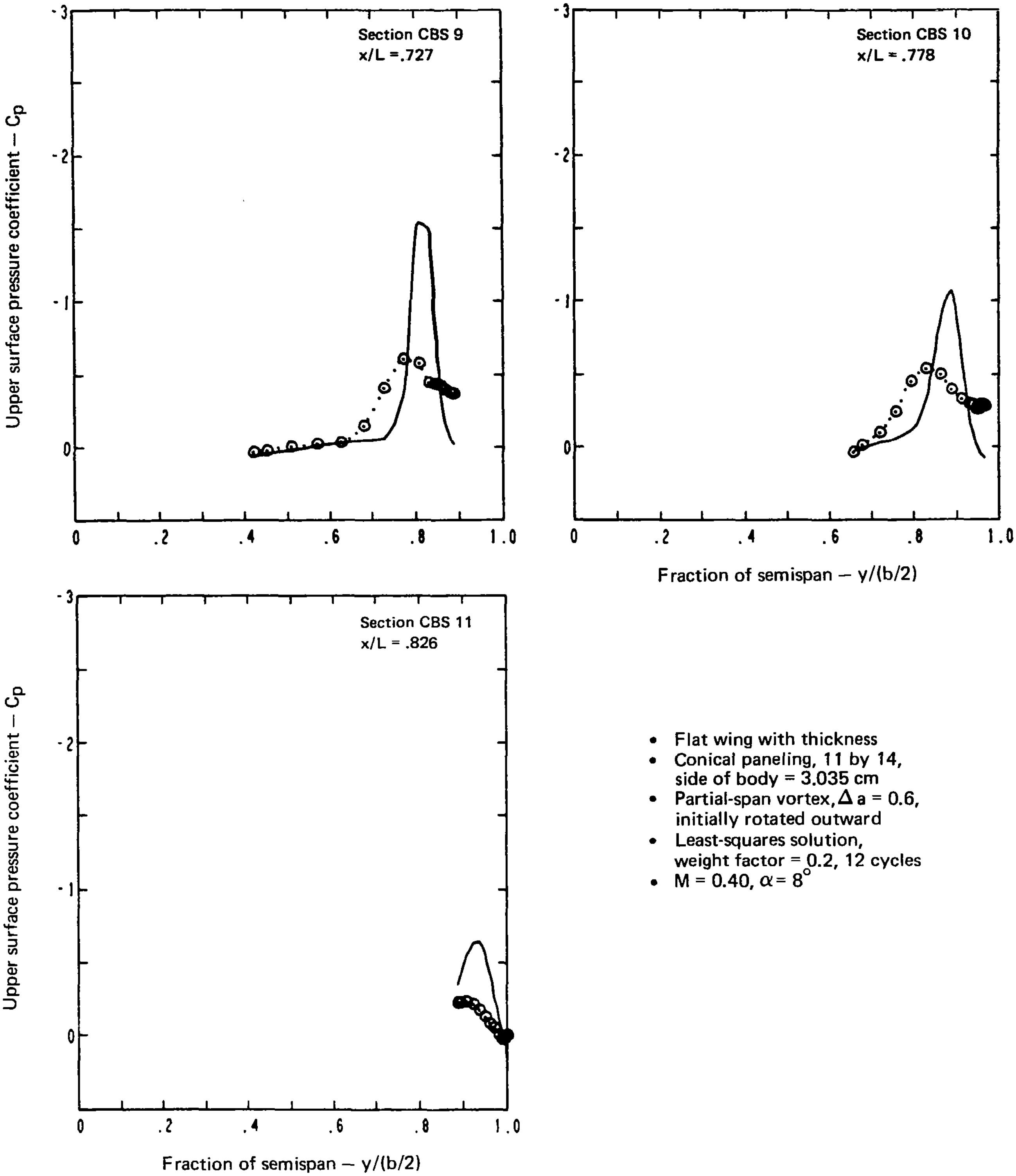

- Flat wing with thickness
- Conical paneling, 11 by 14, side of body = 3.035 cm
- Partial-span vortex, Δ a = 0.6, initially rotated outward
- Least-squares solution, weight factor = 0.2, 12 cycles
- M = 0.40, α = 8°

(a) (Concluded)

Figure 43.—(Continued)

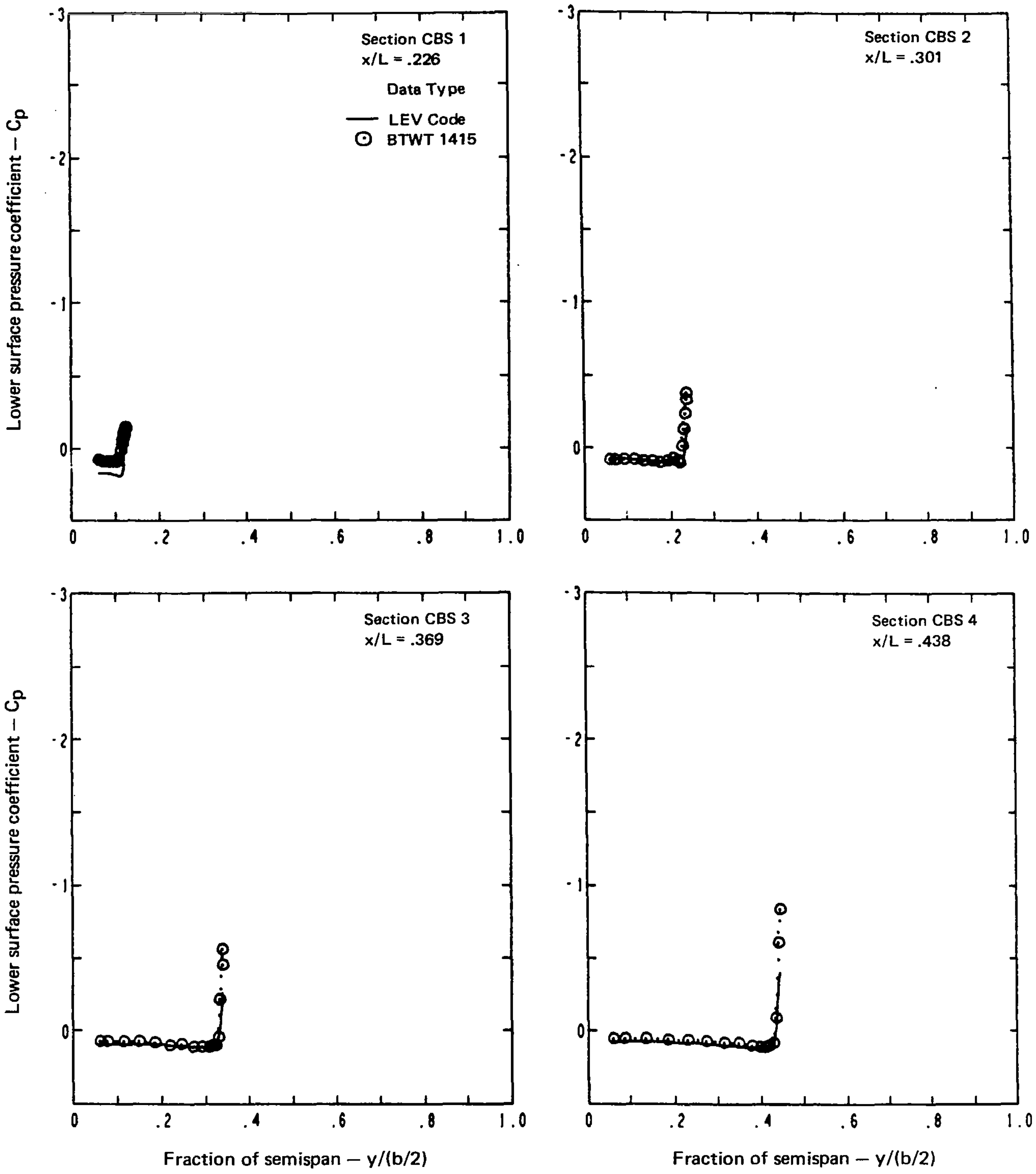

(b) Lower Surface Chordwise Pressure Distributions

Figure 43.—(Continued)

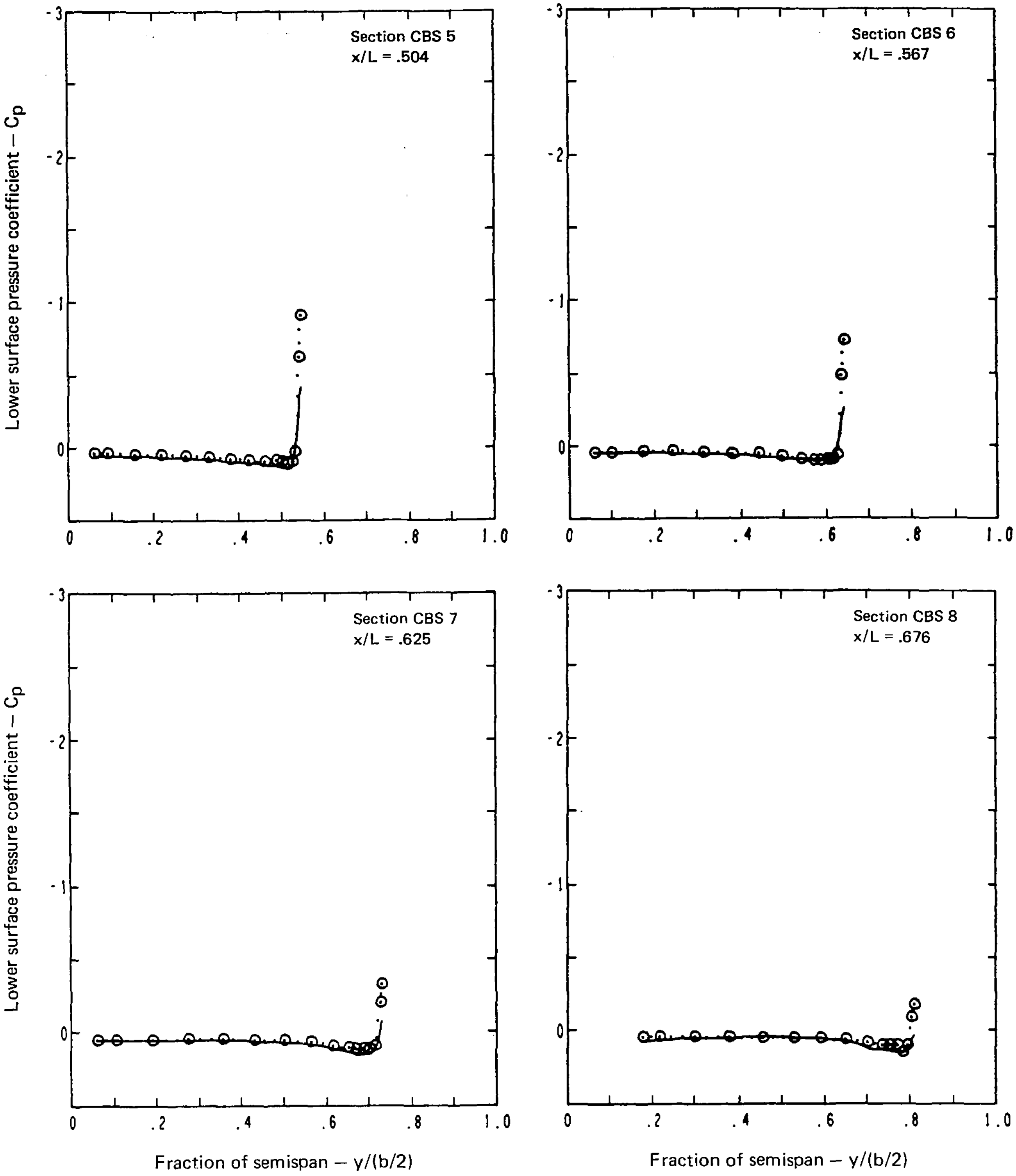

(b) (Continued)

Figure 43.—(Continued)

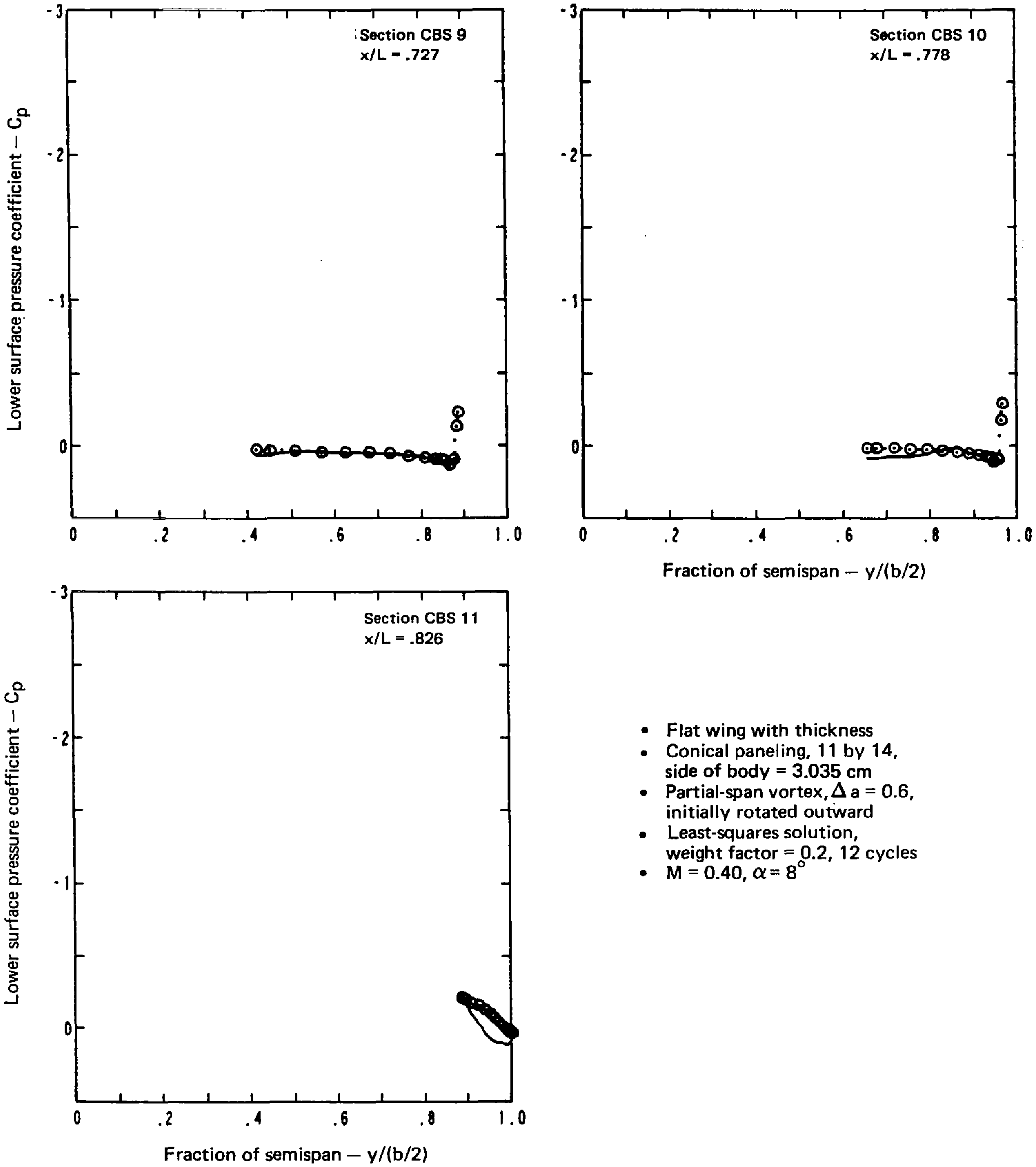

- Flat wing with thickness
- Conical paneling, 11 by 14, side of body = 3.035 cm
- Partial-span vortex, Δa = 0.6, initially rotated outward
- Least-squares solution, weight factor = 0.2, 12 cycles
- $M = 0.40$, $\alpha = 8^\circ$

(b) (Concluded)

Figure 43.—(Continued)

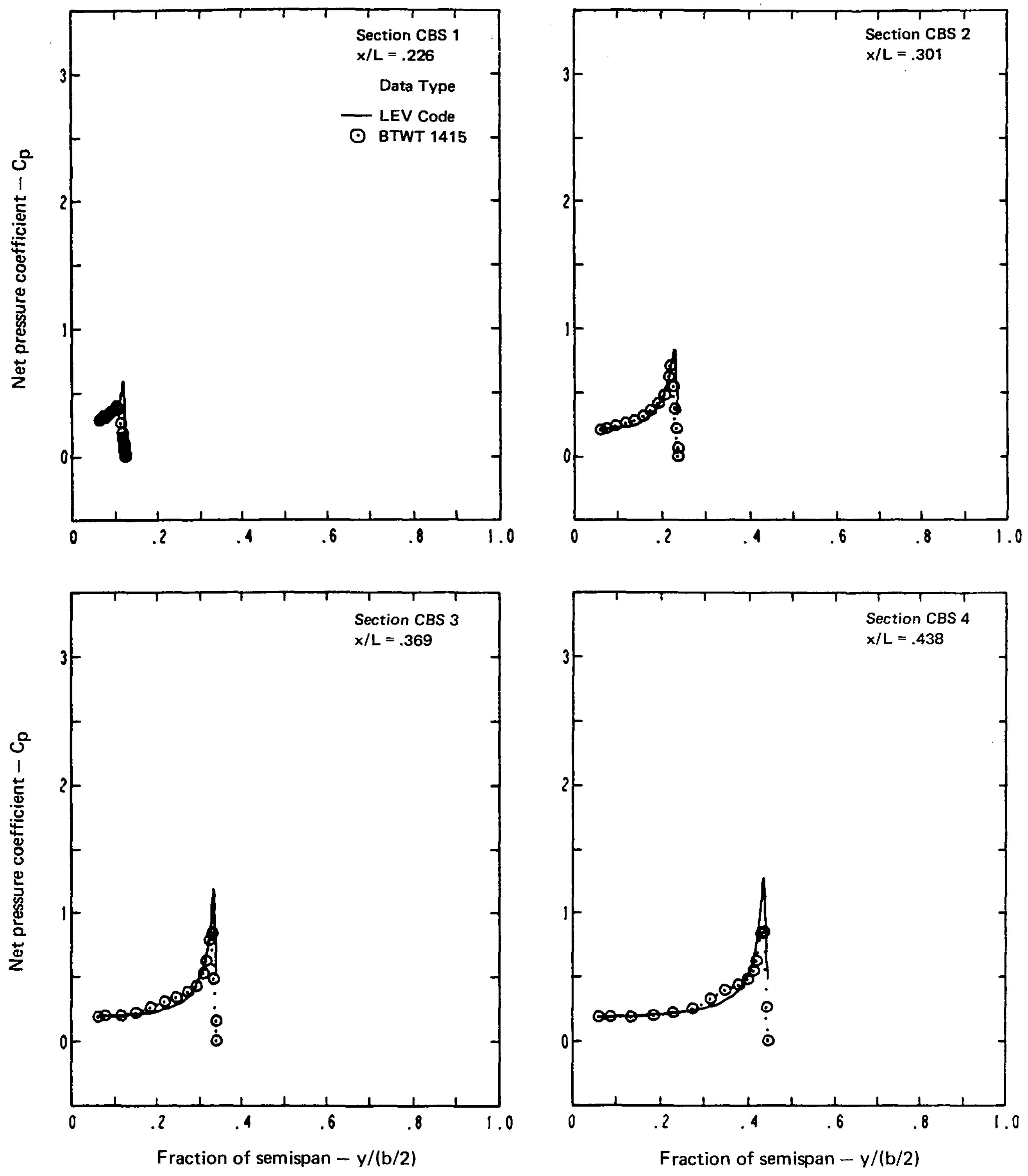

(c) Net Chordwise Pressure Distributions

Figure 43.—(Continued)

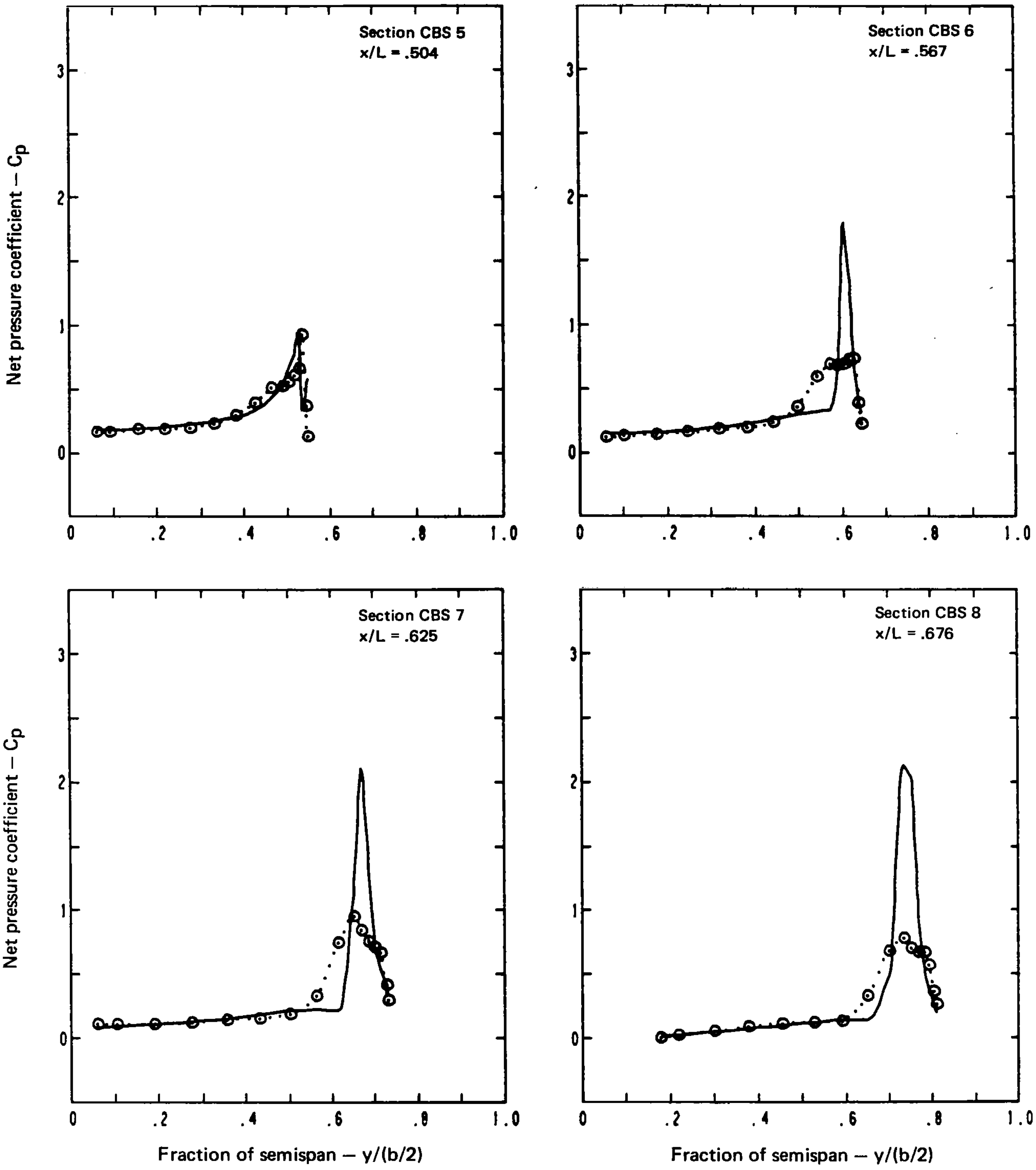

(c) (Continued)

Figure 43.—(Continued)

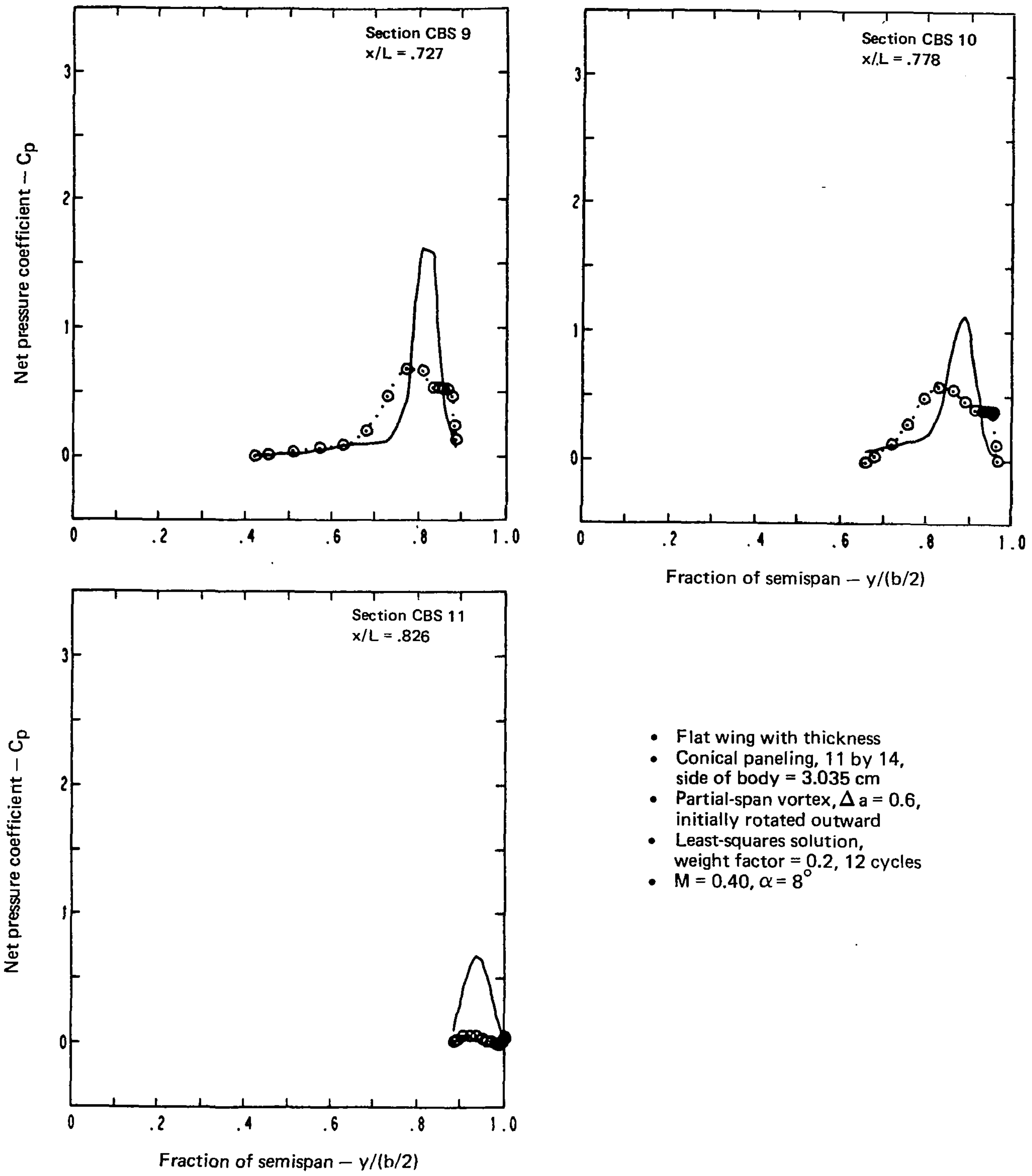

- Flat wing with thickness
- Conical paneling, 11 by 14, side of body = 3.035 cm
- Partial-span vortex, $\Delta a = 0.6$, initially rotated outward
- Least-squares solution, weight factor = 0.2, 12 cycles
- $M = 0.40, \alpha = 8^{\circ}$

(c) (Concluded)

Figure 43.—(Concluded)

☆U.S. GOVERNMENT PRINTING OFFICE: 1983 -6?? -008/ 6 REGION NO. 4

1. Report No. NASA CR-3642	2. Government Accession No.	3. Recipient's Catalog No.

4. Title and Subtitle AEROELASTIC LOADS PREDICTION FOR AN ARROW WING. Task III – Evaluation of the Boeing Three-Dimensional Leading-Edge Vortex Code	5. Report Date April 1983 6. Performing Organization Code
7. Author(s) Marjorie E. Manro	8. Performing Organization Report No. D6-51762-3
9. Performing Organization Name and Address Boeing Commercial Airplane Company P.O. Box 3707 Seattle, Washington 98124	10. Work Unit No. 11. Contract or Grant No. NAS1-15678
12. Sponsoring Agency Name and Address National Aeronautics and Space Administration Washington, D.C. 20546	13. Type of Report and Period Covered Contactor Report 14. Sponsoring Agency Code 743-01-12-02

15. Supplementary Notes

Technical monitor – Percy J. Bobbitt, Chief, Transonic Aerodynamics Division, NASA Langley Research Center, Hampton, Virginia.

Principal investigator – Marjorie E. Manro, Boeing Commercial Airplane Company.

16. Abstract

The accurate prediction of loads on flexible, low aspect-ratio wings is critical to the design of reliable and efficient aircraft. The conditions for structural design frequently involve nonlinear aerodynamics.

Two separated flow computer programs and a semi-empirical method for incorporating the experimentally measured separated flow effects into a linear aeroelastic analysis were evaluated under this contract. These three tasks are documented separately.

This report describes the evaluation of The Boeing Company's Three-Dimensional Leading-Edge Vortex (LEV) code (Task III). This code is an improved panel method for three-dimensional inviscid flow over a wing with leading-edge vortex separation. The governing equations are the linear-flow differential equation with nonlinear boundary conditions. The solution is iterative; the position as well as the strength of the vortex is determined. Cases for both full- and partial-span vortices were executed. The predicted pressures are good and adequately reflect changes in configuration.

The evaluation of R. P. White's (RASA Division of Systems Research Laboratories) separated flow method (Task I) is presented in NASA CR-3640. The development and evaluation of a semi-empirical method to predict pressure distributions on a deformed wing from an experimental data base (Task II) is described in NASA CR-3641.

These evaluations were based on a large, experimental data base (for three wing shapes), which was obtained under previous NASA contracts: NAS1-12875, NAS1-14141, and NAS1-14962. Linear theoretical methods were also evaluated under these contracts.

17. Key Words Aeroelasticity Experimental pressure distributions Aerodynamic theory Arrow-wing configuration Wind tunnel test	18. Distribution Statement Unclassified-unlimited Subject category 02

19. Security Classif. (of this report) Unclassified	20. Security Classif. (of this page) Unclassified	21. No. of Pages 218	22. Price A10